ABSTRACT

Title of dissertation: SHOCK TRAIN/BOUNDARY-LAYER INTERACTION IN RECTANGULAR SCRAMJET ISOLATORS

Jonathan Simon Geerts,
Doctor of Philosophy, 2015

Dissertation directed by: Associate Professor Kenneth H. Yu
Department of Aerospace Engineering

Numerous studies of the dual-mode scramjet isolator, a critical component in preventing inlet unstart and/or vehicle loss by containing a collection of flow disturbances called a shock train, have been performed since the dual-mode propulsion cycle was introduced in the 1960s. Low momentum corner flow and other three-dimensional effects inherent to rectangular isolators have, however, been largely ignored in experimental studies of the boundary layer separation driven isolator shock train dynamics. Furthermore, the use of two dimensional diagnostic techniques in past works, be it single-perspective line-of-sight schlieren/shadowgraphy or single axis wall pressure measurements, have been unable to resolve the three-dimensional flow features inside the rectangular isolator. These flow characteristics need to be thoroughly understood if robust dual-mode scramjet designs are to be fielded.

The work presented in this thesis is focused on experimentally analyzing shock train/boundary layer interactions from multiple perspectives in aspect ratio 1.0, 3.0, and 6.0 rectangular isolators with inflow Mach numbers ranging from 2.4 to 2.7. Secondary steady-state Computational Fluid Dynamics studies are performed to compare to the experimental results and to provide additional perspectives of the flow field. Specific issues that remain unresolved after decades of isolator shock train studies that are addressed in this work include the three-dimensional formation of the isolator shock train front, the spatial and temporal low momentum corner flow separation scales, the transient behavior of shock train/boundary layer interaction at specific coordinates along the isolator's lateral axis, and effects of the rectangular geometry on semi-empirical relations for shock

train length prediction.

A novel multiplane shadowgraph technique is developed to resolve the structure of the shock train along both the minor and major duct axis simultaneously. It is shown that the shock train front is of a hybrid oblique/normal nature. Initial low momentum corner flow separation spawns the formation of oblique shock planes which interact and proceed toward the center flow region, becoming more normal in the process. The hybrid structure becomes more two-dimensional as aspect ratio is increased but corner flow separation precedes center flow separation on the order of 1 duct height for all aspect ratios considered. Additional instantaneous oil flow surface visualization shows the symmetry of the three-dimensional shock train front around the lower wall centerline. Quantitative synthetic schlieren visualization shows the density gradient magnitude approximately double between the corner oblique and center flow normal structures. Fast response pressure measurements acquired near the corner region of the duct show preliminary separation in the outer regions preceding centerline separation on the order of 2 seconds. Non-intrusive Focusing Schlieren Deflectometry Velocimeter measurements reveal that both shock train oscillation frequency and velocity component decrease as measurements are taken away from centerline and towards the side-wall region, along with confirming the more two dimensional shock train front approximation for higher aspect ratios.

An updated modification to Waltrup & Billig's original semi-empirical shock train length relation for circular ducts based on centerline pressure measurements is introduced to account for rectangular isolator aspect ratio, upstream corner separation length scale, and major- and minor-axis boundary layer momentum thickness asymmetry. The latter is derived both experimentally and computationally and it is shown that the major-axis (side-wall) boundary layer has lower momentum thickness compared to the minor-axis (nozzle bounded) boundary layer, making it more separable. Furthermore, it is shown that the updated correlation drastically improves shock train length prediction capabilities in higher aspect ratio isolators.

This thesis suggests that performance analysis of rectangular confined supersonic flow fields can no longer be based on observations and measurements obtained along a single axis alone.

Knowledge gained by the work performed in this study will allow for the development of more robust shock train leading edge detection techniques and isolator designs which can greatly mitigate the risk of inlet unstart and/or vehicle loss in flight.

Shock Train/Boundary-Layer Interaction in Rectangular Scramjet Isolators

by

Jonathan Simon Geerts

Dissertation submitted to the Faculty of the Graduate School of the
University of Maryland, College Park in partial fulfillment
of the requirements for the degree of
Doctor of Philosophy
2015

Advisory Committee:
Associate Professor Kenneth H. Yu, Chairman/Advisor
Professor James D. Baeder
Associate Professor Christopher P. Cadou
Distinguished Professor Ashwani K. Gupta, Dean's representative
Associate Professor Allen Winkelmann

© Copyright by
Jonathan Simon Geerts
2015

Dedication

To the crews of Columbia STS-107, Challenger STS-51L, and Apollo 1. Your courage, commitment, and professionalism continue to inspire many to follow in your footsteps.

Acknowledgments

This work was conducted as part of the UMD-AEDC Hypersonic Center of Testing Excellence project, sponsored by AFOSR, TRMC, and AEDC. I would like to acknowledge the financial support from the Air Force Office of Scientific Research under grant FA9550-10-1-0535, managed by Dr. Michael Kendra. A special thank you to Dr. Kendra for actively providing me, and other graduation students, with contacts for post-graduation job opportunities.

I would like to extend my deepest gratitude to my research adviser Dr. Kenneth Yu for allowing me to grow tremendously as an engineer, researcher, and person. Without his avid support, enthusiasm, and invaluable insight this work would not have been possible. I want to acknowledge his unwavering support for his graduate students, making room in his always busy schedule to brainstorm, troubleshoot, or explain complex engineering problems and opportunities. Allowing me to travel to numerous conferences, his experience and guidance were invaluable in shaping my skills and confidence in presenting and communicating my research results and ideas.

I want to thank my committee members for the valuable insight and conversations regarding my work, and for teaching the great courses from which i have learned so much. Special thanks to Dr. Christopher Cadou for offering me a research position in his lab as an undergraduate sophomore which initiated my curiosity and interest in research. To Dr. Allen Winkelmann for allowing me to use the supersonic wind tunnel and for helping me in numerous experimental setups. To Dr. James Baeder for teaching the Computational Fluid Dynamics courses that formed the foundation for my computational work, and to Dr. Ashwani Gupta for the insightful discussions regarding my early work in Background Oriented Schlieren and Focusing Schlieren Deflectometry.

Invaluable technical support was also received from the personnel at AEDC's Hypervelocity Wind Tunnel 9 in White Oak, Maryland. A very special thank you is extended to Mike Smith for being my mentor at Tunnel 9 and providing me with the diagnostics direction of this thesis. His expertise in optical diagnostics is truly one of a kind, and from him I have learned most of the critical skills that has made the data acquisition portion of this thesis work possible. Numerous technical conversations with Dr. Eric Marineau are also greatly appreciated, as is the exemplary

leadership of directors John Lafferty and Dan Marren, as well as Dr. Mark Lewis, for making the UMD-AEDC program such a great environment for the growth of the hypersonics leadership of tomorrow.

The experimental portion of this research would not have been possible without the skill, dedication, and professionalism of our machinist Howard Grossenbacher. Thank you for taking the time out of your always busy schedule to teach me how to use a variety of machines and tools dating back to my time as an undergraduate co-op student at the Glenn L. Martin wind tunnel. I am the engineer I am today thanks to the great opportunity and experience provided by the Glenn L. Martin Wind Tunnel undergraduate co-op program. Many thanks to Hareen Aparakakankanange (now CEO of Aerolab LLC), Ahmad Kassaee, and Dr. Jewel Barlow (director) for teaching me countless practical engineering skills and techniques. These important lessons have helped me tremendously to date and will undoubtedly play a major role in my future endeavors. A special thank you goes out to Paul Vasilescu, vice president of engineering at Aerolab LLC, for guiding me through my computational work and for letting me use the 16-core workstation on which the simulations were performed.

Having previously graduated from the University of Maryland with a Bachelor's and Master's degree in Aeronautical Engineering, the Department of Aerospace Engineering has provided me with incredible opportunities and provided a rigorous academic environment which adequately prepared me for an intellectually challenging graduate program. Thank you to all the professors and lecturers for continuously challenging and demanding the best out of the graduate students in the department. Special thank you to LaVita Williams and Laura Thorsen for handling many material purchase orders and to Tom Hurst, Becky Sarni, and Deborah Chandler for clarifying and guiding me through many complex administrative processes. The help received from Andrew Lee Jr. in re-configuring the supersonic wind tunnel doors is also greatly appreciated.

No one can get through a collegiate career alone, and I have to thank my family for all the support over the last 9 years of continued undergraduate and graduate education. A very special thank you to my parents, Dr. Hugo Geerts and Michele Asselman, for teaching me the values and

importance of a well-rounded lifestyle and a thorough education from a very young age, and for financially supporting my undergraduate education. I owe a lot to my fellow researchers and lab mates at the Advanced Propulsion Research Laboratory and within the greater UMD Hypersonics community. Many thanks to Drs. Ryan Houim, Kevin Ryan, Camilo Aguilera, and Jeremy Knittel for thoroughly preparing me for my doctoral comprehensive exams. Technical discussions regarding my research with Nathan Shumway, Sammy Park, Jason Burr, Joe Chung, Robert Feiveshon, Vijay Ramasubramanian and Drs. Amardip Gosh and Neil Smith are also greatly appreciated. Special thanks to Sammy Park for helping me set up my wind tunnel triggering hardware, Jason Burr for helping me program the National Instruments data acquisition software, and Jonathan Brooks for helping me set up the Tunnel 9 calibration wind tunnel Mie-scattering experiment.

I would also like to thank Lt. Col. Nizar Bechara (USAF, ret.), Chief Flight Instructor at Royal Air Flight Training, for teaching me so many valuable lessons in and out of the airplane. His enthusiasm for teaching remains unmatched, and I thank him sincerely for guiding me through what remains personally my proudest achievement to date, obtaining my Private Pilots License.

Physical fitness has played a major role in my graduate school career. From the weight-room to the pool, and from the hill sprints to the Mixed Martial Arts sparring sessions, thank you to the countless training and workout partners that have helped me to develop into a physically and mentally stronger person. A big thanks goes out to the MMA-crew over the years for the valuable training and entertaining company during Saturday night UFC viewing events. Mixed Martial Arts training has taught me the discipline, grit, and work-ethic required to succeed in all aspects of life. Last but certainly not least, I can not express in words how much I appreciate the endless support received from the wonderful Elizabeth Woytowicz. It is safe to say that the last two years have been the best of my life.

Table of Contents

List of Tables

List of Figures

A	Clear aperature of schlieren lens (Focusing Schlieren)
A_3	Effective diameter of camera lens (Schlieren)
a	Static speed of sound or deflection of undisturbed image (Focusing Schlieren)
Δa	Deflection of disturbed image (Focusing Schlieren)
a_I	Interrogation window area (BOS)
b	Cutoff grid opaque line spacing (Focusing Schlieren)
c, c'	Speed of light through a vacuum, medium
c_I	Contrast of the schlieren system
C	Sutherland's temperature
d_{FS}	Image resolution limit due to slit diffraction (Focusing Schlieren)
d_S	Image resolution limit due to circular aperature diffraction (Schlieren)
D	Axisymmetric duct diameter (circular cross section)
D_{cav}	Cavity depth scale (Focusing Schlieren Deflectometry)
D_H	Hydraulic diameter (rectangular cross section)
D_i	Particle displacement in the flow field (BOS)
D_J	Jet (Helium/Nitrogen) diameter (Focusing Schlieren Deflectometry)
DS	Depth of sharp focus (Focusing Schlieren)
DU	Depth of unsharp focus (Focusing Schlieren)
f	Focal length of camera lens/schlieren mirror
f_w	Friction coefficient at the wall (Fanno flow)
F_{FS}	Distance from cutoff grid to image plane (Focusing Schlieren)
F_S	Distance from knife-edge to image plane (Schlieren)
f_1	Generic cross-correlation signal 1 (Focusing Schlieren Deflectometry)
$G(\lambda)$	Gladstone-Dale coefficient
g	Generic cross-correaltion signal 2 (Focusing Schlieren Deflectometry)
H	Boundary layer shape factor or minor axis duct length scale (duct height)
H_F	H-factor (boundary layer)
k	Convective speed ratio, U_c/U_∞ (Focusing Schlieren Deflectometry)
L	Isolator longitudinal length scale
L_{cav}	Cavity length scale (Focusing Schlieren Deflectometry)
L_{diff}	Wind tunnel diffuser length (UMD SSWT)
L_{FS}	Distance from source grid to imaging lens (Focusing Schlieren)
L'_{FS}	Distance from schlieren lens to cutoff grid (Focusing Schlieren)
L'_S	Distance from receiving mirror to physical cutoff (Schlieren)
l_{FS}	Distance from object in flowfield to schlieren lens (Focusing Schlieren)
l_S	Distance from object in flowfield to receiving mirror (Schlieren)
l'_{FS}	Distance from schlieren lens to iamge plane (Focusing Schlieren)
l'_S	Distance from receiving mirror to image plane (Schlieren)
Pr	Prandtl number
M	Mach number
M_0	Camera lens magnification factor (BOS)
m_{cav}	Cavity (shear layer) acoustic mode
m_{FS}	Image magnificaiton factor, l'_{FS}/l_{FS} (Focusing Schlieren)
m_S	Image magnificaiton factor, l'_S/l_S (Schlieren)
N	Image density (BOS)
n	Index of refraction
n_{cutoff}	Number of grid lines per millimeter at cutoff grid (Focusing Schlieren)
n_{source}	Number of grid lines per millimeter at source grid (Focusing Schlieren)
n_{tot}/V	Total number of molecules per volume (BOS)
P	Static pressure
q_{scat}	Mie-scattering q-factor
r	Recovery factor (boundary layer) or particle diameter (Mie-scattering)
R	Specific gas constant (J/kg.K) or l_{FS}/A (Focusing Schlieren)

Re	Reynolds number
Re_θ	Boundary layer momentum thickness based Reynolds number
S	Total shock train length
S_C	Upstream corner separation length scale
S_T	Centerline derived shock train length scale
s_I	Sensitivity of the schlieren system
T	Static temperature
t	Time
U	Flow velocity
u_*	Friction velocity at the wall (CFD)
V_0	Light energy transfer function (BOS)
w_{FS}	Inage resolution limit due to grid diffraction (Focusing Schlieren)
w_S	Image resolution limit due to lense edge diffraction (Schlieren)
x	Longitudinal duct axis coordinate
y	Vertical duct axis coordinate
Δy_0	Particle displacement on object plane (BOS)
Δy_i	Particle displacement on image plane (BOS)
Y^+	Non-dimensional wall distance (CFD)
Z_B	Distance from background plane to camera image plane (BOS)
Z_C	Distance from test section to camera lens (BOS)
Z_D	Distance from background to test section (BOS)
Z_F	Distance from BOS pattern to Fresnel lens (BOS)
Z_I	Distance from camera lens to camera image plane (BOS)
Z'_L	Distance from Fresnel lens to light source focal plane (BOS)
Z'_P	Distance from light source focal plane to background wall (BOS)
Z_{TS}	Test section width
z	Lateral duct axis coordinate

Subscripts

0	Stagnation conditions
i	Station index or inlet entrance station (DSMJ cycle)
1	Duct minor axis boundary layer parameter
2	Isolator entrance station or duct major axis boundary layer parameter
3	Combustor entrance station (DSMJ cycle)
4	Exhuast nozzle entrance station (DSMJ cycle)
e	Boundary layer edge condition or exhaust nozzle exit station (DSMJ cycle)
avg	Average value
∞	Freestream conditions
FS	Focusing schlieren
S	Schlieren
w	Wall bounded value

Greek symbols

α	Rossiter formula empirical constant (Focusing Schlieren Deflectometry)
β	Light refractivity (n-1)
ϵ	Light refraction angle through variable density gradient medium
ϵ_{FS}	Focusing schlieren sensitivity
ϵ_S	Schlieren system sensitivity
δ	99% Velocity boundary layer thickness
$\delta*$	Displacement thickness of boundary layer
θ	Momentum thickness of boundary layer
ρ	Flow density (kg/m^3)
γ	Ratio of specific heats
λ	Wavelength of light

λ_{mfp}	Mean-free path length
ϕ	Line pairs needed to form each point in image (Focusing Schlieren)
ϕ_p	Background particle diameter (BOS)
τ	Normalized test time ($t/t_{unstart}$) or
	Characteristic time lag between two signals (Focusing Schlieren Deflectometry)
τ_f	Flow time scale (Mie-scattering)
τ_l	Point spread function of imaging lens (BOS)
τ_p	Particle aerodynamic response time (Mie-scattering)
τ_w	Wall shear stress
ω	Diffraction limited resolution (Focusing Schlieren)
μ	Kinematic viscosity of fluid ($kg/m.s$)
σ	Image smoothness parameter (Focusing Schlieren) or
	velocity standard deviation (Focusing Schlieren Velocimetry)
σ_p	Particle diameter (BOS & Mie-scattering)

Acronyms

AEDC	Arnold Engineering Development Center
AFOSR	Air Force Office of Scientific Research
AFRL	Air Force Research Laboratory
APD	Avalanche Photodiode
AR	(isolator) Aspect Ratio
BOS	Background Oriented Schlieren
C-D	Converging-Diverging (nozzle)
CFD	computational fluid dynamics
CII	Combustor Inlet Interaction
CTBL	Compressible Turbulent Boundary Layer
DARPA	Defense Advance Research Project
DES	Detached Eddy Simulation
DNS	direct numerical simulation
DMSJ	Dual-Mode Scramjet
FFT	Fast Fourier Transform
FS	Focusing Schlieren
FSD	Focusing Schlieren Deflectometry
FSDV	Focusing Schlieren Deflectometry Velocimeter
ICBM	Intercontinental Ballistic Missile
JHU	Johns Hopkins Univeristy
LED	Light Emitting Diode
LEO	Lower Earth Orbit
LES	Large Eddy Simulation
MATLAB	Matrix Laboratory
MOC	Method of Characteristics
NASA	National Aeronautics and Space Administration
NASP	National Aerospace Plane
OPL	Optical Path Length
PGS	Prompt Global Strike
PMT	PhotoMultiplier Tube
PSC	Propulsion Subsystem Controller
RANS	Reynolds Averaged Navier Stokes
RLV	Reusable Launch Vehicle
RMS	Root Mean Square
SBLI	Shock/Boundary-Layer Interaction
SDES	Stimulated Detached Eddy Simulations
SSR	Solid State Relay
SSTO	Single Stage to Orbit

SSWT	Supersonic Wind Tunnel
STBLI	Shock/Turbulent Boundary-Layer Interaction
STTBLI	Shock Train/Turbulent Boundary-Layer Interaction
T9	(USAF AEDC) Hypervelocity Wind Tunnel 9
T&E	Testing & Evaluation
TKE	Turbulent Kinetic Energy (model)
TRMC	Test Resource Management Center
UMD	University of Maryland
USAF	United States Air Force

Chapter 1: Introduction

1.1 Background & Motivation

The airbreathing dual mode supersonic combustion ramjet (DMSJ) engine cycle concept has long held promising potential in propelling a wide range of applications requiring long range and high cruise flight velocities (Mach number ranging from 3 to 10 for hydrocarbon and up to orbital velocities for hydrogen based cycles) [1]. Applications include high-altitude atmospheric cruise, access-to-orbit ascent, and advanced long-range strike systems. Traditionally, rocket-based power cycles are the most common form of propulsion used to accelerate vehicles to hypersonic conditions. A vehicle propelled to hypersonic flight velocities by an airbreathing-based engine cycle along the majority of its in-atmosphere flight envelope does not require large on-board oxidizer storage. The resulting increase in payload mass fraction and specific impulse is thus one of the most significant advantages to lead to reduced costs and enhanced system reliability and vehicle safety [2–4].

In an effort to mature air-breathing hypersonic propulsion technology, both traditional and novel experimental diagnostic tools have to be tailored to match the characteristics of the flow-field of interest. One such flow-field is that of the DMSJ isolator, an internally-confined supersonic compressible flow regime characterized by asymmetric and non-uniform shock-separated, mixed supersonic and subsonic flow, and dynamically changing inlet and outlet conditions. The isolator is used in this study as a flow environment in which different qualitative and quantitative diagnostic techniques are developed or refined. Using these tools, isolator flow physics are observed and analyzed. This thesis thus contains two major elements:

- The design, development, refinement, and implementation of a variety of qualitative and quantitative diagnostic tools making the above mentioned experimental observations feasible.
- The analysis of dynamic isolator flow physics and the effects of aspect ratio on three-dimensional low momentum corner flow separation and modified pseudo-shock length relations. These areas are addressed through primary experimental observation and secondary computational investigation.

The first element is motivated by a collaboration between the University of Maryland (UMD) and the United States Air Force's (USAF) Arnold Engineering Development Center (AEDC). Spanning a range of sponsored studies over a number of institutions, this initiative is intended to develop diagnostics and techniques (both experimental and numerical) for use in the hypersonic Testing & Evaluation (T&E) community. The development and refinement efforts of the experimental diagnostic tools presented in this work, performed in supersonic flow facilities, will serve as a stepping stone for application to large-scale, hypersonic environments such as those found at AEDC's Hypervelocity Wind Tunnel 9 in White Oak, Maryland. The diagnostic techniques refined in this work are characterized by a few important aspects critical to Tunnel 9's needs: they are completely non-intrusive, they yield quantitative measurement, and they are compatible with the multitude of other diagnostics incorporated in the typical testing environment. These diagnostic technique, however, can also be readily implemented in a variety of other flow environments within AEDC's wide family of test facilities. The implementation of these techniques in the current supersonic facilities are furthermore motivated by the need to analyze the three-dimensional flow features expected in a rectangular cross section isolator duct.

The second element is intended to contribute dynamic Shock Train/Turbulent Boundary-Layer Interaction (STTBLI) knowledge to the literature. Of particular interest is the behavior of flow in regions confined by two viscous walls, as found in the four corners of the rectangular isolator duct. The four primary areas of interest regarding the study of shock train dynamics covered in this thesis include:

- Visualizing the three-dimensional shock train front to expand on observations made with

traditional, line-of-sight, two-dimensional projection visualization techniques.

- Evaluating precursors to engine-unstart for next-generation shock train leading edge sensing and position control applications.
- Improving upon traditional empirical correlations for circular cross-sectional duct shock train length estimation.
- Compiling qualitative and quantitative data sets for use in evaluating the capability of Computational Fluid Dynamics (CFD) studies to resolve the complicated flow physics.

To construct a foundation upon which the discussion of Shock Train/Turbulent Boundary-Layer dynamics can be expanded, an introduction to the isolator and associated flow features is provided below. Prior to this, a brief introduction to the DMSJ propulsion cycle which houses the isolator is offered.

1.1.1 The Dual-Mode Scramjet Cycle

As the name implies, the DMSJ concept can operate in both ramjet (subsonic combustion) and scramjet (supersonic combustion) mode covering a flight Mach number regime of 3 to up to 20 through the use of a single fixed geometry combustor [5,6]. The DMSJ cycle in itself is not capable of producing static thrust, thus it must be accompanied by another cycle capable of bringing it from rest up to ramjet starting flight velocities. Candidates for such initial cycles include turbine- [7] and rocket based [8] applications.

To cover the wide flight Mach number regime, thermal efficiency and high static temperature induced dissociation of working fluids dictate that the DMSJ must operate in ramjet mode for flight Mach numbers of less than 5, and scramjet mode for flight mach numbers greater than 7, with a ramjet-to-scramjet transition region in between [3]. The results presented in this study will cover the initial operating regime discussed above, with a predominant isolator inlet flow Mach number of 2.4.

For completeness, a brief description of the pure ramjet and pure scramjet is offered below,

followed by a description of the DMSJ cycle. The ramjet configuration, sketched in Fig. 1.1a, operates on the principle of subsonic combustion. Well suited to operate in the flight Mach number regime of 3.0-6.0, it achieves these subsonic combustion conditions by compressing the incoming supersonic air stream through initial forebody oblique shock wave compression, followed by a diffuser (a converging duct) designed to trigger further flow deceleration and transition to subsonic flow by means of a terminal normal shock (positioned just upstream of the combustor). This compression process culminates in the primary throat. Combustion takes place subsonically and high pressure gasses accelerate from subsonic to supersonic conditions through a secondary throat.

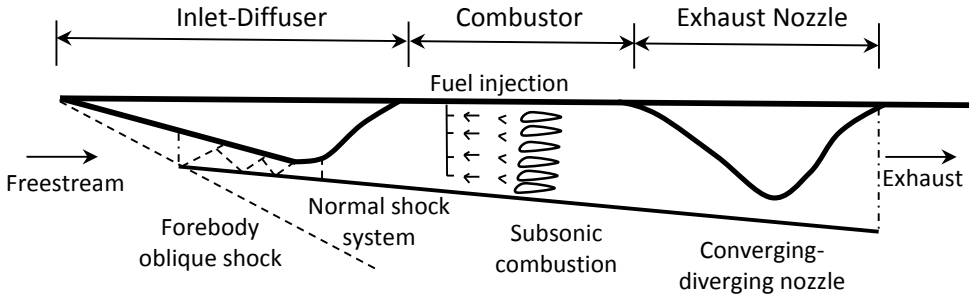

(a) Planar ramjet geometry

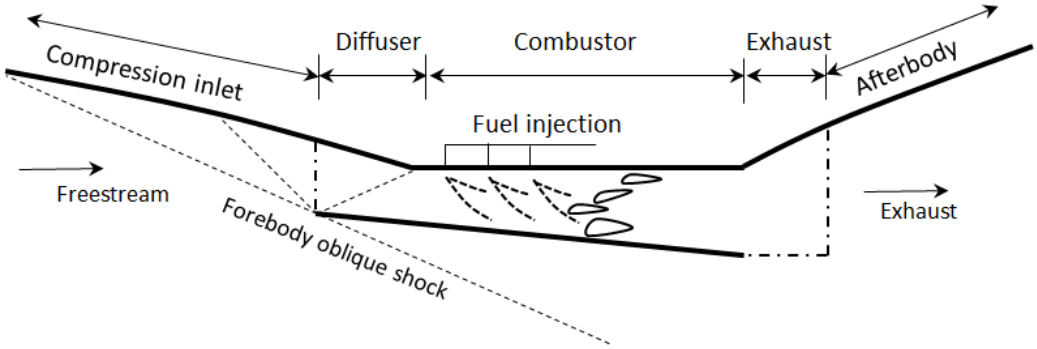

(b) Planar scramjet geometry

Figure 1.1: Planar geometries of pure ramjet and pure scramjet engine configurations (sketch adapted from Ref. [3]).

In the Mach number regime encountered by scramjet operation (Mach number greater than 6.0), the trade-off between kinetic energy (velocity decrease) and internal energy (temperature, pressure, density increase) brought about by subsonic deceleration would result in adverse perfor-

mance characteristics. Unlike the ramjet configuration (with two physical throats), the scramjet cycle utilizes locally supersonic combustion to avoid the previously discussed performance issue and thus avoids the requirement of a physical throat. Shown in Figure 1.1b, the engine cycle utilizes partial compression of the incoming air stream through the use of a converging inlet-diffuser in order to achieve static pressure rise and raise the thermodynamic potential of the flowfield prior to combustion. Fuel is injected, mixed with the incoming air, and burnt in short residence times characteristic of supersonic combustion. Acting as a free expansion surface, the supersonic products are further accelerated by the diverging vehicle afterbody. The pure scramjet cycle must be accelerated to scramjet starting flight velocities, usually accomplished by a rocket powered primary booster phase.

To cover both flight regimes in a physically throat-less geometry, the DMSJ concept was introduced by Curran and Stull in the early 1960s as means of combining both cycles in a single, fixed geometry. This was proposed by utilizing the main scramjet duct for subsonic combustion in the lower Mach number regime to provide the thrust required to reach scramjet take-over flight velocity (Mach 6-7) [9].

A generic representation of a DMSJ engine cycle operating in the lower hypersonic regime (Mach 3 to 6) is shown in Fig. 1.2. The vehicle forebody and inlet houses a series of shock waves which offer flow compression prior to entering a duct called an isolator. Depending on the mode of operation, the isolator delivers subsonic (ramjet-mode) or supersonic (scramjet-mode) flow to the burner section where fuel-air mixing and combustion occur. Finally, a diverging afterbody downstream of the combustor acts as a free expansion surface, accelerating the supersonic outflow. There are no physical throats in the flowpath (unlike the pure ramjet cycle). Supersonic reacceleration prior to entering the exhaust in ramjet-mode is made possible by the introduction of a thermally choked throat. Superimposed onto Figure 1.2 is the station nomenclature used throughout this work. In alignment with traditional cycle analysis, the inlet plane of the isolator is labeled station 2, whereas its exit plane (combustor inlet plane) is labeled station 3.

Along with its conception, efforts to demonstrate the viability and potential of dual mode

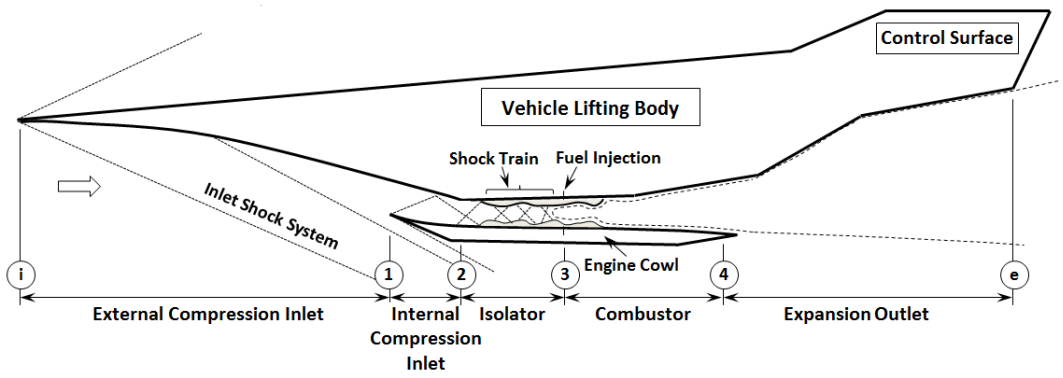

Figure 1.2: Simplified two-dimensional planar sketch of a DMSJ powered hypersonic airbreather.

cycles have been pursued since the early 1960s [10]. During that time, several programs pursued primarily by NASA, the U.S. Air Force, and the U.S. Navy looked to develop significant advances in dual-mode and pure scramjet engine technological maturation for a variety of purposes, with the latter two organizations primarily focused on weapon delivery platform development [11]. Fundamental research into similar dual-mode and scramjet cycle technologies was likewise pursued by Russian researchers at this time. [12].

The introduction of the National Aerospace Plane (NASP) program by the Defense Advance Research Projects Agency (DARPA) in the mid 1980s as an experimental Single Stage To Orbit (SSTO) platform (named the X-30) revitalized large scale, flight-worthy scramjet development in the United States. Representing a multidisciplinary effort spread across both industry and academia, research directly supporting the program resulted in advances made in the fields of high speed aerodynamics, computer modeling, materials, and short residence time mixing and combustion to name a few [13]. The program was canceled at the start of 1995, before any of the planned test flights had taken place.

At the turn of the century, NASA's 3rd generation air-breathing based Reusable Launch Vehicle (RLV) program projected launch cost of $ 100/lb of payload to Lower Earth Orbit (LEO) and 10^{-6} failure rate [6, 14]. This has re-invigorated technological maturation of the pure scramjet and DMSJ concepts during the past decade. The first major, flight worthy test-bed program of these re-invigoration efforts was NASA's Hyper-X program and its flagship vehicle, the hydrogen

fueled and scramjet powered X-43A. Accelerated by a Pegasus rocket first stage to a scramjet take-over velocity of approximately Mach 5, two successful scramjet powered flight tests were performed in 2004 culminating in a top flight speed exceeding Mach 9.0 [15–17]. A dual-mode ram/scramjet cycle was proposed for the follow-on vehicle, the X-43B, but no variations on the X-43A were ever fielded.

A hydrocarbon (JP-7) fueled variation of the original X-43A engine was pursued by the Air Force Research Laboratory (AFRL) for the Scramjet Engine Demonstrator program, which resulted in the X-51A WaveRider concept. Similarly boosted to scramjet take-over speed by a first stage rocket, the X-51A program performed a total of four test flights between 2010 and 2013 [18, 19]. With the first and fourth flight a success, the second flight test experienced an unstart event early after first stage separation. Other innovative supersonic combustion flight test programs including HyShot [20], HIFiRE [21], and a number of international efforts continue to contribute valuable knowledge regarding the capabilities and feasibility of sustained supersonic combustion propelled vehicles.

Motivated by recent shifts in U.S. foreign policies toward the pacific, often referred to as the 'Pacific Pivot' , hypersonic based platforms will be critical in providing capabilities of traversing long distances in minimal time. More generally, the idea of delivering a precision-guided weapon anywhere in the world within one hour, otherwise known as Prompt Global Strike (PGS), is considered to be a critical and required capability for the United States to more rapidly respond to a large variety of threats [22, 23]. Furthermore, the predictability of Inter Continental Ballistic Missiles (ICBMs) and limited maneuverability envelope of conventional rocket powered hypersonic weapon platforms have motivated the search for an additional hypersonic capability for the past four decades [11].

The theory and (simplified) ground-simulations of pure supersonic and combined-mode combustion concepts have been developed and pursued for decades, yet the technology is still at its infancy in the realm of being proven flight-worthy. Flight testing is a critical portion of the technological maturation process, as performance data can be collected that cannot be obtained using

ground testing alone. Parameters such as installed engine performance, transient flight conditions, and inherent ground testing limitations are all areas that flight testing is responsible for addressing [18]. Due to the technological challenge, no flight-worthy DMSJ cycles known to the public have been tested, but advances made in flight-worthy scramjet cycles will be combined with the knowledge of ramjet-operation to pave the way for DMSJ cycle concepts to take to the sky.

1.1.2 The Dual-Mode Scramjet Isolator

Operating across a wide flight envelope (Mach numbers, altitudes, dynamic pressures etc.), the DMSJ cycle must be adequately robust to avoid Combustion-Inlet Interaction (CII), one of the prime catalysts of engine unstart. To describe the unstart process and illustrate the importance of avoiding this transient phenomena, the concept of the isolator and its responsibilities are first described. The unstart process is briefly described in Section 1.1.2.4. The component in the DMSJ system responsible for mitigating the unstart risk is the isolator, which together with the inlet compresses the flow prior to combustion. The isolator is a constant cross-sectional area duct in order to avoid excessive losses due to continuously present compression and/or expansion features triggered by a variable cross-sectional area. It is located between the low static pressure inlet and the high static pressure combustor (Fig. 1.2). As the name implies, the isolator is responsible for isolating the inlet flow field from combustor pressure perturbations.

1.1.2.1 The isolator shock train

The inlet provides flow compression through the formation of shocks emanating from the vehicle forebody. In ramjet-mode of combustion, further pre-combustion flow compression is provided by a series of shock structures inside the isolator, commonly referred to as a shock train (Fig. 1.2). The shock train can be formed through a number of processes. An upstream mixed-compression inlet causing multiple shock/boundary-layer interactions (SBLIs) can impose severe adverse pressure gradient on the internal boundary layer at each interaction in the isolator. More often, it is the combustion of fuels creating large back pressures that call for the presence of the

shock train to increase the thermodynamic potential of the incoming flow. Large local pressure surges downstream of the isolator caused by chemical energy release due to combustion processes can cause boundary-layer separation within both the combustor and isolator. The resulting separation causes incoming flow to turn into itself and generate a series of shock structures composing the shock train [24].

The shape of the shock train is primarily dependent on the inlet conditions. Isolator shock train shape is traditionally classified from a single side-view planar perspective, stemming from observations made by techniques that integrate all disturbances in the flow along the entire optical path length. Visualizing the shock train from more than one perspective to shed new light onto the composition of these features is a major contribution in this work and will be discussed below. As an introduction however, shock train shapes will be discussed from the traditional single plane perspective and expanded upon later in this work.

The traditionally visualized shape (as viewed from a single planar perspective) of the primary shock structure in the shock train is predominantly depended on the incoming Mach number, with the degree of normal shock bifurcation increasing along with Mach number [25]. Numerous studies on shock trains in constant cross-sectional area ducts have classified shock/turbulent boundary layer interaction and formation of flow patterns into two major types: a single normal shock, and shock trains composed of either bifurcated normal or oblique structures [26–30].

The single normal family of shock trains is generally divided into three sub-categories depending on the magnitude of the inflow Mach number [31] and is sketched in Fig. 1.3a-c. At low inflow Mach numbers ($M_2 < 1.2$), shock/turbulent boundary layer interaction is weak (1) and the normal shock is relatively straight (2) with no noticeable separation. At slightly higher inflow Mach numbers ($1.2 < M_2 < 1.3$), the flow is characterized by a slightly stronger interaction (1) and a curved shock front, with inclination increasing as centerline is approached (2) and minimal separation taking place at the foot of the shock. Continuing with the incremental increases in inflow Mach number ($1.3 < M_2 < 1.5$), the single normal shock feature bifurcates (1) with extensive boundary layer separation (3) and shock front curvature (2). The bulk flow velocity behind each

of these shocks is transitioned to subsonic prior to entering the combustor.

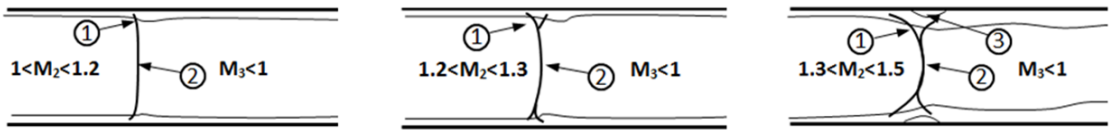

Figure 1.3: Illustration of single normal shock forming in a constant area duct (sketch adapted from Ref. [31]). Flow is left to right.

The formation of multiple shock structures to form a shock train takes places at isolator inflow Mach number above approximately 1.5, as shown in Fig. 1.4a-b with corresponding wall static pressure rise behavior. As the inflow Mach number is increased, the degree of bifurcation of the primary normal shock increases, and the pure normal component is reduced in length and confined to the center region of the flow field. For Mach numbers above approximately 2.0, the normal shock structure transitions to an interacting family of left- and right-running oblique shocks. Static wall pressure rise in the normal shock train is more abrupt than its oblique counterpart, with the bulk of the static wall pressure rise associated with the primary normal shock feature. The length over which the wall static pressure rise occurs is labeled S_T. The wall static pressure rise in the oblique shock train case occurs more gradually, with the expansion regions (dashed line) downstream of the compression regions (solid line) reducing the initial wall static pressure rise. Since the flow immediately downstream of the primary normal shock portion is subsonic, a re-acceleration process must take place for multiple shock structures to occur. A detailed description of this re-acceleration process derived from experimental observations is provided in Chapter 5.

1.1.2.2 Corner flow Separation in rectangular ducts

Traditionally, isolator shock train features are described from a single planar perspectives, categorizing interactions as either normal or oblique. General discussion regarding isolator shock train physics in the majority of previous works do not mention the effects of corner flow separation on center flow field behavior and the resulting three-dimensionality of the flow field. Subsequently, measurements have focused mainly on center-flow regions. There are, however, a number of excel-

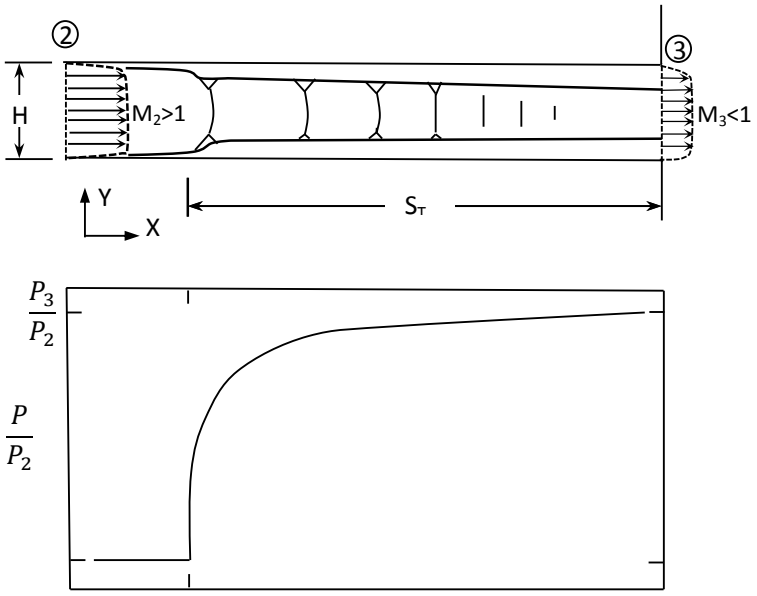

(a) Normal shock train geometry $1.5 < M_2 < 2$

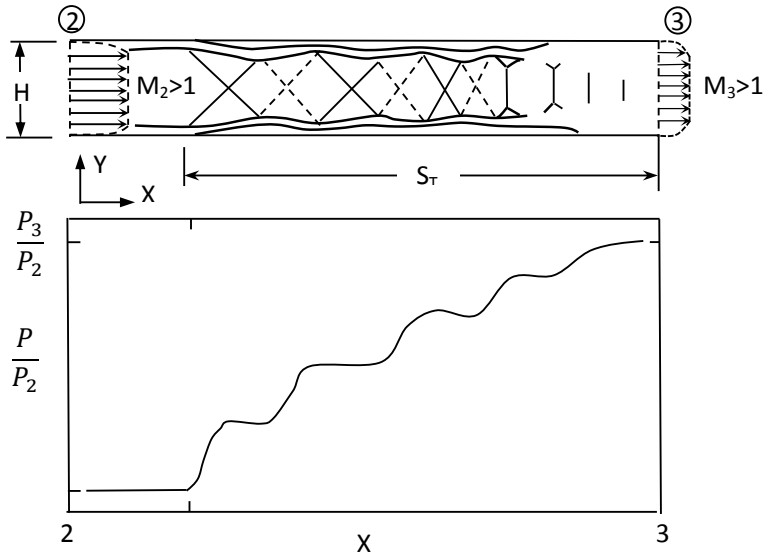

(b) Oblique shock train geometry for $M_2 > 2$

Figure 1.4: Normal and Oblique shock train geometries with wall static pressure outline, flow is left to right (sketch adapted from Ref. [3]).

lent studies focusing on the effects of single stationary oblique & normal shocks interacting with side-wall and corner boundary layers both experimentally [32–36] and computationally [37–42]. A thorough review of work performed on canonical shock/corner boundary-layer interaction can be found in the work by D'Ambrosio & Marsilio [43].

Observations of flows near corners in the form of lateral secondary flow circulation (Fig. 1.5a) have been documented since the 1920's. Nikuradse observed that axial mean velocity contours bulged outwards near the corners and inwards near the wall mid-points (Fig. 1.5b) [44]. Prandtl suggested that these deviations from the linear behavior observed in circular ducts were a result of the continuity equation near the corners, requiring a return flow to the mid-point of the both walls bounding the corner [45]. Prandtl furthermore reasoned that the circulation regions vector mass, momentum, and energy along the corner bisector and away from the corner walls, also termed "secondary flow of the second kind" [46].

Work performed by Bundrett & Baines showed that the secondary velocities were generated by gradients of Reynolds stresses (predominantly the normal stress components) in the plane of the duct cross-section [47]. This effect is catalyzed in the corners because the flow is impacted by viscous shear stresses from velocity gradients in two planes. Furthermore it was shown that for increasing values of Reynolds number the secondary flow penetrates deeper toward the corners, and that the corner bisector separates independent secondary flow circulation, with the secondary flow production at the bisector equaling zero and of opposite sense on either side of the bisector.

The effect on secondary flow circulation in the corners was quantified by the measurement of mean axial velocity contours (isovels) by a number of authors through several technique including hot wire [47, 49–51] and laser-Doppler anemometry [48]. It was found that secondary circulation causes the isovels to bulge outward near the corner and inward near the wall mid-point, depositing low velocity and momentum flow near the corner regions (Fig. 1.5b).

Although turbulent corner flows are well studied in canonical flow fields, their effects on shock train/turbulent boundary layer interaction in rectangular isolators remains relatively undiscovered. A number of experimental approaches utilizing a 'unit physics' approach involving single

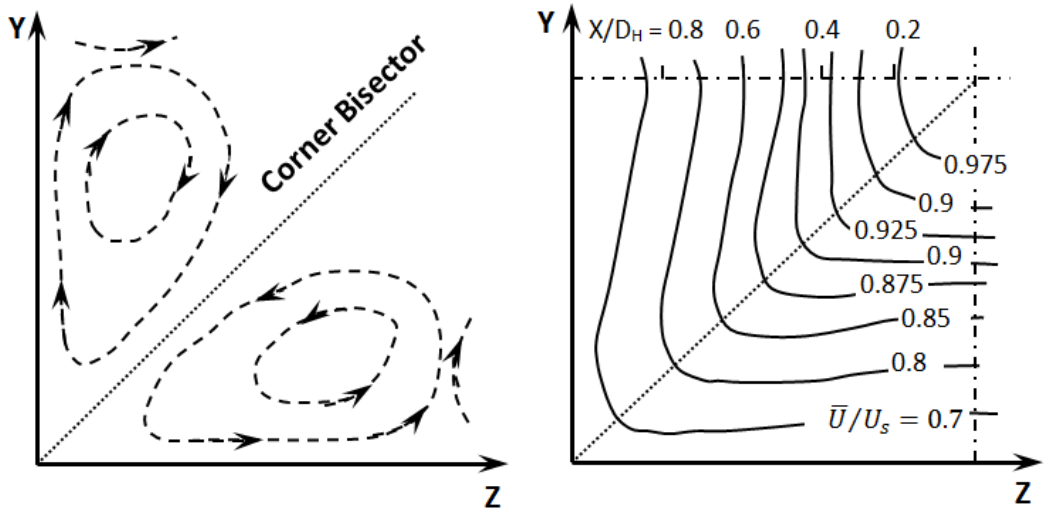

Figure 1.5: Corner flows: (a) secondary flow circulation, and (b) resulting isovel behavior (sketch adapted from Refs. [47, 48]).

stationary shocks interacting with side-wall and corner flows are reviewed in Chapter 2. Furthermore, a number of computational studies investigating a more complex flow field including the presence of shock trains are also summarized. This work aims to further contribute to the knowledge of corner flow separation effects in dynamic shock train/turbulent boundary-layer interaction, including the first experimental visualization of the three-dimensional shock train front spawned by low momentum corner flow separation.

1.1.2.3 The pseudo-shock train & empirical length relations

An important piece of nomenclature is introduced and illustrated in Fig. 1.6. If the flow downstream of the shock train is assumed to be subsonic in the bulk, static pressure is expected to decrease due to friction effects [26]. It has been shown however, that downstream of the shock train static pressure continues to increase [52–55]. Additionally, static pressure measurements taken along the center-axis (green curve) and the wall centerline (black curve) display the same increasing behavior [56]. The oscillatory behavior of the center-axis static pressure distribution is due to the re-acceleration process introducing rarefaction events inbetween the shock train elements, a process that is discussed in greater detail in Chapter 5.

Due to decreasing core flow area and boundary layer effects, a post shock train 'mixing region' forms downstream of the shock train if the isolator duct length is adequately long. Taken together, the shock train and mixing region are called the pseudo-shock region, and is denoted by S_T in Fig. 1.4. This term was originally proposed by Crocco in 1958 in describing the proper mechanism of transition from supersonic to subsonic conditions [57] in a ramjet-mode type environment. This terminology will become relevant in the refinement efforts of pseudo shock train length empirical relations presented in Chapter 6.

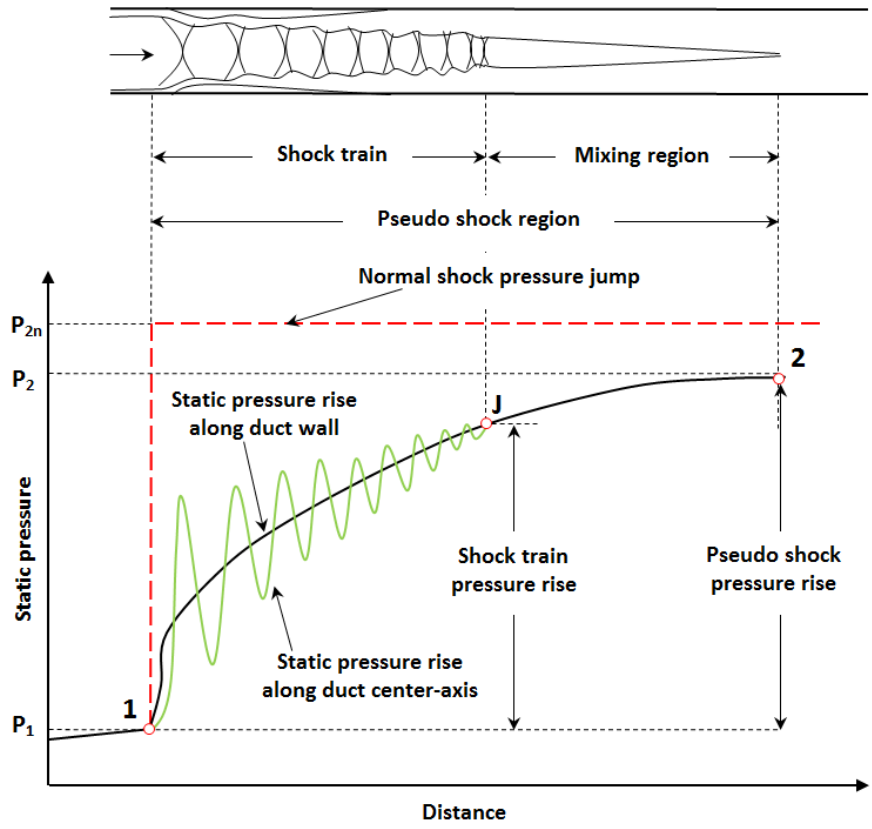

Figure 1.6: Illustration of pseudo shock train nomenclature (sketch adapted from Ref. [31]). Flow is left to right.

Estimates of pseudo shock train length are an important part of proper isolator design. The isolator needs to be long enough to house a pseudo shock system that offers near normal shock static pressure rise (without the magnitude of stagnation pressure losses) and be able to contain and isolate the leading edge of the shock system from the inlet flow field with a certain

safety margin. The isolator can not be excessively long however, as weight and drag penalties can significantly affect the performance of the whole power cycle. The latter is especially severe at the supersonic flows experienced during scramjet-mode of combustion.

The classic empirical relation for shock train length in axi-symmetric (circular) ducts, presented in Eq. 6.1 as introduced by Waltrup & Billig in 1973 [58] with the exception of Mach and pressure subscripts matching the station designations in Fig. 1.2, is widely considered to be the fore-most empirical relation for shock train length estimation.

$$\frac{S_{CL}(M_2^2-1)Re_{\Theta}^{1/4}}{D^{1/2}\theta^{1/2}} = 50(\frac{P_3}{P_2}-1)+170(\frac{P_3}{P_2}-1)^2 \tag{1.1}$$

Through experimentally varying the flow parameters including inflow Mach number (M), momentum thickness boundary layer (Re_θ), duct diameter (D), and momentum thickness of the upstream boundary layer (θ), it was found that the pseudo shock train length (S_{CL}) for a given pressure ratio (P_3/P_2) varies directly with $\theta^{1/2}D^{1/2}$ and inversely with $(M^2-1)Re_\theta^{1/4}$ to form the quadratic expression in Eq. 6.1. Since the relationship is derived from data obtained at the centerline, the designation S_{CL} is used in Eqs. 6.1-1.2. Furthermore, given that the relation above was obtained in a circular duct, it does not account for low momentum corner flow separation that could affect the location of the initial boundary-layer separation in rectangular ducts.

$$\frac{S_{CL}(M_2^2-1)Re_{\Theta}^{1/5}}{H^{1/2}\theta^{1/2}} = 50(\frac{P_3}{P_2}-1)+170(\frac{P_3}{P_2}-1)^2 \tag{1.2}$$

To this end, a modification was originally introduced by Billig in a 1992 conference proceeding and later in a 1993 journal article [59] to account for potential effects due to rectangular cross sections. Not explicitly written in the original work by Billig, the proposed modification of a $1/5^{th}$ power dependency on Re_θ was first explicitly written (and referenced) by Sullins & McLafferty [60] in a proceeding at the same 1992 conference. The modification is expressed in Eq. 1.2, with H symbolizing the duct height (duct minor-axis length scale). The modification was theoretically derived from the original relation for circular ducts (Eq. 6.1) and no explicit experimental data

obtained in rectangular ducts was used to derive the modified fit. Sullins' work, exposing an aspect ratio 2.5 rectangular isolator duct to inflow Mach numbers of 2 and 2.85, showed fair agreement with the proposed modification. Compared to the original circular cross section relation, the $1/5^{th}$ power dependence of Re_θ results in a longer shock train length for identical flow parameters. The modification still does not account for rectangular aspect ratio, corner flows, and potential minor- and major-axis boundary layer asymmetry. These shortcomings are addressed in Chapter 6 in the form of a complementary modification to Eq. 6.1.

1.1.2.4 Inlet/isolator unstart

Disturbances inside the isolator, such as the effects of the mixed compression inlet or large pressure gradients originating from combustor chemical energy release, can lead to a transient process known as engine unstart [1, 3]. Unstart generally occurs when the leading edge of the isolator shock train system propagates upstream into the inlet region where, due to the diverging geometry as seen by the upstream propagating shock front, it is highly unstable. This results in the shock displacing out of the inlet and settling as a detached bow shock with high pressure loading and severe loss of inlet mass flow [3]. Engine flame out and unstart results in mission failure and/or complete vehicle loss. Aside from a fully unstarted state, two isolator modes of operation are termed in this work:

- Fully started mode: occurring immediately after wind tunnel start and lasting on the order of several seconds, the isolator duct is fully supersonic and the backpressure is low enough to resist boundary layer separation and thus no shock train is present inside the test section.
- Partially unstarted mode: a critical backpressure rise is reached which promotes boundary layer separation and formation of the shock train. As the backpressure continues to rise, the shock train propagates upstream towards the inlet and is eventually forced to settle inside the diverging portion of the C-D nozzle, which marks the fully unstarted mode of operation.

In the ramjet-mode of operation the shock train system is present in the isolator to provide the static pressure rise necessary to accommodate combustor inlet pressure and shock the bulk

velocity down to subsonic. This shock system can propagate upstream if the combustor pressure rise increases above the magnitude that is supported by the static pressure rise capability of the shock train. If allowed to interact with the inlet flow field, engine unstart will occur.

In scramjet-mode of operation, heat addition to supersonic flows can cause the flow to become thermally chocked (reaching sonic conditions) resulting in unstart. Even before this critical point is reached, heat addition can create excessive boundary layer separation which can extend upstream to the inlet flow field and likewise result in engine unstart.

Due to the importance of understanding the physics behind the unstart process, numerous experimental and computational studies have been performed to shed light on the dynamics driving shock train propagation dynamics and inlet unstart. Relevant works are summarized in Chapter 2. Developing a better understanding of the unstart process will mature the DMSJ technology as it would allow the design of engines less likely to unstart and aid in the development of more robust shock train leading edge location control techniques. Likewise, an improved understanding of the three-dimensional corner flow separation concept obtained through experimental efforts described in Chapter 5, will significantly benefit the ability to mitigate unstart risks in next generation DMSJ cycle designs.

1.1.3 Diagnostics Techniques to Resolve Three-Dimensional Flow Features

To gain an understanding of the flow physics in experimentally derived, geometrically confined supersonic flow fields, diagnostic techniques capable of resolving desired quantities must be applied. This process spans the spectrum from simply gaining the ability to make qualitative observations of the flowfield (i.e. make the invisible visible) to making temporally and/or spatially resolved, high-bandwidth, quantitative measurements at any three component [X,Y,Z] coordinate within the isolator duct. Three diagnostic techniques specifically designed, refined, and implemented to study the shock train dynamics are the multiplane shadowgraph method, the Background Oriented Schlieren (BOS) method, and the focusing schlieren derived deflectometry (FSD) technique. These techniques offer capabilities not supported by traditional schlieren and

shadowgraphy methods. Since these are relatively uncommon diagnostic techniques, the motivation behind the refinement efforts of these diagnostics is introduced below, with the methods described in detail in Chapter 3. Refinement and optimization of the techniques is discussed in Chapter 4, along with a review of pertinent literature regarding previous development efforts.

Traditional flow visualization techniques such as schlieren and shadowgraph are not well suited to resolve three-dimensional flow features due to their line-of-sight nature. They are however, great tools to easily obtain initial qualitative, and in some special configurations quantitative, global visualization information regarding the flow behavior of interest. The collimated beam schlieren/shadowgraph concept as applied in the present research is illustrated in Fig. 1.7. A collimated beam (in this case white light) is send through a medium of variable density gradient ($\delta\rho/\delta y > 0$) and thus variable index of refraction ($\delta n/\delta y > 0$). For simplicity only one direction of density gradient is shown, but in a realistic flow environment the gradient would be omnidirectional. This variable density gradient field is primarily generated by the shock train structure and the establishment of boundary layers in the isolator wind tunnel model. Huygen's principle causes individual wavelets (forming a wavefront of light) to grow at a faster rate in regions of lower n. Since the light wavefront forms as a tangent to the individual wavelets, the wavefront is deflected toward regions of higher index of refraction as seen in Fig. 1.7. These deflections are projected on an image plane and subsequently recorded. A mathematical description of the schlieren phenomena is provided in Appendix A, along with a more detailed outline of the experimental apparatus in Chapter 3.

The changes in illumination projected on the image plane represent the second derivative of density. Applying a knife-edge at the focal point of the schlieren beam allows for the visualization of the first derivative of density (schlieren) at the image plane. Without the use of a knife-edge, the opposite of the illumination is visualized at the image plane as the second derivative of density (shadowgraph). Both measurements are line-of-sight visualization techniques, with any disturbance along the optical path length recorded at the image plane. Aside from flow features, these disturbances can include abberations on the test section window and ambient thermals in

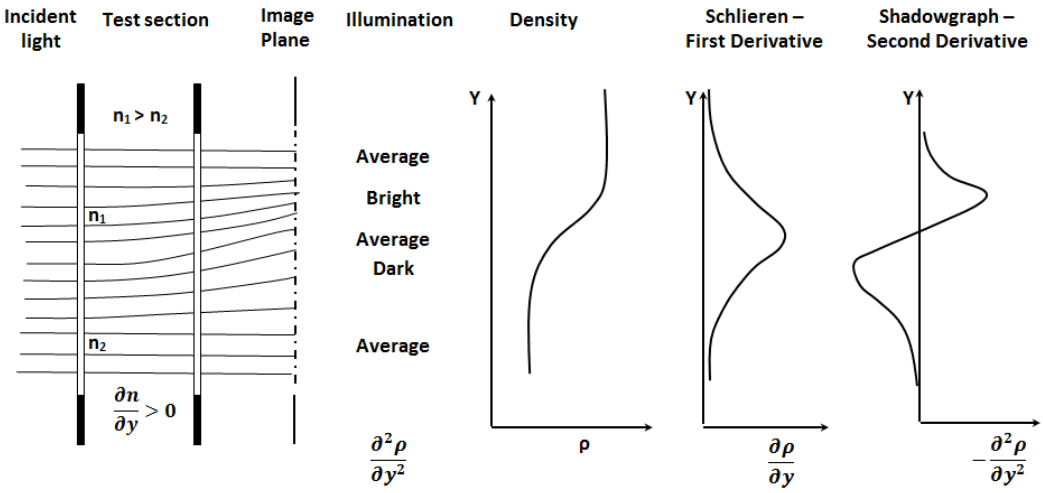

Figure 1.7: A skematic of a traditional line-of-sight flow visualization technique (skematic based on Ref. [61]). Different quantities projected on the image plane are shown in the plots.

the laboratory.

To address the inability of schlieren and shadowgraph to represent three-dimensionality in the flow field, three non-traditional flow visualization techniques are used in this work and are illustrated in Chapter 3. Two techniques, the multi-plane shadowgraph and Background Oriented Schlieren (BOS) techniques, are still based on the line-of-sight principle yet are inherently capable of representing the three-dimensional nature of the flow field in different ways. The third, the focusing schlieren method, provides narrow planes of sharp focus across which the integration of density occurs, effectively leaving end effects out of sharp focus.

The BOS and Focusing Schlieren methods, two existing techniques, were optimized and refined for use in the particular compressible flow regime encountered in the DMSJ isolator. The multiplane shadowgraph method is a novel concept developed and implemented in this work to provide a previously unattainable perspective of the shock train structure. Along with illustrating the working principles of the diagnostic techniques in Chapter 3, extensive optimization and validation efforts are discussed in Chapter 4.

1.1.4 Computational Fluid Dynamics Simulations

To complement the primary experimental observations made in this work, a secondary numerical effort was pursued to study both the fully started and partially unstarted modes of isolator operation. The former was used to validate the baseline model against multiple experimentally obtained flow parameters. Furthermore, flow parameters difficult to obtain in the current experimental setup, such as corner flow momentum thickness and side-wall boundary layer profiles, were analyzed for use in the formation of the modified shock train length empirical length relation presented in Chapter 6. The partially unstarted mode of operation was simulated to document the ability of common one- and two-equation Reynolds Averaged Navier-Stokes (RANS) based turbulence models to resolve the complex three-dimensional flow dynamics visualized and measured in experiment. The one-equation standard Spalart-Allmaras [62] and two-equation Shear Stress Transport (SST) Menter $k-\omega$ [63] turbulence models are used to simulate the fully started, no flow separation case. Due to its improved performance for boundary layers under adverse pressure gradients compared to the Spalart-Allmaras models, only the $k-\omega$ turbulence model is considered for the partially unstarted simulation case, where the aim is to resolve the three-dimensional boundary layer separation driven shock train structure.

The rapid growth in computational hardware and storage capabilities over the last two decades has transformed the area of CFD into a powerful tool for wide variety of disciplines. The complex, reactive, and highly compressible flow-fields encountered in a typical hypersonic airbreathing engine cycle are prime candidates upon which CFD methods and techniques can expand and mature. During a time of increased interest in scramjet technology development in the 1970s, pioneering work on the development of multistep/multicomponent chemical models for nozzles and combustors was performed by several groups under the direction of Ferri [64], Spalding [65], and later Knight [66] contributing finite-difference solutions to viscous flow equations in high-speed inlets. Accelerated by the NASP program in the mid to late 1980s, CFD methods and practices were further fine-tuned for supersonic and hypersonic modeling [67]. Fast forward to the present day, and the expense of obtaining ground test and (especially) flight-test data in

hypersonic regimes along with the reduced number of ground-test facilities capable of supporting the required flow regimes, suggests that the role of CFD will continue to grow as a major component in the design cycle of any new hypersonic airbreathing engine cycle.

The increase in the application of CFD within the design cycle must, however, be approached with caution. Numerical simulations performed in this study did not employ chemically reacting flows, yet are heavily dependent on the turbulence modeling approach used particularly in the partially unstarted mode of operation. Widely used RANS turbulence equations model the flow through physical analogies rather than solving for the turbulence directly, commonly relying on relations derived from velocity fluctuation measurements in incompressible flows, and thus will not be able to account for compressibility effects that tend to mitigate the generation of turbulence [11].

The use of CFD as a complementary secondary analysis tool to the experimental results is performed in a step-by-step process, including:

1. Comparing computational results to quantitative experimental flow data obtained during steady-state mode of operation, allowing for careful calibration and comparison of the numerical models employed. Quantitative data includes longitudinal-axis lower wall static pressure measurement, duct-minor axis vertical pitot probe boundary layer surveys, and duct-major axis static pressure and side-wall pitot rake surveys.

2. Accompanying the above validation efforts with a volumetric mesh convergence and wall y^+ dependency study.

3. Resolving the complex three-dimensional flow physics with the numerical models in the partially unstarted mode of operations. Comparisons are made to the qualitative flow visualization results.

4. Extending the partially unstarted mode dynamics to a wide range of aspect ratios to study the effects on three-dimensional shock train formation and explore previously documented shock train modes in high aspect ratio/high Mach number configurations [12].

1.2 Objectives & Method of Approach

This work is composed of two main branches: (1) the study of rectangular isolator shock train dynamics and the inherent flow three-dimensionality, and (2) the development, refinement, and implementation of 'unconventional' experimental diagnostic techniques capable of resolving the flow three-dimensionality. These techniques, together with more traditional diagnostics such as wall static pressure and pitot total pressure surveys, were used to achieve the four objectives listed below. A brief outline of the method of approach is offered in the bolded sub bullets.

1. Enhance the understanding of the three-dimensional shock train structure and their interactions with the isolator boundary layer.

    - **Visualize the three-dimensional shock front:** develop a multiplane shadowgraph technique to resolve the derivative of the density gradient along both the duct major (lateral) axis and the duct minor (vertical) axis simultaneously.
    - **Measure the low momentum corner flow separation time-scales:** perform a lower wall, fast-response dynamic pressure survey along the duct minor axis capable of comparing the center- and outer-flow boundary layer separation magnitudes and time scales.
    - **Resolve the global density gradient magnitude distribution in the shock train structure:** calculate a measure of density gradient magnitude from the Background Oriented Schlieren (BOS) tare- and flow-image pair cross-correlation derived pixel displacement.
    - **Compare center-axis and side-wall shock train oscillation frequency and propagation velocity component:** record high temporal bandwidth, sharp plane of focus fluctuations in density gradient magnitude with a fine-tuned Focusing Schlieren Deflectometry Velocimeter configuration.
    - **Perform secondary, fully three-dimensional RANS simulations to compare to experiment and extend observation capabilities:** simulate both the fully started

and partially unstarted modes of operation to evaluate the accuracy of the experimentally derived boundary conditions and the two-equation $k-\omega$ turbulence model.

- **Modify existing semi-empirical isolator shock train length relations based on circular ducts:** utilize the above observations together with duct minor- and major-axis boundary layer pitot probe and pitot rake measurements to improve the correlation between experimental and semi-empirical estimates of shock train length in rectangular isolators.

2. Study the effects of rectangular isolator aspect ratio on transient shock train flow physics experimentally and computationally.

   - **Evaluate aspect ratio 1.0, 3.0, and 6.0 isolator ducts:** The above diagnostics suite is applied to study the shock train dynamics in aspect ratio 3.0 & 6.0 isolators, with select studies performed in an aspect ratio 1.0 isolator.
   - **Extend observations to higher aspect ratios utilizing RANS simulations:** a computational approach is used to study isolator shock train formation in high aspect ratio configurations not resolved experimentally.

3. Quantify the length of three-dimensional shock trains as a function of rectangular isolator parameters.

   - **Modify existing semi-empirical isolator shock train length relations based on circular ducts:** utilize the above observations together with duct minor- and major-axis boundary layer pitot probe and pitot rake measurements to improve the correlation between experimental and semi-empirical estimates of shock train length in rectangular isolators.

4. Extend improved optical measurement capabilities to large scale AEDC T&E facilities.

   - **Develop a flexible interface to optimize diagnostic components for low density flow fields:** increase the sensitivity and depth of sharp focus of the Focusing

Schlieren technique by designing the system based on an quantitatively optimized cutoff grid. Maximize the density gradient interrogation envelope of the Background Oriented Schlieren method by calculating the desired background pattern diameter, density, and placement.

1.3 Scope of Current Work & Thesis Outline

The shock train environment used to simultaneously develop the diagnostic tools summarized above and contribute to the knowledge base of such transient flow features represents a simplified interpretation of realistic shock train dynamics. The atmospheric indraft wind tunnel facilities used to generate the shock train environments relies on the inherent backpressure rise during tunnel operation to drive the shock train dynamics. Since the focus of the present work was the analysis of three-dimensional, transient flow behavior, no throttling device or plug was installed to control the backpressure magnitude. Likewise, no active combustor was placed downstream of the isolator to observe sensitivity of shock train behavior to common combustion parameters such as the fuel-air equivalence ratio and chemical heat release induced pressure gradients. Using the wind tunnel trigger configuration described in Chapter 3, the backpressure rise profile driving the shock train dynamics was approximately linear and proved repeatable on a run by run basis. The absence of a downstream combustor section thus allowed the focus to be on the change in aspect ratio alone.

The facilities employed used a converging-diverging (C-D) nozzle to accelerate the flow to supersonic conditions at the isolator inlet plane. Flight worthy vehicles would utilize a supersonic compression inlet to decelerate the flow to the desired inflow conditions. Nevertheless, pitot probe surveys at the inlet plane of the isolator test section produced flow conditions that can be considered an adequate representation of the system operating within ramjet-mode, providing a clean supersonic flow field at the entrance of the isolator. Finally, operating as an atmospheric indraft wind tunnel, the experimental setup did not use a heated or entropy matched inlet condition.

The secondary observations made through full three-dimensional numerical simulations were

accomplished utilizing one- and two-equation RANS turbulence models. Although it has been noted that the RANS approach to turbulence modeling may not be optimal for flows expected to be characterized by low-frequency unsteadiness [68], the vast majority of the numerical work presented in this study is performed as steady-state computations. The three major goals of the computational side-study are to:

Complementing the introduction above, a thorough literature review of relevant work is presented in Chapter 2. This review is accompanied by a summary of the issue and knowledge gaps that remain in understanding transient isolator shock train dynamics. The experimental approach, the facilities and diagnostic methods employed, and the numerical simulation approach are discussed in Chapter 3. Extensive Focusing Schlieren Deflectometry and Background Oriented Schlieren optimization efforts are presented in Chapter 4 along with the refinement and validation of the numerical simulations approach. The study of shock train dynamics is broken up into local (observations of just the primary shock structure) and global (analysis of the entire pseudo-shock region) analysis, presented in Chapters 5 & 6 respectively. Finally, observations are summarized, conclusions are made, and reflections for future work are articulated in Chapter 7.

Chapter 2: Literature Review

This chapter reviews pertinent literature on isolator flow dynamics, covering both experimental and numerical work. A brief summary of relevant diagnostics development literature is reserved for the diagnostics refinement discussion in Chapter 4.

2.1 Local Shock Train Physics & Flow Three-Dimensionality

Boundary layer separation is the principle driver behind shock-train dynamics and signals incipient arrival of the shock train leading edge. Due to the asymmetry between minor- and major-axis length scales of a typical rectangular cross-sectional duct with an aspect ratio greater than 1.0 and preceded by a planar nozzle, boundary layer asymmetries can influence the behavior of boundary layer separation. Two-dimensional planar nozzles feeding rectangular ducts and momentum deficits in corners bounded by two viscous walls are two major causes of three-dimensional boundary layer separation.

In order to field robust and reliable shock train leading edge location architectures as part of a Propulsion System Controller (PSC), the leading edge shock train boundary layer separation behavior needs to be thoroughly understood in order to optimize sensor placement along all three axes of the isolator duct. Furthermore, thorough knowledge of low-momentum corner flow separation prevalent in rectangular ducts is required to understand the potential upstream length scales of three-dimensional boundary layer separation away from centerline. In addition to contributing to the development of more robust shock train leading edge detection techniques, this improved insight can also contribute to the formation of more accurate empirical relations for rectangular isolator duct, total pseudo shock train length [69, 70].

2.1.1 Corner Flow Separation

The concept of secondary circulation zones in the corner regions of rectangular ducts and the important role it plays in boundary layer separation driven flow dynamics is introduced in Chapter 1. An excellent summary is provided by Gessner (Ref. [71]). A variety of studies have focused on detailed corner flow analysis and have provided tangible physical explanations on the origins of corner flows [48–51, 71, 72].

Experimental studies focusing on corner boundary layer separation and flow behavior in association with isolator shock train dynamics are relatively scarce. More canonical environments using a single steady or normal shock to study the effects of corners and general minor- and major-axis boundary layer asymmetries on supersonic flow behavior have, however, been of great interest in past research efforts [32–36, 73–75]. Due to their resemblance of the shock train flowfield of interest, these canonical studies are briefly reviewed below prior to the discussion of specific work concerning corner flows in rectangular isolators.

A classic configuration used in the study of shock/boundary-layer three-dimensionality in a corner is the use of two intersecting wedges. One of the first works to make extensive use of the two intersecting wedge experimental configuration was performed by Charwat & Redekeopp [75]. Wall and inflow pressure measurements, along with surface oil-flow visualization were used in the construction of the corner flow model sketch shown in Fig. 2.1. It was proposed that the intersecting shocks produced four zones. Zone I is bound by the central transition wedge and the slip lines in a conical flow approximation. Transition to the more two-dimensional planar behavior is proposed to occur through zones II & III bounded by relatively strong & weak compression events respectively.

Subsequent studies [32, 33, 73, 74] using the orthogonal wedge experimental configuration utilized Reynolds number sweeps to study the inviscid/viscous nature of the corner flow behavior. West & Korkegi observed the flow features in the corner to be conically invariant across a Reynolds number range from $3x10^6/ft$ to $60x10^6/ft$, characteristic of an inviscid corner flowfield [32]. In a 1972 study, Korkegi found that for a laminar flow, corner separation occurred with a small shock-

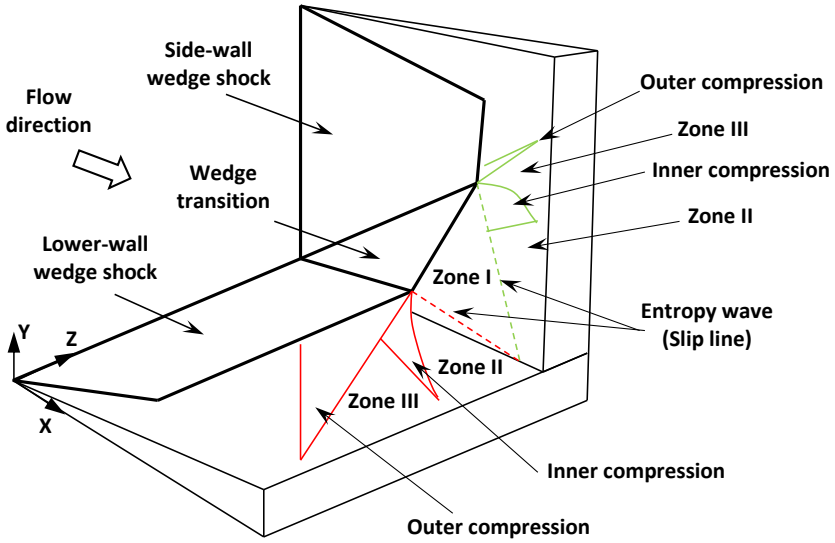

Figure 2.1: Illustration of two intersecting orthogonal wedge shocks (sketch adapted from Ref. [75]).

induced pressure rise whereas the turbulent case required pressure rise 1.5 time greater to result in separation [74]. In a later study, Korkegi observed that the structure of the three-dimensional corner shock interaction is primarily dependent on the extent of separation, and not the extend of the flow being laminar or turbulent [33].

It has been observed that in rectangular cross-section ducts with single normal shock or stationary oblique shock interactions, the lower momentum corner flow boundary layer being bounded by two viscous walls separates ahead of the center-flow regions. Departing from the double orthogonal wedge configuration, Reda & Murphy utilized a shock generator to produce a stationary oblique shock interacting with a turbulent boundary layer. Surface pressure measurements were made along the major (lateral) axis of the duct to investigate the three-dimensional interaction region and associated pressure rise in both the attached and separated regions [37]. Attached interaction regions were characterized by pressure distributions increasing more rapidly off-centerline compared to centerline measurements, with both sets of data eventually reaching similar magnitudes. In separated regions, pressure distributions tended toward spanwise unifor-

mity. Oil-flow visualizations in the separated regime, however, suggested significant departure from two-dimensionality, with inflow from the corners driving a pair of large standing vortices within the reverse flow region of the well-separated case. Sidewall oil flow patterns furthermore revealed separation occurring on the side wall boundary layers corresponding to the incident shock slicing diagonally through the side wall boundary layer. This caused 'low energy ' air in these boundary layers to sweep upwards into the corners of the channel, and then laterally into the reverse flow regions.

In more recent experimental work, the behavior of a single normal shock interacting with a corner boundary layer was analyzed [34–36]. Utilizing oil flow visualization, pressure sensitive paint (PSP), and surface pressure measurement, Bruce et al. observed that for larger ratios of major axis δ^* to major axis facility length scale (tunnel width), the classical quasi two dimensional centerline separation was delayed [34]. Furthermore, by altering the corner flow experimentally, it was shown that the shock induced separation in the center flow region is linked to the size of the corner flow separation. The three-dimensional bifurcated shock wave structure and upstream corner separation in a duct with aspect ratio is sketched in Fig. 2.2, adapted from Ref. [34]. The boundary layer separation in the center-flow field region is approximately two dimensional with reversed flow and separation and reattachment zones. The corner boundary layer separation, on the other hand, is characterized by strong vortices and no obvious points or line of reattachment.

Work performed by Burton & Babinsky utilized laser-Doppler anemometry, pressure measurements, pressure sensitive paint, and surface oil flow- and traditional schlieren visualization to observe the effects of corner flow separation compression waves on the adverse pressure gradient found in the center flow region [35]. It was found that a reduction in corner separation resulted in an increased centerline separation and vice versa due to the magnitude of the corner separation induced compression waves 'smearing' out the adverse pressure gradient near the center flow-field.

Figure 2.3, adapated from Ref. [35], illustrates the complex physics involved in three-dimensional shock/boundary layer interaction. Interaction between the lower-wall and side-wall boundary layer spawns the generation of a pair of triple points, from which shock bifurcation pro-

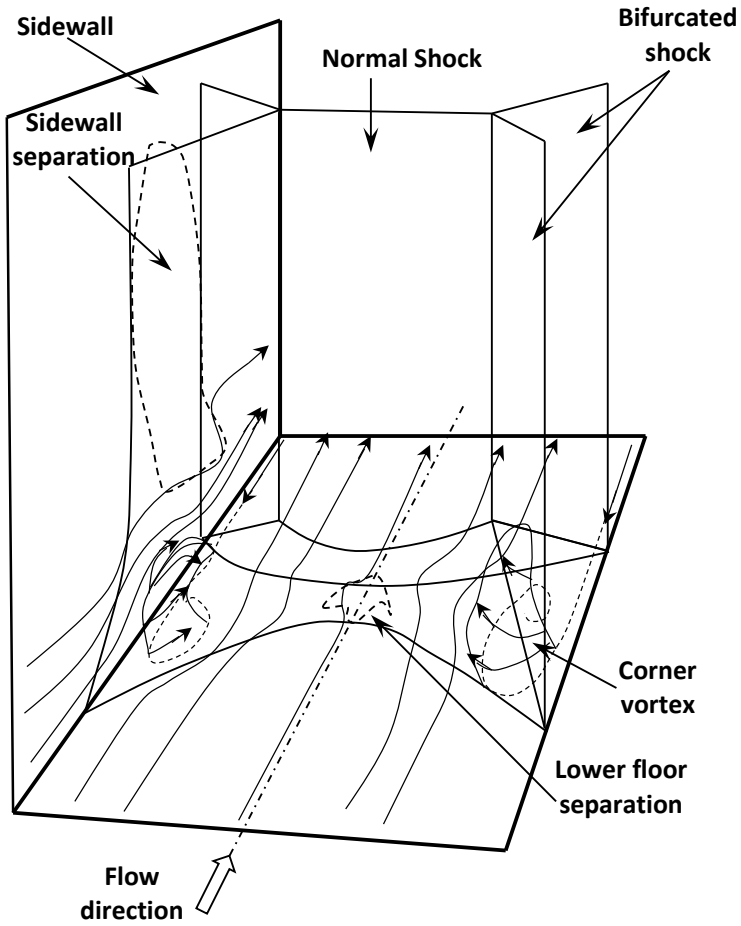

Figure 2.2: Bifurcated normal shock wave corner interaction in duct with aspect ratio (sketch adapted from Ref. [34]).

ceeds toward both walls. Bifurcated shock interaction with the boundary layer leads to pressure gradient induced flow separation (on the side- and lower-walls). Due to the momentum deficit, corner flow separates ahead of the side- and lower-wall flow, in turn triggering compression waves due to the introduction of an effective ramp angle. The corner separation induced compression shock structure (dashed line) occurs upstream of extends to the center-flow regions on both the lower- and side-wall.

Babinsky et al. investigated the effects of oblique shock wave induced corner flow separation on center-flow boundary layer behavior. It was found that both the shape and length of the center flow separation was affected by the magnitude of corner separation by influencing the adverse

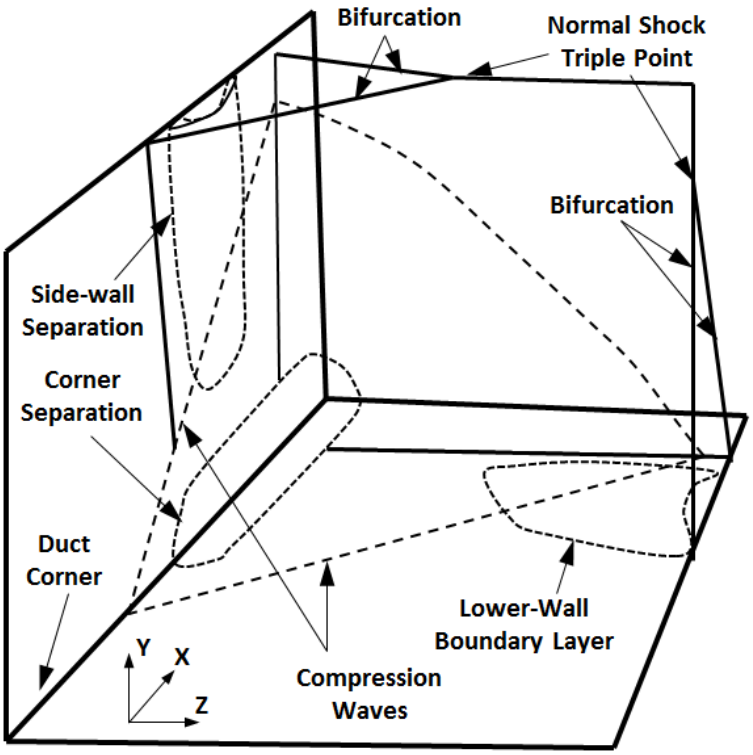

Figure 2.3: Illustration of the corner shock formation (sketch adapted from Ref. [[35]]).

pressure gradient near the center flow-field. Furthermore, the effect of reducing duct width was explored, with corner shocks from opposite walls merging in the main separated zone below some critical width, resulting in extensive separation along the center flow field.

The bulk of detailed experimental work on corner flow separation in a rectangular duct with unforced geometries (a regular corner geometry instead of a pair of orthogonal wedges) and single stationary shocks has been performed in the last ten years [34–36]. The notion that upstream lower momentum corner flow separation could affect the overall dynamics of the shock train formation and propagation has been subject of discussion for sometime. Carroll et al. studied shock train/turbulent boundary-layer interactions in rectangular ducts with incoming Mach numbers of 1.6 and 2.45 [25]. Utilizing surface oil flow visualization along the duct minor axis, and separate spark schlieren visualization along the duct major axis, large three-dimensional separation regions were observed in the Mach 2.45 case. From the oil-flow surface visualization, corner flow separation

is observed to occur upstream of the centerline separation, as marked by accumulation lines of the oil. A U-shaped separation, with the open end facing downstream, follows this initial separation front.

Although one of the first studies to show the XZ-plane perspective of the flow separation, the fact remains that the oil flow visualization technique represents a time-averaged mean of the flowfield near the wall only. Furthermore, transient events such as shock train propagation can alter the distribution of oil particles in a way that the actual characteristics of the flow structure are rendered unidentifiable. Detailed examination of the three-dimensional flow structure is likewise not possible using oil flow visualization alone.

Experimentally studying corner flow behavior in supersonic confined flows remains difficult, in large part due to: (a) visualizing the flow in three-dimensions, and (b) the difficulties imposed by geometry constraints in placing sensors in critical regions of the duct. Given the ability and flexibility of acquiring data in multiple wall bounded regions, corner flows have been the subject of numerous computational studies [38–41, 76].

A numerical simulation of the double orthogonal ramp configuration was performed by Shang et al. [38] in 1978, with the computational results agreeing favorably with the experimental data available at the time. Slip lines and compression structures similarly proposed in Refs. [32, 75] were resolved using a two-layer model of Cebeci-Smith [77] with a turbulence length-scale derived from the modified Gessner's method [78]. Like its experimental counterpart, the double orthogonal wedge configuration was applied in several other computational studies [79, 80].

Computational studies utilizing the isolator duct geometry and variations of inflow parameters and backpressure ratios to generate shock train dynamics are valuable in supplementing and expanding the knowledge of the role of corner flows in isolator shock train dynamics. Nedungadi & Van Wie performed numerical simulations to study the effects of aspect ratio (2.5 and 10) and inflow Mach number (2.0 and 4.0) on rectangular isolator flow dynamics [39]. The commercially available finite volume CFD^{++} flow solver was used to solve the three-dimensional Reynolds-Averaged Navier Stokes (RANS) equations. It was observed that the separation region lead to a

three-dimensional oblique shock wave propagating across the entire width and height of the isolator duct. Increasing the Mach number resulted in corner separation regions failing to re-attach and extending longitudinally downstream into the combustor region, and as with an increase in aspect ratio, lead to a limited stable range of operating conditions.

Full wind-tunnel span corner flow separations have been studied by Garnier using Stimulated Detached Eddy Simulations (SDES) [40]. FLU3M, a compressible flow finite-volume Navier-Stokes solver, was used. Corner separations are shown to reduce the effective section of the wind tunnel and strengthen the interaction. Furthermore, the strongest wall pressure fluctuations are found in the corner flows, characterized by low frequency movements contributing to 30% of the total fluctuations.

Parametric CFD simulations performed by Baruzzini et al. adressed the interactions between the magnitude of the corner flow separation and the thickness of the side-wall boundary layer in high-speed inlets [41]. Both Large Eddy Simulation (LES) and two-equation Reynolds Averaged Navier-Stokes (RANS) with $k-Kl$ turbulence model were considered. It was observed that migration of the subsonic layer on the side-wall boundary layer in the direction of the corner played a significant factor in determining the magnitude of the corner flow separation. Furthermore, it was reported that introducing a corner chamfer with radius on the order of the incoming boundary layer thickness impeded the downward migration of the side-wall subsonic layer and reduced the magnitude of the corner separation.

Extensive LES work studying the uncertainties introduced by certain physical modeling assumptions in simulations with multiple, coupled shock/boundary-layer interactions was performed by Morgan et al. [76]. It was observed that local flow confinement properties, more than the local pressure ratio properties, were the key to determining initial shock location for a stabilized shock case employing a constant backpressure. Simulations with resolved side walls displayed better correlation to experimental measurements of displacement thickness and momentum thickness than simulations using span-wise periodic boundary conditions. Ultimately, it was concluded that in situations were the inviscid global shock train structure is most important, lower fidelity schemes

could be implemented without significant loss of accuracy, while higher fidelity is needed if the location or the steadiness of the shock train is to be determined.

2.1.2 Shock Train Leading Edge Detection

The ability to accurately locate the shock train leading edge is a critical component of a robust Propulsion System Controller (PSC) [81]. From early work on ramjet diffuser terminal shock position sensors for the YF-12 family of aircraft [82–86] to more recent development efforts of the PSC logic for the X-43A scramjet engine controller [81, 87] and beyond [88–93], the ability to locate the shock train leading edge is critical in preventing the occurrence of CII.

Wall pressure measurements are traditionally used to determine the location of boundary layer separation accompanying the leading front of the shock train. In almost all publicly available studies dealing with shock train detection in rectangular isolators, PSC efforts were dependent on centerline pressure measurements evaluating the center-field boundary layer separation induced pressure rise. [88, 90–92, 94–96].

A handful of studies compared simultaneous visualization of the shock train leading edge with simultaneous wall pressure measurements [92, 96]. Due to the importance of the corner flow work presented in this thesis to shock train leading edge detection techniques, a brief summary of these studies are offered below. Even though the flow visualization techniques used in the reviewed literature were exclusively single plane, line-of-sight techniques (and thus would be unable to resolve the corner flow separation induced flow three-dimensionality), knowledge of how the centerline pressure measurements compare to the visualization of the shock train leading edge is critical in developing a complete understanding of the unstart mechanics.

Wagner et al. utilized simultaneous traditional schlieren and high frequency wall pressure measurement to study the dynamics in an isolator/inlet model at Mach 5 inflow [96]. Various shock train propagation velocities were recorded as a function of longitudinal position from the inlet entrance plane. Several modes of post-unstart flow were observed, including a high amplitude low frequency (124Hz) flow, a lower amplitude lower frequency (84Hz) flow, and a non-oscillatory

unstarted flow with even lower pressure fluctuations. As the study focused on the global unstart perspective, no comments in particular were made regarding the comparison between the position of the leading edge of the shock train as visualized by the schlieren technique and the leading edge boundary layer separation locations obtained by static pressure measurements obtained along the center-line.

Hutzel et al. compared several leading edge location techniques with high-speed shadowgraph flow visualization of a normal shock train in a direct-connect, cold flow Mach 1.76 isolator [92]. A 50% steady state static pressure increase, measured along an array of lower-wall centerline pressure sensors, was utilized as a suitable indicator of shock train leading edge location. Dynamic shock train leading edge detection architectures were subsequently designed based on linear and non-linear Auto-Regression with eXogenous variables (ARX/NARX) models. Compared to the single plane visualization of the shock train, the detection algorithms were capable of resolving shock train leading edge location (shock foot) to within one duct height.

Work performed by Le et al. utilized time resolved pressure measurements along all four wall centerlines for shock train leading edge detection in an aspect ratio 1.5, Mach 2.0 isolator [94, 95]. Fast response Kulite sensors were equipped on the upper and lower walls, while low frequency static pressure transducers were included in all four planes. No simultaneous flow visualization was performed to compare the quantitative pressure rise measurement to the actual location of the leading edge shock train. Three static pressure detection parameters were utilized, in addition to the analysis of the frequency content of the pressure signal through power spectra analysis. The frequency spectra analysis of wall bounded boundary layer statistics showed a difference in frequency content of the pressure signal upstream and downstream of the shock train leading edge. Although no dominant peak was observed, the large range of moderate to high power frequency components in the downstream signal (up to 4kHz) differed up to two orders of magnitude from the upstream signal. Fast response pressure behavior along the upper and lower wall showed temporal symmetry throughout the shock train dynamics envelope captured. No comments on all four wall static pressure comparisons were presented.

As will be shown in Chapter 5, placing pressure transducers along the lateral (major) axis of the duct, upstream corner flow separation can be detected prior to centerline detection. This holds potential in the area of shock train leading edge detection algorithm development and refinement since the vast majority of work performed to date has focused on evaluating boundary layer content along the duct longitudinal centerline.

2.1.3 Shock Train Visualization

Flow visualization techniques have been used extensively in the past to study isolator shock train dynamics, including the effectiveness of shock train leading edge detection approaches discussed above. A selection of previously obtained schlieren images of shock train formation at various isolator inlet Mach numbers are shown in Fig. 2.4, with some relating to the visualization techniques used in the shock train leading edge detection work described above.

A significant portion of the literature featuring experimental flow visualizations of shock trains is located in the lower Mach number regime (Mach numbers of 1.5-2.0) [28,55,56,92,97,98]. A number of other isolator flow field visualization efforts, particularly in the area of combustion mode-transition, cover the higher Mach number regime (Mach 4-7) [91,96,99,100]. Furthermore, the majority of flow visualization studies in literature are performed in low aspect ratio rectangular isolator ducts with aspect ratios of 2.0 or less [28,55,56,91,92,96–100]. There is an observed gap in literature concerning the visual analysis of shock trains in the isolator inlet Mach 2-4 regime as well as higher aspect ratios (aspect ratio greater than 3.0). Both areas are addressed in this work.

The works shown in Fig. 2.4 are all performed with the line-of-sight schlieren technique. The transformation between normal and oblique shock train as a function of increasing Mach number is evident, as discussed in Chapter 1. The two-dimensional projections give rise to the terminology ‘ planar normal and oblique shock waves’ , as no significant corner and side-wall effects can be discerned from this single perspective projection of the density gradient. The ability to more accurately resolve the expected three-dimensionality of the rectangular isolator duct shock train dynamics is a major contribution in this work.

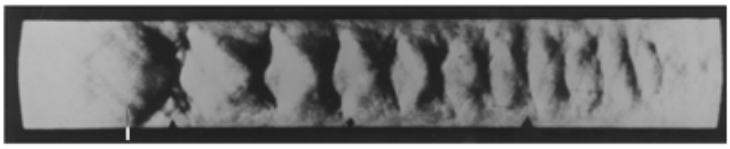

(a) Mach 1.7 shock train (Ikui 1969) [97]

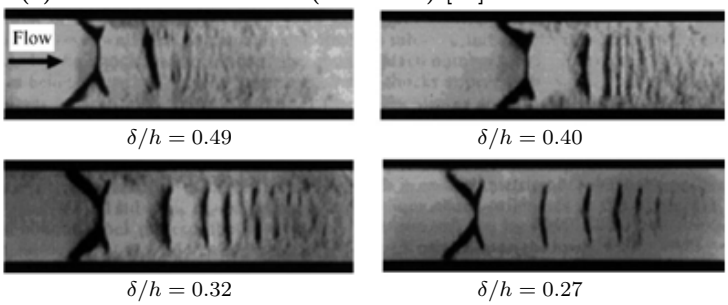

(b) Mach 1.6 shock train: various δ/h (Carroll 1992) [55]

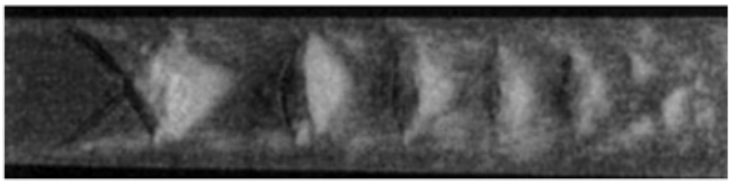

(c) Mach 1.75 shock train (Matsuo 1993) [56]

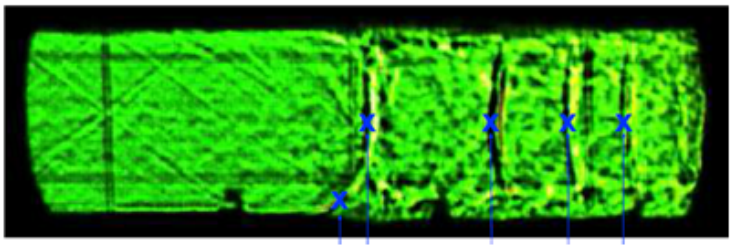

(d) Mach 1.76 shock train (Hutzel 2011) [92]

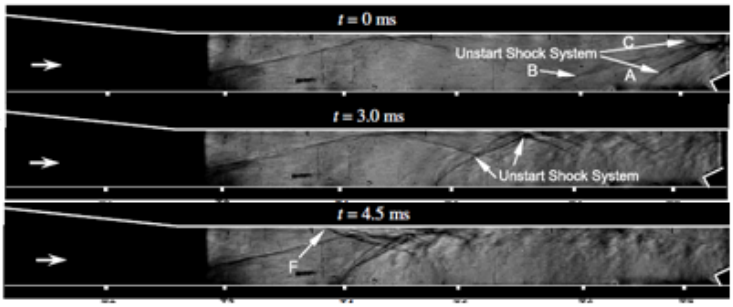

(e) Mach 5.0 shock train: time history (Wagner 2011) [96]

(f) Mach 7.7 shock train (Fischer 2011) [99]

Figure 2.4: A selection of previous shock train visualization efforts: (a) Ikui and Matsuo (Ref [97]), (b) Carroll and Dutton (Ref [55]), (c) Matsuo et al. (Ref. [56]), (d) Hutzel et al. (Ref. [92]), (e) Wagner et al. (Ref [96]), and (f) Fischer and Olivier. (Ref [99]). Flow is left to right.

2.2 Global Isolator Flow Physics

2.2.1 Pseudo Shock Train Length Relations

As introduced in Eq. 6.1, the original quadratic pseudo-shock train length estimate proposed by Waltrup & Billig in 1973 [58] for circular cross section ducts is a function of the duct diameter (D), the boundary layer momentum thickness Reynolds number (Re_θ), the inlet Mach number (M_2), and the pressure ratio across the duct (P_3/P_2). Experimental data gathered using a large parametric variation of flow parameters including the Mach numbers ($1.53 < M_2 < 2.72$), momentum thickness Reynolds number ($5x10^3 < Re_\theta < 6x10^4$), duct diameter ($1 < D < 6.1in$), and boundary layer momentum thickness ($0.007 < \theta < 0.036in$) was collapsed into the quadratic equation shown.

Large data bases for confined supersonic flow physics in circular and annular ducts and isolators have been established in the past to support fundamental research for various weapon platform initiatives. [24, 58, 101–105] . Most next-generation DMSJ cycle based vehicle designs however, call for rectangular or elliptical isolator designs to more efficiently integrate the propulsion module with the airframe. It is therefore important that inherent three-dimensional features of rectangular confined flow fields (that may not weigh heavily on the performance in circular isolators) are understood so that proper similarity transformations can be established in order to take advantage of the large data base for circular and annular ducts.

A theoretically derived modification for rectangular isolators was introduced by Billig in 1993 [59] and is shown in Eq. 1.2. It is a function of the duct minor axis length scale (H), and has a Re_θ power dependency of $1/5^{th}$ compared to $1/4^{th}$ for the circular cross-section ducts. It appears to the author that this modification was derived based on Billig's insight to the flow physics, as no extensive experimental data base similar to the original efforts of Waltrup & Billig's circular cross-section relation were found in literature. As briefly mentioned in Chapter 1, the first work to explicitly state the modification presented in 1.2 was the work by Sullins & McLafferty [60], in turn referencing a conference preceding of the work presented in the journal entry by Billig [59].

The aspect ratio is expected to play a large role in behavior of the shock train leading edge and thus potentially contribute to the overall length of the isolator pre-combustion static pressure rise. Yet, the modification presented in 1.2 only includes the minor-axis length scale, height. The contribution of a $1/5^{th}$ power dependency however, results in longer shock train lengths for identical inflow parameters and isolator pressure ratios. This contribution could implicitly take into account the upstream corner separation length scale to some extent. Comparisons of the existing relations to experimental data accounting for the upstream corner separation length scale are presented in Chapter 6.

By comparing the originally derived circular relation to pseudo shock train lengths formed in rectangular ducts, a modification to include key characteristics of flows in rectangular geometries can be considered. Bement et. al compared experimentally measured combustion induced pseudo shock train lengths to Waltrup & Billig's original relation [106]. By stabilizing the shock train in the isolator, it was observed that for longer pseudo shock train length, higher combustor heat release was allowed. Significant spread in computed pseudo shock train length within the rectangular isolator through the circular prediction relation led to the suggestion that corner flow and cross sectional aspect ratio effects on shock train behavior must be resolved.

Combustion-mode transition work performed by Sullins highlighted the sensitivity of the shock train leading edge location to mode-transition deviations in fuel-flow in a rectangular cross-section isolator/combustor setup [107]. Inflow Mach number was increased by means of increasing the combustor entrance temperature and fuel flow rate was simultaneously decreased to maintain constant equivalence ratio, simulating vehicle acceleration between Mach numbers of 5.85 to 6.2. Located in a constant area combustor with step prior to the main diverging combustor, the shock train leading edge location shifted by approximately 50% the constant area combustor length for a change in fuel flow rate from a 'light off' equivalence ratio of 0.38 to an equivalence ratio of 0.6. The combustor exit stream thrust is shown to be constant during this transition period.

2.2.2 Shock Train Dynamics & Aspect Ratio

A comprehensive review of isolator and supersonic diffuser work in the former Soviet Union was articulated in a publication by Penzin in 1995 [12]. Two modes of isolator operation are defined: the desirable pseudo-shock mode, and the undesirable separation-shock mode. The former, occurring at lower aspect ratios and isolator inflow Mach numbers, is characterized by an approximately constant lateral static wall pressure at any location along the longitudinal-axis and offers uniform flow at the exit plane of the isolator. Furthermore, the isolator flow field under this mode of operation is relatively insensitive to the inflow properties and pressure fluctuations are on the order of 20% RMS pressure or lower [39].

The separation-shock mode occurs at high Mach numbers and high aspect ratios, and is accompanied by non-uniform wall static pressure and large amplitude, unsteady fluctuations (on the order of 150% RMS pressure) within the isolator flow dynamics [39,108]. This mode is furthermore characterized by non-symmetric flow fields with three-dimensional separated regions in the duct corners and long duct length requirements to support the required combustor inlet pressure rise. These characteristics in turn yield undesirable, non-uniform isolator exit conditions. The approximate distribution between the two modes is shown in Fig. 2.5, along with previous research performed at Johns Hopkins University (JHU) Applied Physics Laboratory (APL) by Rice [108] and Nedungadi & Van Wie [39]. Current experimental and numerical simulation efforts are also mapped.

Substantial isolator research has been performed at JHU/APL since the 1970s. Relatively recently, experimental work performed by Rice aimed at investigating the implications of separation-shock mode on isolator performance [108]. By parametrically varying the aspect ratio between 2.5 and 10 and inflow Mach number between 3.0 and 4.0, the goal was to obtain data in the separation-shock mode region illustrated in Fig. 2.5. Time-averaged static wall pressure measurements were obtained along the lower and both side wall centerlines.

Large pressure fluctuations were observed during the unstart of the high aspect ratio isolators, compared to lower fluctuations for the low aspect ratio isolators. Based on the multi-wall

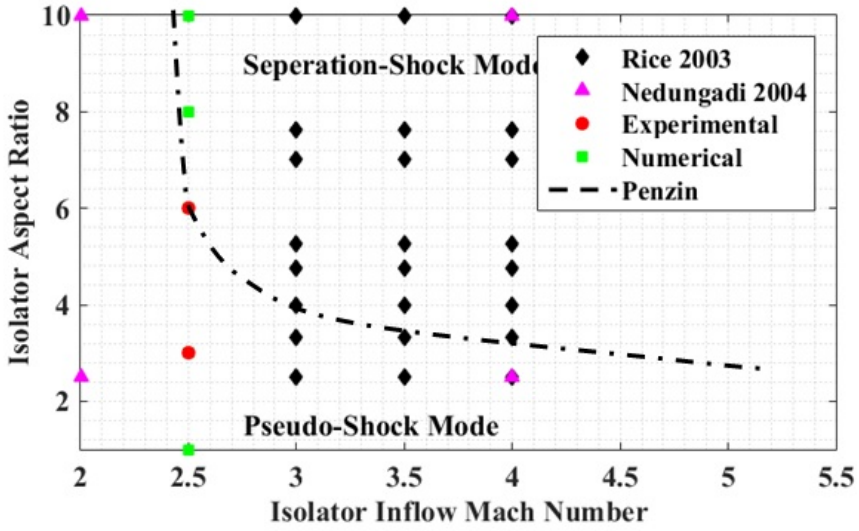

Figure 2.5: Isolator operating mode performance chart (adapted from Ref. [108]).

pressure measurements obtained, small three-dimensional separation regions were observed. These separation regions are hypothesized to not extend across the entire width of the isolator, unlike the larger two-dimensional separation regions expected in lower Mach and aspect ratio isolator flows.

Numerical simulations of isolators operating in separation-shock mode was performed by Nedungadi & Van Wie [39]. Two aspect ratio ducts (2.5 and 10) were exposed to two inflow Mach numbers (3-4) to compare simulation in pseudo-shock and separated-shock modes. Boundary layers 25% of the duct height were prescribed along the lower wall at the isolator entrance, with the upper and side-walls not having an incoming boundary layer. The $k - \epsilon$ turbulence model was used.

Operating in fully started mode, it is shown that Mach number decreases while static pressure increases with axial distance from the isolator inlet due to frictional effects. In the aspect ratio 10 case, the flow chokes (M=1) at a normalized longitudinal location of approximately 26 ($X/D_H = 26$), where D_H is the duct hydraulic diameter. In the Mach 2 aspect ratio 2.5 case, visualization of zero axial velocity isosurfaces in the duct corner regions show clear corner flow separation and subsequent reattached approximately 12 hydraulic diameters downstream of the initial separation point. Although this operating mode falls under the pseudo-shock region in Fig. 2.5, axial pressure distributions are not constant at planes located near the leading edge of the

shock train. Concerns about both the resolution of experimental sensors and accuracy of the CFD approach are discussed.

Simulating the aspect ratio 2.5 duct with an inflow Mach number of 4.0 results in extensive corner flow separation with no apparent reattachment point, as shown by the zero axial velocity isosurface visualizations. Initial corner flow separation is shown to spawn an oblique shock that propagates across the duct width. Increasing the aspect ratio is shown to increase the required length to contain the backpressure rise due to the initial shock wave originating from the corner separation propagating across a wider duct. Similar to the aspect ratio 2.5 case, varying the Mach number in the aspect ratio 10 case resulted in flow reattaching inside the isolator for a Mach number of 2, but failing to reattach at a Mach number of 4. Visualization of initial pressure rise contours show the aspect ratio 10 case is characterized by initial shock train fronts that are more planar than the lower aspect ratio case. It is proposed that duct height plays an important role in the formation of the three-dimensional shock front.

For all cases evaluated in the study by Nedungadi, the duct corner flow separation found at the junction of the side wall and lower wall was considered the dominant feature in the isolator. This event leads to a three-dimensional oblique shock wave that propagates across the entire width and height of the test section, leading to longer isolator length requirements for higher aspect ratio isolators. Corner separation regions reattach for lower Mach numbers in both aspect ratio configurations but never reattach for the higher Mach number cases. It is thought that these non-reattaching separation regions play a principle role in the initiation of the undesirable shock-separation modes.

2.3 Remaining Issues

Although isolator flow fields have been studied ever since the dual mode scramjet concept was introduced in the 1960s, distinct knowledge gaps remain. Due to the use of line-of-sight visualization techniques and predominantly single axis acquisition of flow parameters such a surface pressure and temperature, the shock train dynamics have been regarded as planar events in the

past, neglecting the potential for corner flow and other three-dimensional flow features to drive both the shape of the shock train and the transient dynamics (ex. shock train propagation and inlet unstart dynamics).

The first major issue that is addressed is the lack of simultaneous shock train visualization from multiple perspectives to evaluate the shock train front three-dimensionality. Widely used traditional single perspective line of sight techniques such as schlieren and shadowgraph do not lend well to the analysis of three-dimensional flow features. The planar oblique and planar normal shock train terminology used in literature stems from the use of these techniques as a sole visualization tool. The work performed in this thesis addresses this issue by visualizing the shock train front simultaneously from two different perspectives to provide a three-dimensional view of the flow feature inside the test section. Although a useful tool in the study of stationary flow features (ex. single stationary oblique or normal shock impinging with the boundary layer), time-averaged oil flow visualization techniques used in the past to obtain a second perspective in addition to the traditional side-view schlieren do not offer a time-resolved representation of the dynamic flow field of the shock train isolator and furthermore only represent the behavior of the flow very close to the wall. The multiplane shadowgraph technique specifically designed for this research study addresses this issue by resolving the flow features simultaneously and instantaneously, as well as interrogating both the near wall and freestream regions.

Two other approaches used in this work will help to resolve the three-dimensional shock front. The optimization of the synthetic schlieren (Background Oriented Schlieren) provides a global representation of density gradient magnitude in the test section. This allows for the comparison of the strength of the disturbances in different parts of the shock train revealing the presence of both oblique and normal structures in what was previously termed a planar oblique shock train. The second additional approach is the application of the steady state, three-dimensional CFD calculations performed as a complementary diagnostic to the experimental results. Primary calculations are applied across aspect ratios of 1.0, 3.0, and 6.0 and their three-dimensional shock fronts are evaluated and compared. Aside from studying corner flow effects, the numerical simula-

tions also allow for the analysis of side-wall boundary layer and its contribution to the formation of the shock train structure. Due to the geometry of the wind tunnel test section, experimental measurements and visualization of the side-wall boundary layer remained limited.

The second knowledge gap that is addresses is the study of the transient flow dynamics away from the center-region of the duct. Static and fast response pressure sensors used in past studies of isolator/inlet unstart dynamics have predominantly been located along the duct centerline. This does not allow for the analysis of boundary layer separation induced flow physics near the outer regions, where the low momentum, preliminary corner flow separation is expected to initiate alot of the transient characteristics. Dynamic pressure measurements are taken near the corner regions to compare to the center flow field characteristics observed. A second diagnostic tool employed to reveal additional information regarding the flow behavior away from the centerline/center axis region of the isolator is the Focusing Schlieren Deflectometry Velocimeter configuration. Due to the capability of evaluating density gradient across a small depth of sharp focus, the technique allows for high temporal bandwidth, point measurements of disturbance of light intensity (and thus indicating the presence of density gradient) within the test section at specific three-dimensional coordinates. Utilizing two point measurements spaced a known distance apart, velocity component is resolved as well as the frequency of the oscillating shock train. Results are compared between the center-axis and side-walls of the duct.

The work performed in this thesis advocates the use of observations and measurements along more than one axis is required to more fully comprehend the isolator shock train dynamics. This approach can prove useful to study other portions of the isolator, in particular evaluating the flow state at the exit plane of the isolator to help determine combustor performance parameters. Furthermore, this approach could be implemented in the study of other internal gas flows and flow devices other than the isolator shock train such as supersonic ejectors, shock tubes, and any other instance where shock features are meant to decelerate the supersonic flows and interact with the boundary layer [31].

Chapter 3: Experimental and Computational Approach

This section describes both the experimental and numerical approaches used in this study. Wind tunnel facilities are described and the various experimental diagnostic techniques are introduced. Basic flow parameters characterizing the fully started mode of operation of the aspect ratio 3.0 and 6.0 configurations are presented. The flow physics assumptions and turbulence models used in the numerical calculations are furthermore described.

3.1 Supersonic Indraft Wind Tunnels

3.1.1 University of Maryland Mach 2.5 Wind Tunnel

To simulate internally confined, supersonic isolator flow in a repeatable and adjustable experimental environment, a modular isolator model was designed to be housed in the University of Maryland's supersonic wind tunnel (UMD SSWT). The UMD SSWT serves as the main wind tunnel facility used in this study. Shown in Fig. 3.1, the in-draft wind tunnel contained an 833mm (33") long, 152x304mm (6x12") rectangular cross-sectional working test section into which a variety of nozzle and test section geometries can be incorporated. The total diffuser length leading to the vacuum tank measured 5590mm (220") long and transitions from the 152x304mm rectangular cross-section to a 300mm (12") diameter circular cross-section. The vacuum tank contains a volumetric capacity of approximately $53m^3(1871ft^3)$. Shock train dynamics are driven by the inherent backpressure rise of the facility throughout the run time (Fig. 3.7). A detailed description on how a typical run is executed is described below together with Fig. 3.2.

The generic test section outline together with the wind tunnel and data acquisition trigger architecture is shown in Fig. 3.2. The test section houses an upstream converging subsonic ramp,

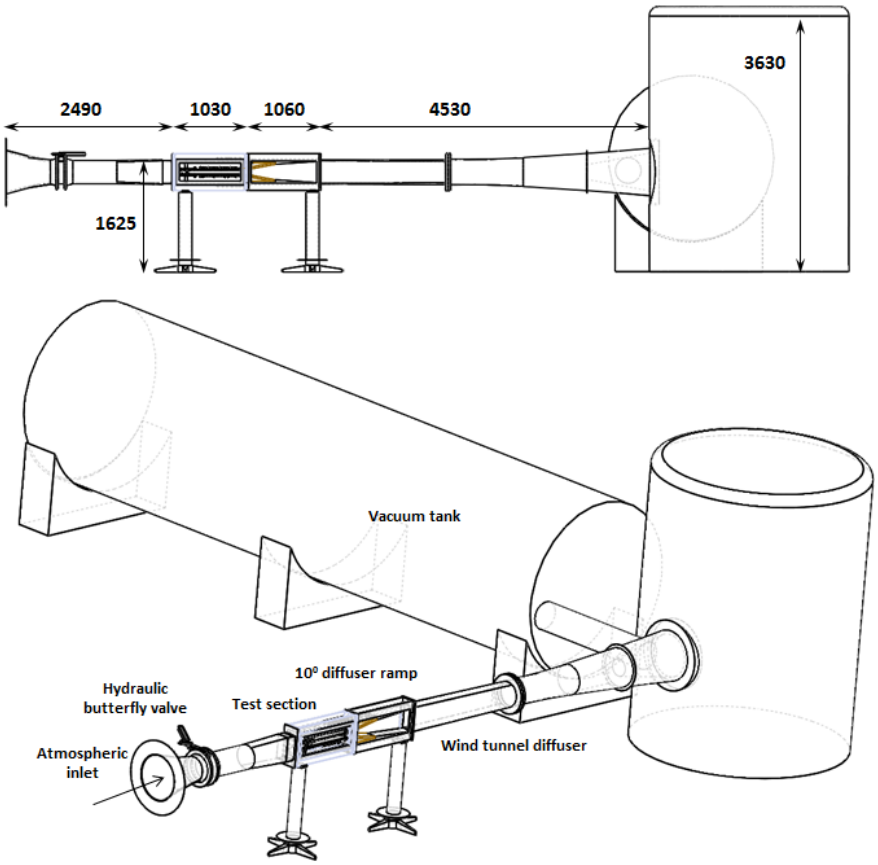

Figure 3.1: University of Maryland atmospheric indraft supersonic wind tunnel facility. Dimensions in mm.

a converging-diverging (C-D) Mach 2.5 nozzle, a constant rectangular cross-section isolator, and a 10^o diffuser housed in the rectangular portion of the diffuser. Given that the facility is an atmospheric indraft wind tunnel, variations in ambient thermodynamic variables can affect the day-to-day operations and flow behavior inside the isolator. Days with lower ambient pressure would result in lower backpressure to the isolator, which could result in different test section unstart time scales. To improve consistency of run-quality on a day-to-day basis (i.e. to minimize differences in isolator starting states), a normalized backpressure ratio based wind tunnel and diagnostics trigger mechanism was employed, as described below.

The diffuser is equipped with two 30PSIA, 0-5VDC pressure transmitters (Dywer Instruments Series 626) to provide an averaged real-time backpressure measurement. An additional atmospheric pressure input located outside of the wind tunnel facility (Dywer Instruments Series

626) was used to normalize the averaged backpressure value. This atmospheric value is also referred to as the stagnation value and the ratio of isolator exit to stagnation pressure is mathematically expressed as the ratios P_{back}/P_0 or P_3/P_2. This normalized backpressure measurement was used to reference the start of the wind tunnel run as a trigger event, thus accounting for specific variations of day-to-day stagnation pressure differences.

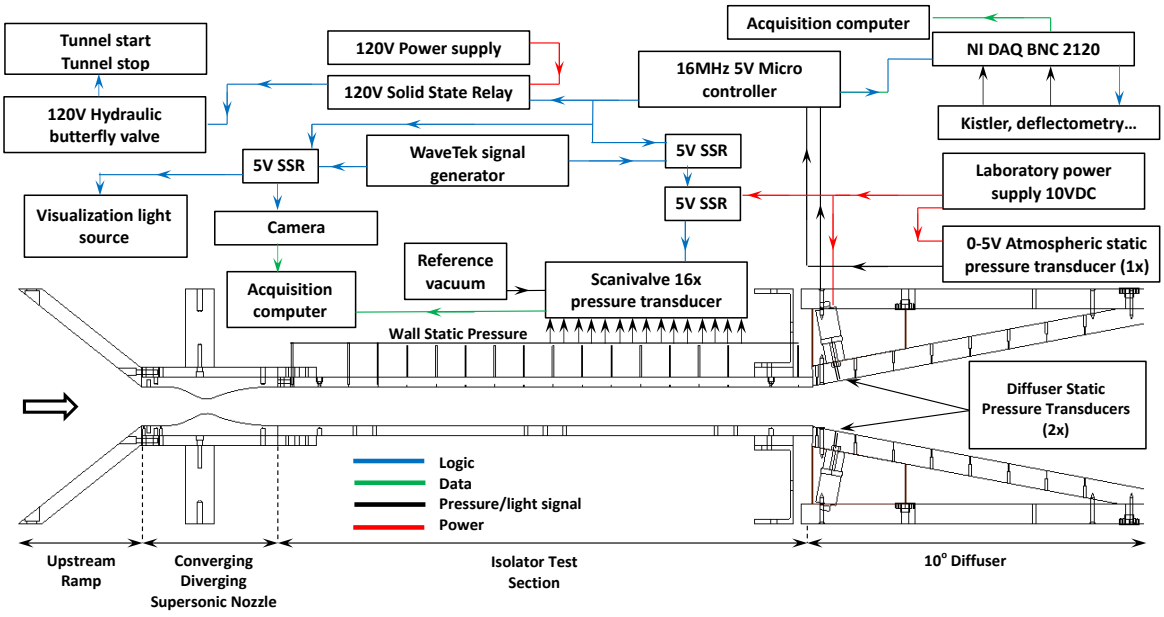

Figure 3.2: Generic isolator wind tunnel model outline with trigger architecture.

The wind tunnel control and trigger architecture, outlined in Fig. 3.2, was used to standardize and synchronize tunnel start time and data acquisition. This outline will be referenced frequently in the discussion of the diagnostic techniques below. The trigger system is based on normalized backpressure measurement. The two diffuser and single atmospheric static pressure transducers are absolute 0-30PSIA sensors outputting a linear 0-5VDC signal. These three signals are processed by the 16MHz microprocessor (Arduino Uno) capable of accepting five different input channels and supporting 12 different output channels. Arithmetic was programmed to evaluate the ratio between the diffuser mean and atmospheric static pressures. A constant P_3/P_2 ratio of 0.135 was chosen as the starting point for all wind tunnel runs. This was equivalent to a resulting voltage magnitude of 66 milliVolts (mV) as monitored by the arithmetic operation programmed

into the microprocessor.

A typical wind tunnel run started by evacuating the entire wind tunnel facility downstream of the hydraulic butterfly valve (Fig. 3.1), reducing the normalized isolator outlet plane static pressure ratio to the desired P_3/P_2 ratio. Logic programmed to the microprocessor triggered one of the 5V output channels if the resulting voltage ratio reached the 66mV condition on the downward slope. The hydraulic butterfly valve was operating off of a 120V signal, thus a 120V step-up CryDom Solid State Relay (SSR) was introduced to convert the original 5V microprocessor trigger signal into a 120V trigger signal capable of initiating the valve operation. As can be observed in Fig. 3.7, a finite valve opening time of approximately a quarter of a second is followed by the expected drop in static pressure throughout the isolator due to the supersonic expansion. As facility backpressure increases with run-time, pressure-gradient induced boundary layer separation proceeds upstream, as shown by the time-history of static pressure increase along the duct longitudinal axis in Fig. 3.7.

To evaluate the different aspects of the isolator flowfield dynamics, a consistent and reliable data time-structure is needed to synchronize and properly compare different types of measurement. The butterfly valve opening signal marked the commencement of the run-time recording. Different types of diagnostics could be synchronized and compared through utilizing either the run-time clock value or the magnitude of the backpressure.

Figure 3.3a shows the overall setup of the University of Maryland supersonic wind tunnel facility, with flow from right to left to show the data acquisition and tunnel control hardware. Key features are annotated and expanded upon in the figure caption. A close up of the tunnel trigger system and associated diagnostics hardware is shown in Fig. 3.3b. Solderless protoboards allowed for rapid modification of the trigger and data acquisition logic sequence as various diagnostic techniques were implemented. A bank of BNC binding posts (3) fed electrical signals through BNC cables to the various diagnostic related hardware.

Aspect ratio (ratio of duct width over height) 3.0 & 6.0 isolator ducts are tested experimentally, and their model outlines are shown in Fig. 3.4. The isolators are characterized by duct

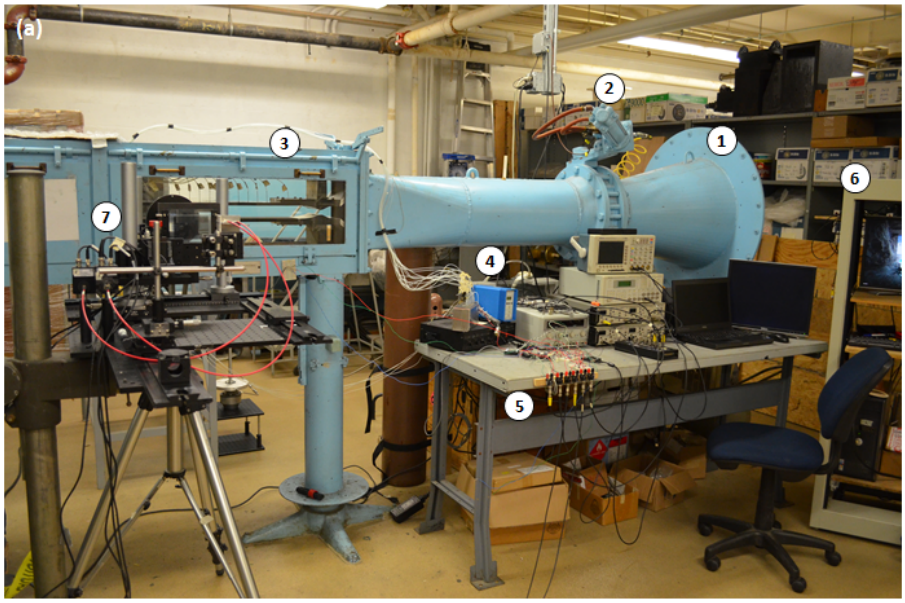

(a) UMD Supersonic Wind Tunnel facility layout (Flow is right to left): (1) atmospheric inlet, (2) hydraulic butterfly valve, (3) wind tunnel test section, (4) data acquisition systems, (5) data acquisition logic station, (6) desktop data acquisition computer, (7) receiving end of the Focusing Schlieren Deflectometry setup (Chapter 3).

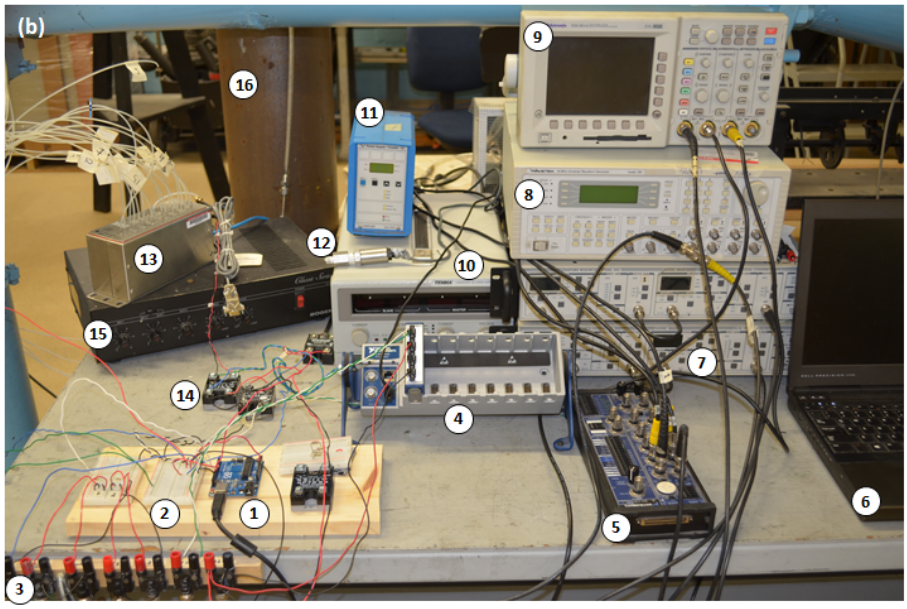

(b) Close-up of the trigger and data acquisition arrangement including hardware used during the Focusing Schlieren Deflectometry calibration studies (Chapter 4): (1) 16MHz microprocessor and controller, (2) solderless protoboards, (3) BNC dual binding post station, (4) NI-9188 data acquisition module, (5) NI-1200 BNC data acquisition module, (6) laptop data acquisition computer, (7) Stanford dual bandpass filter, (8) WaveTek signal generator, (9) Oscilloscope, (10) 0-30VDC power supply, (11) Kistler dynamic pressure sensor power supply and amplifier, (12) trigger circuit atmospheric static pressure transducer, (13) ScaniValve static pressure module, (14) solid state relay, (15) acoustic signal amplifier, (16) FSD calibration Helium tank.

Figure 3.3: UMD supersonic wind tunnel facility and data acquisition layout.

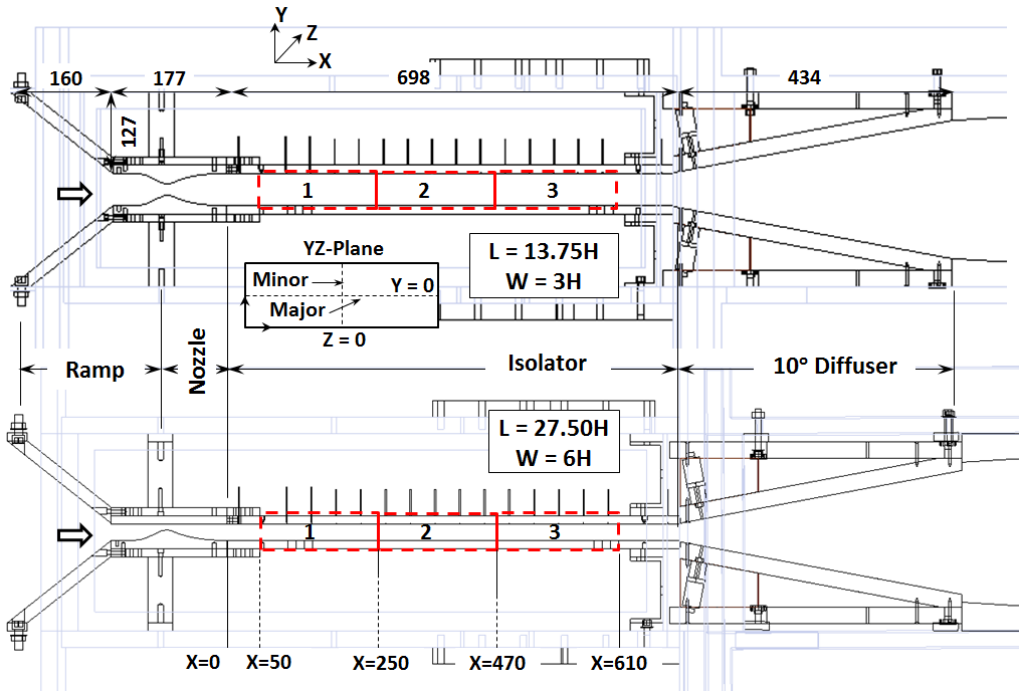

Figure 3.4: Aspect Ratio 3.0 & 6.0 geometry outlines. Dimensions in millimeters.

heights of 50.8mm (2") and 25.4mm (1"), length-to-height ratios (L/H) of 13.75 and 27.5, and isolator unstart times of 33 and 56 seconds respectively. The Method of Characteristics (MOC) approach was used to design a Mach 2.5 nozzle contour of minimum length, producing a supersonic sharp corner nozzle with a flow straightening throat region. Due to the reduced duct height, the aspect ratio 6.0 configurations is composed of a lower wall half-nozzle symmetry, maintaining the appropriate Mach-Area relationship nozzle throat height. Principle isolator dimensions are shown in millimeters. The duct minor- and major-axis, important terminology in discussing the shock front three-dimensionality, as well as duct axis orientations are illustrated in Fig. 3.4.

Both the lower and upper walls are equipped with 16, 0.5mm (0.02") diameter centerline static pressure ports spaced 38mm (1.5") apart, connected to a 16 channel piezoelectric static pressure module (Scanivalve DSA3217) through the means of 1.6mm (0.06") diameter stainless steel tubulations and supporting Tygon tubing. These channels were used as a rudimentary approach to track the leading edge shock train location through monitoring boundary layer separation pressure rise and to provide a measure of normalized unstart time τ (time between the arrival and exit

of shock train inside the duct divided by the total run time from valve opening). A customized 10^o diffuser section was manufactured to decrease total pressure loss, increase total run-time, and provide a smooth transition to the downstream region of the tunnel facility.

With the shock train dynamics driven by the inherent rise in facility backpressure, the influence of diffuser length downstream of the isolator test section is materialized by the time-dependent oscillatory motion of the upstream propagating shock train. One phenomena that quantifies the frequency at which this oscillation occurs is the concept of air resonance in a cavity, described by Helmholtz resonance. As an analogy to the well known 'blowing across the top of an empty bottle'example, the test section and diffuser components downstream of the shock train can be thought of as the resonator system. The isolator duct cross-section serves as the open face and the length of the isolator serves as the neck of the bottle, with everything downstream of the isolator serving as the bottle.

$$f_H = \frac{a}{2pi}\sqrt{\frac{A}{VL_{diff}}} \tag{3.1}$$

Presented in Eq. 3.1, the Helmholtz frequency is a function of the speed of sound (a), the cross-sectional area of the duct (A), the static volume of the tunnel facility (V_0), and the equivalent length of the isolator section (L_eq) [109]. The equivalent length is calculated as $L_eq = L_n + 0.6D_H$, where L_n is the physical isolator length and D_H is the duct hydraulic diameter. Results for the two experimental aspect ratios are presented in Fig. 3.5. The oscillatory frequency component of the shock train propagation dynamics due to the diffuser acting as a Helmholtz resonator are relatively low. The oscillation frequency due to Helmholtz resonance is highest when the shock train is positioned near the exit plane (at the start of the normalized unstart time), and lowest when the shock train is about to exit the isolator (at the end of the normalized unstart time). This is likewise observed in flow visualization and wall-bound, fast-response dynamic pressure measurements. The majority of the schlieren and shadowgraph visualization efforts were performed at a frame rate of 250Hz to capture the dynamics. The shock train oscillatory frequency measured with the velocimetry application of the Focusing Schlieren Deflectometry technique presented in

Chapter 5 correlates well to the frequency estimates shown in Fig. 3.5.

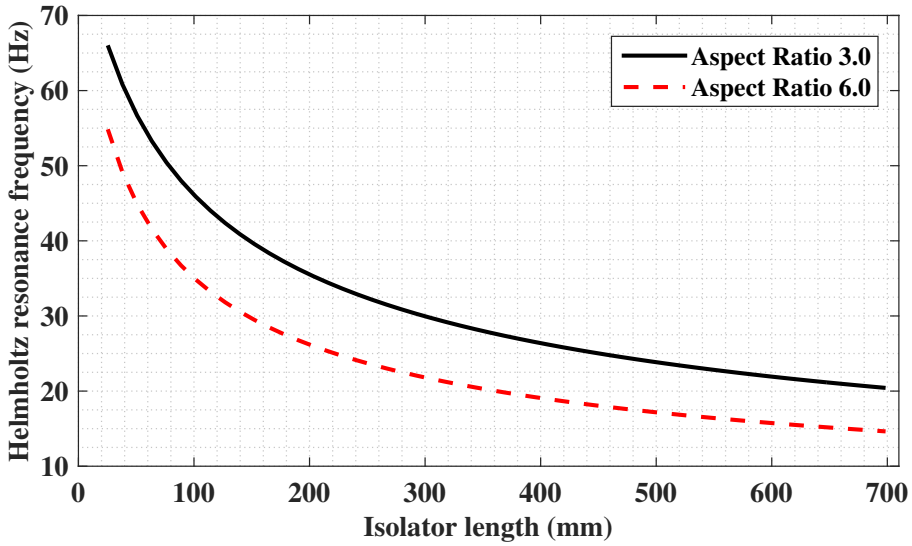

Figure 3.5: Diffuser interaction driven Helmholtz resonance frequency for aspect ratio 3.0 & 6.0 isolators.

3.1.2 AEDC Tunnel 9 Mach 2.7 Calibration Wind Tunnel

The AEDC Tunnel 9 Mach 2.7 calibration wind tunnel is a supersonic atmospheric indraft facility designated primarily for sensor calibration and fundamental research efforts supporting AEDC Hypervelocity Wind Tunnel 9. Featuring a 540mm (21") long, 67x67mm (2.6x2.6") aspect ratio 1.0 square test section (Fig. 3.6), the facility was predominantly used in proving the Background Oriented Schlieren and Focusing Schlieren Deflectometry experimental diagnostics tools discussed below prior to implementation in the UMD supersonic wind tunnel for more extensive refinement and optimization.

In addition to providing insight into shock train flow dynamics in aspect ratio 1.0 ducts, laser planar Mie-scattering visualization along the previously inaccessible YZ-plane provided insight into the core flow state pre and post shock train passage. Additionally, the application of the multiplane shadowgraph visualization method allowed for comparison in the analysis of three-dimensional isolator shock train front formation between aspect ratios of 1.0, 3.0, and 6.0.

The facility features three diagnostics stations with both XY-plane and XZ-plane flow vi-

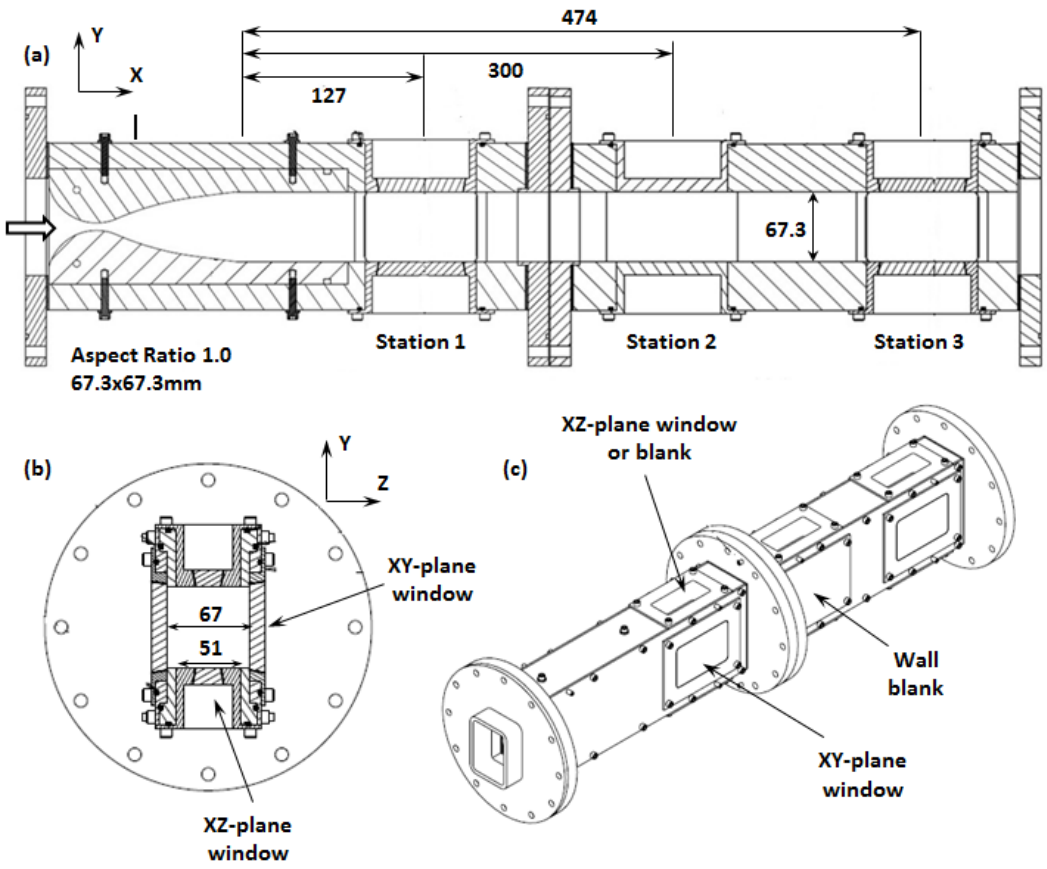

Figure 3.6: AEDC Tunnel 9 Mach 2.7 supersonic calibration wind tunnel. Dimensions in mm.

sualization access. The ability to swap out a window side-wall plate for an all-aluminum blank side-wall plate allowed the application of dynamic pressure measurements along all three duct axes. Acrylic bottom and upper wall inserts were used for the multiplane shadowgraph application (Fig. 3.22). Due to the XZ-plane insert geometry (Fig. 3.6b), only 75% of the test section XZ-plane width was accessible for diagnostics, with both port and starboard side wind tunnel wall structure taking up the remaining 25% and blocking the field of view. Even though this meant that getting close to the isolator corner was optically impossible, valuable insight into the aspect ratio 1 isolator shock train formation are still obtained.

3.2 Isolator Flow Parameters & Boundary Layer Profiles

3.2.1 Time-Averaged Wall Static Pressure Measurement

Both lower and upper isolator walls of the aspect ratio 3.0 & 6.0 configurations support a series of 16 centerline static pressure taps for time-averaged static wall pressure measurements. Figure 3.2 can be referenced for the following description of the static pressure system. Spaced 38.1mm (1.5") apart and with a diameter of 0.4mm (0.01") and a depth of 2mm (0.08"), the static pressure cavities give way to 1.5mm (0.06") diameter stainless steel tubulations that connect to a 16-channel piezoelectric static pressure module (ScaniValve DSA3217) through 1.5mm inner-diameter Tygon tubing. The ScaniValve static pressure module has an accuracy of $\pm 0.05\%$. Accepting a 1-500HZ 9-13VDC signal, a 0-35V, 0-10A DC laboratory power supply and 40MS/s WaveTek signal generator (Model 281) are used together with a pair of 0-32VDC Crydom Solid State Relays (SSR) to obtain static pressure measurements at select user frequencies (mostly at 250Hz to synchronize with image acquisition). Tygon tube length was minimized to increase measurement response rate [110].

Due to the relatively slow response-rate, the time-history of static pressure measurements presented in Fig. 3.7 represent time-averaged values of wall static pressure. Nevertheless, analysis of the boundary layer separation induced pressure rise allows for the location of the shock train leading edge as the backpressure rises. A normalized run time τ is used to indicate the time of the shock train inside the isolator, starting at the first instance the shock train is captured in the isolator and ending when the shock train exits the isolator. Normalized unstart times of 22.01 and 42.40 seconds are recorded for the aspect ratio 3.0 and 6.0 configuration respectively.

Due to the smaller cross-sectional area, the backpressure rise is more gradual and the shock structure is held in the downstream diffuser end for a longer time, as is evident in the 92.6% increase in τ. Wall static pressure is used to measure boundary layer separation induced pressure rise, estimate location of the leading edge of the shock train, and measure overall pseudo-shock train length, as presented in Chapter 6.

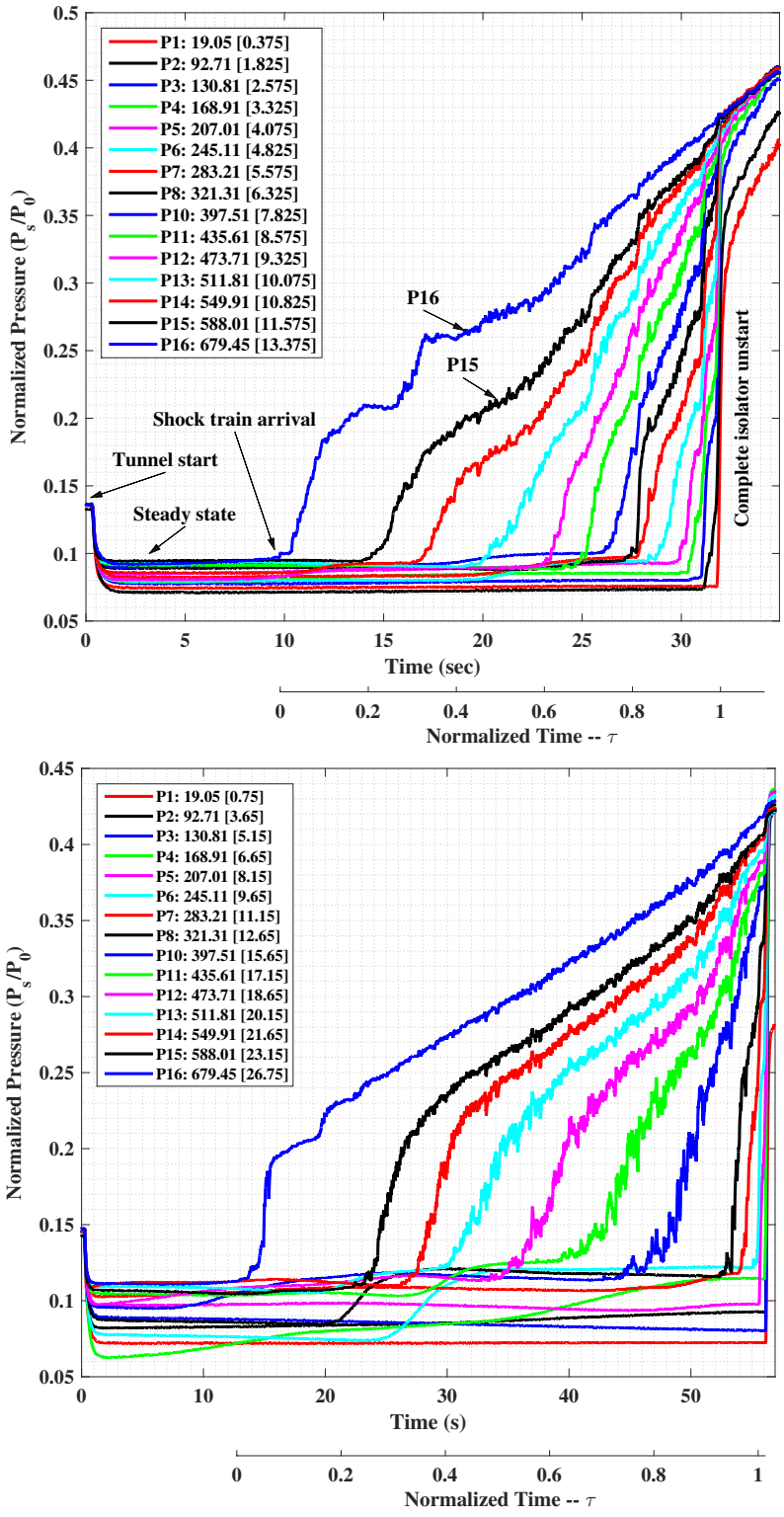

Figure 3.7: Time history of time-averaged static pressure rise in AR 3 & 6 isolator.

3.2.2 Lower Wall Boundary Layer Pitot-Probe Surveys

To characterize the isolator lower wall boundary layer, a single total pressure probe survey positioned along the lower wall centerline near the inlet at X = 91mm (3.6"), the center at X=300mm (11.8"), and the outlet at X = 600mm (23.6") from the centerline of the duct is performed along the vertical axis. Shown in Fig. 3.8, the pitot probe is driven by a Thorlabs LS-150 stepper motor with a 5 μm resolution per step. The 1.58mm (0.06") outer diameter total pressure pitot probe is made out of hypodermic tubing and had an inner diameter of 0.79mm (0.03"). The pitot probe was contoured in a manner that the sensing portion of the probe was able to get as close to the wall as possible. Located at the wall surface, two pitot diameter upstream of the pitot tip to avoid excessive pitot probe interaction, is a 0.40mm (0.01") diameter static pressure tap.

The vertically oriented traversing schedule is outlined in Fig. 3.9 for both the lower wall single pitot probe and side wall 7-probe pitot rake (described in the following section). Both aspect ratio configurations are shown. This visual representation is bounded by the Y- and Z-axis, equivalent to looking orthogonally along the longitudinal X-axis downstream into the flow (i.e. flow coming out of the page). The vertical Y-axis has its origin at the center-axis of the duct, meaning that the lower wall is designated by negative Y-axis values.

Raw pitot survey data is shown in Fig. 3.10 for the upstream station survey in the aspect ratio 3.0 configuration. Pitot surveys were only taken during the fully started mode of operation with no shock train present inside the boundary layer. The pitot probe traversing schedule, controlled by the LS-150 software interface, is set at vertical increments of 1mm (0.04") and at on-station times of 100ms for time-averaged results. Schlieren visualization in the upstream pitot station of the aspect ratio 3.0 configuration confirms a boundary layer thickness (δ) of approximately 4mm (0.2"). Plateaus in the total pitot pressure shown in Fig. 3.10 represent the different vertical stations targeted as a function of time, and are annotated accordingly with subsequent measurements taken at 1mm intervals. Due to the finite diameter of the pitot probe, the first measurement was taken at a vertical axis location of Y = -24.6mm. The Y-axis designation is utilized to represent the distance from the origin which aligns with the center-axis of the duct.

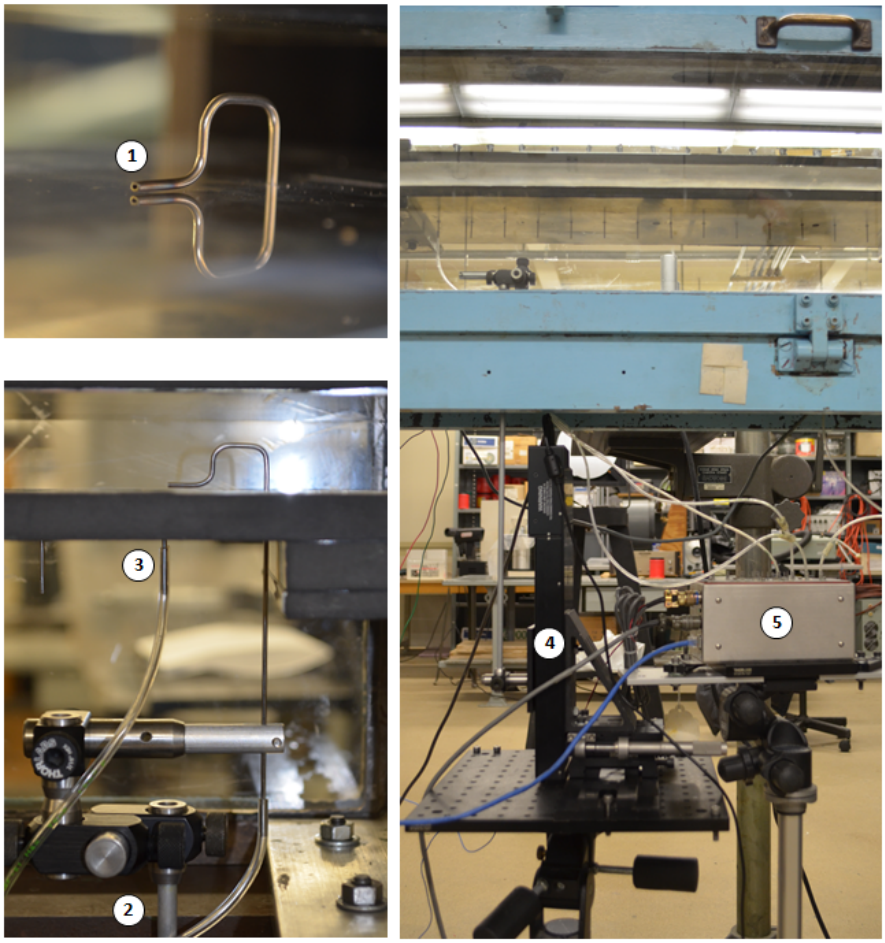

Figure 3.8: Minor axis pitot probe experimental setup: (1) total pressure port, (2) vertically traversing linkage, (3) static wall pressure port, (4) ThorLabs LS-150 stepper motor, (5) ScaniValve DS 16ch static pressure module. Survey conducted at X = 91mm and X = 600mm.

The Y' designation represents the local distance from the lower wall. Subsequent figures will use the actual Y-axis vertical coordinate of the measurement as the independent axis.

Evaluation for the flow parameters of interest are presented below for aspect ratios 3.0 and 6.0. Detailed analysis for the inlet and outlet stations are covered, with flow parameter values for the middle station included in the Table 3.1 summary.

Compressible turbulent boundary layer (CTBL) calculations derived by an implicit numerical method and the Turbulent Kinetic Energy (TKE) model for the aspect ratio 3.0 case are performed using the Virginia Tech Boundary Layer Applet [111] for comparison in order to build confidence in the experimental measurements. The detailed numerical approach can be found in

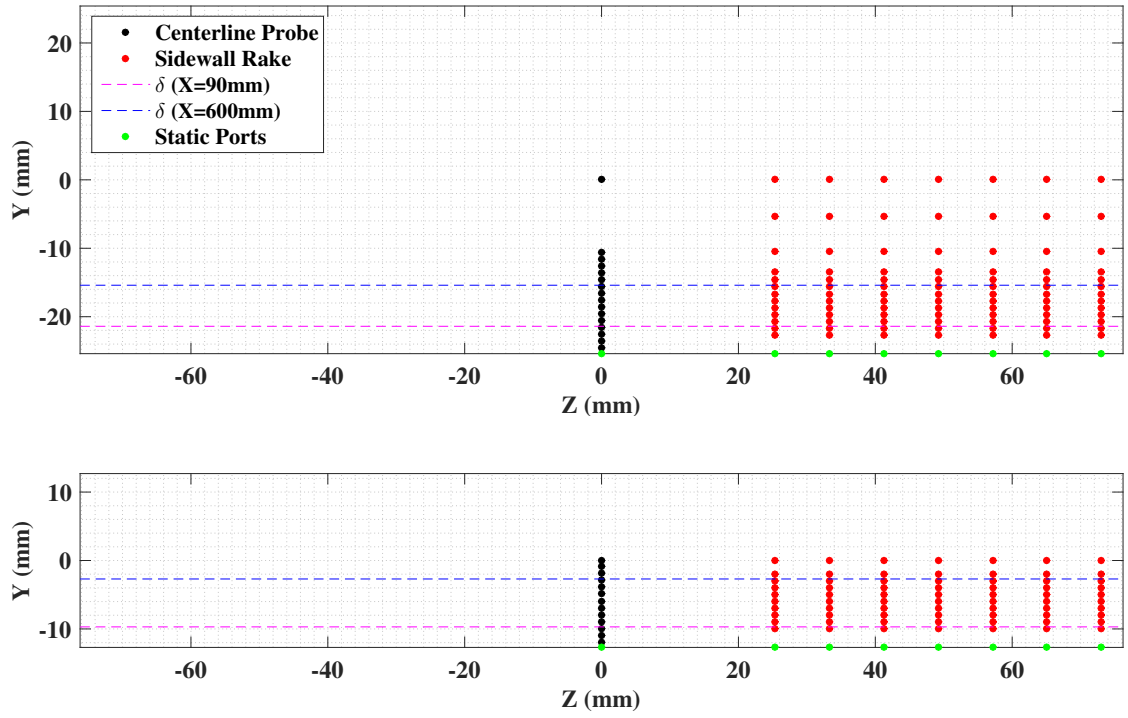

Figure 3.9: Lower wall pitot probe and side wall pitot rake vertical boundary layer profile for the aspect ratio 3.0 & 6.0 configuration. Boundary layer thickness (δ) for the upstream (X = 90mm) and downstream (X = 600mm) stations as derived from schlieren visualization are plotted.

'Boundary Layer Analysis' by Schetz & Bowersox [112]. Calculations with initial velocity, pressure, Mach number, mesh cell size, and boundary layer thickness of $570m/s$, $5950Pa$, 2.5, $2E-5m$, and $1.5mm$ respectively are progressed through 5000 iterations. Uniform grid spacing along the normal direction is employed as is the Law of the Wake to provide an initial velocity profile. Solutions of u/U_e, v/U_e and T/T_e are obtained. Mach number results are subsequently calculated using $R = 287J/Kg.K$ and $\gamma = 1.4$.

A polynomial root finder is used to implicitly calculate the Mach number according to the Rayleigh supersonic pitot probe formula provided in Eq. 3.2 [61], given the pitot static pressure ratio shown in Fig. 3.10. The ratio of specific heats, γ, is held constant at 1.4.

$$\frac{P_{02}}{P_1} = \frac{P_{02}}{P_2}\frac{P_2}{P_1} = \left[\frac{(\gamma+1)^2 M_1^2}{4\gamma M_1^2 - 2(\gamma-1)}\right]^{\left(\frac{\gamma}{\gamma-1}\right)} \frac{1-\gamma+2\gamma M_1^2}{\gamma+1} \tag{3.2}$$

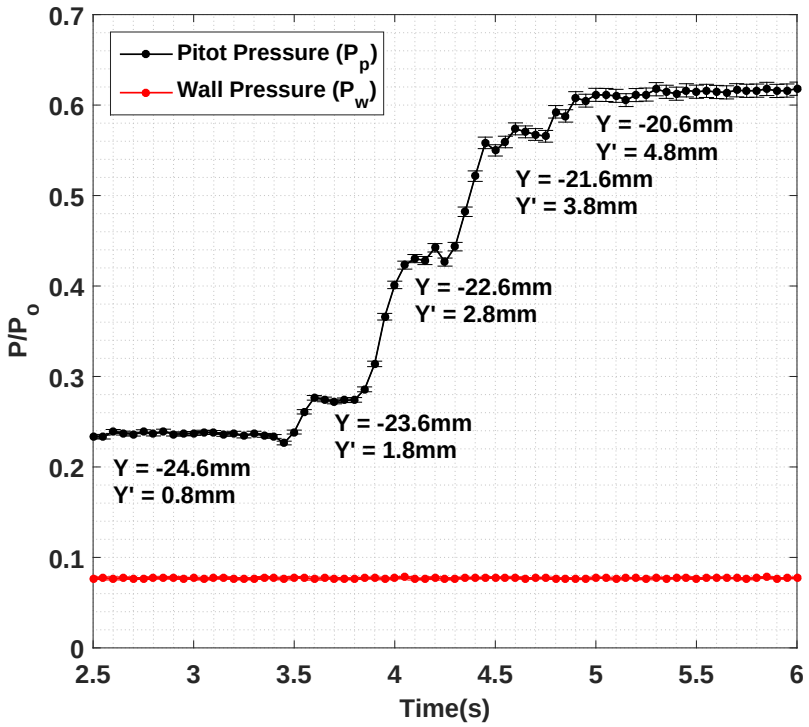

Figure 3.10: Pitot total and static wall pressure raw data file shows the total pressure increasing as the pitot probe is traversed vertically through the boundary layer and ultimately into the freestream.

Calculated flow parameters are presented in Fig. 3.11-3.13 for both aspect ratios. The theoretical derivations provided by the boundary layer analysis tool of Schetz & Devenport is included in green for the Mach, velocity, and temperature plots as a confidence check in the pitot probe derived flow measurements [111, 112]. These parameters are used to calculate momentum thickness based Reynolds numbers in Chapter 6 and to validate the numerical studies in Chapter 4. The Mach number profiles, calculated from Eq. 3.2, are presented in Fig. 3.11. The Y-axis represents the vertical distance from the centerline (Y=0), with the lower wall of the isolator location represented by the minimum Y-axis values in the plots.

Due to the finite diameter of the pitot probe, the subsonic boundary layer is not probed. As expected, Mach number is maximum at the upstream pitot station. Friction effects cause the Mach number to fall as measured by the downstream station. The aspect ratio 3.0 freestream Mach number at the inlet is measured to be 2.4, a 4% decrease from the design nozzle Mach

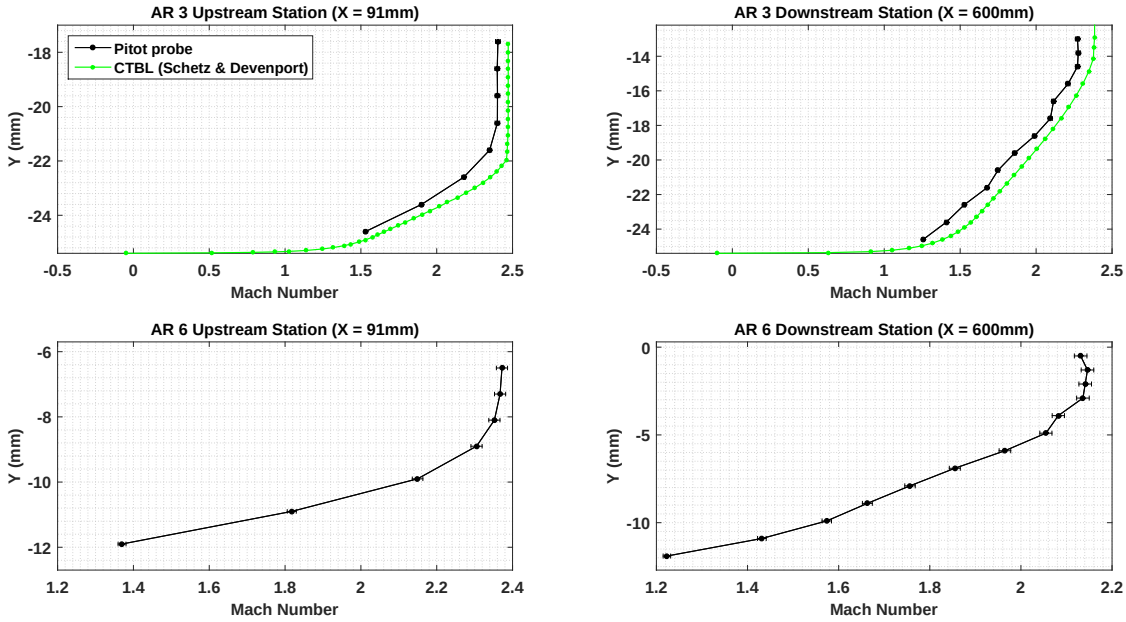

Figure 3.11: Mach number calculations from centerline Pitot-probe survey utilizing Eq. 3.2. Measurements taken at 1mm intervals from the lower isolator wall.

number of 2.5. This drop in inflow Mach number can be explained by expansion and friction effects experienced by the nozzle flowfield. A slightly more significant drop is shown for the aspect ratio 6.0 inflow Mach number calculation with a maximum Mach number of 2.37, a 5% decrease. A smaller degree of expansion in this half nozzle geometry is expected to adversely affect the inflow Mach number.

Static temperature along the vertical profile is calculated through the Walz's equation (modified Crocco relation), shown in Eq. 3.3 [113, 114], where the subscript e indicates a freestream parameter, T_r is the recovery temperature, and r is the recovery factor. The adiabatic wall assumption is used to render $T_w = T_r$. The recovery factor r is known to vary little across the boundary layer profile, and is calculated as $r = Pr^{1/3}$, where Pr is the Prandtl number and is chosen to be 0.7 [114]. A relationship between the recovery factor and the recovery temperature is provided in Eq. 3.4. The original form of the modified Walz equation (Eq. 3.3) can be simplified to Eq. 3.5, which allows for the calculation of the temperature profile as a function of the Mach number at each vertical location and the constants of freestream temperature and γ.

$$\frac{T}{T_e} = \frac{T_w}{T_e} + \frac{T_r - T_w}{T_e}\left(\frac{U}{U_e}\right) - r\frac{\gamma-1}{2}M_e^2\left(\frac{U}{U_e}\right)^2 \tag{3.3}$$

$$T_r = T_e\left(1 + r\frac{\gamma-1}{2}M_e^2\right) \tag{3.4}$$

$$T = Te * \frac{(1 + r(\frac{\gamma-1}{2})M_e^2)}{(1 + r(\frac{\gamma-1}{2})M^2)} \tag{3.5}$$

Freestream parameters are estimated by the assumption of an isentropic expansion through a supersonic nozzle. The well known isentropic relations are provided in Eq. 3.6a-c, where the subscript 0 indicates stagnation values, represented by the ambient conditions outside the wind tunnel. By utilizing the inlet freestream Mach number derived from Eq. 3.2, static freestream temperature, pressure, and density can be calculated.

$$\frac{T_e}{T_0} = \left(1 + \frac{\gamma-1}{2}M^2\right)^{-1} \tag{3.6a}$$

$$\frac{P_e}{P_0} = \left(1 + \frac{\gamma-1}{2}M^2\right)^{\frac{-\gamma}{\gamma-1}} \tag{3.6b}$$

$$\frac{\rho_e}{\rho_0} = \left(1 + \frac{\gamma-1}{2}M^2\right)^{\frac{-1}{\gamma-1}} \tag{3.6c}$$

With the freestream parameters known along with the vertical profile Mach number results shown in Fig. 3.11, static temperature approximations through the boundary layer can be made. Results are shown in Fig. 3.12 for both aspect ratios. The expected trend in decreasing temperature with increased distance from the wall is observed. Inflow freestream temperature can be readily compared to the isentropic expansion freestream temperature provided by Eq. 3.6a. With an isentropic freestream temperatures of 133K and 135K respectively, the freestream temperature estimates provided by Eq. 3.5 are within 0.5% and 3.5% respectively for both aspect ratio configurations. Due to the higher Mach number flow field in the aspect ratio 3.0 flow field compared to

the aspect ratio 6.0 configuration, lower temperatures are expected.

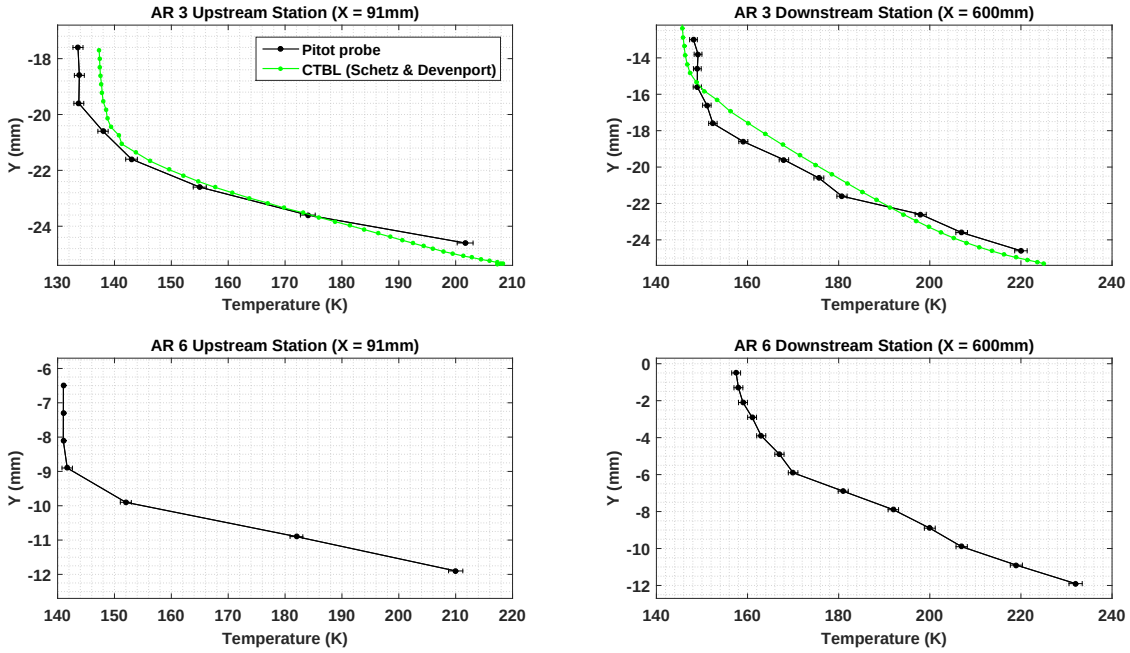

Figure 3.12: Temperature calculations from centerline Pitot-probe survey utilizing Eq. 3.5. Measurements taken at 1mm intervals from the lower isolator wall.

With temperature calculated in accordance to Eq. 3.5, the relation between Mach number and speed of sound can be used to calculate the flow velocity according to $M = \frac{U}{a}$. The speed of sound is calculated as $a = \sqrt{R\gamma T}$, with the specific gas constant of air as $R = 287 J/KgK$. Results are shown in Fig. 3.12 for both aspect ratios.

The ideal gas assumption is utilized to approximate the density profiles in the boundary layer utilizing the measured pressure and calculated temperature distributions. Such measurements were desired to calculate the boundary layer displacement (δ^*) and momentum thickness (θ) integrals according to Eqs. 3.7 and 3.8 respectively [112]. The boundary layer displacement thickness represents the measure of mass flux deficit caused by the slower moving BL flow compared to the freestream region. The boundary layer momentum thickness in turn represents the momentum flux deficit caused by the reduced velocity inside the boundary layer.

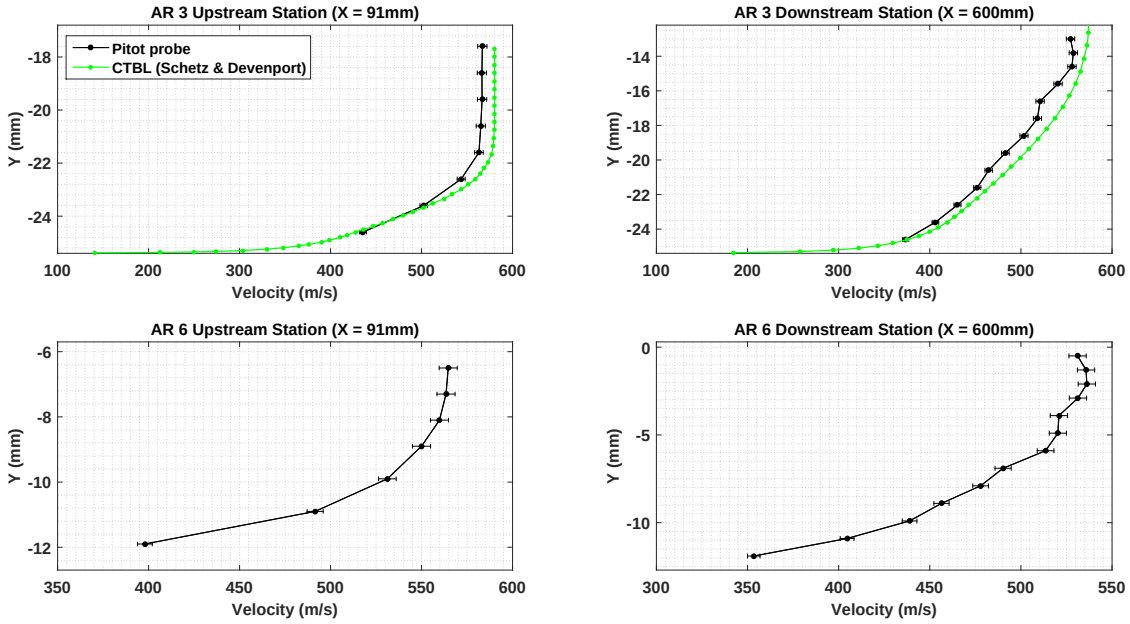

Figure 3.13: Velocity calculations from centerline Pitot-probe survey. Measurements taken at 1mm intervals from the lower isolator wall.

$$\delta^* = \int_0^e \left(1 - \frac{\rho(y)u(y)}{\rho_e u_e}\right) dy \tag{3.7}$$

$$\theta = \int_0^e \frac{\rho(y)u(y)}{\rho_e u_e}\left(1 - \frac{u(y)}{u_e}\right) dy \tag{3.8}$$

The pitot survey data for velocity and density are used to evaluate the above integrals. Edge velocity and density are appropriately chosen based on the boundary layer thickness at each station. The ratio of the displacement thickness to the momentum thickness is referred to as the shape factor, or H-factor, calculated according to Eq. 3.9. The shape factor is used to determine the state of the boundary layer as a measure of the adverse pressure gradient magnitude. Higher values of H represent stronger adverse pressure gradients within the boundary layer. Coincidentally, higher adverse pressure gradients can reduce the Reynolds number at which transition to turbulence occurs. Likewise, higher adverse pressure gradients promote boundary layer separation. The

$$H = \frac{\delta^*}{\theta} = \frac{\int_0^e \left(1 - \frac{\rho(y)u(y)}{\rho_e u_e}\right) dy}{\int_0^e \frac{\rho(y)u(y)}{\rho_e u_e}\left(1 - \frac{u(y)}{u_e}\right) dy} \tag{3.9}$$

A commonly used non-dimensionalized parameter to characterize the flow-field is the Reynolds number, also known as the ratio of inertial over viscous forces. Presented in the classic sense in Eq. 3.10, the Reynolds number is a function of length scale. The dynamic viscosity of the fluid (μ) is calculated according to Sutherlands law (Eq. 3.11). For air, the reference viscosity and temperature, mu_{ref} and T_{ref}, are equivalent to $1.716x10^{-5}\,\frac{kg}{ms}$ and $273.1K$ respectively. The Sutherland temperature, C, is equivalent to $110.6K$. The calculations of δ^* and θ above subsequently allow for the calculation of the boundary layer displacement and momentum thickness Reynolds numbers. Facility based Reynolds number is calculated using the isolator hydraulic diameter as length scale.

$$Re_x = \frac{\rho_e U_e x}{\mu_e} \tag{3.10}$$

$$\mu = \mu_{ref} \frac{T_{ref} + C}{T + C} (\frac{T}{T_{ref}})^{3/2} \tag{3.11}$$

Findings from the lower wall centerline boundary layer pitot probe survey along with associated calculations are summarized in Table 3.1. The subscript of 1 associated with the boundary layer parameters represent the duct minor-axis boundary layer parameters used alongside the major-duct parameters (pitot rake work described below) in Chapter 6. This nomenclature approach is illustrated in Fig. 3.14 utilizing straight lines as the boundary layer edge approximation. These parameters serve multiple purposes. Aside from articulating the state of the flow field inside the isolator for future follow on or comparative studies, the parameters are used to verify and validate the fully started numerical results discussed in Chapter 4. Additionally, boundary layer momentum thickness calculations are used in the modification of the empirical shock train length model presented in Chapter 6.

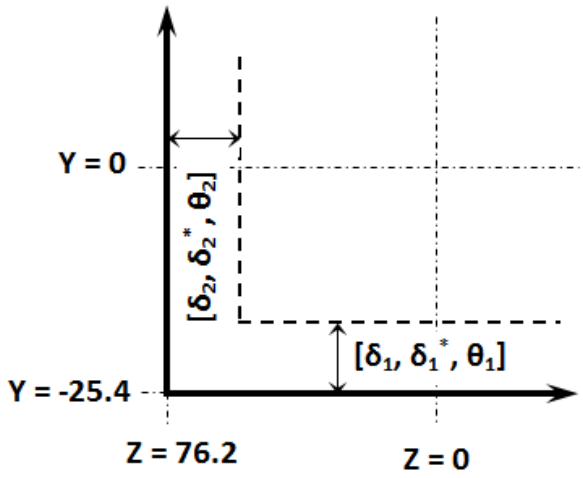

Figure 3.14: δ_1 and δ_2 corner schematic. Flow out of the page.

	Aspect ratio 3.0			Aspect ratio 6.0		
	Inlet	Middle	Oulet	Inlet	Middle	Oulet
M_∞	2.44 ± 0.029	2.39 ± 0.028	2.34 ± 0.026	2.38 ± 0.028	2.31 ± 0.027	2.27 ± 0.026
$U_\infty(m/s)$	560 ± 7.28	554 ± 7.20	549 ± 7.12	542 ± 7.01	535 ± 6.92	528 ± 6.84
$T_\infty(K)$	131 ± 1.71	134 ± 1.75	137 ± 1.79	141 ± 1.84	144 ± 1.88	149 ± 1.95
$P_w(Pa)$	7802 ± 156	8045 ± 160	8410 ± 168	7412 ± 148	7697 ± 153	7903 ± 158
$\delta_1(mm)$	4.17 ± 0.187	6.74 ± 0.303	9.90 ± 0.445	3.89 ± 0.175	5.94 ± 0.267	9.71 ± 0.431
$\delta_1^*(mm)$	1.01 ± 0.015	2.11 ± 0.031	3.38 ± 0.051	0.55 ± 0.008	1.02 ± 0.015	2.34 ± 0.035
$\theta_1(mm)$	0.28 ± 0.007	0.64 ± 0.016	1.01 ± 0.025	0.27 ± 0.002	0.36 ± 0.009	1.11 ± 0.027

Table 3.1: Lower wall experimental pitot survey parameters (subscripts: e represents freestream value, w symbolizes wall value

3.2.3 Side-Wall Pitot Rake Surveys

Analysis of the boundary layer is critical in the formation of the modified shock train length relation presented in Chapter 6. The pitot probe survey described above allowed for a detailed analysis of the upstream and downstream lower wall boundary layer along the duct longitudinal axis. To experimentally evaluate the state of the side-wall boundary layer, a supersonic pitot rake was employed. Because wind tunnel windows and heavy steel cover doors did not permit orthogonal access to the side-wall boundary layer, the side-wall boundary layer was examined using a pitot rake positioned near the starboard side wall, and traversed vertically using the same stepper-motor driven configuration as the single total pressure pitot probe survey. Shown in Fig.

3.15, the side-wall pitot rake is constructed out of a 12^o copper tailed-wedge equipped with seven total pressure tubes measuring 1.58mm (0.06") inner diameter. Spaced 4.76mm (0.2") apart, the closest total pressure probe is positioned at a distance of 3mm (0.1") to the starboard wall (Z = 73.2mm). Due to the wedge geometry, the closest the total pressure probes are positioned to the lower wall is 2.75mm (0.1"). A detailed outline of the survey points is shown in Fig. 3.9.

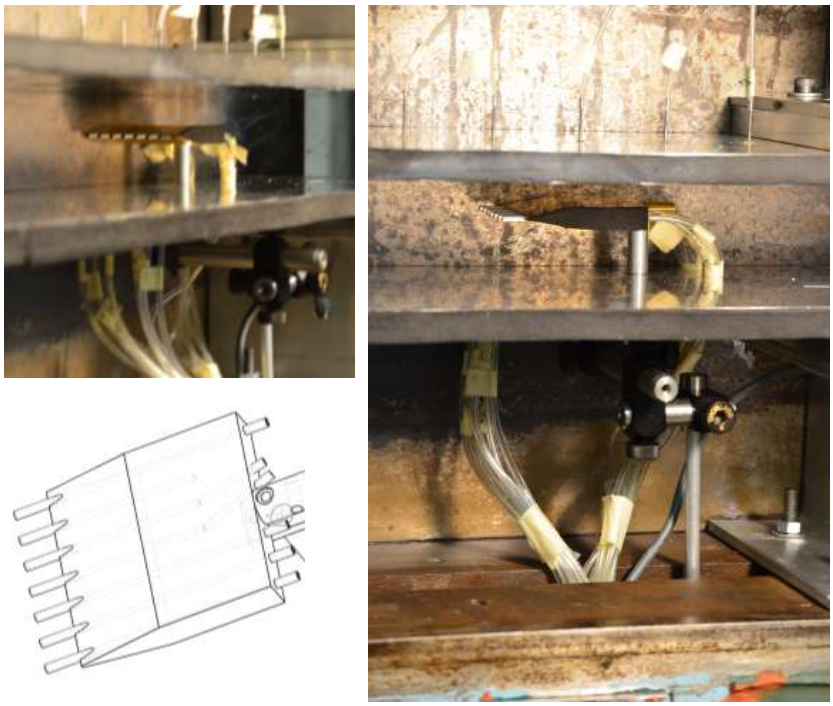

Figure 3.15: Side wall pitot rake configuration.

The pitot rake is primarily used to get an initial estimate of duct major-axis boundary layer momentum thickness. Calculated by Eq. 3.8, the pitot rake derivations of Mach number, velocity, and density are shown in Fig. 3.16-3.18. The duct major axis location is plotted on the x-axis with the physical side-wall location (Z = 76.2mm) representing the upper bound and the duct centerline (Z = 0mm) represented by the lower bound.

Although the outermost probe on the pitot rake is positioned 3mm (0.1") from the outer

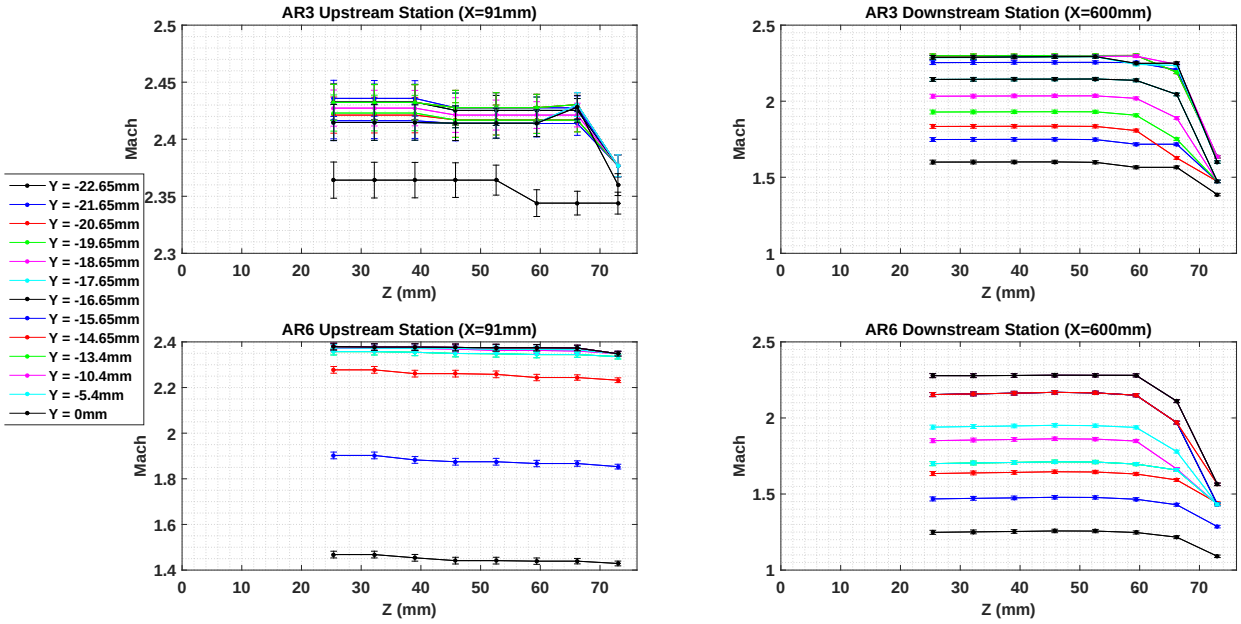

Figure 3.16: Mach number calculations from side-wall pitot rake survey utilizing Eq. 3.2. Measurements taken at 1mm intervals from the lower isolator wall.

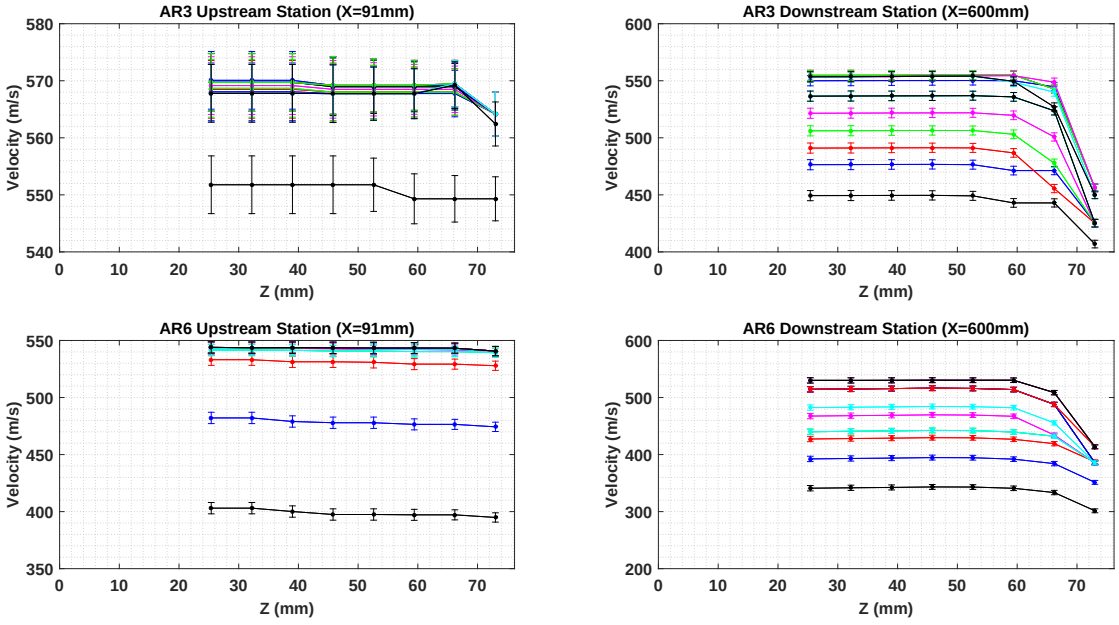

Figure 3.17: Velocity calculations from side-wall pitot rake survey. Measurements taken at 1mm intervals from the lower isolator wall.

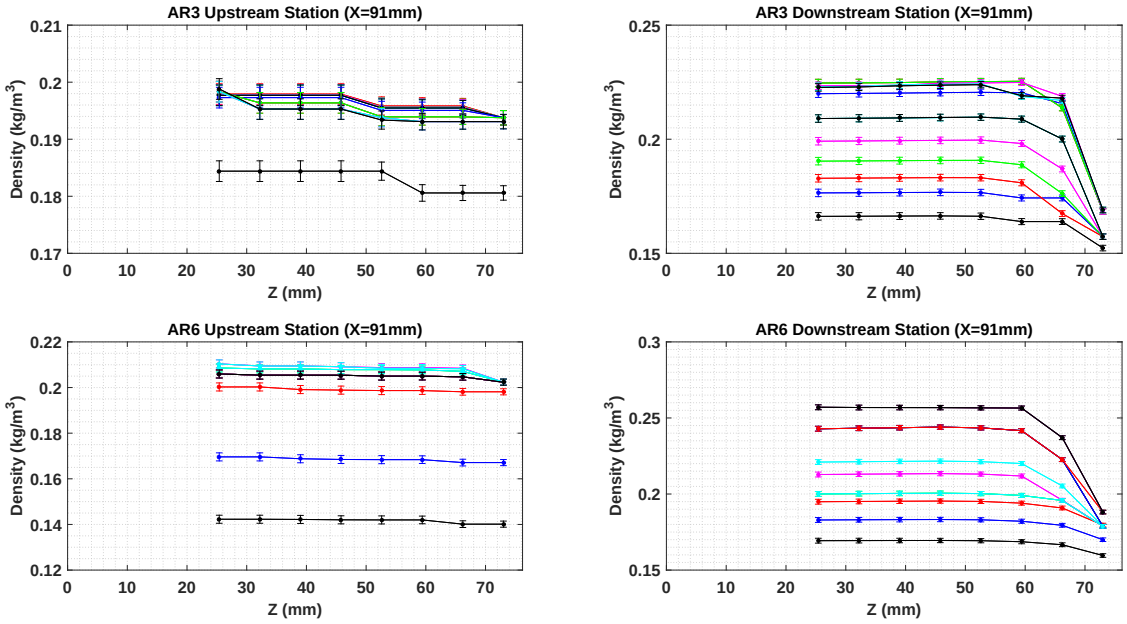

Figure 3.18: Density calculations from side-wall pitot rake survey. Measurements taken at 1mm intervals from the lower isolator wall.

wall, valuable information can still be derived from the point measurements obtained by the rake. Magnitudes of Mach number, velocity, and density correspond to those acquired by the centerline probe, and lower momentum flow is observable toward the starboard wall region of the duct.

Side-wall boundary layer thickness is approximated by using the behavior of the measurements in Figs. 3.16-3.18. Given that the lowest measurement position (Y=-22.65mm) is located in or near the edge of the lower wall boundary layer, the selection of parameters to calculate θ_2 will vary from station to station. The subscript 2 designates the major-axis boundary layer parameters. Table

3.3 Diagnostic Techniques

As discussed in Chapter 1 (Fig. 1.7), the line-of-sight schlieren and shadowgraph visualization techniques provide an initial perspective on isolator dynamics. Schlieren and shadowgraphy techniques have been around for over a century [115], yet a thorough understanding behind the schlieren concept can yield useful information in the development and refinement of more novel

	Aspect ratio 3.0		Aspect ratio 6.0	
	Inlet	Oulet	Inlet	Oulet
M_∞	2.43 ± 0.028	2.36 ± 0.024	2.37 ± 0.028	2.27 ± 0.026
$U_\infty(m/s)$	567 ± 6.8	553 ± 6.3	544 ± 6.1	530 ± 6.1
$T_\infty(K)$	136 ± 1.81	142 ± 1.98	144 ± 1.91	151 ± 2.1
$P_w(Pa)$	8040 ± 120	7406 ± 111	7686 ± 115	7897 ± 118
$\delta_2(mm)$	3.0 ± 0.22	10.0 ± 0.74	3.0 ± 0.21	10.0 ± 0.75
$\delta_2^*(mm)$	0.98 ± 0.05	3.16 ± 0.15	0.51 ± 0.02	2.47 ± 0.12
$\theta_2(mm)$	0.24 ± 0.01	0.96 ± 0.05	0.17 ± 0.01	1.15 ± 0.07

Table 3.2: Duct center axis flow parameters derived from the 7-probe pitot rake side-wall boundary layer survey at two longitudinal stations (subscripts: e represents freestream value, w symbolizes wall value

flow visualization/diagnostic techniques. Three particular techniques used in this study, Multiplane Shadowgraphy, Background Oriented Schlieren (BOS), and Focusing Schlieren Deflectometry (FSD) are all based on the schlieren concept. The line-of-sight concept of the schlieren technique is introduced in Chapter 1 as a motivation to pursue complimentary diagnostics techniques capable of resolving the flow in a three-dimensional sense. A detailed theoretical outline of the schlieren and shadowgraph working principles is provided in Appendix A. These principles play an important role in the refinement efforts of both BOS and FSD, as discussed in Chapter 4. The experimental layout of the diagnostic techniques is expanded upon below.

3.3.1 Traditional Schlieren & Shadowgraphy

The modified schlieren Z-type configuration illustrated in Fig. A.2 consists of two 250mm diameter parabolic mirrors (focal lengths of 1520mm and 2030mm for the transmitting and receiving mirrors respectively) guiding a collimated beam of white light through the wind tunnel test section parallel to the duct major (lateral) axis. The WaveTek signal generator is used to externally synchronize the light source and camera. The light-source, a PerkinElmer LS-1100 Xenon flashpack providing white light ($\lambda_{avg} = 550nm$), is placed at the focal length of the transmitting mirror. Given the top-down perspective of the schlieren schematic, the various density gradient regions (corresponding to the shock train, boundary layer, shear layers, etc.) are represented as a single qualitative representation of varying $\delta\rho/\delta x$ density gradient magnitude for illustration

purposes. Light passing through the test section with the density gradient information is directed toward the image acquisition hardware by the receiving parabolic mirror. A physical, horizontal knife-edge is placed at the focal length of the receiving mirror for schlieren application, targeting the vertical density gradient $\delta\rho/\delta y$. The knife-edge is omitted entirely for the application of the shadowgraph variation. Both planar and circular knife-edges were used. An IDT NR3-S1 camera equipped with a 1.3megapixel (15x12.3mm, 1280x1024px, CMOS Sirius) sensor and a Nikon 24-85mm f/2.7-4 IF AF-D Macro Lens shooting at 5 μs exposure and 250 frames per second was used to acquire the images. A neutral density filter with an F-stop reduction of 6.0 placed just upstream of the camera was utilized to smear the Gaussian distribution of light intensity and increase light source uniformity across the entire field of view.

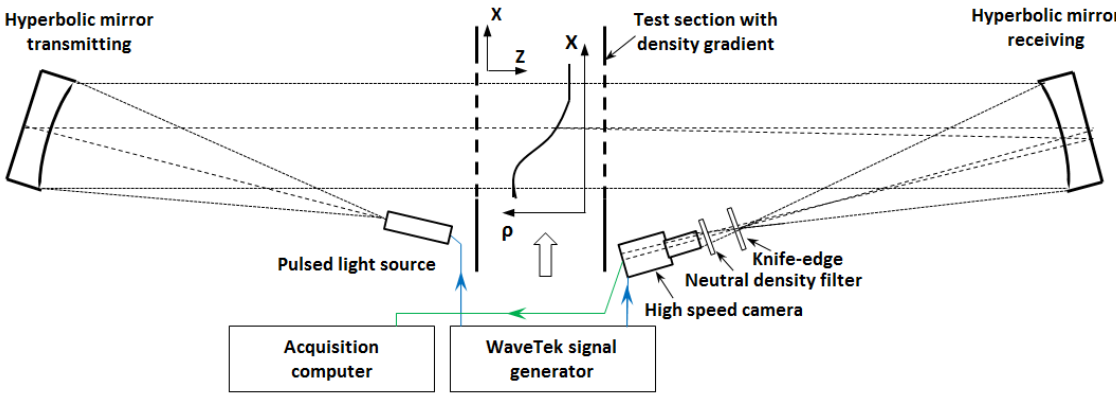

Figure 3.19: Z-type schlieren setup diagram. Shadowgraphy performed without knife-edge.

3.3.2 XY-XZ Multiplane Shadowgraph

The capability of simultaneously visualizing the flow field from multiple planar perspectives provides the opportunity to observe the shock train/turbulent boundary layer interaction behavior with both the traditionally viewed XY-plane lower and upper wall boundary layer interactions (as provided by the setup in Fig. A.2, and the XZ-plane side-wall boundary layer interactions. Fig. 3.20a shows the concept behind the multiplane shadowgraph visualization technique, with a pair of 45° first surface mirrors located inside the wind tunnel, separated from the test section by a pair of 12mm thick acrylic lower and upper wall test section plates. A 20W PerkinElmer

LS-1130 arc lamp with a 3 μs flash duration illuminated a pair of 254mm diameter parabolic mirrors in a Z-type schlieren configuration, feeding a collimated beam to the test section (as is done in traditional schlieren) which is subsequently split up between orthogonal XY- and XZ-plane beams. The collecting (top) first-surface mirror was held fixed, while the transmitting (bottom) first-surface mirror was used to fine tune alignment with the XY plane beam. An IDT NR3-S1 camera equipped with a 1.3megapixel (15x12.3mm, 1280x1024px, CMOS Sirius) sensor and a Nikon 24-85mm f/2.7-4 IF AF-D Macro Lens shooting at 3μs exposure and 250 frames per second was used to acquire the images.

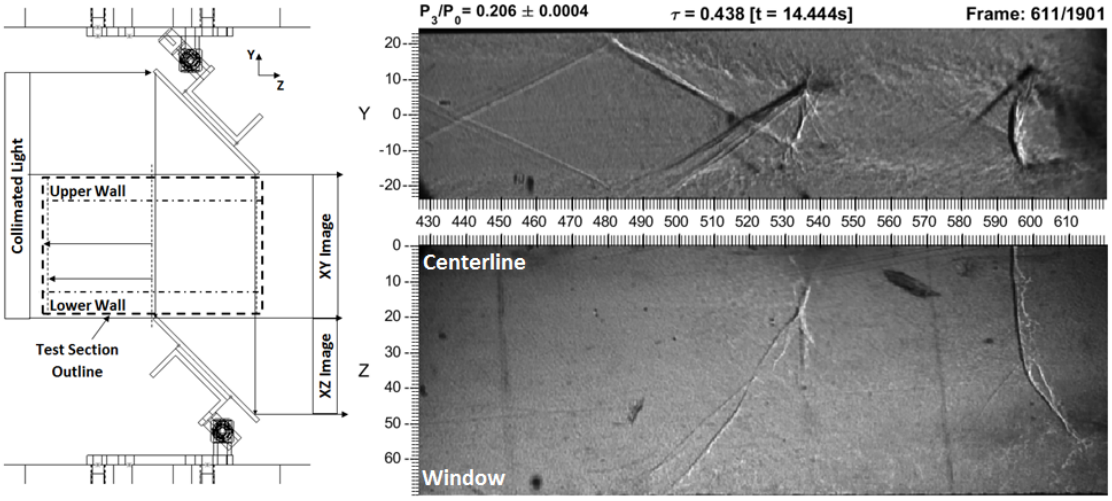

Figure 3.20: XY XZ plane shadowgraph concept: (a) visualization method utilizing a single collimated beam, (b) flow field visualization with superimposed dynamic pressure sensor position. Flow is left to right, dimensions in mm.

Figure 3.20b shows the multiplane shadowgraph result. The XZ-plane visualization represents half of the test section width, with Z=0 indicating the duct centerline. Only the starboard half (positive Z-axis) of the duct was visualized. Due to geometric constraints placing the first surface mirrors inside the wind tunnel structure, effective visualization half-width was approximately 73mm (compared to physical test section half-width of 76mm) and the outermost region of the shock train/side wall boundary layer was not captured, as seen in the bottom left of Fig 3.20b.

This visualization technique is based off of the shadowgraph concept, owing to the refractions of light in regions of variable density gradient being translated into 'shadows' when visualized

on an image plane. Density gradients are assumed to be predominantly originating from pressure gradients in the flow such as formations of shocks and separation of boundary layers. The shadowgraph technique represents a measure of the second derivative of density, or the rate at which density gradient converges. The angle at which the light refracts through the test section (ϵ) is governed by the integration length across which the density gradient take place, and the actual magnitude of the density gradient (or disturbance). To this end, the multiplane technique introduced in Fig. 3.20 is still a line-of-sight technique, but the ability to visualize two orthogonal perspectives simultaneously allows for subjective image analysis to reveal three-dimensional features not resolvable through traditional single-plane schlieren/shadowgraph visualization.

The experimental multiplane shadowgraph setup for the University of Maryland Mach 2.5 supersonic wind tunnel is shown in Fig. 3.21. To reduce the longitudinal load on the 700mm long (27.5"), 12.7mm (0.5") thick acrylic plates, a 3mm (0.1mm) thick gasket was placed along both sides of the test section plate, resulting in a total width of 155.5mm (with a wind tunnel test section width of 152.4mm). This additional 3mm of gasket was squeezed by the wind tunnel window doors upon closing and provided longitudinal support in addition to the 4 1/4-28 anchor bolts located at the inlet and outlet attachment brackets of the isolator duct. Due to the orthogonality of the light, deflections through the multiple layers of glass and acrylic were minimal. The intensity loss in the XZ-plane due to the additional 25.4mm (1") of acrylic test section plates was accounted for by adjusting the saturation values of low and high pixel intensities of the XZ-plane portion of the shadowgraph image.

The AEDC Wind Tunnel 9 Calibration wind tunnel experimental multiplane shadowgraph setup is shown in Fig. 3.22. This visualization effort was undertaken to observe the effect of aspect ratio on the formation of the three-dimensional shock front. Referring back to the calibration wind tunnel test section outline in Fig. 3.6, the XZ-plane access was provided by lower- and upper-wall acrylic inserts. Due to the construction of the wind tunnel, these inserts (shown in Fig. 3.22), measured 51mm (2") in width, or about 75% of the entire wind tunnel width. Although corner flow interactions could not be visualized in this configuration, the visualization performed along

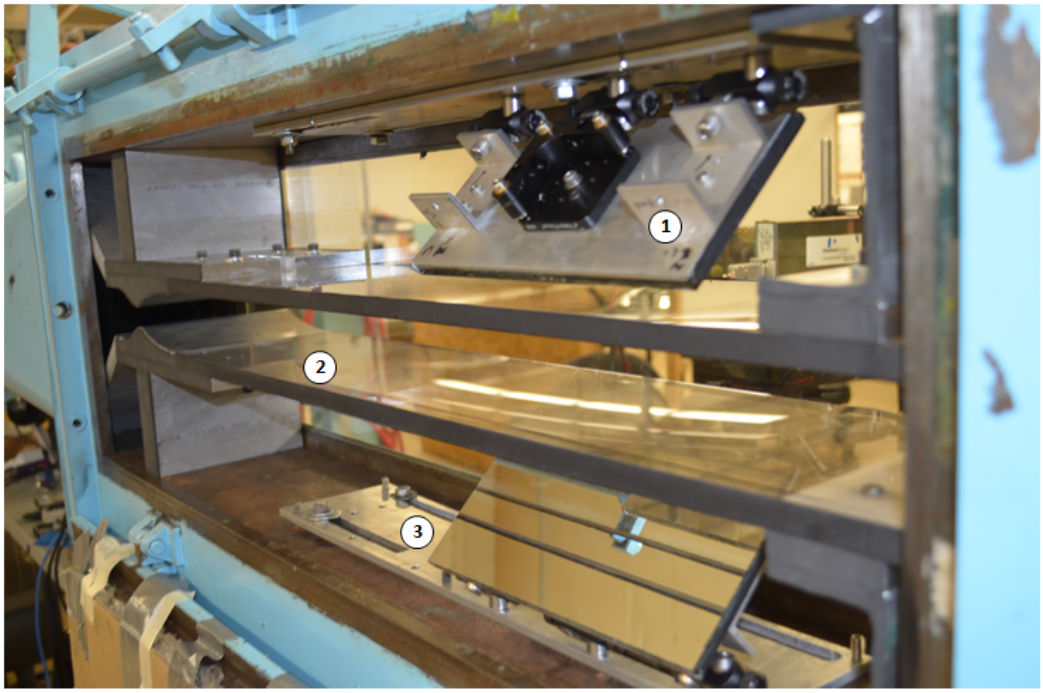

Figure 3.21: University of Maryland multiplane shadowgraph experimental setup: (1) receiving front-surface mirror, (2) acrylic (transparent) lower wall plate, (3) transmitting front-surface mirror.

the center flow region still provides valuable insight into the formation of the three-dimensional shock train front in lower aspect ratio isolators.

3.3.3 Fast Response Dynamic Pressure Measurement

To quantitatively compliment the corner flow interactions qualitatively visualized using the multiplane shadowgraph technique in Fig. 3.20, high-frequency dynamic pressure transducers were placed along the duct-minor (lateral) located at Z=0mm, Z=25.4mm (1") and 50.8mm (2"). As shown in Fig. 3.23, three dynamic pressure stations were located at the same longitudinal locations as the minor axis centerline pitot probe survey, (X=100mm, X=320mm, and X=600mm). The dynamic pressure sensors used are high-frequency quartz Kistler 601B1 series sensors with a sensor diameter of 6mm (0.2") housed in series 220 flush-mounted sensor housings with outer diameter of 14mm (0.5"). A low noise coaxial cable connected each of the Kistler sensors to a Kistler 5010B four channel input/output dual mode amplifier. Dynamic pressure data was taken at 60kHz, with

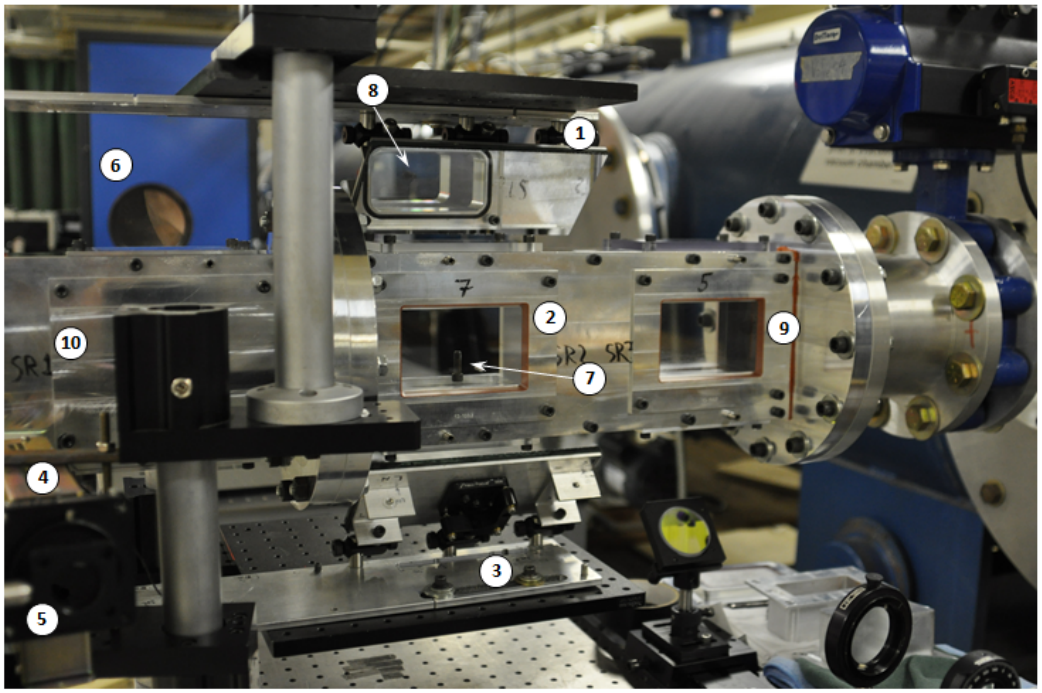

Figure 3.22: AEDC Tunnel 9 multiplane shadowgraph setup: (1) transmitting front surface mirror, (2) XY-plane visualization window, (3) receiving front surface mirror, (4) pulsed light source, (5) neutral density filter, (6) receiving XY-plane parabolic mirror, (7) focusing screw, (8) XZ-plane perspective of focusing screw, gasket of the XZ-plane acrylic visualization window is also visible, (9) downstream XY-plane visualization window.

a 60Hz high-pass and 30kHz low-pass Stanford Research SR650 hardware bandpass filter. A 20x linear gain was applied to the voltage signal. The output was fed to a National Instruments BNC-2120 Analog-to-Digital conversion board prior to being recorded by LabVIEW data processing software. Factory supplied calibrated factors for each sensor were used to convert the voltage output to a pressure reading, which was subsequently normalized with respect to the upstream stagnation pressure (atmospheric).

Dynamic pressure surveys in stations 1 & 3 are discussed in Chapter 5. Sensor labeling follows the nomenclature set forth in Fig. 3.20b, with K2 on the centerline and K3-K4 on the starboard side (positive lateral axis) of the isolator duct for the station 3 configuration. Due to the need for transparent test section walls in the multiplane shadowgraph technique, simultaneous shadowgraphy and dynamic pressure measurements could not be performed. Instead, the two data sets were synchronized with the reference backpressure ratio measurements obtained during each

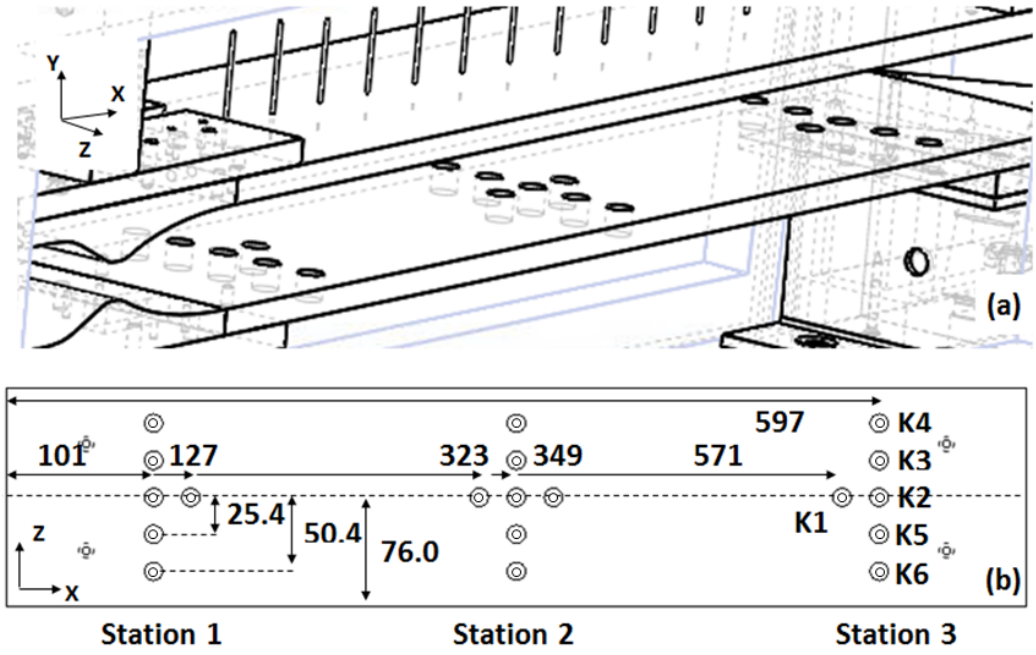

Figure 3.23: Position of the duct minor-axis dynamic pressure survey in the University of Maryland Mach 2.5 wind tunnel. Large circles represent the dynamic pressure housing while small circles represent the actual pressure sensing surfaces.

run. Simultaneous single-plane spark schlieren and dynamic pressure measurements were also performed to correlate the shock train leading edge position to the wall-bound pressure measurements. Shock arrival is quantified by measuring the inherent pressure rise associated with boundary layer separation, and a pressure rise threshold equivalent to three steady-state standard deviations is used to indicate boundary layer separation.

3.3.4 Background Oriented Schlieren

The Background Oriented Schlieren (BOS) method, outlined in Fig. 3.24, was pursued due to its ability to deliver a quantitative estimate of the global density gradient magnitude distribution within the isolator shock train. Like the traditional schlieren method, BOS is based on the analysis of the variations of refractive index in a fluid flow. Unlike the traditional schlieren method however, the BOS technique does not require any optical devices on the transmitting side apart from an optional Fresnel lens if uniformly, back-lit patterns are desired. The method allows

for the visualization of an optically refracted background caused by density gradients within the flow field. The background pattern, located a distance Z_D from the flow field centerline, consists of a collection of black dots on a white background in its simplest sense.

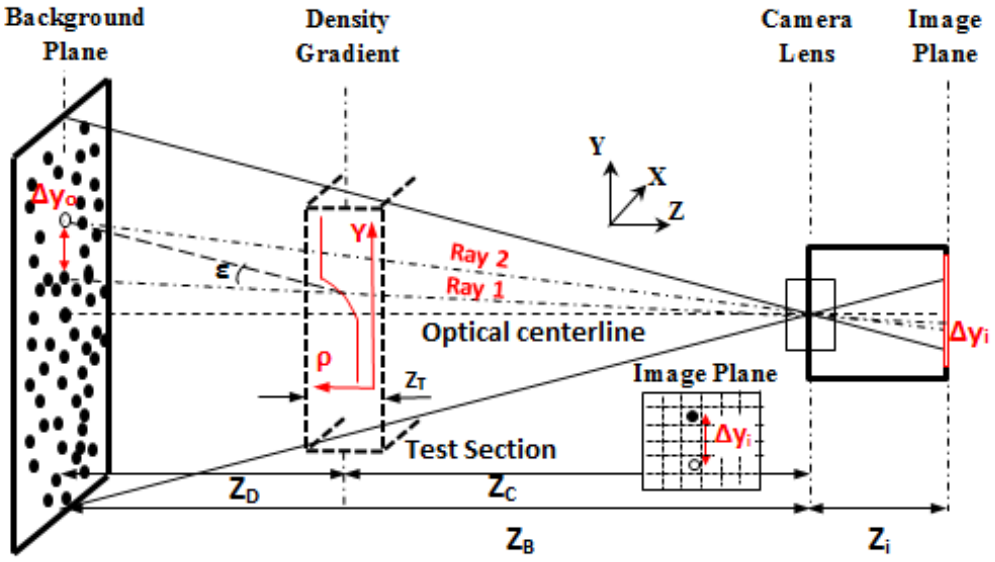

Figure 3.24: The BOS technique: visualizing an optically displaced background pattern.

As light passes through a flowfield with variable density gradient ($\delta\rho/\delta x$, $\delta\rho/\delta y$, $\delta\rho/\delta z$), refractions (ϵ) of light caused by the density gradient result in the optical distortion of the background pattern as imaged by the camera. This causes the particles in the background image to be optically 'displaced' as symbolized by the Δy_o displacement in the background (object) plane. The sensitivity of the BOS method is primarily a function of lens focal length, position and overall magnitude of the density gradient in the test setup, and smallest detectable pixel shift (in-part related to the construction of the background pattern) [116]. Air-off (tare) and air-on (flow) image pairs are acquired by a camera, where high frame rate and resolution must be balanced for optimal performance. Commercial or in-house cross-correlation software can be used to analyze the displacement vectors of the particles in the image pairs. In this study, PIVLab was used to perform the cross-correlation process [117]. A thorough review of the BOS technique can be found in work done by Richard et al. [118].

Three novel BOS configurations were designed and implemented in this study. Shown in Fig.

3.25a-b, the wind tunnel test section is equipped with two visualization windows, whereas in Fig. 3.25c the port-side window is replaced by a steel wall plate. The Fresnel-lens illuminated back-lit BOS system shown in Fig. 3.25a is employed during both the pattern optimization ramp study and main shock train propagation visualization efforts described in Chapter 4 and 5 respectively. A 20W PerkinElmer LS-1130 arc lamp with a 3 μs flash duration illuminates a 610mm (24") focal length Fresnel lens, uniformly illuminating the BOS pattern. The pattern was printed on 700-series 3M Highland transparency film utilizing an HP LaserJet Pro printer, with care taken to match the printer's native resolution (47x47dots per mm). An IDT NR3-S1 camera equipped with a 1.3megapixel (15x12.3mm, 1280x1024px, CMOS Sirius) sensor and a Nikon 24-85mm f/2.7-4 IF AF-D Macro Lens shooting at 5μs exposure and 250 frames per second is used to acquire the images. The Fresnel back-lit method was employed to provide flexibility in parametric pattern selection.

One additional backlit method providing background flexibility that can be explored is the digital screen backlit projection method, shown in Fig. 3.25b. In this configuration, the background pattern is projected from a laptop screen (420x236mm, 1920x1080px) for small field-of-views, and a SHARP AQUOS monitor (1370x800mm, 1920x1080px) for larger field-of-view studies to visualize the entire isolator length. The digital backlit projection technique was the first BOS method used in the calibration efforts described in Chapter 4, due to its ease in background pattern variation. Adequate for low frame-rate visualization with long exposures (30Hz and 1000 μs respectively), the relatively low light intensity produced by the screen projection was insufficient for high frame-rate and low exposure times required to capture shock train dynamics (250Hz and 3 μs respectively). To this end, the backlit digital projection method was only used in the early stages of the calibration study (Chapter 4), where the stationary oblique compression shock calibration flow environment allowed greater exposure times.

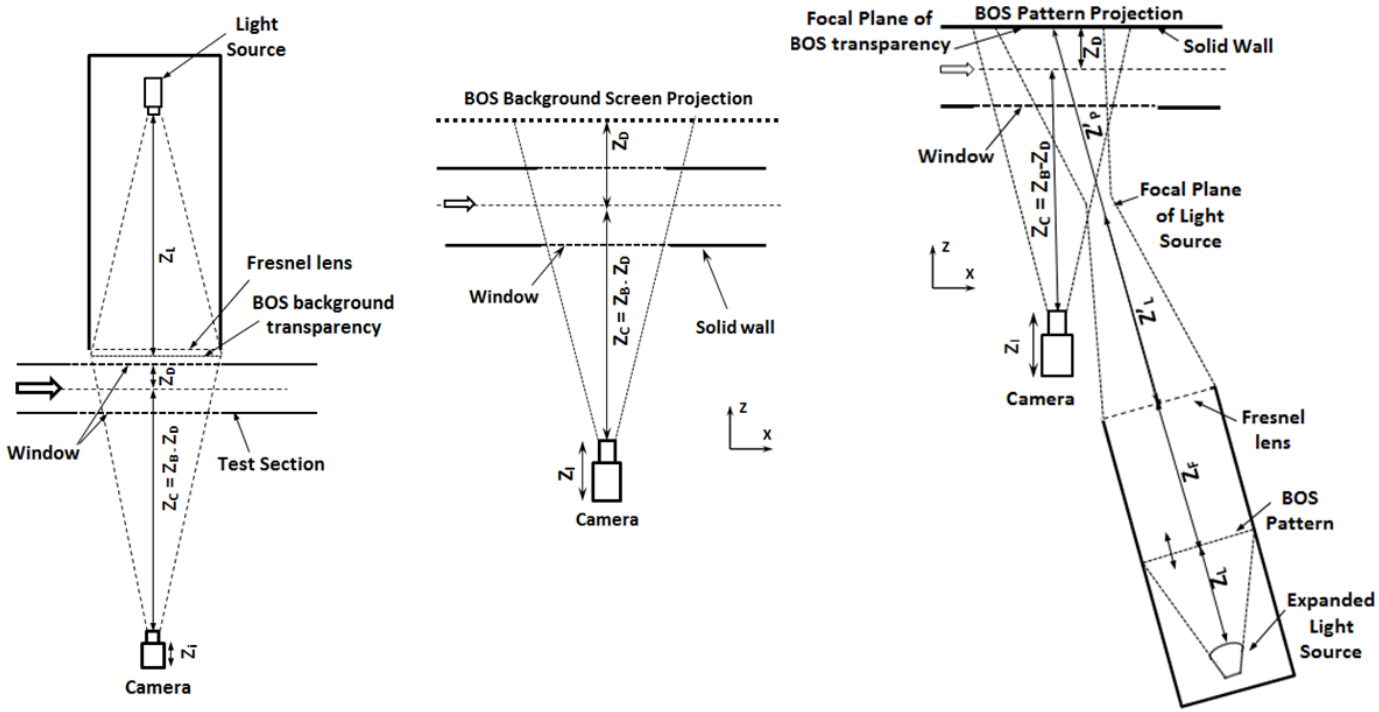

Figure 3.25: Three experimental Background Oriented Schlieren (BOS) methods devised: (a) Fresnel back-lit, (b) digital screen backlit projection, and (c) mechanical projection.

One of the main advantages of BOS is the placement of the transmitting optics (the pattern) directly on the wind tunnel wall. To emulate this configuration while maintaining the flexibility required for a parametric study, the background patterns in the backlit configurations are placed directly behind the port-side window, resulting in the following geometric parameters: Z_D at 76.2mm (3"), Z_C at 550mm (21.6"), and Z_L at 500mm (19.7"). As will be shown in Chapter 4, the value of Z_D can have a significant effect on the sensitivity of the system.

The background pattern design and optimization approach in this work (discussed in Chapter 4) is performed algorithmically and requires the patterns to be printed out on transparencies. This requires the two-window, back-lit wind tunnel configuration shown in Fig. 3.25 and excludes placing the pattern directly on the wind tunnel wall, one of the biggest advantages of the BOS technique. To address this shortcoming, two background pattern projection methods were evaluated to accommodate the wind tunnel configuration shown in Fig. 3.25c. Digital projection was obtained through the use of a 2000-lumen DLP projector (ViewSonic PJ458D) projecting the background pattern directly onto the port-side wind tunnel wall, which was covered in white reflective paint (Rust-Oleum 214944) to increase image intensity backscatter and reduce camera exposure time (on the order of 100 μs). While the projected background pattern was sharp and focused, limited refresh rates hampered proper visualization of the shock train dynamics.

To address this issue, a mechanical projector was build (Fig 3.25c) to explore the feasibility of the projection technique as applied to a high-speed facility. Two 1500-lumen continuous LEDs illuminated the background pattern transparency, placed at the focal length of a 203mm (8") focal length Fresnel lens with lens dimensions of 330x380mm. Unlike the back-lit configuration where the camera lens focuses the Fresnel lens illuminated pattern background image, the projection BOS method relies on the Fresnel lens for a focused image of the background pattern on the desired plane in the test section. Due to the reduction of depth on the lens surface, projection applications of Fresnel lenses are prone to distortion, whose degree of severity increases radially outward from center. As a result, a smaller, usable 100x50.4mm (4x2") field-of-view was obtained with the preliminary design. With Z_D fixed at 76mm (3") from test section centerline, geometric

parameters for the mechanical projection method were set at the following distances from the test section centerline: Z_P at 1000mm (39.3"), Z_C at 500mm (19.6"), and Z_L at 508mm (20"). Results obtained with the mechanical pattern projection technique are briefly discussed in Chapter 5. Refined digital and mechanical projection technique can be explored as suitable options for facilities with limited optical axis.

Post-processing is needed to compare the background image subjected to the refractive flowfield to the air-off reference image. Image pairs are computer processed using a PIV cross-correlation package based on block-matching algorithm architecture. While other processing algorithms such as density based (Lucas-Kanade, Horn-Schunck) and variational (Brox) algorithms exist [119], the block-matching algorithm is applied across the entire study due to its ease-of-use and common datasets in literature. A 50% multi-grid (four-pass) linear FFT window deformation algorithm with principle (square) interrogation window size of 128pixels and subsequent window sizes of 64, 32, and 16 are used. The choice in interrogation window size is an integral part of the pattern design, as described below. A 2x3 point Gaussian sub-pixel interpolation method is applied to yield displacement estimation beyond the resolution of the camera pixel element. Non flow-field areas causing reflections such as the compression ramp profile and outline of the isolator plates are masked in order to be excluded from analysis. Finally, the visual representations (including displacement vectors) are plotted using a standard deviation filter to reduce noise in the resulting image where applicable.

3.3.5 The Focusing Schlieren Method

The focusing schlieren method is used in conjunction with a pair of Avalanche photodiodes (APD1A2, Thorlabs) in a Focusing Schlieren Deflectometry (FSD) configuration to obtain high temporal bandwidth, time-resolved point measurements of density gradient at different locations with known spatial intervals. This allows for the reduction of the shock train oscillatory velocity component using the technique's ability to bring different planes within the test section into sharp focus. The Focusing Schlieren technique was first conceptualized and developed by a number of

authors in the mid-20th century [120–122], and improved over time until Boedeker introduced the use of a Fresnel lens to greatly improve the field-of-view and illumination of the resulting schlieren image [123]. The foundation behind the currently applied focusing schlieren deflectometry method is based on the focusing schlieren technique refined and standardized by Weinstein [124], and the optical deflectometry technique first proposed by McIntyre et al. [125]. Regarding the former, one of Weinsteins principal contributions to the field of focusing schlieren was the outline of a methodical design approach through a series of quantitative formulae describing a suite of diagnostic parameters including sensitivity, depth of field, and resolution. This quantitative approach is used to design the focusing schlieren system and is described below.

3.3.5.1 Focusing schlieren theory & fundamentals

The fundamental principle behind the focusing schlieren diagnostic tool is the ability to discern detail and focus over a narrow plane of interest within the flowfield, significantly attenuating the contribution of density gradients outside of this plane of focus (also the plane of unsharp focus). The system is outlined in Fig. 3.26 in a lens-and-grid configuration, with a density gradient distribution ($\delta\rho/\delta y$) resembling that of the Helium/Nitrogen jet utilized in Chapter 4 calibration efforts located inside the test section. The system is composed of a continuous, expanded light source illuminating multiple source and knife-edge pairs. These pairs are materialized in the form of a source and cutoff grid, as shown in Fig. 3.26. The spacing between the opaque cutoff lines in the cutoff grid, annotated by the parameter b plays an important role in the system's capabilities, as will be explored below.

By simulating multiple light sources through the source grid, light from the various source points illuminate each point in the test section flow field, resulting in a final image composed of multiple overlapping images at the image plane. A number of these overlapping images can be brought in sharp focus by translating the image plane along the optical axis. Since the image plane and plane of sharp focus inside the test section are focal pairs of each other, the plane of sharp focus inside the test section can be selected by movement of the image plane along the optical axis.

This process is visualized in Fig. 3.26.

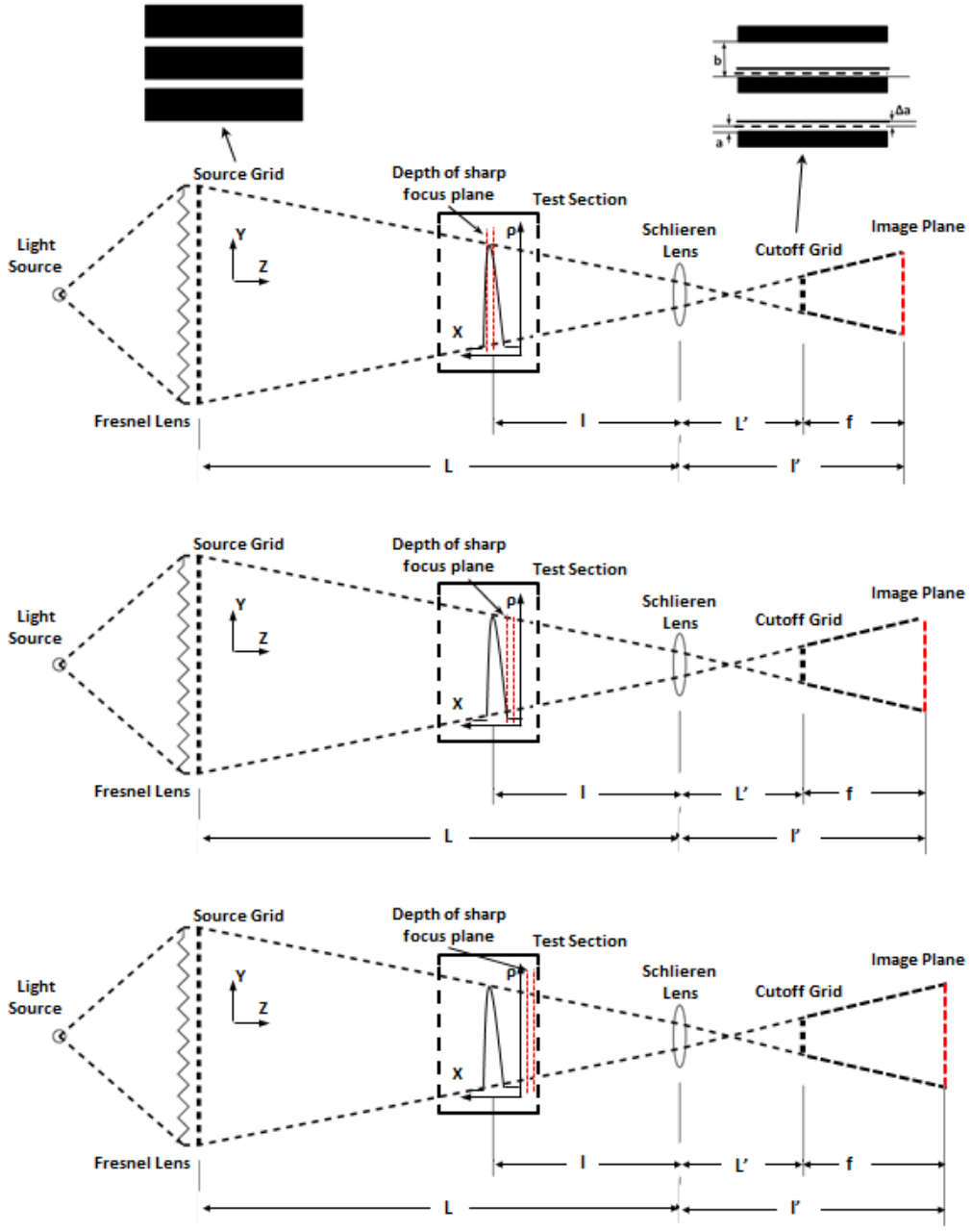

Figure 3.26: Focusing Schlieren method outline with source and cutoff grid schematic. Position of the image plane along the optical axis determines plane of sharp focus.

The construction of a high quality focusing schlieren system represents a mixture of art and precision optics. Quantifying the system's performance is made possible through a landmark 1991 paper written by Weinstein [124], in which critical performance parameters are mathematically

articulated.

The four main parameters governing the focusing schlieren performance are image resolution (ω), depth of sharp focus (DS), image smoothness (ϕ), and image sensitivity (ϵ). Construction of a focusing schlieren system must be tailored to the specific parameters that are most important. Wherever possible, the system must have a certain flexibility in construction that allows different performance parameters to be emphasized.

As in most focusing schlieren applications, depth of sharp focus (DS) is the most important performance parameter in the current study. To understand how DS can be quantified, the diffraction limited resolution ω must first be considered. Diffraction limited resolution is another performance parameter and is quantified in Eq. 3.12 as the resolution limited by diffraction effects due to the cutoff grid. Resolution limits due to a cutoff grid slit is defined as $d = \frac{2(l'-L')\lambda}{b}$, where l' is distance from the schlieren lens to final image location, L' is the distance from the lens to the cutoff grid location, b is the spacing between opaque cutoff lines on the cutoff grid, and λ is the average wavelength of the light source in use [126]. The diffraction limited resolution accounting for the magnification from test section to image plane is offered in Eq. 3.12.

$$\omega = d/m = 2(l' - L')\frac{\lambda}{mb} \tag{3.12}$$

The depth of sharp focus (DS) plane, or the effective thickness of the two-dimensional slice of flow that can be examined, is generally categorized according to two definitions [124]:

- The resolution of the optical acquisition system can not capture loss of resolution due to being out of focus.
- The loss of resolution due to being out of focus exceeds a certain threshold, such as the smallest detail required to be visualized in the flow field.

For any schlieren based system, the depth of focus is governed by the maximum angle between different light rays traversing through each point in the density gradient field. For the focusing schlieren system specifically, this maximum angle is determined by the schlieren lens

aperture, and thus the first definition of DS stated above is appropriate and can be quantified according to Eq. 3.13. The grid diffraction limited resolution is shown in Eq. 3.12, R is the object distance divided by the lens diameter (l/A), and the factor of 2 accounts for both sides of the DS plane. The focusing lens, a critical component in the focusing schlieren system, is a high quality triplet schlieren lens (ILEX Optical Company No. 5 Synchro) designed to minimize optical aberrations. It has a focal length of 269mm (10.6") and an effective aperture (A) of 101.6mm (4").

$$DS = 2R\omega = \left[\frac{4l^2\lambda}{Al'b}\right](l' - L') \tag{3.13}$$

Table 3.3 summarizes the focusing schlieren system parameters for the deflectometry configuration outlined in Fig. 3.29, and can be referenced in the calculation of performance parameters discussed below. Geometric length scales of the experimental setup (L, l, L', l') where chosen to fit the laboratory spacing, the focal length (f) and effective aperture (A) of the schlieren lens, and a desirable depth of sharp focus (DS). The aforementioned importance of the cutoff grid spacing is shown in Eq. 3.13, showing the inverse dependence of DS on b. Larger cutoff grid line spacing provides a smaller depth of sharp focus. This relationship is visualized in Fig. 3.27 as a function of b, where the Y-axis represents the log-scale of the performance parameter.

An associated parameter to DS is the measure of depth of unsharp focus (DU). This definition adheres to the second category listed above, namely the depth of (unsharp) focus that results in a loss of detail exceeding a certain threshold value. The thickness of the DU plane is calculated according to Eq. 3.14, where the factor of 2 accounts for the distance required to provide adequate unsharpness (this can be varied for different systems). DU is an important parameter and should remain as small as possible, as features inside the region of DU will be resolved to a certain degree, potentially obscuring finer details inside the DS.

$$DU = 4R = \frac{4l}{A} \tag{3.14}$$

The third performance parameter depending directly on b is the measure of image 'smooth-

ness'. The more image pairs from the source/cutoff grid pairing blend together at the image plane, the smoother the image will be. A low number of image pairs is accompanied by out-of-focus grid lines showing up at the image plane. The number of image pairs, denoted as σ, that are blended at the image plane location can be increased by either decreasing b or increasing the distance from the cutoff grid to the image $(l' - L')$. The mathematical equation to calculate σ is provided by Eq. 3.15. For adequate image smoothness, a blended pair number of 5 or greater is desired, with $sigma \geq 8$ considered to provide the best image [124].

$$\sigma = \frac{A\left(\frac{1}{b}\right)(l' - L')}{l'} \geq 5 \tag{3.15}$$

Figure 3.27 summarizes the three performance parameters discussed above as a function of b. These parameters are calculated with the experimental setup parameters shown in Table 3.3. As can be seen, a reduction in b has adverse effects on the DS and the resolution of the system, but has constructive effects on the number of grid lines blended. Both DS and σ need to meet certain criteria. The DS must be at least as small as the DU, and preferably an order of magnitude smaller. The number of blended line pairs must meet the criteria established in Eq. 3.15. DS and ω were the two driving performance parameters of the system, and the minimum value of σ to provide best image was chosen as to minimize DS. Like DS, the image resolution ω increases with increasing b.

The fourth performance parameter is the image sensitivity ϵ'. Shown in Eq. 3.16, ϵ' is derived from the concept of the smallest change in brightness that can be detected with a physical knife-edge in position. The knife-edge grid is outlined at the top of Fig. 3.26 and is illustrated in greater detail in Fig. 3.28. The light source height extended above the physical cutoff (a) and its change after a refracting disturbance is introduced into the flow field (Δa) are illustrated in Fig. 3.28. In this sense, a represents the undeflected image, whereas Δa represents the degree of collimated light bending induced by light refractions caused by density variations in the test region. Such movement (with respect to the knife-edge) causes a change in brightness at the respective image plane location, the basic principle upon which the schlieren technique illustrates the first

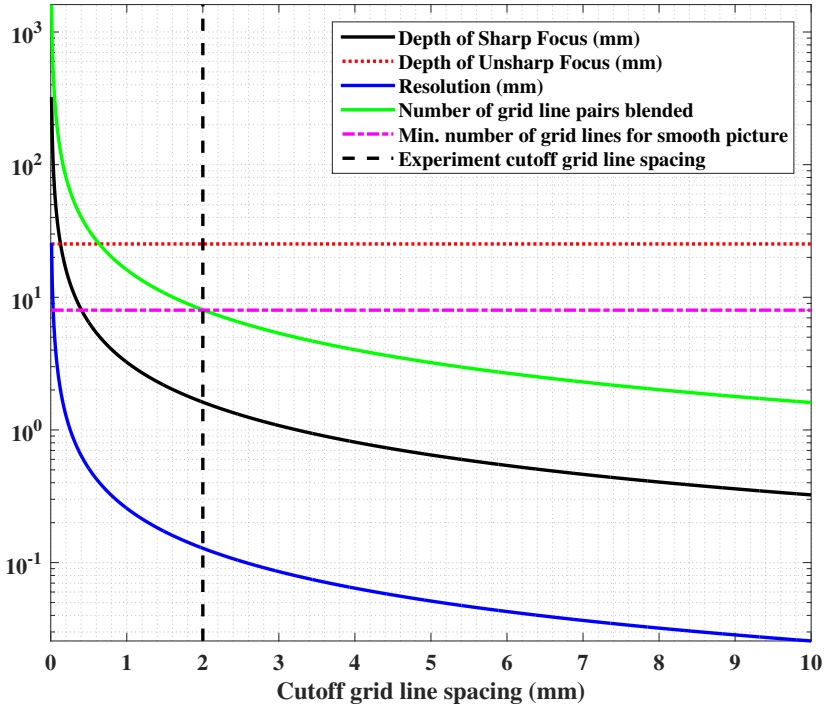

Figure 3.27: Quantitative representation of the focusing schlieren system: depth of sharp focus, image resolution, and image smoothness.

derivative of the density gradient. A commonly used criteria for system sensitivity is the smallest change in brightness that can be detected from a disturbance inside the test section, specified as 10% in this experiment.

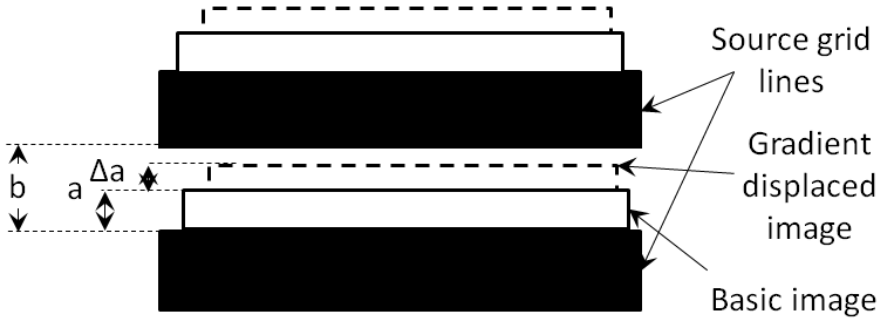

Figure 3.28: Detailed outline of the Focusing Schlieren grid and its effect on image sensitivity. The parameter of source image deflection (h) is identical to the parameter used in Fig. 3.26 (a).

$$\epsilon' = 0.1\left(\frac{aL}{L'(L-l)}\right) radians = 20626\left[\frac{aL}{L'(L-l)}\right] arcsec \tag{3.16}$$

Equation 3.16 shows why the focusing schlieren technique is generally less sensitive than the conventional schlieren technique ($\epsilon = 20626\left(\frac{a}{L'}\right)$) since L' is considerably smaller in a focusing schlieren setup as compared to a traditional schlieren system. To account for this difference and still provide adequate sensitivity, a is desired to be small in the focusing schlieren system. Aside from focusing lens limitations, grid line spacing can play a role in the reduction of a. Along with altering the vertical position of the knife-edge by means of a fine-adjust stage, lower values of b can provide lower values of a by effectively reducing the transparent area between cutoff grids for the undisturbed image to occupy. This must be balanced with the actual thickness of the opaque cutoff grid line b to provide for adequate separation of the grid pairs.

One additional parameter that can be tied with the system's sensitivity is the image contrast c', defined in Eq. 3.17. Like the image sensitivity, image contrast can benefit from a reduction in b as it reduces the available transparent area between opaque cutoff grid lines to host the light of the undisturbed image.

$$c' = \frac{\Delta a}{a} \tag{3.17}$$

Table 3.3: Design point specifications.

Variable	Description	Value
A	Clear aperature of focusing lens	101.6mm
f	Distance from cutoff to image	269.0mm
L	Distance from source grid to focusing lens	1644.6mm
L'	Distance from focusing lens to cutoff grid	355.6mm
l	Distance from test section focus plane to focusing lens	641.3mm
l'	Distance from focusing lens to image	558.8mm
DS	Depth of sharp focus	1.625mm
DU	Depth of unsharp focus	25.25mm
M_0	Image magnification factor (l'/l)	0.8713
b	Cutoff grid opaque line spacing	2mm
n	Grid lines per mm on cutoff grid	0.5
σ	Number of blended line pairs in focused image	8.05
ω	Diffraction limited resolution	0.128mm
ϵ	sensitivity of focusing schlieren system	41.12arcsec

The two most important components of the focusing schlieren system are the focusing

schlieren lens and the cutoff grid. Regarding the latter, it is critical that the cutoff grid represents a de-magnified photo-negative of the source grid so that source and cutoff pairs are lined up appropriately. Due to the inherent optical aberrations in the schlieren lens, traditional means of constructing the cutoff grid have involved exposing a piece of high contrast black and white photo-negative film to the focused image of the original source grid. Since the cutoff and source grid are focal pairs of each other, this exposed photo-negative of the source grid is taken at the cutoff grid plane [123, 124, 127].

This technique was originally utilized in the present study, employing a 101x127mm (4x5") Arista II Ortholithographic film held by a film holder of similar dimensions for quick swapping of the exposed film. The technique was tedious and time consuming, requiring the correct combination of exposure time from a pulsating light source (ensuring no stray light enters the work area) and fine-tuning the position of the photo-negative film containing container to ensure a focused image of the source grid is obtained. Determining the correct exposure time (duration of the light pulse) remained an abstract art form, meaning that several different pieces of film had to be exposed using different pulse lengths. After developing the photo-negative films, the grid with the most opaque cutoff lines and the most transparent source lines was chosen.

In addition to the time-consuming cutoff grid manufacturing process the above method had one performance limiting shortcoming, which was the inability to fine-tune the value of b. A backlit cutoff-grid projection method similar to that employed by Floryan and later Hofferth [128, 129] to simplify the cutoff-grid design process is utilized in the present study. The cutoff grid is designed as an original in order to drive the system performance through the control of b. Printed on a high quality transparency, care is taken to match the printer's native resolution to ensure a sharply defined cutoff grid (ensuring that opaque cutoff lines do not bleed into the transparent segments). With the grid firmly mounted, a continuous 1300Lumen LED is used to backlight the cutoff grid and project the focused image on the source grid plane through the schlieren lens. Given the larger dimensions of the source grid, it is easier to manufacture and replicate. This cutoff-grid manufacturing technique is used in the current study, and significantly improved the system's

performance and flexibility compared to the traditionally manufactured cutoff grid.

3.3.5.2 Focusing schlieren deflectometry

Development work of the focusing schlieren system described above is coupled with the application of simultaneous, time-resolved measurements of density gradient at different locations with known intervals, providing a completely non-intrusive method of obtaining flow velocity information. Early work involving time-resolved measurement of density gradient at a point in the flowfield had two main characteristics in common: the analysis of schlieren/shadowgraph images to obtain the time-resolved measurement, and the integral of flow properties along the entire light optical path length [130–132]. This earlier work was thus limited to image acquisition equipment frame rates (and other performance parameters of the particular system) and best suited for two-dimensional approximated flows where the homogeneous assumption was valid. The former was addressed by work performed by McIntyre [125], introduced above, utilizing fiber-optics and photomulitplier tubes (PMTs) together with a traditional schlieren method to record light intensity fluctuations at discrete locations with high spatial and temporal resolution. The method was dubbed 'deflectometry'. Applications to low- and high-speed flows resulted in quantitative observation of convection velocity of large-scale turbulent structures in the boundary layer in addition to the power spectra of their fluctuations.

Garg et al. [133] applied McIntyres deflectometry method in unison with the focusing schlieren technique to evaluate broadband convection velocity of large-scale structures inside the turbulent boundary layer of a Mach 3.0 facility, where large-scale structures inside the boundary layer were found to propagate with the local mean velocity. The technique was described as an excellent supplemental diagnostic tool to more traditional hot-wire anemometry and LDV measurements, with the major drawback listed being the resolution of the optimized depth of sharp focus being larger than the structures in question.

The present study aims at evaluating shock train oscillation velocities within the isolator flowfield, where light fluctuations and density gradients at the point of measurement are sporadic

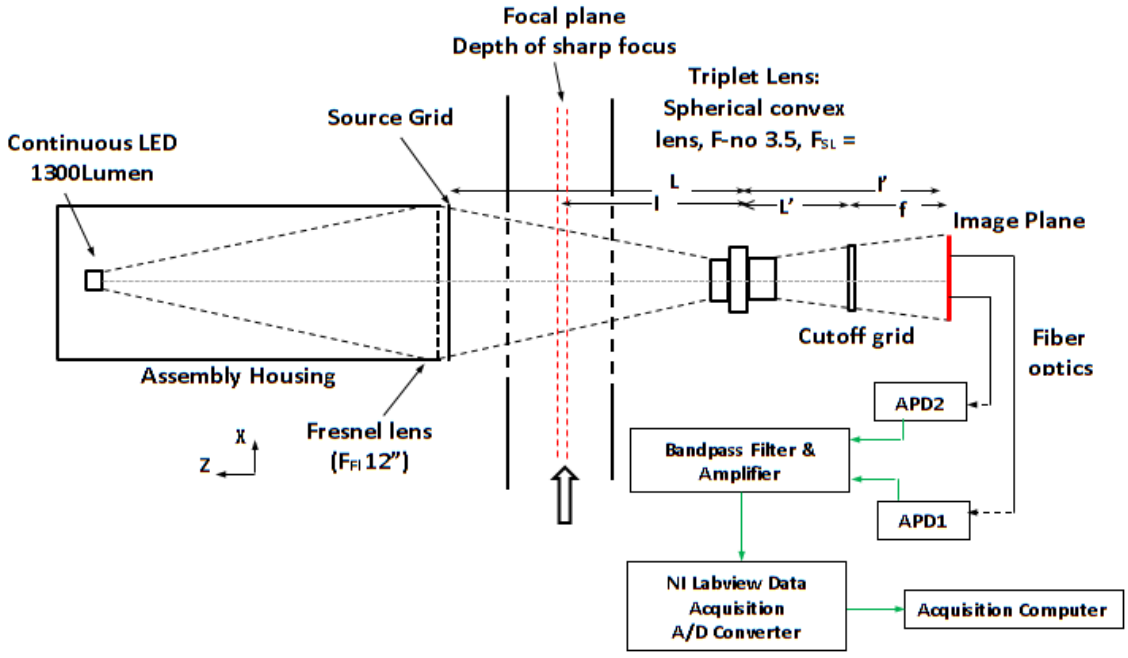

Figure 3.29: Top-view outline of Focusing Schlieren Deflectometry Velocimeter system.

in nature and are characterized by a large range of light fluctuation amplitudes. Based on the fundamental focusing schlieren concept described above, the Focusing Schlieren Deflectometry system is outlined in Fig. 3.29 in a velocimetry configuration, equipped with two fiber-optic fed photodiodes measuring point-wise, high temporal band-width fluctuations of light intensity. The physical setup is furthermore shown in Fig. 3.30.

A housing was constructed to fix the location of the extended light source, a 18W 1300Lumen continuous LED. This was housed together with a 250mm (9.8") focus square Fresnel lens (Edmund Optics, 280x280mm) and a custom-made source grid composed of a transparency printout mounted in-between two pieces of Plexiglas. The receiving side of the optics is supported by hardware capable of allowing fine-tuned changes in multiple directions. The high-quality triplet schlieren lens (ILEX Optical Company No. 5 Synchro), designed to minimize optical aberrations, has a focal length of 269mm (10.6"). The cutoff-grid, the most sensitive component to misalignment, is mounted on a combination of Newport kinematic mounts that allow translation and rotation around all three axes. A handheld focusing device is used to ensure that the cutoff grid was located at the

focal plane of the source grid. To promote opaqueness, two cutoff grid images are superimposed on one another while the source grid consisted of three superimpositions. Great care was taken to keep the transparent lines completely unobstructed. The image plane consisted of a 12.5mm (0.5") thick piece of aluminum with precision drilled holes (tolerance $\pm 0.025mm$) to accommodate the $500\mu m$ (0.02") diameter fiber optics (Thorlabs multimode). The fiber-optic mount is coupled to a stepper-motor driven linear translation stage (LTS150, Thorlabs) to allow precise positioning of the fiber optics within the image plane. The fiber optic cables are fed to two Silicon Avalanche photodiodes (APD1A2, Thorlabs) with a maximum responsivity of 25A/W at a wavelength of 600nm and an active lowpass filter to suppress out-of-band noise. Photodetector output current is converted to voltage over an external 50ω impedance (factory recommended). The APD signal is sent to a hardware bandpass filter/amplifier where 20dB pre-amp and 10dB post-amp amplification are added together with a 70Hz highpass filter. The same National Instruments BNC-2120 A/D conversion board used to acquire dynamic pressure data, finalizes the acquisition process prior to recording on a computer.

3.3.5.3 Focusing schlieren visualization

Due to the lack of a narrow bandwidth, high amplitude light source to mitigate the light intensity loss associated with both the source and cut-off grids, focusing schlieren flow visualization was not a priority in the current study. The light amplitude provided by the continuous LEDs is adequate for the highly sensitive avalanche photodiodes employed in the deflectometry configuration of the Focusing Schlieren application. The high-speed camera sensor sensitivity is orders of magnitude lower than the photodiode, and thus a high amplitude short pulse duration laser light source is desired to adequately resolve flow features of interest within the test section. Copper vapor lasers have been previously used in focusing schlieren visualization efforts [127].

Lacking access to a high pulse-rate laser system, the PerkinElmer LS-1100 Xenon flashpack was utilized to visualize the high density gradient flowfield produced by the calibration 'Helium jet in ambient air 'configuration employed for calibration purposes. These depth of sharp focus

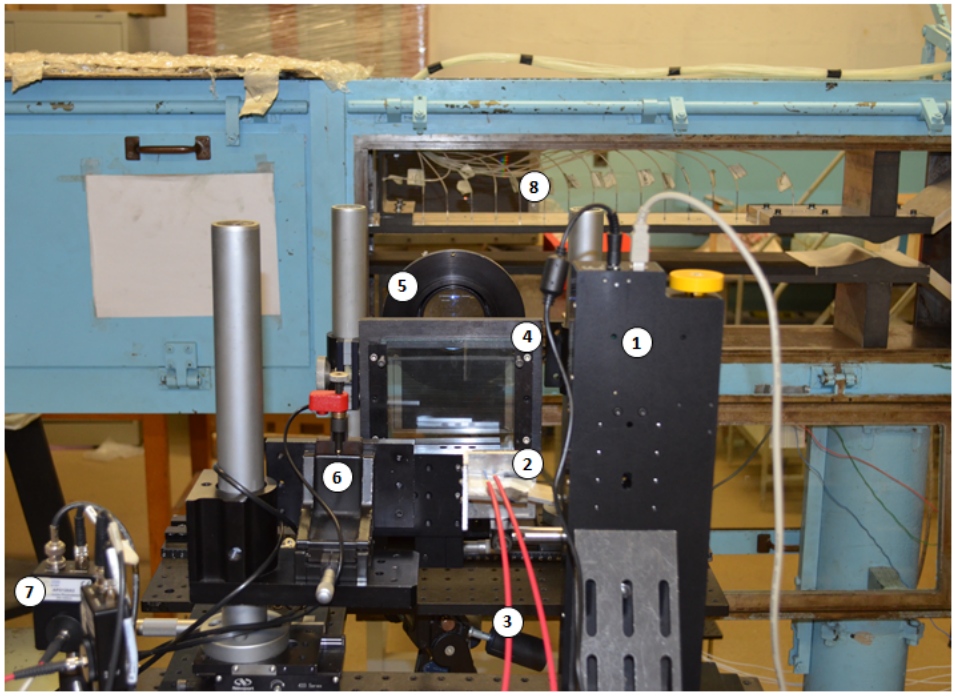

Figure 3.30: The experimental Focusing Schlieren Deflectometry Velocimeter setup: (1) stepper motor translation stage, (2) image plane, (3) fiber optics, (4) cutoff grid transparencies and mount, (5) focusing schlieren lens, (6) cutoff grid XYZ fine-tune kinematic mount, (7) Avalanche photodiodes, (8) Fresnel and source grid housing.

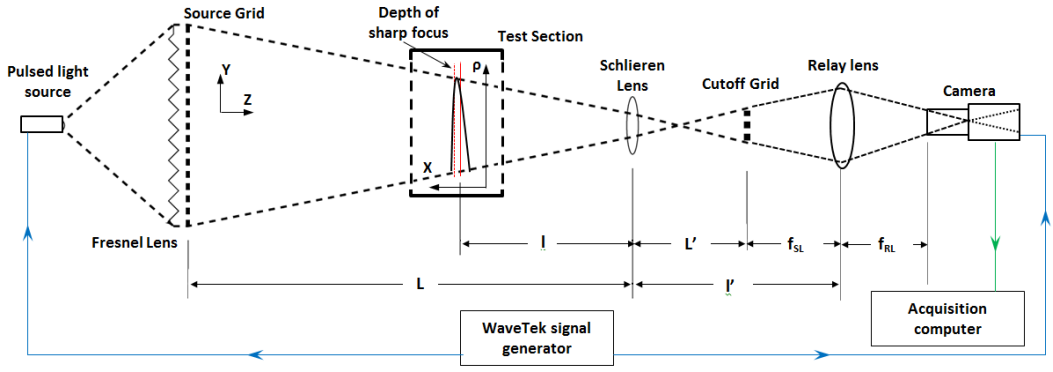

Figure 3.31: Side-view outline of the Focusing Schlieren visualization system utilized in the Helium jet calibration study presented in Chapter 4.

validation studies are discussed in Chapter 4. The visualization configuration, shown in Fig. 3.31, is similar to the deflectometry system, with one additional relay lens used to focus the cutoff grid image into the camera lens.

3.3.6 Lower Wall Oil Flow Visualization

A minor oil-flow visualization side-study was performed in the aspect ratio 3.0 configuration to explore lower-wall centerline behavior and symmetry. The experimental setup is shown in Fig. 3.32. A flat black anodized isolator lower-wall plate was used in conjunction with a mineral oil-Talcum powder mixture for maximum contrast. Images were taken at an exposure of 80 μs and a frame-rate of 250Hz through the port-side window in real time using the IDT NR3-S1 camera with a set of six 1200 lumen LED bulbs providing adequate test-section lighting for the desired exposure time. Additional image capturing was provided by the higher resolution, but slower frame rate Nikon D5100 camera. Visualization oil was applied to the lower-wall and starboard side-wall prior to evacuating the facility in preparation for the wind tunnel run. Due to this process taking on the order of around five minutes, gravitational run-off resulted in the side-wall region not being adequately covered by the start of the run. Nevertheless, great uniformity was maintained on the lower wall. Due to oil build up on the port-side (near) wall during the run, the duct-minor field of view was limited to a range of Z = -25.4mm to Z = 76.2mm.

3.3.7 Planar Mie-Scattering Visualization

The importance of thoroughly understanding the leading edge shock train front is articulated in Chapter 1. Another area of interest in the ram-jet mode of operation is accounting for the isolator exit-plane flow quality prior to entering the combustion. Ideally, a uniform flow state of adequate thermodynamic potential is desired for optimal combustor performance. The lateral plane flow field at the exit of the test section (downstream station) of the aspect ratio 1.0 isolator (X=490mm) is visualized through instantaneous laser induced planar Mie-scattering.

The Mie-scattering visualization technique is based on the reflection of light off molecules or small particles entrained in the flow field of interest. Particle radius (r), the refractive index of the medium (n_m), and the wavelength of the light (λ) used determine the type of scattering according to the q-factor defined in Eq. 3.18 [134].

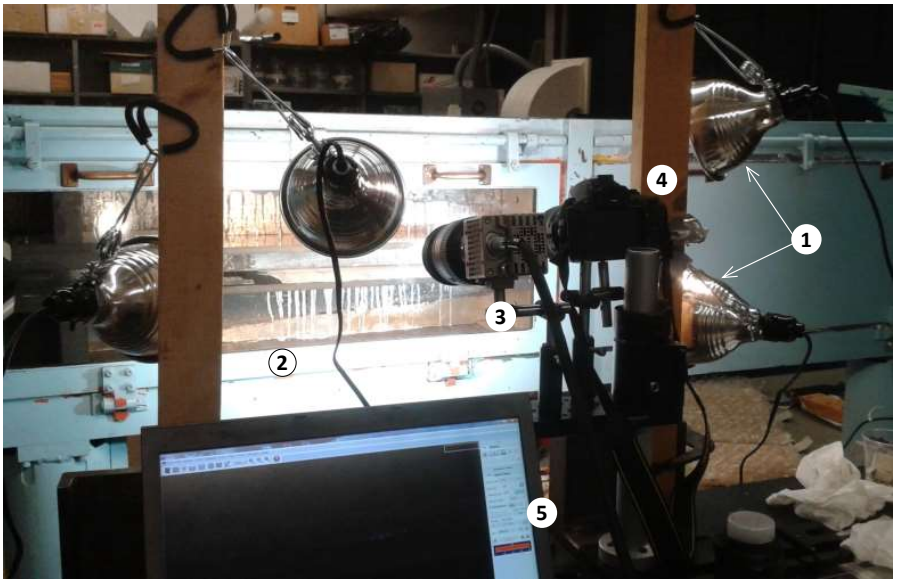

Figure 3.32: University of Maryland isolator oil flow visualization experimental setup: (1) continuous LED external lighting, (2) wind tunnel test section with oil deposit on lower and starboard wall, (3) IDT NR3-S1 high speed camera, (4) Nikon D5100 high resolution camera, (5) image acquisition computer.

$$q_{scat} = \frac{2\pi r}{\lambda_m} = \frac{2\pi r n_m}{\lambda} \tag{3.18}$$

Mie-scattering is traditionally defined by a q_{scat} between 0.1 and 10. Two other types of scattering are Rayleigh scattering (q_{scat} ¡¡ 1) and geometric scattering (q_{scat} ¿10). A 15Hz SOLO120 Nd:YAG 532nm laser with maximum pulse amplitude of 120mJ and a pulse width of 3-5ns was used in combination with a spherical-cylindrical lens combination to create a 0.3mm thick laser sheet cutting across the test section parallel to duct major axis. The high speed IDT NR-3S camera is position at an angle of approximately 9^o from the flow longitudinal axis, to maximize the transmition and minimize the reflection of the laser sheet passing through the transparent BK-7 window. Since the necessary scattering was primarily provided by condensed moisture particles resulting from the supersonic expansion, additional moisture was added to the ambient air to improve signal strength. This was accomplished by super-saturating a $2.8m^3$ ($100ft^3$) stagnation air bag connected to the wind tunnel inlet by PVC plumbing, as shown in Fig. 3.33. A 5.25cL/minute

humidifier was placed inside the stagnation air bag to increase the moisture content of the air.

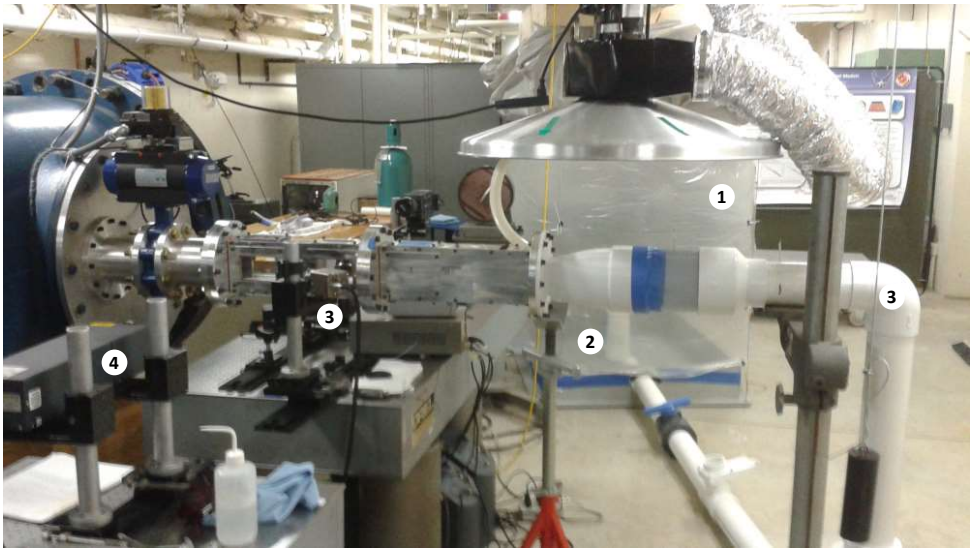

Figure 3.33: AEDC Wind Tunnel 9 calibration lab Mie-scattering experimental setup: (1) stagnation bag supplying working fluid (air) to test section, (2) 5.25cL/minute humidifier to increase moisture content in the stagnation flow, (3) wind tunnel conduit to guide moisturized air to test section, (4) IDT NR3-S1 high speed camera positioned to visualize the YZ-plane in the downstream station (X = 490mm), (5) NewWave Research 120mJ SOLO PIV Nd:Yag laser for planar laser illumination.

Using this technique, structures are defined by the amount of condensed moisture particles they contain. A major function of temperature, condensation content (and therefore scattering magnitude) is larger in areas of colder temperatures (freestream) compared to areas of warmer temperatures (boundary layer). Deriving flow field knowledge from the light scattering off of embedded particles assumes that the particles follow the flow features faithfully. A common performance parameter quantifying this 'tracking accuracy ' is the Stokes number τ, defined in Eq. 3.19 as the ratio between the particle aerodynamic response time (τ_p) and the flow time scale (τ_f) multiplied by the characteristic freestream velocity. The particle response time is defined by ρ_{H_2O} representing the density of water (particle material), σ_p representing the average condensation particle diameter, and μ representing the kinematic velocity of the flow. The flow time scale is simply defined by a characteristic length scale (l_0), evaluated as a variety of boundary layer station

heights.

$$\tau = \frac{\tau_p}{\tau_f} U_0 = \frac{\frac{\rho_{H_2O} * \sigma_p^2}{18\mu}}{l_0} U_0 \tag{3.19}$$

The calculation of the stokes number is a function of the location along the duct minor axis considered, with temperature and velocity inevitably varying from the boundary layer to the core flow. A centerline pitot probe survey performed in the aspect ratio 1.0 results in the calculation of Mach number and temperature vertical profile, as shown in Fig. 3.34 utilizing Eqs. 3.2 and 3.5.

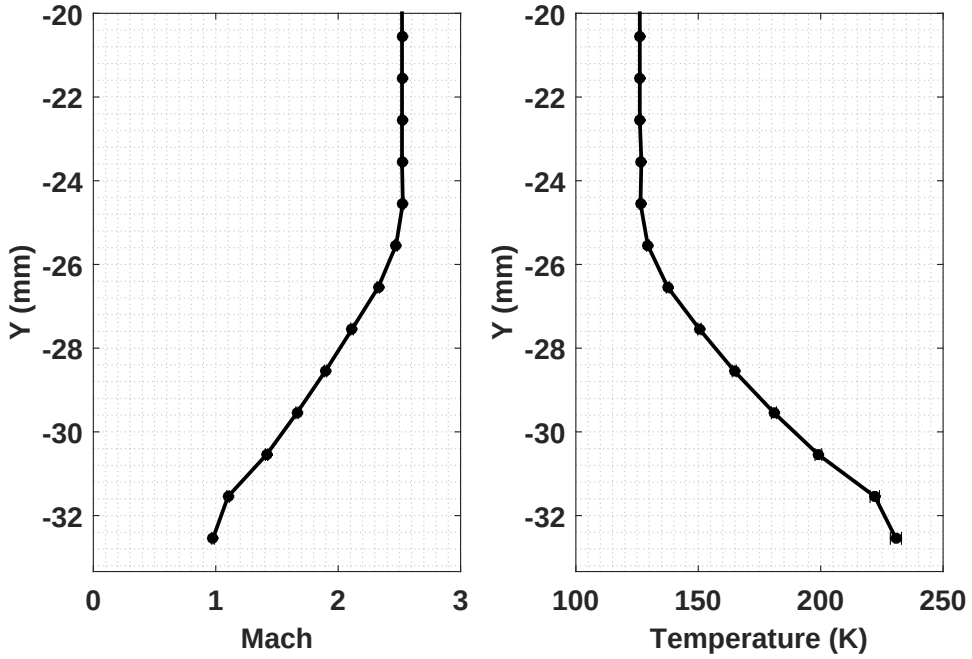

Figure 3.34: Mach and temperature calculations from aspect ratio 1.0 centerline Pitot probe survey at the downstream station (X=490mm). Measurements taken at 1mm intervals from the lower isolator wall.

Errors caused by particle dispersion relative to the fluid must be considered prior to analyzing the information provided by the Mie-scattering technique. The particle aerodynamic response time and stokes number calculations are presented in Fig. 3.35a-b for a variety of possible particle diameters (σ_p). Samimy and Lele cite a value of $\tau < 0.05$ for planar Mie-scattering visualization to avoid misinterpretation of the flow field by the fluid particles.

Since the Mie-scattering efforts presented in this thesis represent a minor portion of the

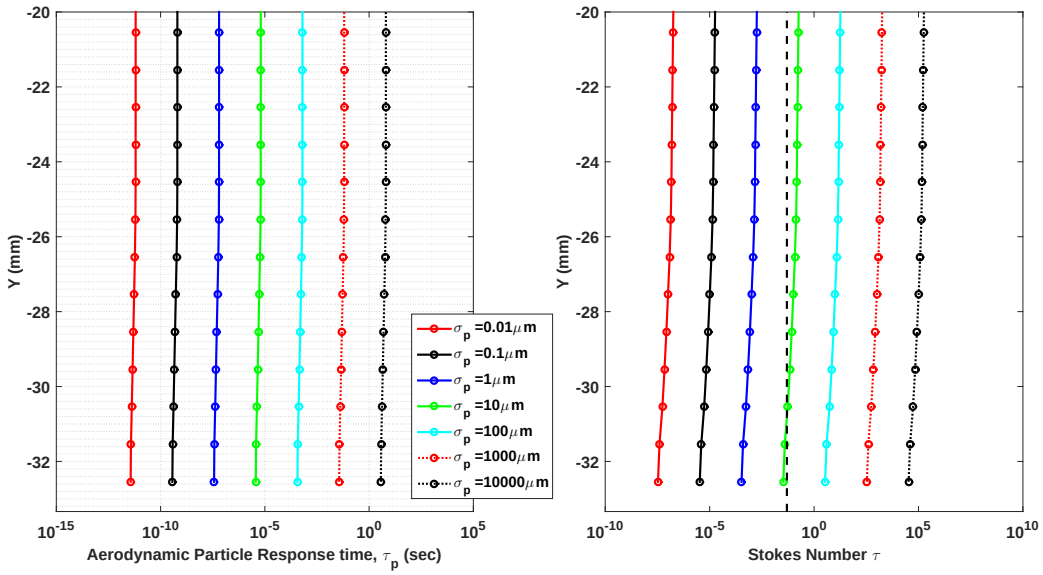

Figure 3.35: Particle aerodynamic response time and Stokes number calculations in the Tunnel 9 calibration tunnel. Stokes number limit of 0.05 is highlighted.

work performed, accurate measurements of particle diameter is beyond the scope of the current application. Results for Stokes number presented in Fig. 3.35 are provided for a variety of possible particle diameters, with the most likely order of particle diameter magnitude located between 1 and 10 microns. The limit on Stokes number to yield accurate flow representations is represented by a dashed black line. The higher bound of the expected particle diameter ($\sigma_p = 10\mu m$) produces a Stokes number that is still acceptable by the 0.05 Stokes number limit. With the majority of the particles expected to be 1 to 10 microns in diameter, the current application of the Mie-scattering technique is expected to provide accurate representation of the boundary layer structures analyzed in Chapter 6.

3.4 Computational Simulation

The secondary numerical simulation analysis was carried out as a compliment to the experimental measurements. Both the fully started and partially unstarted modes of operation are simulated in full-scale three-dimensional control volumes (Fig. 3.36) using STAR-CCM+ 10.04, a commercial engineering physics simulator capable of solving problems involving flow (fluids or

solids), heat transfer, and stress. All numerical simulation work is performed on a Dell PowerEdge R900 workstation equipped with 16 7400 series Intel® Xeon® processor cores.

3.4.1 Control Volume Geometry & Meshing

The original SolidWorks Computer Aided Drafting (CAD) models used in the manufacturing of the physical isolator models are used as imported geometries into STAR-CCM+, including the detailed Mach 2.5 nozzle contours. Figure 3.36 shows the extension of aspect ratios considered for simulation. Only the nozzle and isolator test section are considered in the current numerical approach. The aspect ratio 6.0 isolator is modeled as both the experimental configuration (half-nozzle geometry) and an axisymmetric nozzle configuration, maintaining a duct height of 50.8mm and increasing the duct width to 304.8mm. An aspect ratio 10.0 duct was also computationally modeled, although the test section flow did not start for the given experimentally derived boundary conditions. This observation is likewise made in work performed by Nedungadi & Van Wie [39], where for aspect ratio 10.0 ducts and a pressure ratio of $P_3/P_2 < 0.75$ the flow diffuses to the point of choking near the outlet plane of the isolator. For the scope of this research, only Mach 2.5 nozzle flows are considered, although follow-up work can easily employ higher Mach numbers to further explore the operation modes discussed in Fig. 2.5.

Given the relatively straightforward geometries of the isolator control volume, applying a high-quality triangulated surface mesh remains automated. The control volume mesh is provided by a unstructured trimmer cell mesher, predominantly composed of a hexahedral mesh with minimal cell skewness (the measure of diffusion permitted across a face without the quantity that is being diffused becoming unbounded). Prior to the application of the near-wall prism layer mesher, the trimmer cell mesher employs 'trimmed'cells, or polyhedral cells, next to the surfaces for optimal accuracy. The core flow/trimmer meshing operation is based on the initialization of a base cell size. A description of the mesh resolution dependency study is provided in Chapter 4.

A critical region of the mesh is the near-wall or extrusion layer. The prism layer mesher is employed to generate orthogonal prismatic cells next to the wall surfaces and boundaries. The

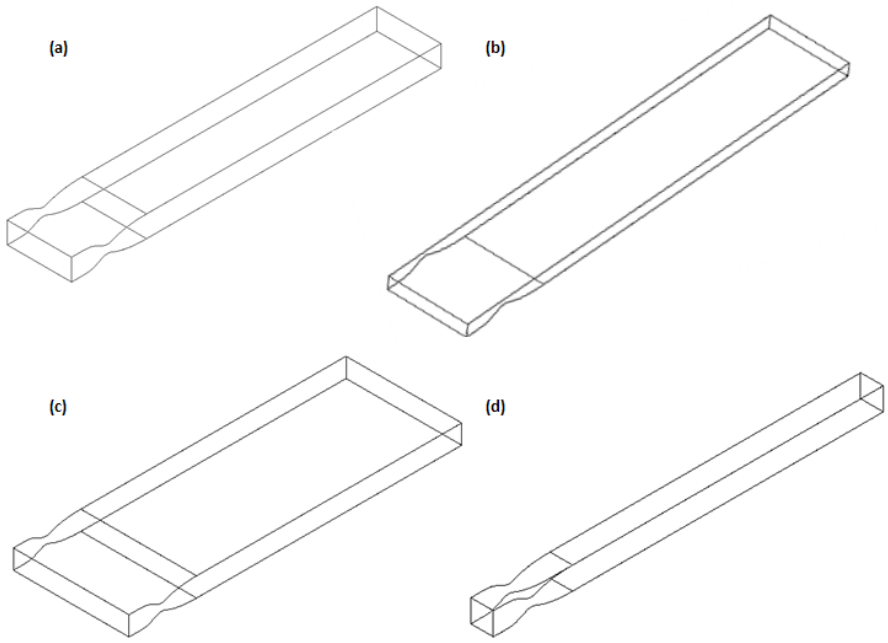

Figure 3.36: The different aspect ratio ducts considered in the numerical simulation: (a) experimental aspect ratio 3.0, (b) experimental aspect ratio 6.0, (c) computational aspect ratio 6.0 (axisymmetric nozzle), and (d) computational aspect ratio 1.0.

characteristics of the prism layer are defined by four parameters: (1) the total thickness, (2) the total number of cells within the layer, (3) the size distribution (i.e. growth factor), and (4) the distribution function employed to distribute the cells inside the layer (geometric progression or hyperbolic tangent). These factors determine the size of the first cell near the wall, an important parameter in the calculation of the wall Y^+ value. Representing a measure of non-dimensional wall distance, Y^+ given by Eq. 3.20, where $u_* = \sqrt{\frac{\tau_w}{\rho}}$ is the friction velocity at the wall, $nu = \frac{\mu}{\rho}$ is the kinematic viscosity, and $\tau_w = \mu \left(\frac{\delta u}{\delta y}\right)_{y=0}$ is the wall shear stress.

$$Y^+ = \frac{u_* y}{\nu} = \frac{\sqrt{\tau_w \rho} y}{\mu} \tag{3.20}$$

The importance of the Y^+ value will be noted in the outline of the turbulence models used in the present numerical work. To evaluate the smallest cell size provided by the prism layer meshing approach, Fig. 3.37 shows the distribution within the boundary mesh for a given number of layers, as well as the value of the smallest cell size nearest the wall. A geometric progression is used along

with a maximum boundary layer size of 14mm. Experimental schlieren and pitot probe surveys suggest a maximum boundary layer thickness of 11mm, thus a prism layer thickness of 14mm is chosen to ensure the entire boundary layer is captured inside the prism layer mesh.

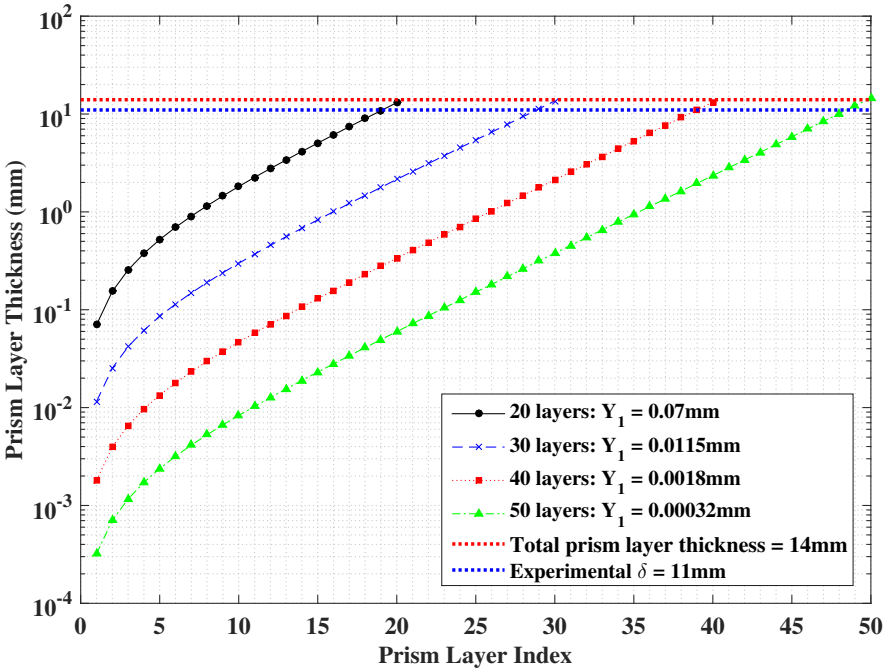

Figure 3.37: Boundary layer prism layer thickness and smallest cell size parametric study.

3.4.2 Governing Equations & Turbulence Modeling

For steady-state calculations, turbulence models offering closure of the Reynolds-Averaged Navier-Stokes (RANS) equations are used. For the three-dimensional geometry considered, the four governing equations are the conversations of mass, momentum, and energy summarized in Eq. 3.21a-d. A thorough discussion regarding the RANS approach is covered in Refs. [135–137].

$$\frac{\delta\rho}{\delta t} + \frac{\delta}{\delta x}(\rho u) + \frac{\delta}{\delta y}(\rho v) + \frac{\delta}{\delta z}(\rho w) = 0 \tag{3.21a}$$

$$\frac{\delta}{\delta t}(\rho u) + \frac{\delta}{\delta x}(\rho u^2 + P) + \frac{\delta}{\delta y}(\rho uv) + \frac{\delta}{\delta z}(\rho uw) = \frac{\delta}{\delta x}(\sigma_{xx}) + \frac{\delta}{\delta y}(\tau_{xy}) + \frac{\delta}{\delta z}(\tau_{xz}) \tag{3.21b}$$

$$\frac{\delta}{\delta t}(\rho v) + \frac{\delta}{\delta x}(\rho uv) + \frac{\delta}{\delta y}(\rho v^2 + P) + \frac{\delta}{\delta z}(\rho vw) = \frac{\delta}{\delta x}(\tau_{xy}) + \frac{\delta}{\delta y}(\sigma_{yy}) + \frac{\delta}{\delta z}(\tau_{yz}) \tag{3.21c}$$

$$\frac{\delta}{\delta t}(\rho w) + \frac{\delta}{\delta x}(\rho uw) + \frac{\delta}{\delta y}(\rho vw) + \frac{\delta}{\delta z}(\rho w^2 + P) = \frac{\delta}{\delta x}(\tau_{xz}) + \frac{\delta}{\delta y}(\tau_{yz}) + \frac{\delta}{\delta z}(\sigma_{zz}) \tag{3.21d}$$

$$\frac{\delta}{\delta t}(\rho e) + \frac{\delta}{\delta x}(\rho ue + pu) + \frac{\delta}{\delta y}(\rho ve + pv) + \frac{\delta}{\delta z}(\rho we + pw) = \frac{\delta}{\delta x}(\theta_x) + \frac{\delta}{\delta y}(\theta_y) + \frac{\delta}{\delta z}(\theta_z) \tag{3.21e}$$

where e is the internal energy per unit mass, P is the pressure, ρ is the density, and u, v, w are the x, y, z velocity component vectors. The viscous stress tensors, σ_{ij} and τ_{ij}, are defined in Eq. 3.22. Other terms used include the dynamic viscosity coefficient (μ), the second viscosity coefficient (λ), and the work terms of the viscous stresses and heat conduction in the fluid ($\theta_x, \theta_y, \theta_z$) [137].

$$\begin{aligned} \sigma_{xx} &= \lambda\left(\frac{\delta u}{\delta x} + \frac{\delta v}{\delta y} + \frac{\delta w}{\delta z}\right) + 2\mu\frac{\delta u}{\delta x} & & \tau_{xy} = \mu\left(\frac{\delta u}{\delta y} + \frac{\delta v}{\delta x}\right) \\ \sigma_{yy} &= \lambda\left(\frac{\delta u}{\delta x} + \frac{\delta v}{\delta y} + \frac{\delta w}{\delta z}\right) + 2\mu\frac{\delta v}{\delta y} & \& \quad & \tau_{xz} = \mu\left(\frac{\delta w}{\delta x} + \frac{\delta u}{\delta z}\right) \\ \sigma_{zz} &= \lambda\left(\frac{\delta u}{\delta x} + \frac{\delta v}{\delta y} + \frac{\delta w}{\delta z}\right) + 2\mu\frac{\delta w}{\delta z} & & \tau_{yz} = \mu\left(\frac{\delta w}{\delta y} + \frac{\delta v}{\delta z}\right) \end{aligned} \tag{3.22}$$

To account for turbulence in the flow field using various RANS turbulence models, the governing equations for the instantaneous velocity and pressure fields are decomposed into a mean and fluctuating component ($f = \overline{f} + f'$). This restructuring results in nine new terms added to the momentum equations, collectively called the Reynolds stress tensor, T_t [137]. The eddy viscosity approach is used to model the Reynolds stress tensor in terms of mean flow quantities in order to give closure to the governing equations, as well as to provide a derivation of the turbulent viscosity μ_t.

Two turbulence models that employ the eddy viscosity approach are used in the fully started, steady-state calculations: the two-equation SST Menter K-Omega ($k-\omega$) model and the single equation Spalart-Allmaras model. The $k-\omega$ model is initially employed since two-equation models have the capability to predict more complex flow fields than one-equation models [136, 138]. For the partially unstarted simulations, only the two-equation $k-\omega$ model is used due to its improved

performance for adverse pressure gradient boundary layers and Spalart-Allmaras' known deficiencies in these flow regimes. Both models are introduced below. Although detailed derivation is beyond the scope of this work, references are provided.

The $k-\omega$ model solves the transport equations for the turbulent kinetic energy (k) and the specific dissipation rate (ω) [139]. A known advantage of the $k-\omega$ model over other models is its performance for boundary layers under adverse pressure gradients and the fact that it can be applied throughout the entire boundary layer (including the viscous dominated region) without further modification. The specific $k-\omega$ turbulence model used in this study is the SST-Menter $k-omega$ which combines a $k-\epsilon$ approach in the far field with a $k-\omega$ approach in the near-wall regions, correcting the original $k-\omega$ method's sensitivity to free-stream and inlet conditions [63].

The second turbulence model used is the Standard Spalart-Allmaras model, a single trapsnport equation that determines the turbulence viscosity. The advantage to this model is that it is readily adaptable to an unstructured CFD solver and performs well for internal compressible flows featuring mild boundary layer separation [62,140]. Like the $k-\omega$ model, it is resolved throughout the entire boundary layer, thus not employing wall functions.

As alluded to above, when working with turbulence models the concept of the non-dimensional length scale y^+ (distance from wall measured in terms of viscous lengths) becomes important in order to accurately resolve the flow near the wall. A simplified representation of a near-wall flow can be divided into three distinct layers: (1) the linear velocity profile, viscous dominated sublayer, (2) the logarithmic velocity profile log layer, and (3) the large scale turbulent eddy dominated outer layer.

Both the $k-\omega$ and Spalart-Allmaras turbulence models support the direct resolving of the viscous sublayer, thus wall functions are not used. All turbulence models use the $all-y^+$ wall treatment method, optimized for both low- and high-resolution near-the-wall meshes. The $high-y^+$ wall treatment is the classic wall function approach utilizing a coarse boundary layer mesh that does not resolve the viscous sublayer, with turbulent parameters derived from equilibrium boundary layer theory. The $low-y^+$ approach does resolve the viscous sublayer and no wall

functions are needed. The $all-y^+$ wall treatment is a hybrid approach that automatically executes the $low-y^+$ approach for $y^+ \to 0$ and the $high-y^+$ approach for $y^+ > 30$. Although the majority of the simulations were performed using a y^+ on the order of 1.0, the $all-y^+$ wall treatment is utilized due to its stability and overall performance.

3.4.3 Boundary Conditions

Stagnation inlet and pressure outlet boundary conditions are applied to the inlet and outlet faces of the control volume respectively. All other contact surfaces are characterized by the no-slip condition. Pressure based boundary conditions are acquired experimentally and shown in Fig. 3.38 as a function of wind tunnel run-time. The pressure outlet boundary condition is defined by a static pressure and temperature boundary value, with the former derived from the static wall pressure measurements (CH13) obtained during the fully started mode of operation ($P_3 = 9600Pa$) and the latter derived from isentropic supersonic expansion ($T_3 = 135K$).

The stagnation inlet boundary condition is defined by a static pressure (CH3), static temperature, and total pressure value (CH2). To initialize the inlet flow state, a velocity profile is prescribed to the stagnation inlet plane. To experimentally capture these inlet parameters, a pitot-probe study is performed along with an accompanying static pressure tap in the upstream, subsonic portion of the converging-diverging nozzle. Shown in Fig. 3.38, the upstream static pressure is $92,712Pa$, the stagnation pressure $96,785Pa$, and the temperature is assumed to be that of the ambient air ($T_inlet = 298K$).

Mach number is derived from the compressible flow, subsonic pitot formula shown in Eq. 3.23. Temperature and velocity are subsequently derived as before. An initial velocity of approximately $V_{inlet} = 80m/s$ in the subsonic portion of the C-D nozzle is calculated and used in the initialization of the computational flow field.

$$M^2 = \frac{2}{\gamma - 1}\left[\left(\frac{P_0}{P}\right)^{\frac{\gamma-1}{\gamma}} - 1\right] \tag{3.23}$$

The uniform velocity profile applied to the inlet face produces an initial boundary layer

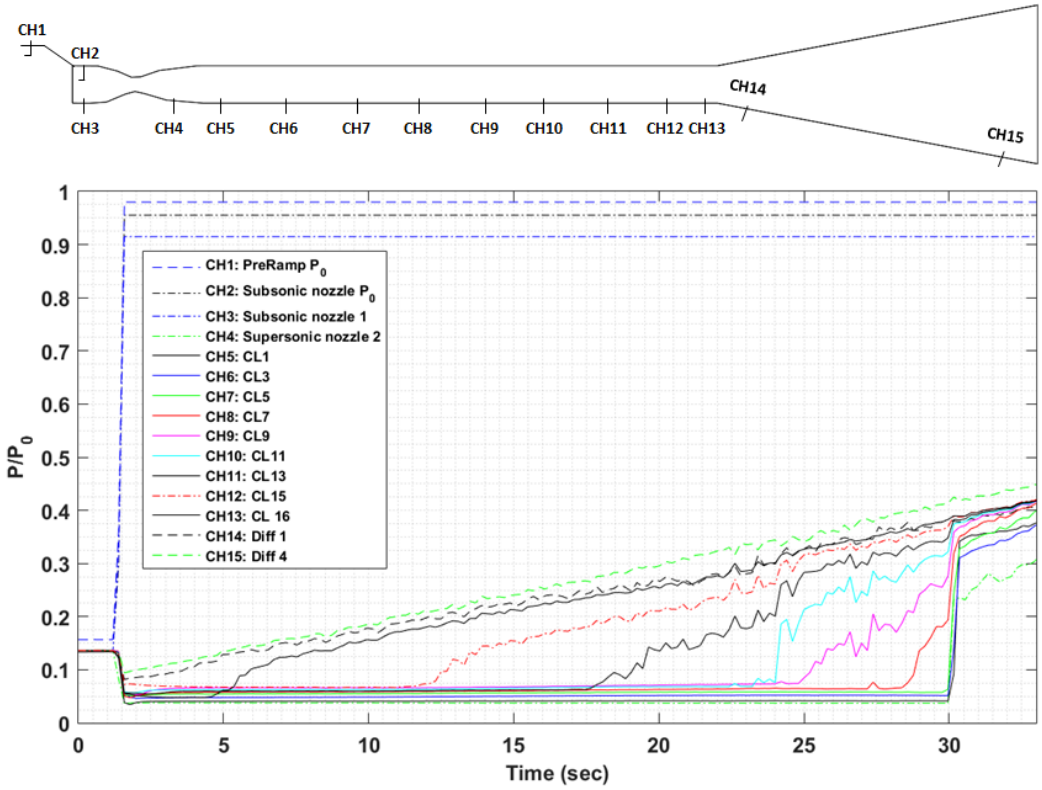

Figure 3.38: Experimentally obtained boundary conditions for the aspect ratio 3.0 configuration. Diffuser section is shown.

thickness in the subsonic portion of the C-D nozzle that continues to grow and interact with the nozzle profile itself. Computational boundary layer thickness is compared to the experimental boundary layer pitot-profile in Chapter 4 and good correlation is achieved. Figure 3.39 shows the formation of the boundary layer both at the starting point of the computational domain as well as at the isolator inlet plane origin location.

The boundary layer visualizations shown in Fig. 3.39a-c represent velocity and Mach number threshold representations of the boundary layer content. The boundary layer grows along the nozzle contour and initializes the isolator flow field with the boundary layer shown in Fig. 3.39b-c. As expected, the sonic line of the boundary layer is significantly smaller than the closest available pitot measurement described in Fig. 3.11 (0.78mm for the pitot probe compared to 0.1mm thick sonic line). Extensive validation of the fully started simulations are performed in Chapter 4 by comparison to experimental pitot survey data.

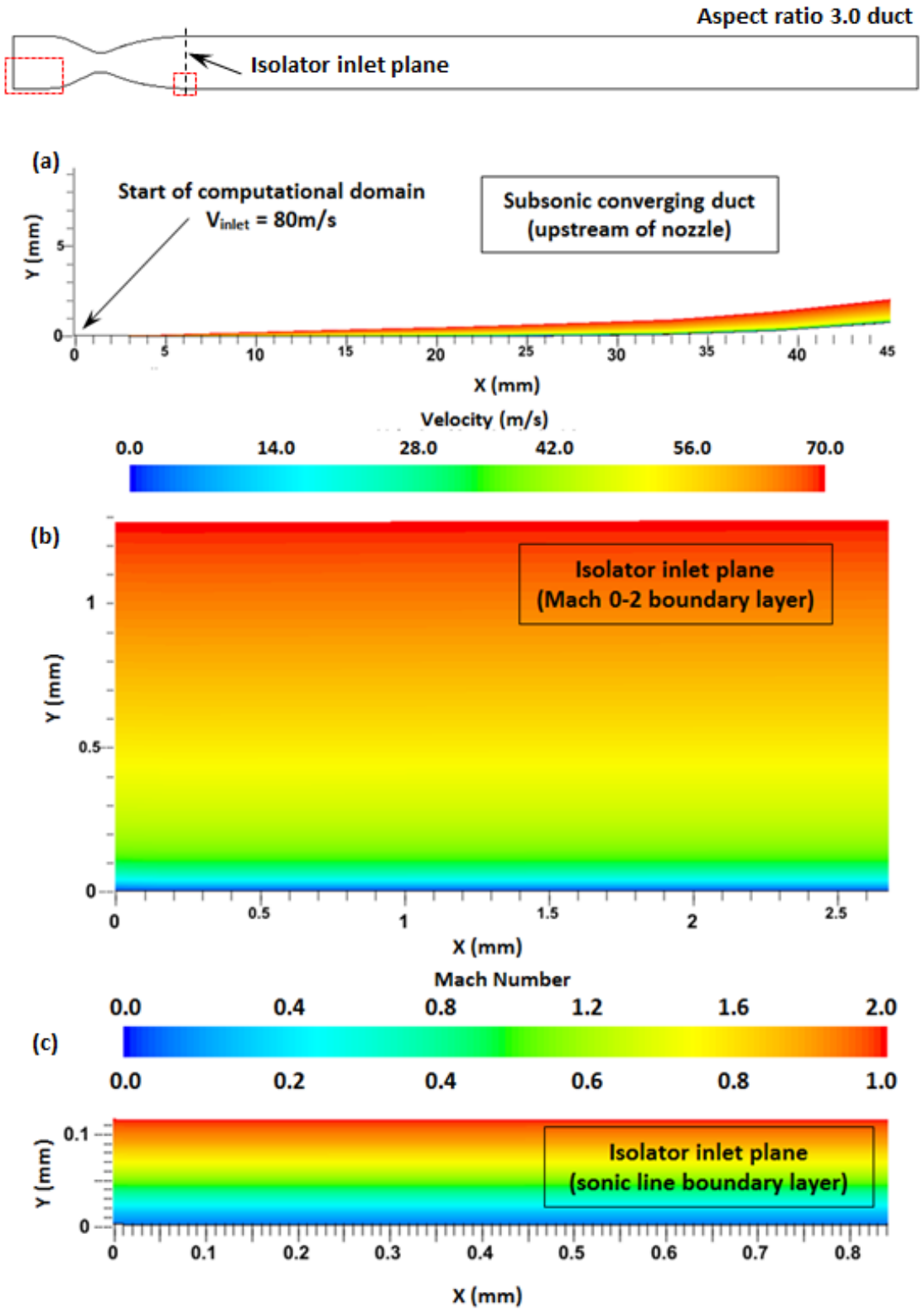

Figure 3.39: Computational boundary layer initialization: (a) inlet velocity profile, (b) isolator origin Mach 0-2 boundary layer structure, and (c) isolator origin sonic boundary layer structure.

Chapter 4: Diagnostics Development & Validation

Although they are not new techniques, the Background Oriented Schlieren (conceptualized in the early 2000s) and Focusing Schlieren Deflectometry (introduced in the early 1990s) methods remain relatively underdeveloped and unstandardized in comparison to more conventional diagnostics tools. Unlike the traditional schlieren and shadowgraph techniques, whose performance is a relatively straight forward function of the quality of optical components employed and the geometrical parameters chosen, the performance of the BOS and FSD techniques is characterized by a more complicated relationship to the components within the system due to the increased number of possible performance parameters.

To address this matter, significant work is performed to optimize the Background Oriented Schlieren and Focusing Schlieren Deflectometry methods as applied to the confined supersonic flow field found in the scramjet isolator environment. This process is carried out in a systematic manner, and could potentially be employed to optimize the techniques for a wide range of flow environments.

In addition to the experimental diagnostics, this chapter covers the validation and verification efforts of the numerical simulations. Numerical results of the fully started mode of operation are compared to experimental flow measurements in a variety of dependency studies including mesh fidelity, prism layer resolution and resulting y^+, and application of turbulence model. As mentioned in Chapter 3, the one-equation Spalart-Allmaras and two-equation $k-\omega$ turbulence models are used to simulate the fully started flow, while only the two-equation $k-\omega$ model is used for the partially unstarted mode simulations.

4.1 Background Oriented Schlieren Optimization

Background Oriented Schlieren refinement efforts focus on the quantitative optimization of the background pattern. The working theory of the method is discussed in Chapter 3. The refinement efforts discussed in this chapter are performed using the Fresnel lens backlit method from Fig. 3.25.

Advancements in image acquisition technology and cross-correlation algorithm capability (for the post-processing of image pairs) have experienced a substantial growth over the last decade with their application in numerous other fields. Efforts to impart a complimentary advancement to the third major component of the BOS system, namely the background pattern, is the primary goal in refining this technique. The design and manufacture of the BOS background pattern, a significant variable in the resolution and overall capability of the system, has been mostly qualitative in the past. Background pattern generation methods have included splashing droplets of paint with a brush directly on a wind tunnel wall [141] and projecting laser speckles generated through ground glass [142], to utilizing computer generated, randomized monochromatic and colored pixel segments [143, 144]. The focus in this study will be to investigate the effectiveness of optimizing the background pattern to the strength of the expected density gradient field, through a user-controlled and fully customizable approach.

To approach a quantitatively optimized background pattern parametric study, previous work in the fields of PIV and BOS can be consulted. Vinnichencko et al. performed numerical tests for accuracy and spatial resolution of BOS methods using various backgrounds including wavelet-noise backgrounds, linear backgrounds, and regular and randomized dot patterns [145]. Quantitative analysis on post-processing error evaluation and spatial accuracy revealed that the chaotic, randomized dot pattern with dot size of 2-3pixels performed best. This is furthermore cemented by observations made in the field of PIV, with Raffel noting that the optimum particle image diameter resulting in the lowest RMS-uncertainty for cross-correlation (using three-point Gaussian peak approximations) falls within the range of 2-5pixels [146]. To optimally capture a

schlieren disturbance, the background pattern should be tuned to the envelope of density gradient strength expected to be encountered in a variable density gradient flow field. The first portion of this paper discusses the background pattern optimization efforts, with the second part discussing its application to the visualization of the isolator shock train.

4.1.1 BOS Background Pattern Design Procedure

The systematic design of the BOS background pattern is performed in a series of steps in order to make the process applicable to a wide range of flows and experimental settings. A 10° compression ramp with a base length of 7.2mm (0.28") was placed two duct heights downstream of the isolator inlet plane (lower wall) in the aspect ratio 3.0 test section configuration (Fig. 3.4a) to provide the calibration environment used for the background pattern optimization study (Fig. 4.1).

In addition to providing the reference density gradient of the primary weak oblique shock, a wide range of density gradients are generated by the calibration environment that provide the opportunity to analyze the effect of quantitatively optimizing the BOS background pattern by observing the ability to resolve a wide range of density gradient magnitudes. Some key density gradients visible in Fig. 4.1 include: 1) trip induced weak pressure waves, 2) incoming boundary-layer, 3) primary weak oblique shock wave, 4) oblique shock/boundary-layer interaction accompanied by an upstream shock caused by the adverse pressure gradient thickening the boundary-layer, 5) reflected shock, 6) ramp expansion fan, and 7) ramp shear layer. Besides the wide range of density gradients established, the 10° compression ramp environment was chosen for the calibration efforts due to the primary oblique shock wave angle closely emulating the oblique shock train front orientation expected.

To improve the performance of the BOS technique, the background pattern needs to be designed so that it is capable of resolving a wide range of density gradients. The design process is outlined below for the calibration flow environment and is based on two major design principles:

- The estimation of a reference density gradient in the flow-field of interest, preferably in

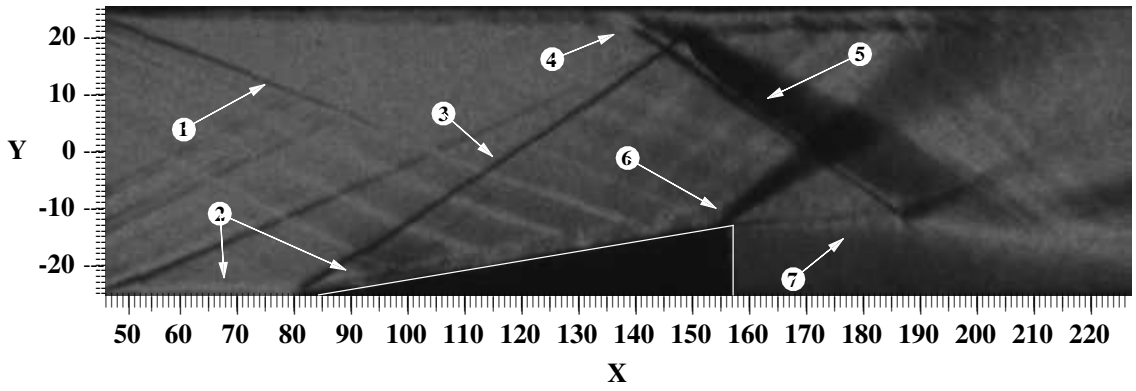

Figure 4.1: 10° compression ramp for background pattern design study. Flow is left to right, dimensions in mm.

the higher bounds of the density gradient envelope. This will allow the calculation of a reference background pattern particle displacement through the schlieren effect, upon which the pattern design can be based.

- Several key 'design' rules from the field of Particle Image Velocimetry (PIV) are adapted, owning to the resemblance of the post-processing technique across both methods.

4.1.1.1 Estimate of the reference density gradient

Referencing the calibration environment shown in Fig. 4.1, oblique shock theory can be used to estimate the density gradient across the weak incident oblique shock wave. Although a two-dimensional ramp is used, side wall boundary-layer and corner flow effects will lead to a degree of three-dimensionality in the shockwave. Due to the line of sight integration of the schlieren technique (a 2-dimensional representation of a 3-dimensional structure), the standing oblique shock wave appears thicker than the traditional estimate of a few mean-free path lengths.

The grayscale magnitude of the flow features in the horizontal knife-edge schlieren image indicates the magnitude of the density gradient, with darker features resembling a larger $-\delta\rho/\delta y$, lighter features a larger $\delta\rho/\delta y$, and gray areas resembling areas of little disturbance. To give the background pattern design a solid foundation, a known reference density gradient is desired upon

which the pattern parameters can be optimized.

Through a known ramp deflection angle of 10° and an inlet Mach number of 2.5, the $\theta - \beta - M$ relation was used to estimate a wave deflection angle of 31.8°. Given Mach 2.5 isentropic nozzle expansion from atmospheric conditions, the density jump across the primary shock wave was calculated to be $\delta\rho$=0.087kg/m^3. A shock thickness estimate on the order of three mean-free path lengths (δx=1.54$E-5m$) results in a reference density gradient across the shock of $\delta\rho/\delta x$=5700$kg/m^3/m$.

4.1.1.2 Estimate of the reference refraction angle

The sensitivity of a schlieren based visualization system is traditionally characterized by the calculation of the refraction angle as a function of the refractive index gradient integrated along a characteristic width Z_T, as shown in Eq. 4.1:

$$\epsilon = \frac{1}{n}\int_0^{Z_T} \frac{\delta n}{\delta z} dz \tag{4.1}$$

The units of $\delta n/\delta x$ in the traditional calculation of the refraction angle offered in Eq. 4.1 could be expressed in more useful form when estimates of the refraction angle are desired based on the flow at hand. A more convenient engineering approximation of this relation can be formed through the Gladstone-Dale relationship (Eq. 4.2), offering a relationship between the index of refraction and the density gradient (Eq. 4.3). This relation is weakly dependent on wavelength (λ), assumed to be constant at 550nm for the white light source used throughout the study.

$$\frac{n-1}{\rho} = \frac{\beta}{\rho} = G(\lambda) = 2.22x10^4 \left[1 + \left(\frac{6.71x10^{-8}}{\lambda}\right)^2\right] \tag{4.2}$$

$$\frac{\delta n}{\delta x} = G(\lambda)\frac{\delta \rho}{\delta x} \tag{4.3}$$

Re-arranging Eq. 4.1 using Eq. 4.3, an estimate of the refraction angle can be written as:

$$\varepsilon = \frac{G(\lambda)}{n}\int_0^{Z_T}\frac{\delta\rho}{\delta x}dz = \frac{G(\lambda)}{n}\frac{\delta\rho}{\delta x}Z_T \tag{4.4}$$

Disturbances such as oblique shockwaves are known to produce refraction angles (ϵ) on the order of a few hundred arcseconds [147–149]. Since the compression ramp shock is not perfectly two dimensional by nature, using the entire test section width of 152mm (6.0") as an unrealistic approximation of the integral width in Eq. 4.4 yields a refraction angle on the order of 11°. The shock train front three-dimensionality illustrated in Fig. 3.20b is referenced to establish a compromise, with a center flow-field normal structure width scale of approximately 10mm (0.4") representing Z_T. This assumption yields a refraction angle estimate of approximately 2650 arcseconds.

4.1.1.3 Estimate of the reference object plane particle displacement

The object plane particle displacement (Δy_o) is a trigonometric function of ϵ and Z_D, as shown in Fig. 3.24 and Eq. 4.5. The test section centerline is used as the origin plane, with the background pattern displaced $Z_D = 76.2mm$ (3.0") in both the calibration and actual shock train visualization efforts. Using the above parameters, an object plane displacement of $Y_0 = 1mm$ (0.04") is obtained.

$$\Delta y_o = Z_D * tan(\epsilon) \tag{4.5}$$

Z_D plays a critical role in system sensitivity, with larger Z_D allowing smaller density gradients to be visualized by increasing the displacement of the particles, potentially providing contrast not capable of being captured at smaller Z_D. However, a large Z_D runs the risk of placing larger density gradients outside of the user-defined cross-correlation interrogation window. Since most BOS applications involve fixing the background pattern to the far wind tunnel wall opposite the visualization window, the Z_D is fixed at half the wind tunnel width throughout this study. Care must be taken in pattern design to resolve a wide range of density gradients when Z_D is fixed.

4.1.1.4 Estimate of the reference image plane particle displacement

For every Δy_o there is an associated image particle displacement Δy_i, or the distance a particle is displaced on the camera sensor chip. A relationship between Δy_o and Δy_i is governed by the magnification factor used, which in turn is a function of the image/object size ratio or the experimental geometry and lens focal length, according to Eq. 4.6. A camera magnification factor of $M_0 = 0.08$ is employed throughout the study. This results in a $\Delta y_{i,ref} = 0.078mm$ (0.003"), or approximately 6 camera pixels).

$$\Delta y_i = \Delta y_o M_0 = \Delta y_o \frac{\left[\left(\frac{1}{f}\right) - \left(\frac{1}{Z_B}\right)\right]^{-1}}{Z_B} \tag{4.6}$$

4.1.1.5 Application of PIV 'design rules' to pattern design

Due to the similarities in post-processing procedures between the BOS and PIV techniques, several PIV design rules outlined in Raffel [146] and Adrian [150] are employed in the pattern design process. The three principle rules are:

1. An interrogation window size at least 4 times the reference estimated pixel displacement to reduce loss of signal.

2. Particle diameters in the range of 2-5 camera pixels.

3. A high image density or number of particles per interrogation window (N_I) correlates to a high spatial correlation peak amplitude R_s (signal strength) and a low relative noise level. Adrian cites N_I ¿ 10 as a minimum for acceptable signal strength.

The above rules, together with the estimated pixel displacement ($Y_{i,ref} = 6.5px$), magnification factor ($M_0 = 0.08$), and pixel size ($D_{px} = 12\mu m$) are taken into account to guide the pattern design procedure outlined below. Image processing tools in MATLAB® were used to produce the user-defined grids.

1. Calculate the required interrogation window size based on Y_i and design rule #1: A design

interrogation window of 32x32px was used in conjunction with a parent 128x128px and a 4 pass, 50% reduction multi-grid cross-correlation process. The pattern was designed based on the 32x32 window due to the expected maximum $Y_{i,ref}$ of 6.5pixels. A fourth pass utilizing a 16x16px window was included to account for the lower density gradient (lower Y_i spectrum).

2. Assign a particle diameter range based on recommendation #2: While micron and sub-micron scale particles are common in the field of PIV (due to the requirement of particles faithfully following the flowfield), background particles in BOS are not entrained in the flow and selection of particle diameter can be more flexible. The two primary concerns in particle selection for BOS is to: (1) optimize light-dark contrast and (2) provide sufficient particle diameter tailored to the camera's resolution, lack of light-scattering off of the particles decreasing their signal-to-noise ratio, and the total FOV size (170x54mm). Placing particles 2-5pixels (24-60 μm) on the background pattern will not allow for adequate visualization. The magnification factor is therefore applied to recommendation #2 to yield a particle diameter range of 0.3-0.75mm (0.01-0.03") on the background plane.

3. Transfer the image plane interrogation window size to the background plane through the use of M_0: To tailor to the requirements outlined in step #1 and #2, the third pass (32x32px) was chosen to produce background plane particle windows measuring 4.8x4.8mm. The superimposed interrogation windows on the background plane will be called particle windows to distinguish image from background plane reference.

4. Populate the background plane particle windows with the background particles: Each particle window is populated with a collection of particle whose image density (N_I) is user defined and whose position within the background plane window is randomly scattered. Particle diameter was varied between user selected bounds and followed a truncated Gaussian distribution with a mean located at the center of the bounds and a standard deviation of 1 particle diameter. Care is taken to set the proper units in the image production software and to match the printer's native resolution. Particle shape (ex. circle, hexagon), color, and fill (ex. hollow,

double ringed, solid) can also be varied for parametric purposes. All background patterns used in this work utilized solid black dots on a white background.

4.1.2 Qualitative Pattern Analysis

Following design rules #1 and # 2 above, the main parametrization study involved the variation of image density ranging from $N_I = 25 - 200$. Pixel displacement range is set from 0 to 6 pixels to provide greater contrast for the entire range of density gradient, with the estimated maximum image plane displacement presented as dark red. Results are shown in Fig. 4.2 for the optimized N=75 pattern and in the collection of Fig. 4.3a-d for the additional pattern densities evaluated. A color map of pixel displacement is presented along with a single interrogation window pattern sample

Results can be compared to the baseline density gradient schlieren image in Fig. 4.1 for comparison, given that the true one-to-one pixel mapping of the traditional schlieren image will offer higher resolution than the interrogation window based representation of the BOS method. Although the N=75 pattern is presented as a stand-alone visualization, the pattern optimization discussion below covers both Fig. 4.3a-d as well as the final optimized pattern shown in Fig. 4.2.

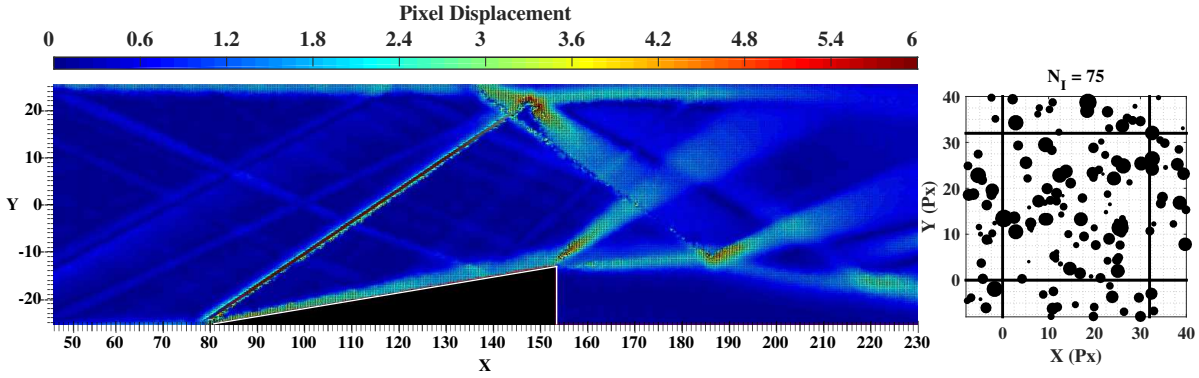

Figure 4.2: Parametric background pattern design results utilizing a 32x32px particle window and magnified 2-5px (0.3-0.75mm) diameter particle diameter range: N=75. Flow is left to right, dimensions in mm.

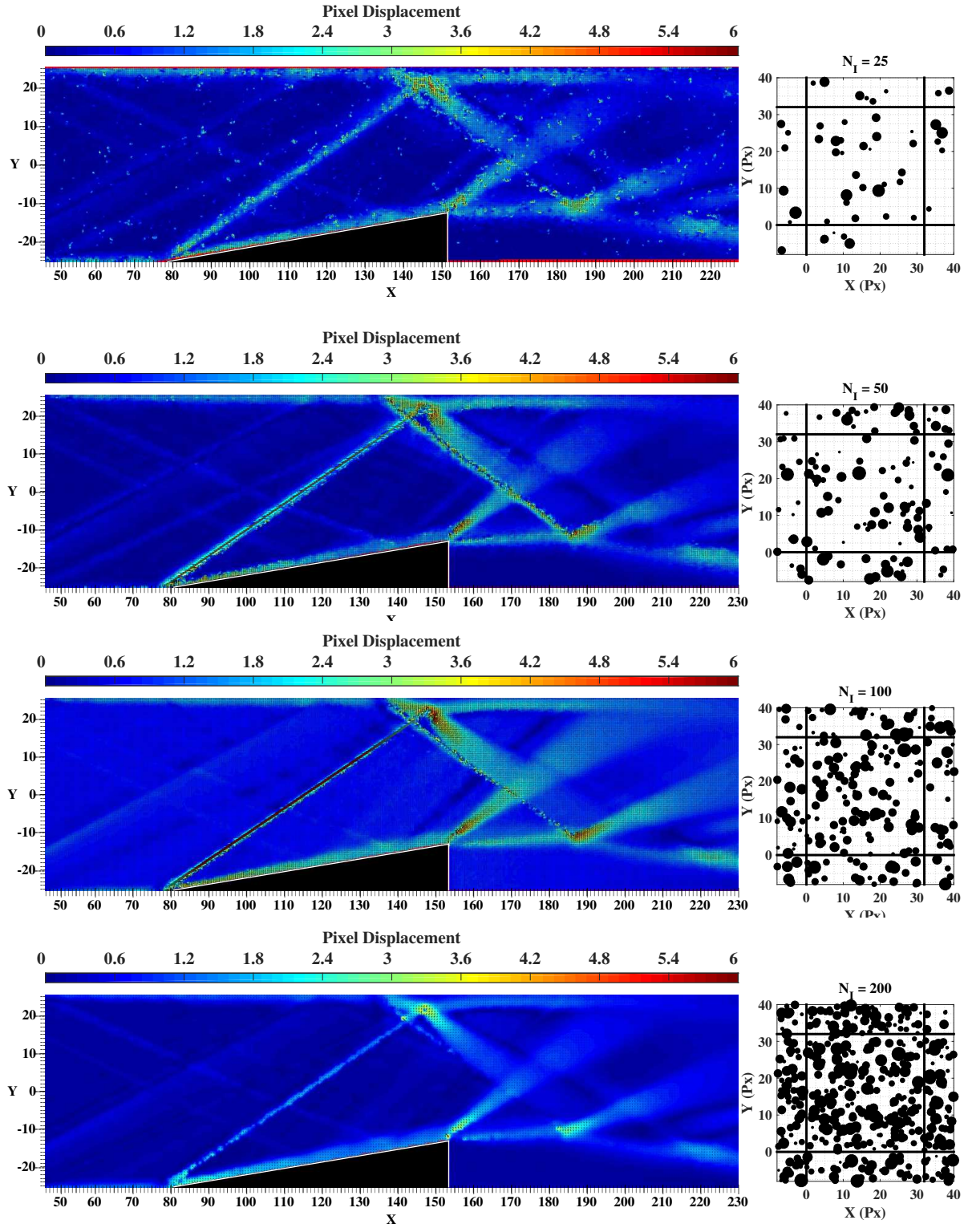

Figure 4.3: Parametric background pattern design results utilizing a 32x32px particle window and magnified 2-5px (0.3-0.75mm) diameter particle diameter range: (a) N=25, (b) N=50, (c) N=100, and (d) N=200. Flow is left to right, dimensions in mm.

The bright spots noticeable in Fig. 4.3a suggest local regions of non-physical, high particle displacement in regions of low and medium density gradient. The case of $N_I = 25$ represented a typical undersampling of the data where in some cases the statistical analysis was unable to agree to the correct homogenous displacement vector inside certain interrogation windows. Furthermore, the principle compression shock is characterized by inadequate pixel displacement, generally below half of the maximum estimated.

Progressing to a denser interrogation window of $N_I = 50$, shown in Fig. 4.3b, a greater representation of the entire density gradient range, sharper features, and the absence of most spatial aliasing due to undersample is observed. Adequate contrast change between the low, medium, and large density gradients provides detail not shown in the preceding case (the interaction between the pressure waves and the windward-face of the ramp attached boundary-layer are now noticeable). Adequate pixel displacement within the primary compression shock is now visible, with a thin line of maximum pixel displacement visible at the center of the shock wave. Lower pixel displacement boundaries to the left and right of the shock feature represent some of the density gradient magnitude smearing at the edge of the shock feature.

A further increase in image density provides the best contrast within the parametric study, with $N_I = 75$ (Fig. 4.2). Upstream-of-ramp boundary-layer is now clearly visible, as is a more detailed representation of the reference shock-upper wall boundary-layer interaction causing localized boundary-layer separation and re-attachment. A sharper reference shock is visible, including the largest pixel displacement.

A further increase in image density ($N_I = 100$) does not qualitatively improve the image quality. While the principle compression shock shows adequate displacement, detail upstream of the compression ramp characterized by lower density gradients is reduced compared to the $N_I = 75$ case. Increasing the image density above $N_I = 75$ may signal a return to spatial aliasing effects due to oversampling inside the interrogation window, characterized by lower contrast and less-defined flow features. This is shown in the $N_I = 200$ case presented in Fig. 4.3d, where the reference compression ramp fails to produce adequate displacement. The high image density causes

interference within the particle interrogation window cross-correlation process, and both the high and low bounds of the density gradients are inadequately resolved.

4.1.3 Quantitative Pattern Analysis

Accompanying the qualitative analysis presented above, two quantitative parameters are evaluated. The first by providing a measure of image sharpness and contrast by evaluating the calculated particle displacement, and the second by estimating of the density gradient magnitude as derived from pixel displacement along the reference compression ramp oblique shock.

Image sharpness and contrast were evaluated for features along two vertical reference lines located at X = 71mm and X = 118mm shown in Fig. 4.4a, representing the low and high regions of density gradients respectively. The low density gradient regime, presented in Fig. 4.4b is characterized by multiple pressure waves crossing the reference line. It is shown that the N=75 grid provides the best representation of the low displacement region by distinguishing the multiple low pressure waves fanning out from the inlet region.

The high displacement regime was evaluated through calculating the modified Q factor, the ratio between the peak height and half-height bandwidth, with high Q factors representing higher resolution representation of the flow feature in question. For the five pattern representations shown in Figs. 4.3-4.3, the following Q factors were calculated for the oblique shock peaks shown in Fig. 4.4c: 1.87, 8.59, 8.69, 8.83, and 1.11. As expected from the qualitative analysis above, BOS representations obtained with grid N_I of 50, 75, and 100 respectively provided the highest resolution flow feature.

Due to the flexibility and ease in pattern design, several other optimization studies were performed.

- Variation of particle diameter including 2-5, 6-10, 10-15 pixels: The finer scale was able to resolve the widest range of density gradient with the least amount of aliasing.

- Particle/background color combinations including black/white and white/black (white color being transparent): Other than potential logistical issues of printing out larger patterns with

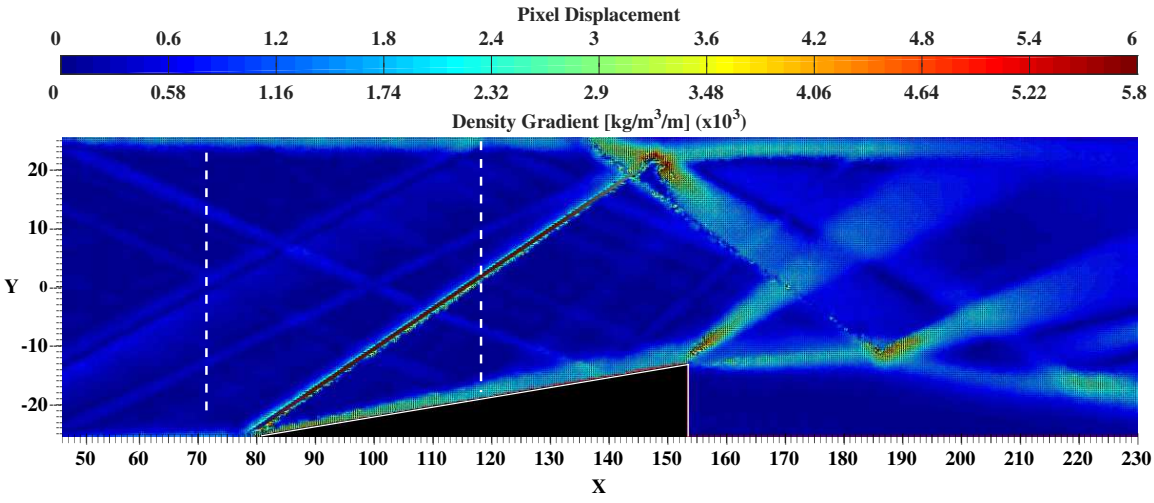

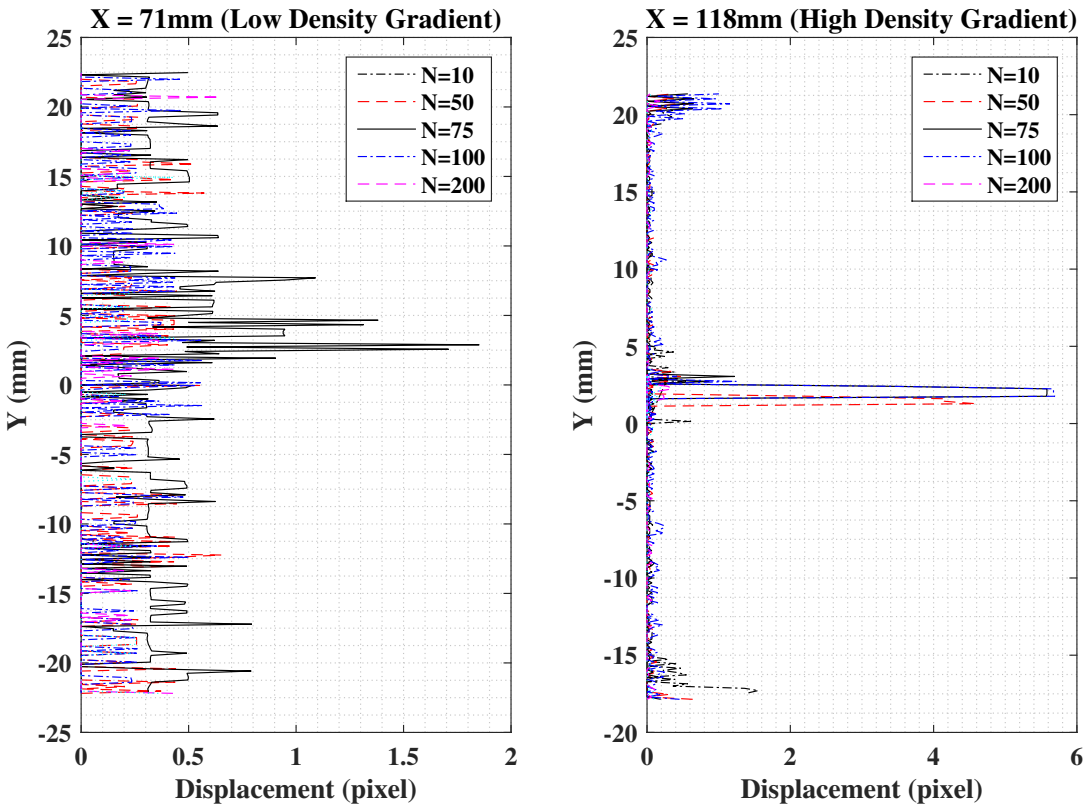

Figure 4.4: Quantitatiave analysis of BOS pattern performance: (a) Global representation of flow field density gradient distribution, and (b) Pixel displacement peaks for low gradient region (X = 71mm) and high gradient region (X = 118mm).

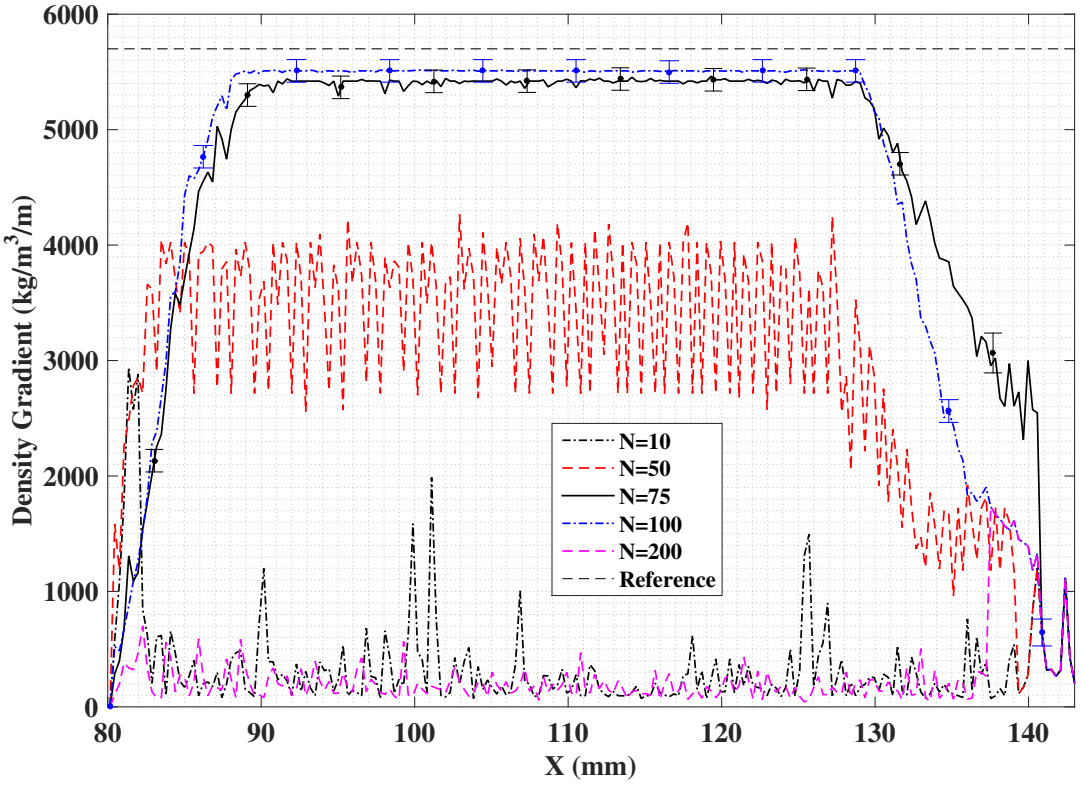

Figure 4.5: Three-line averaged density gradient estimate of compression ramp shock.

a black background, the increased image intensity with the 'white' background allowed for shorter exposure times due to more light getting through. Furthermore, if a black background is used it must be as opaque as possible. Running multiple prints on the same transparency or overlaying separate transparencies will obscure some of the finer transparent particles

- Variation of particle shapes to compare the effects of light-dark contrast on cross-correlation signal-to-noise ratio: This study included circles, stars, and triangles. Due to their geometry, the circular particles were characterized by a 'larger amount' of light-dark contrast for the principle particle dimension and performed best among the particle shapes considered.

4.1.3.1 Density gradient estimate

A useful quantitative extension of the BOS technique is the ability to estimate density gradient magnitude from the calculated vector displacements in the post-processed BOS image. The calculation is performed by re-arranging Eq. 4.4 into Eq. 4.7, shown below. The error in Δy_i due to the 2x3 point Gaussian sub-pixel interpolation method is estimated at $\pm$ 0.1pixels [151], and the error in the measurement of the geometric parameters Z_D and Z_T is $\pm$ 1.0mm.

$$\frac{\delta\rho}{\delta x} = tan^{-1}\left(\frac{\Delta y_i}{M_0 Z_D}\right)\frac{n}{G(\lambda)}\frac{1}{Z_T} \tag{4.7}$$

Density gradient estimates calculated through Eq. 4.7 for the primary compression shock are presented in Fig. 4.4d, averaged across three diagonal rows of pixels. Complementing the qualitative observations made above regarding the pixel displacement within of the primary compression shock, both $N_I = 75 and 100$ patterns provide density gradients magnitudes within 5.0% and 3.5% respectively of what is expected from the initial gradient estimate of 5700 $kg/m^3/m$. Fluctuating value of density gradient inside the primary shock for the $N_I = 50$ pattern suggests the image density is still too low to provide a robust background, with information loss prevalent throughout the structure. Evaluating the performance of the background pattern based on: (a) the ability to resolve a wide range of density gradient, and (b) provide an adequately accurate estimate of density gradient magnitude ($\pm$ 5%), the $N_I = 75$ background patterns is chosen as the optimum for the compressible flow-field in question and is subsequently used in the shock train visualization study presented in Chapter 5.

4.2 Focusing Schlieren Deflectometry Calibration

Calibration of the Focusing Schlieren Deflectometer was carried out by examining the measured frequency content of passively and actively generated acoustic flow structures. First, acoustic frequency modes embedded in shallow open cavity supersonic shear layers are used to validate the working principle of a single-point deflectometry reading. Results of these two-dimensional flow

features are compared to semi-empirical estimates of frequencies peaks over compressible shear layers.

Second, actively forced three-dimensional, low Reynolds number Helium and Nitrogen jets are utilized to further validate the single-point deflectometer spectral measurement capabilities as well as the two-probe velocimetry configuration used in the shock train analysis presented in Chapter 5. Jet velocity results obtained from this non-intrusive two-point velocimetry configuration are compared to traditional pitot probe measurements.

4.2.1 Two-Dimensional Cavity Shear Layer

To test the capabilities of the Focusing Schlieren Deflectometry technique to acquire frequency signals over a two-dimensional control volume, a supersonic shear cavity was built into the aspect ratio 3.0 isolator wind tunnel configuration. Shown in Fig. 4.6b, the cavity consists of a fixed height ($D_{cav} = 6.35mm$) and an adjustable streamwise base length (L_{cav}) through the use of inserts. This approach allowed for a variety of L_{cav}/D_{cav} ratios to be tested, ranging from 3.0 to 5.0. All cavities tested are considered to be 'acoustically open'cavities ($L_{cav}/D_{cav} < 9$) to take advantages of the characteristic distinct peaks in the sound pressure spectra. Acoustically closed cavity flows are characterized by a more broadband sound pressure spectra [152].

A schlieren image of the compressible shear layer is shown in Fig. 4.6a, impinging on the trailing edge of the cavity. Visualizing this flow field projected on the image plane, the white dot represents a typical location analyzed by the fiber optic embedded in the image plane and connected to the avalanche photodiode. Other locations are also sampled and presented below. A fast response Kistler dynamic pressure sensor in a needle nose housing is located at the floor of the cavity to establish the ability of the traditional pressure sensor to capture the sound pressure waves generated by the cavity. Resonance frequencies caused by the needle housing are accounted for.

The original discreet voltage signal in the time-domain produced by the Avalanche photodiode is converted into the frequency domain by the application of the fast Fourier transform (FFT)

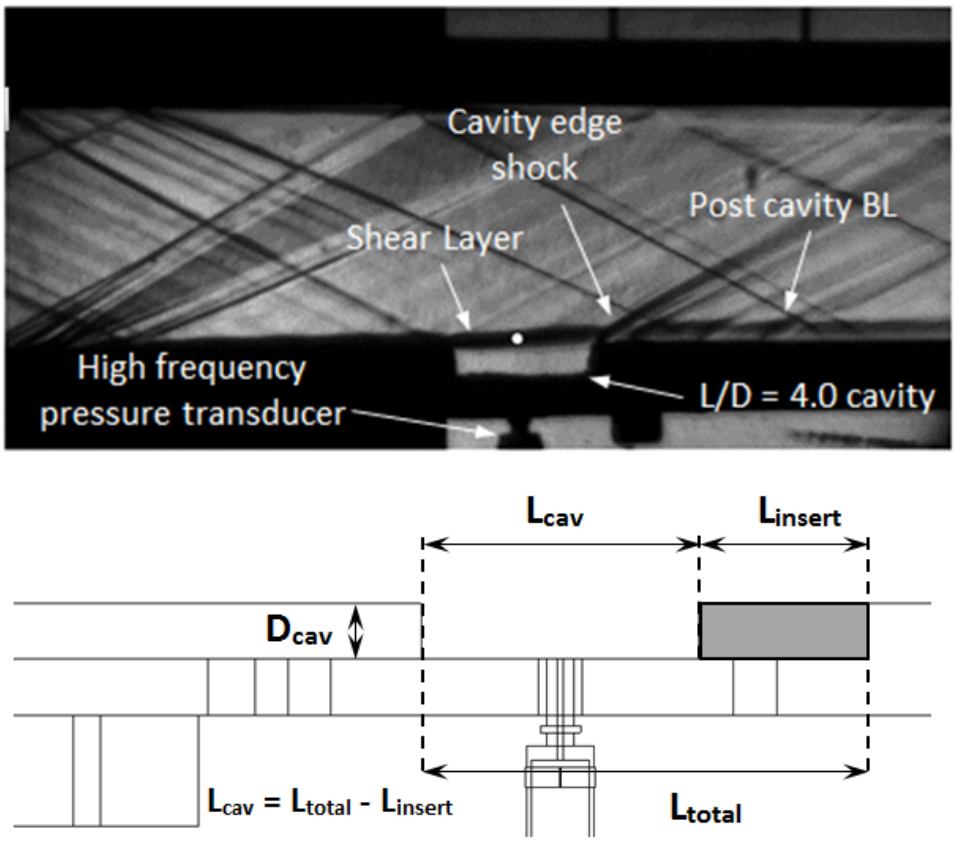

Figure 4.6: Supersonic cavity shear layer used as a FSD calibration configuration. User selected L_{insert} allows for various L_{cav}/D_{cav} cavities to be tested. A fast response, dynamic pressure sensor is located at the bottom of the cavity. Flow is left to right.

algorithm to compute the discrete Fourier transform (DFT). The Cooley-Tukey FFT algorithm is used. To compare the ability of the completely non-intrusive FSD technique to capture frequencies of interest, the acquired frequency measurements are compared to two semi-empirical formulas for predicting frequency modes inside compressible shear layers, namely the Rossiter formula and modified Rossiter formula. The lower subsonic, pure acoustic mode formula by Tam (Ref [153]) was briefly considered but the relatively high Mach numbers in this study did not yield favorable comparison.

In 1964, Rossiter empirically derived a frequency prediction model from wind tunnel experiments exposing rectangular cavities of varying length-to-depth ratios (L_{cav}/D_{cav}) to Mach numbers ranging from 0.4 to 1.2 [154]. Based on shadowgraphs of the cavity shear layer, it was

deduced that convecting vortices within the shear layer impinge on the downstream edge of the cavity to create acoustic disturbances that return upstream and initiate the shedding of new vortices. The empirical relation is shown in Eq. 4.8 as:

$$\frac{f_{cav}L_{cav}}{U_\infty} = \frac{(m_{cav} - \alpha)}{M_\infty + \frac{1}{k}} \tag{4.8}$$

where the left hand side of the equation is effectively the Strouhal number, composed of f_{cav} as the shedding frequency, L_{cav} as the cavity length, and U_∞ as the freestream velocity. The Strouhal number proportional to the difference between the integer mode number (m_{cav}) and empirical constant α, and inversely proportional to the summation of the freestream Mach number (M_∞) and the inverse of the convective speed ratio ($k = \frac{U_c}{U_\infty}$). A modification to Rossiter's formula for Mach numbers up to 3.0 was proposed by Heller et al. in 1970 [155], shown in Eq. 4.9.

$$\frac{f_{cav}L_{cav}}{U_\infty} = \frac{(m_{cav} - \alpha)}{M_\infty(1 + [\frac{\gamma-1}{2}]M_\infty^2)^{1/2} + \frac{1}{k}} \tag{4.9}$$

Results of the shear layer analysis are shown in Fig 4.7a-c for measurements taken at the center of the shear layer (white dot superimposed on the schlieren image of Fig 4.6). As cavity L/D increases, spectral modes become more pronounced. The modified Rossiter formula provided in Eq. 4.9 provides favorable correlations in all cases shown.

The versatility of the technique is furthermore demonstrated in Fig. 4.8a-d. Since the measurement is taken at the image plane, the focusing schlieren deflectometry technique can acquire measurements anywhere in the flow field. This includes measurements away from the wall unlike wall-bounded pressure transducers. Comparison of frequency modes at the floor of the cavity acquired by the Kistler pressure transducer versus the fiber optic fed Avalanche detector is presented in Fig. 4.8b. Both diagnostic techniques pick up a strong third mode, with a faint second mode present as well. Low frequency activity in the pressure sensor is due to the resonance frequency in the needle-nose housing.

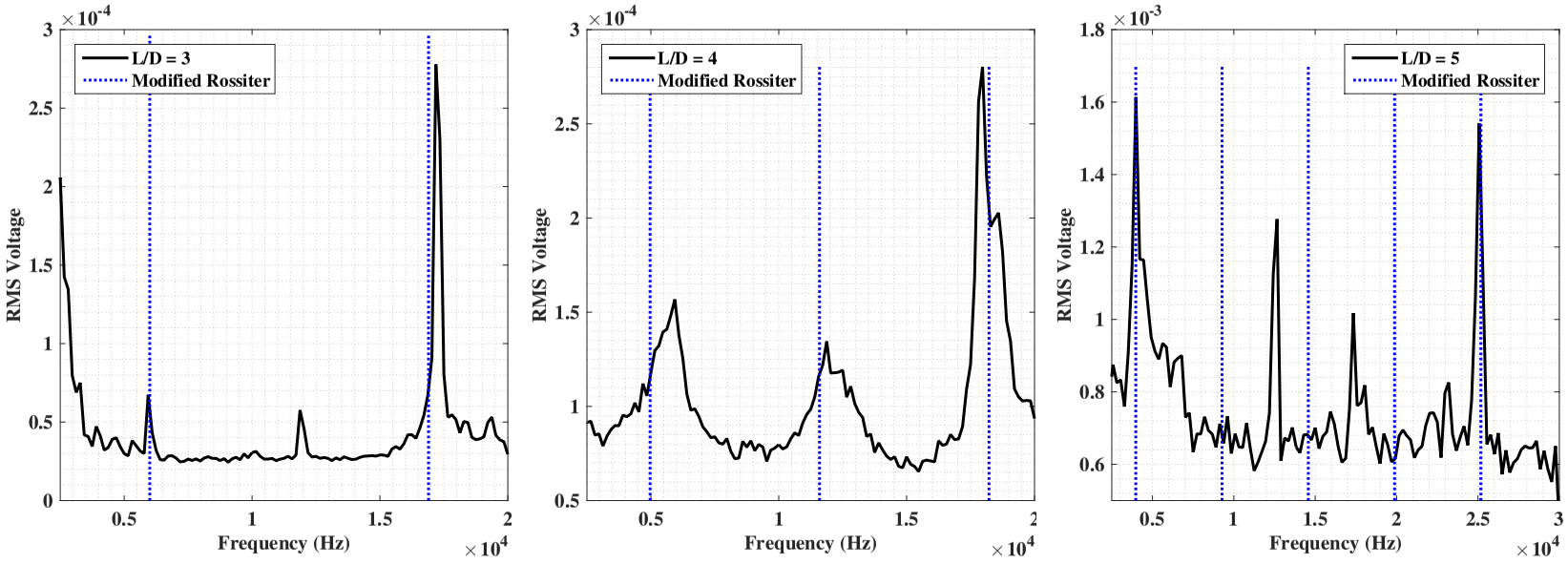

Figure 4.7: Spectral analysis of acoustic modes in supersonic shear layer cavities: (a) L/D = 3.0, (b) L/D = 4.0, and (c) L/D = 5.0. Blue lines represent the semi-empirical predictions of acoustic mode frequencies provided by the modified Rossiter formula (Eq. 4.9). All measurements taken at the center of the shear layer.

Measurements in the center of the shear layer for the L/D = 4.0 cavity configuration are presented in Fig. 4.7b. Measurements away from the center are shown in Fig. 4.8c-d, for the cavity trailing edge interaction and downstream boundary layer respectively. It is expected that the acoustic mode is largest at the cavity trailing edge impingement due to this being the source of the acoustic waves. This is clear in Fig. 4.8c, characterized by a high signal-to-noise acoustic signature, with the third acoustic mode is strongly represented.

The influence of the cavity shear layer to the downstream flow field is shown in Fig. 4.8d. Two cavity length scales removed from the trailing edge of the cavity, the measurement location still provides a clear representation of the third acoustic mode. Although the second acoustic mode is attenuated at this downstream location, the signal still presents a favorable signal-to-noise characteristics.

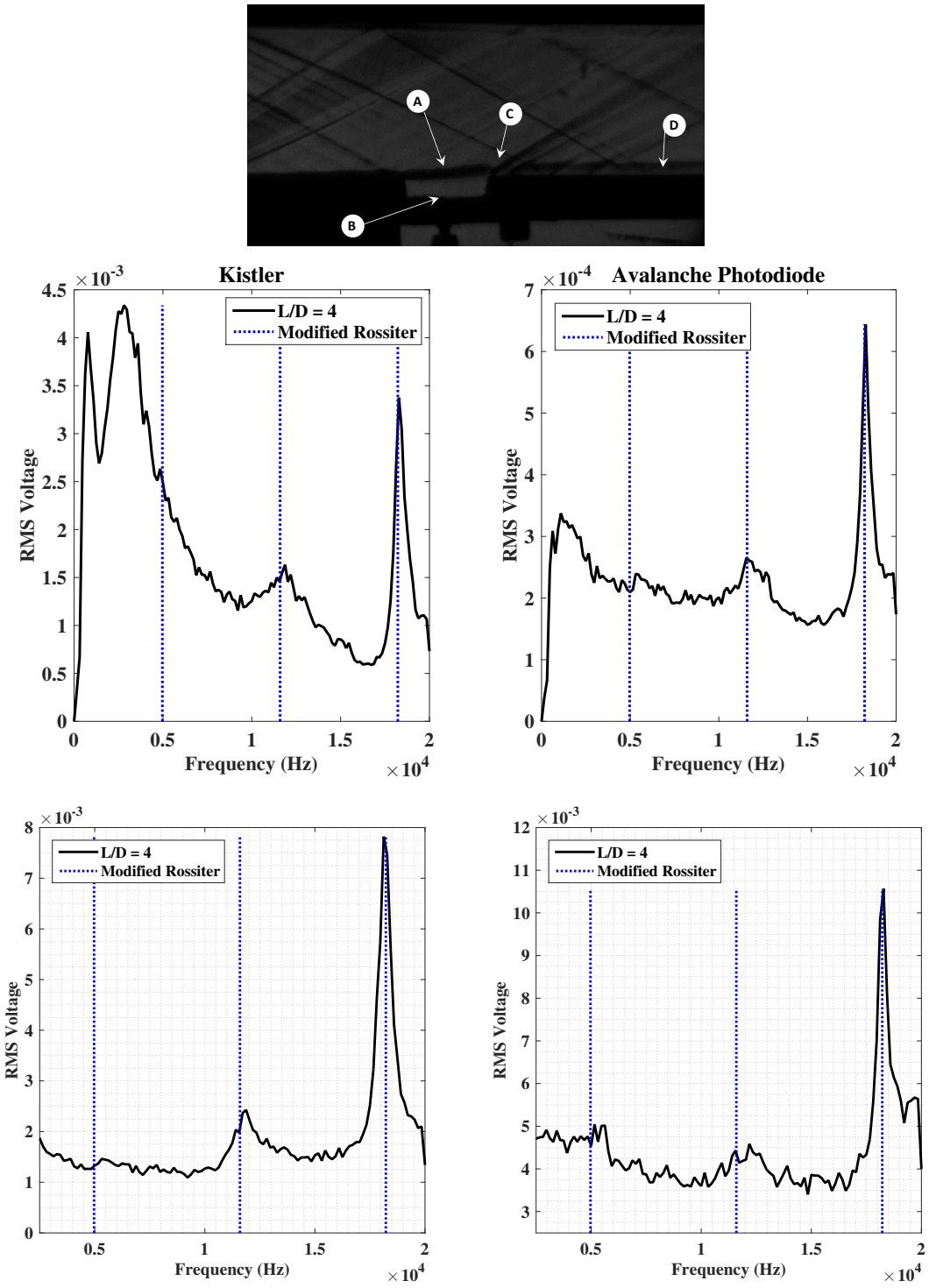

Figure 4.8: Analyzing the cavity shear layer flow environment: (a) Photodiode measurement locations, (b) Kistler pressure vs. Avalanche photodiode deflectometry comparison for cavity floor measurement, (c) deflectometry measurement for cavity trailing edge acoustics, and (d) deflectometry measurement in the downstream boundary layer.

4.2.2 Three-Dimensional Jet

The supersonic shear layer study discussed above was the first application of a single probe deflectometer in a two-dimensional flow feature. To experimentally evaluate the effective depth of sharp and unsharp focus of the FSD system, as well as the ability for the system to capture low magnitude, acoustically forced modes in the three-dimensional flow environment, 3mm (0.12") diameter axisymmetric Helium and Nitrogen jets emanating in ambient air are used. The jet configuration is shown in Fig. 4.9. A 1.2mm (3/64") orifice Parker solenoid valve (# U2812A) connected a Nitrogen or Helium supply to the jet hardware, consisting of a base cavity leading into a 300mm (12") long tube with a 3mm exit diameter. The WaveTek signal generator was used to supply a 100W Bogen Classic Series (C-100) acoustic amplifier with a user defined frequency, in turn allowing a 100W acoustic Sky TU-100 speaker/driver unit to produce the desired frequency noise level. This speaker unit was located at the bottom of the acoustic jet tube and allowing acoustic waves to be carried within the jet and out into the ambient surroundings. Typical jet diameter Reynolds number (Re_D) is approximately 2400.

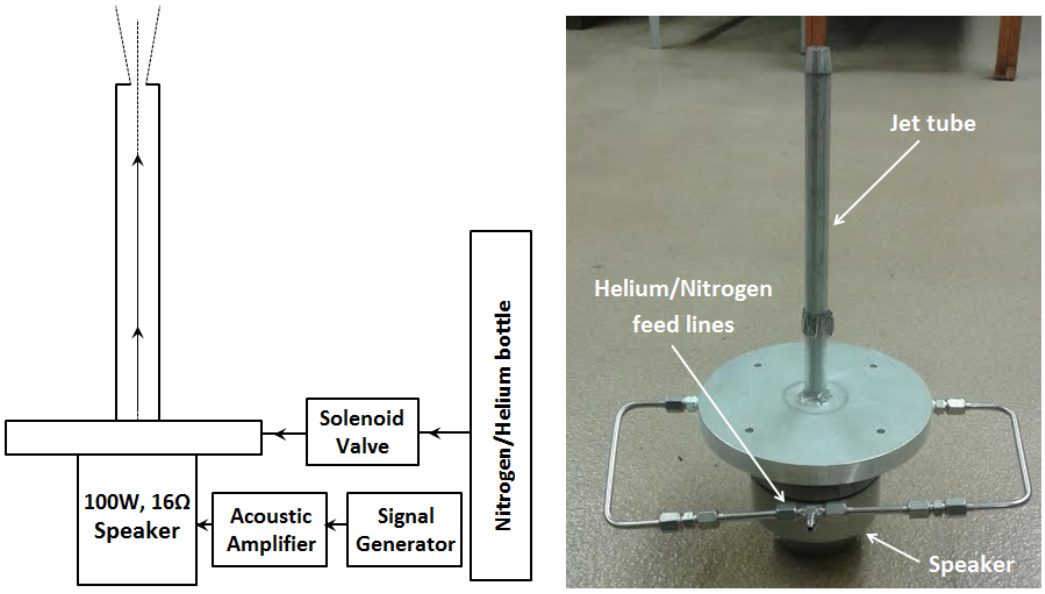

Figure 4.9: Acoustically forced three-dimensional jet configuration for use in verifying the Focusing Schlieren setup's depth of sharp focus and validating the Focusing Schlieren Deflectometry Velocimeter diagnostics configuration.

4.2.2.1 Visualizing the depth of sharp focus

Although the vast majority of focusing schlieren work performed in this thesis involves the deflectometry configuration (Fig. 3.29), a focusing schlieren flow visualization configuration is used to visualize the effect of depth of sharp focus selection (Fig. 3.31). The density gradient distribution sketched in Fig. 3.31 represents the jet flow field. Helium is chosen for visualization purposes due to the relatively large index of refraction spread between the ambient air and Helium, $\Delta n = 2.57x10^{-4}$ versus $\Delta n = 5.40x10^{-6}$ for an ambient air-Nitrogen combination. As can be reduced by Eq. 4.1, a larger n spread will result in larger angles of refraction (ϵ), and thus more defined flow features, important for the relatively insensitive CMOS camera chip used. Deflectometry studies will primarily use the Nitrogen jet to prove the sensitivity of the Avalanche photodiodes.

Figure **??** shows the visualization of the Helium jet with the camera placed at different locations along the optical axis. Calculations for the depth of sharp (DS) and depth of unsharp (DU) focus are offered in Chapter 3, and focusing schlieren system performance parameters are summarized in Table 3.3. A DS and DU of approximately 1.6mm (0.06") and 25mm (1.0") are derived. The jet diameter (D_J) is 3mm (0.12") at the outlet, and grows to approximately two diameters in width at a vertical location equal to three diameters from the outlet, resulting in a non-dimensionalized DS and DU of approximately $0.5D_J$ and $8.3D_J$ respectively. Given the three-dimensional geometry of the jet, the initial position of the camera is such that the image of the edge of the vertical jet tube is in focus (achieved by focusing on the threads of a small # 2-64 screw with major diameter of 2.1mm (0.08") or $.7D_J$. Some error in focal plane placement is expected using this method given that the diameter of the focusing device is larger than the total focusing bandwidth of the focusing schlieren system. Nonetheless, it provided a consistent means of determining focal plane.

Figure **??**a shows the jet in focus with the camera placed at the location corresponding to the focal plane. A distinct mixing layer is present that extends outward in the expected three-dimensional fashion. Figures **??**b-c document the reduced focus as the camera is moved along the optical axis away from plane of best focus. Distinct features are still visible in Fig. **??**b since

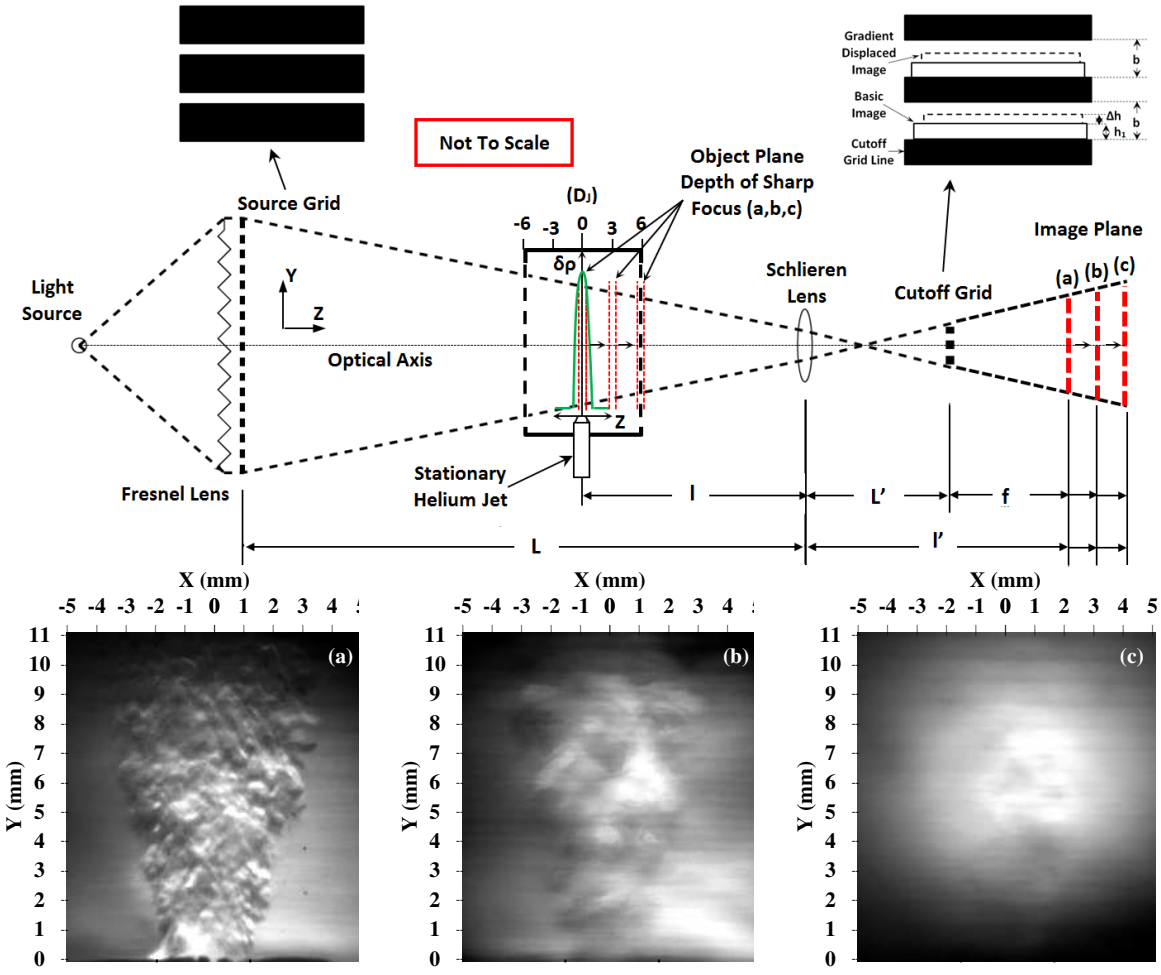

Figure 4.10: The Focusing Schlieren technique: selecting location of depth of sharp focus planes a, b, and c to visualize a stationary Helium jet emanating in ambient air.

the jet expands outwards away from the outlet. With the camera placed at $6D_J$ from the plane of optimal focus (Fig. **??**c), the Helium jet induced density gradient are nearly indiscernible. A similar setup is used to calibrate the capabilities of the deflectometry application described below, which uses sensitive photodetectors to measure light fluctuations in the image plane. Since the Avalanche photodetectors used in this study are highly sensitive to an even weak density gradients such as those in the plane of unsharp focus, a calibration study for quantitative deflectometry is performed with a Nitrogen jet.

4.2.2.2 Focusing schlieren deflectometry depth of sharp focus & sensitivity

To quantitatively analyze the sensitivity and depth of sharp focus of the Focusing Schlieren Deflectometry system, the 3mm (1/8") acoustically forced Nitrogen jet was used along with one photodiode measurements. The image plane and associated fiber optic tip are translated along the optical axis to evaluate depth of sharp focus. The fiber optic is located one jet diameter along the vertical axis from the jet opening.

Shown in Fig. 4.11a, the Nitrogen jet is acoustically forced at 800Hz after a baseline measurement is taken of an acoustically unforced jet. After an acoustically forced reading with the DS plane located at the center axis of the jet, the image plane is moved along the optical axis. A strong 800Hz signal is captured at the jet center-axis. Signal strength is reduced by nearly 50% as the depth of sharp focus plane is moved $1D_J$ from the center-axis, meaning it is displaced approximately $1/2D_J$ from the edge of the jet. Further reduction of the signal strength is seen as the fiber optic equipped image plane continues to move further from the jet center-axis focused image location. A radical reduction of 80% signal strength is observed as the sharp focus plane is moved $2D_J$ from the jet's center-axis. The readings are now fully taken in the depth of unsharp focus plane, and even though the magnitude of the 800Hz signal is reduced, it is still noticeable. Although the focusing schlieren technique allows for evaluation of the signal in narrow depths of focus, the depth of unsharp focus can still play a considerable role and must be accounted for when designing and implementing a focusing schlieren system.

Figure 4.11b shows the frequency response to a case where no Nitrogen is introduced but the ambient air inside the jet tube is still acoustically forced, resulting in a material interface convection propagating out into the freestream. Frequency response is strong for the focused case, and the strength of the signal is reduced once more for increases in optical axis movement. The system show excellent sensitivity to an event that is characterized by very small density gradients.

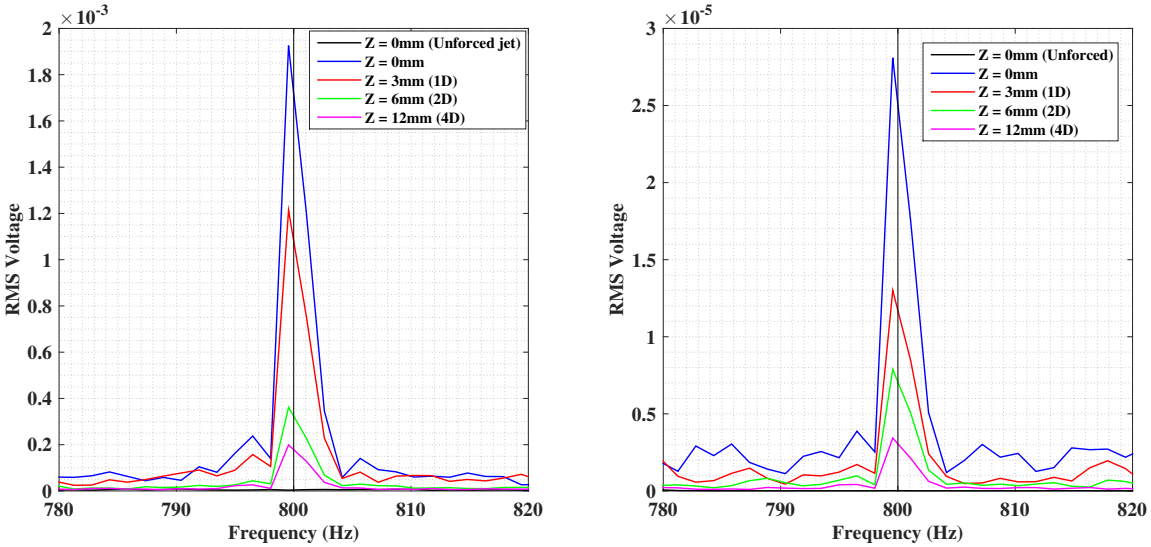

Figure 4.11: Analysis of the Focusing Schlieren Deflectometry system's sensitivity using the 3mm (1/8") Nitrogen jet configuration: (a) Acoustically forced jet at 800Hz, and (b) acoustic modes only at 800Hz (no Nitrogen jet). Vertical black line indicates the acoustically forced frequency.

4.2.3 Focusing Schlieren Deflectometer Velocimetry

The present study aims at utilizing the focusing schlieren deflectometry technique to evaluate shock train oscillation velocities within the isolator freestream region by introducing two fiber optic based photodiode measurements spaced a known distance apart. This velocimetery configuration will allow for the measurement of oscillatory velocity component of the shock train leading edge at various planes of interest along the optical axis by using the depth of sharp focus ability provided by the focusing schlieren technique. To calibrate this configuration, a 12.5mm (1/2") diameter Nitrogen jet was used to measure flow velocities at different three-dimensional coordinate locations as described below.

A sketch of the Nitrogen jet is provided in Fig. 4.12 in the form of a 2-dimensional cross-section. A mixing shear layer (gray outline) originates from the lip of the jet and is assumed to coalesce at approximately 5 jet diameters (D_J) above the jet exit plane. Although this characteristic is expected to slightly depend on jet Reynolds number, it is considered an adequate approximation here. The previous 3mm diameter jet is swapped for a 12.5mm diameter jet to

evaluate the ability of the focusing schlieren deflectometry system and its associated depth of sharp focus to resolve the differences between mixing (gray areas) and non-mixing (white areas) flow velocities.

As annotated, the small dashed box outline represents the depth of sharp focus of the system ($DS = 1.6mm$) drawn to scale with respect to the jet diameter reference length. The depth of unsharp focus is also shown ($DU = 25.25mm$). Convection velocities of refractive entities inside the core and the mixing layer are expected to be noticeably different. By changing the three-dimensional measurement coordinate, this approach was used to study the ability of the two-point deflectometry velocimeter to discern between the core-flow velocity and that of the mixing layer. A cross-correlation (sliding-dot product) routine was used to evaluate the signals from the two Avalanche photodetectors (APD) according to Eq. 4.10:

$$(f * g)(\tau_{FSD}) = \int f(t)g(t + \tau_{FSD})dt \tag{4.10}$$

where f and g are the first and second (time-lagged) photodetector signals respectively, and τ_{FSD} is the characteristic time-lag between the two. The cross-correlation algorithm evaluates the temporal shift of g needed to maximize the product of the two signals, resulting in a cross-correlation coefficient magnitude that is a function of how similar the two functions are at a given time-shift. If this cross-correlation coefficient is maximum, the signal at that specific point in time is assumed to represent the same refractive entity that has traveled across the deflectometry range. To improve the accuracy of the technique, the time shift Δt shown in Eq. 4.10 must be chosen objectively based on the estimated velocity of the flow (and convective velocity of the refractive structures) of interest.

To compare the deflectometry measurement to a more traditional means of acquiring flow velocity, a pitot-probe study was performed both inside the jet-core and the mixing region. Using the subsonic pitot Mach number equation (Ref 3.23) in combination with the ambient air temperature, calculated velocities for various locations are shown in the second column in Table 4.1. Significant velocity changes can be seen as the probe is moved away from the core and into the

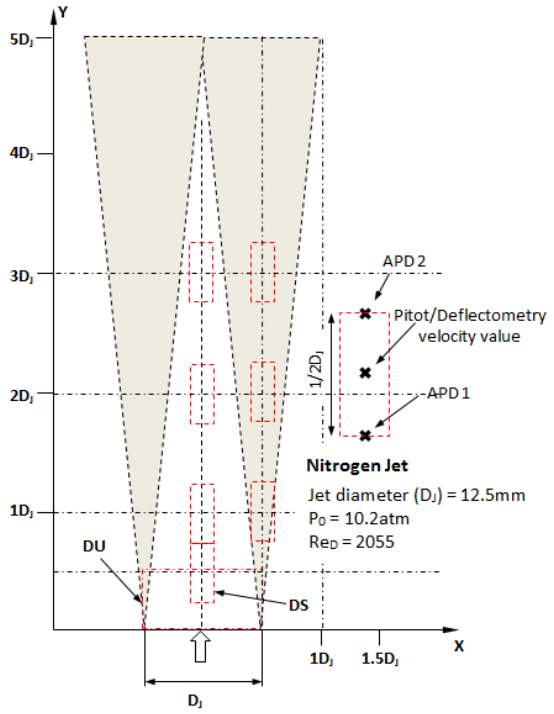

Figure 4.12: 12.5mm diameter Nitrogen jet used for two-point FSD velocimetry calibration.

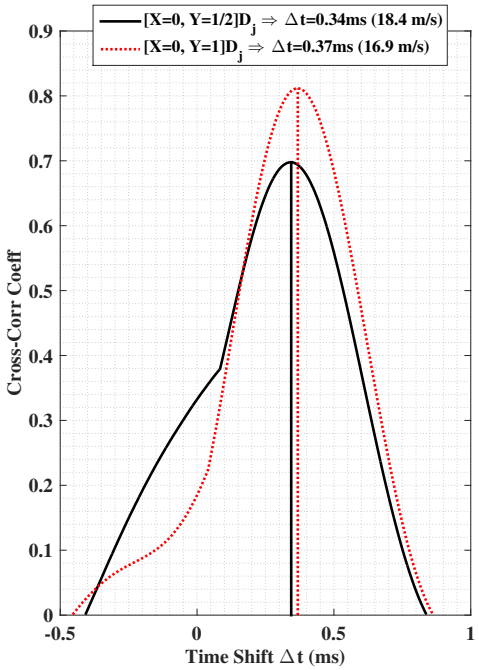

Figure 4.13: Nitrogen jet 2-point cross correlation raw data: $[X,Y]D_j = [0,1/2]D_j$ and $[0,1]D_j$.

mixing layer. Deflectometry velocity measurements were subsequently taken at similar locations, with the two fibers separated by half of a jet diameter. The jet was acoustically forced at 1000Hz and subsequent high- and low-pass filters were set at 940Hz and 1060Hz respectively. A 75% cutoff and sample rate of 500kHz are used. All of the deflectometry studies in this study employed 20dB of pre-amp and 10db of post-amp gain. Sample cross-correlation data for two such positions along the centerline of the jet are shown in Fig 4.13.

Sample FSD velocity calculations are shown in Fig. 4.13 for two positions along the jet center-axis. Since the velocity calculation is performed between two points rather than at one single point (as in the in the case of the pitot jet), the vertical location of the velocity measurement is considered to be the mid-point between the two fiber locations. In calculating the velocity of $[X,Y]D_j = [0,1/2]$, the fibers are placed at $1/4D_j and 3/4D_j$ along the Y-axis. Similarly for the $[X,Y]D_j = [0,1]$ location the fibers are placed at $3/4D_j and 5/4D_j$ along the Y-axis. With the known displacement between the fibers $(1/2D_j)$, the time lag is used to estimate the velocity.

$[X,Y]D_J$	V_P	V_V	$[X,Y]D_J$	V_P	V_V
$[0,1/2]$	18.1 ± 0.36	18.4 ± 0.18	$[1/2,2]$	7.6 ± 0.15	5.2 ± 0.05
$[0,1]$	17.7 ± 0.35	16.9 ± 0.17	$[1/2,3]$	6.4 ± 0.12	1.3 ± 0.01
$[0,2]$	15.7 ± 0.31	13.5 ± 0.13	$[1,1/2]$	0.2 ± 0.01	3.1 ± 0.01
$[0,3]$	12.7 ± 0.25	9.1 ± 0.09	$[1,1]$	1.5 ± 0.05	2.2 ± 0.01
$[1/2,1/2]$	5.5 ± 0.11	2.9 ± 0.02	$[1,2]$	3.2 ± 0.06	2.1 ± 0.02
$[1/2,1]$	9.9 ± 0.19	7.8 ± 0.07	$[1,3]$	3.9 ± 0.07	3.2 ± 0.03

Table 4.1: Nitrogen jet calibration velocity values: pitot probe & FSD velocimeter

Overall, Fig. 4.13 shows a well behaved signal, and results shown in the table 4.1 show promising agreement with the pitot-probe data in the core flow within two jet diameters of the jet exit plane. As shown in the sketch, the depth of sharp focus is expected to be capable of discerning core from mixing layer if the measurement is performed along the center axis close to the jet exit plane. It is important to remember however that the depth of unsharp focus is quiet large compared to the entire jet region, and is expected to contribute to the overall density gradient the photodetector will observe. For a uniform flow, the magnitude of light fluctuation will be larger at the plane of focus compared to within the plane of unsharp focus. When a non-uniform flowfield, containing a shear or mixing layer exists, the contributions in the depth of unsharp focus region may still have a considerable effect if the magnitude of density gradient in the focal plane is expected to be less (as is the case in the core of the jet). Since the shear/mixing layer is expected to have a larger diffraction effect, the shear layer features captured within the plane of unsharp focus can affect the FSDV velocity measurement. In comparison, the pitot probe is a point measurement technique and will not suffer from the integrated signals of density gradient across a finite width.

This important characteristic of the FSDV system is apparent in the measurement of jet velocity just outside of the jet itself. The measurements with the pitot probe at [X,Y]=[1,1/2]D_J are outside of the expected jet control volume. The low velocity measurement is most likely due to some outer-layer component of the mixing region impacting the pitot probe. The FSDV measurement at the same location is significantly larger, due to fact that the depth of unsharp focus will acquire density gradient signals in the core and mixing region of the jet, albeit at attenuated strengths. This is still enough to produce a sensible velocity component from the cross-correlation

process. This inherent characteristic of the FSDV technique must be considered when performing and analyzing the cross-correlation results.

4.3 Validation and Verification of Numerical Simulations

Before the numerical results can be properly interpreted, a thorough verification and validation study should be performed to ensure that the numerical work adequately represents the physical flow field. This verification process was performed for the aspect ratio 3.0 configuration in two phases:

- A mesh dependency study is composed of a grid resolution study followed by a boundary layer Y^+ sensitivity study utilizing a hybrid grid. Convergence rates and residual magnitudes of the governing equations are compared.
- Validation of key flow parameters against experimental measurements including the longitudinal axis, lower-wall static wall pressure measurements as well as the inlet and outlet boundary layer pitot-probe profiles.

Although key flow parameters were compared to experimental data throughout the mesh dependency study to ensure proper simulation, comparisons are presented separate for the most favorable grid resolution and boundary layer fidelity combination to avoid clutter.

4.3.1 Mesh Sensitivity Study

Four levels of grid refinement were examined. Shown in Fig. 4.14a, the base cell size is limited to 20mm, showing the 50.8mm duct height occupied by two core cells and resulting in a total of 74,727 cells in the three-dimensional volume. Fig. 4.14b has the base size reduced to 10mm, increasing the cell count to 5 along the duct's vertical profile and to 210,903 total cells. Further refining the mesh results in a base size of 5mm, with 261,768 total cells over the entire volume (Fig. 4.14c). Numerical simulations that support the partially started mode can be equipped with a hybrid mesh construction, increasing the resolution of the cell count in the region where the shock

train is expected to be located (in steady-state computation with constant backpressure). Shown in Fig. 4.14d, this type of mesh hosts a total of 219,135 total cells. Additionally, an adaptive meshing technique based on the magnitude of the density gradient near the shock front can be used to further refine the mesh in critical regions to improve the scene's resolution and resolve smaller shock structures while keeping the resolution of the mesh at a computationally efficient magnitude.

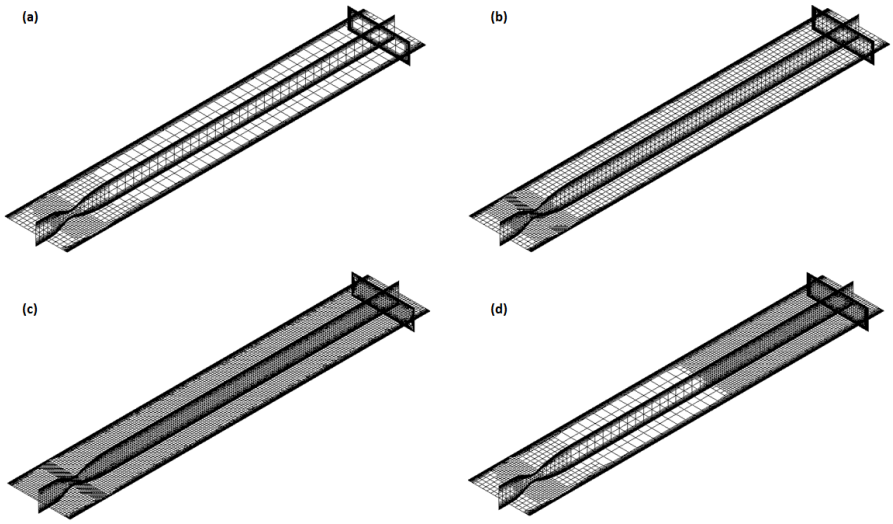

Figure 4.14: Mesh resolution levels considered in the mesh dependency study: (a) 20mm base size (74,727 total cells), (b) 10mm base size (210,903 total cells), (c) 5mm base size (261,768 total cells), and (d) hybrid 20mm-5mm base size (219,135 total cells)

Fully started mode boundary conditions are applied as described in Chapter 3, together with the Spalart-Allmaras turbulence model and a y^+ value of 1.0 to produce the convergence characteristics shown in Fig. 4.15. The one equation Spalart-Allmaras model is represented by the modified diffusivity residual. The proper y^+ value of 1.0 provides a stable convergence for all mesh resolution levels considered. Near identical convergence results are achieved by the two-equation $k-\omega$ model.

The importance of selecting the correct Y^+ value for computational purposes is discussed in Chapter 3. The residual convergence characteristics for the boundary layer refinement and smallest cell size discussed in Fig. 3.37 is shown in Fig. 4.16. It is shown that for values of $Y^+ \leq 1.0$,

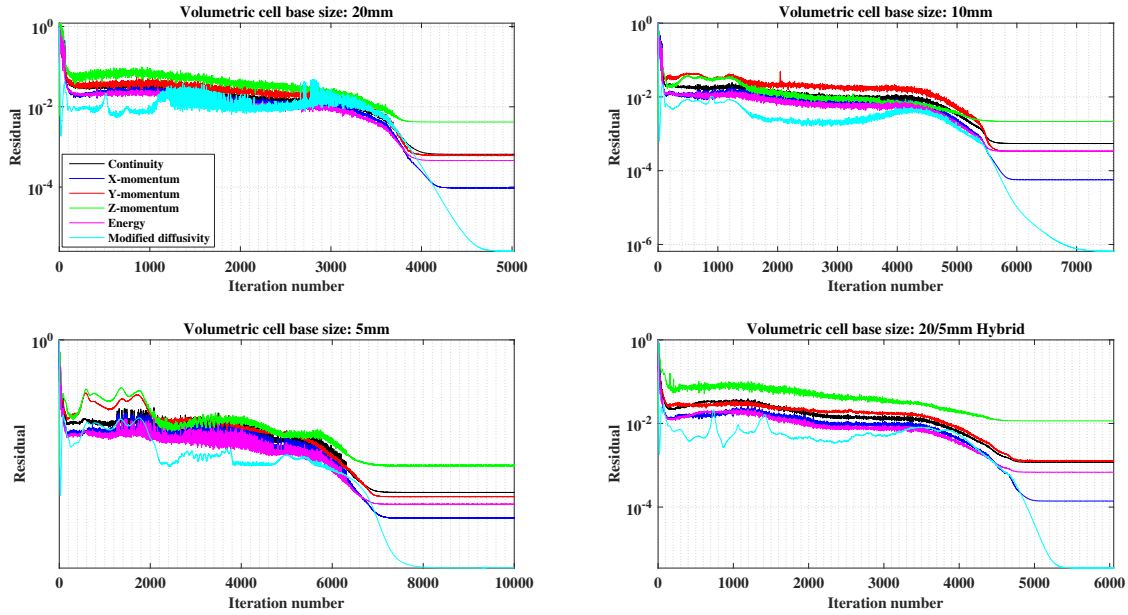

Figure 4.15: Residual convergence of the various mesh resolution levels considered.

satisfactory convergence is reached since the viscous sublayer is resolved. As expected, larger Y^+ values are computationally more efficient due to the coarser grid size near the wall, resulting in faster convergence. Reducing the Y^+ value below 1.0 does not have a significant effect on the convergence quality of the computational results and therefore $Y^+ = 1.0$ is maintained throughout all calculations performed.

Comparison to the experimental data is first performed based on the lower wall normalized static pressure distribution along the longitudinal centerline, as shown in Fig. 4.17. These comparisons are made for the fully started mode of operation. Experimental data is derived from the results shown in Fig. 3.7a, where the static wall pressure during the fully started portion of the operating regime is used. The normalized static pressure distribution in the duct for the fully started case is shown at the top of Fig. 4.17 utilizing a min-max threshold to clip higher pressure values from the nozzle expansion region. As can be seen in the plot, all four mesh cases approximate the static pressure distribution favorably. The hybrid mesh, the primary candidate in the partially unstarted mode of operation, provides improved correlation across the entire longitudinal

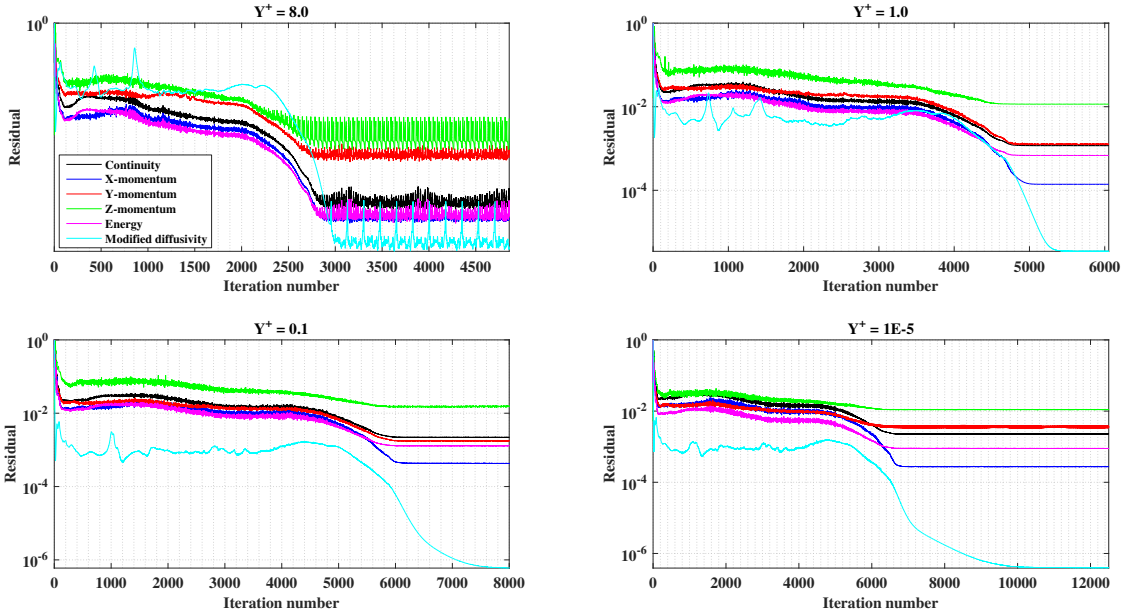

Figure 4.16: Residual convergence of the various Y^+ values considered.

dimension of the duct.

4.3.2 Boundary Layer Verification

The ability of the numerical approach to resolve the boundary layer profile is investigated by comparing the results of the centerline pitot probe surveys (Fig. 3.11) to the numerical solutions. To look at the effect of smallest cell size, values of $Y^+ = 1.0$, 0.01, and $1E-5$ are considered in Fig. 4.18. The width of the experimental Mach measurements in Fig. 4.18 represents the approximate error bandwidth. The Mach number contour plot at the top of Fig. 4.18 represents the Mach number distribution in the fully started mode, with the locations of the boundary layer Mach number measurements annotated by the dashed black line. Figure 4.18 shows that the boundary layer profiles are resolved accurately for $Y^+ \leq 1.0$.

Experimental measurements obtained by the pitot-rake discussed in Chapter 3 are also compared to the simulation results. One of the main motivations behind computing the fully started mode of operation is to obtain more accurate side-wall boundary layer measurements in

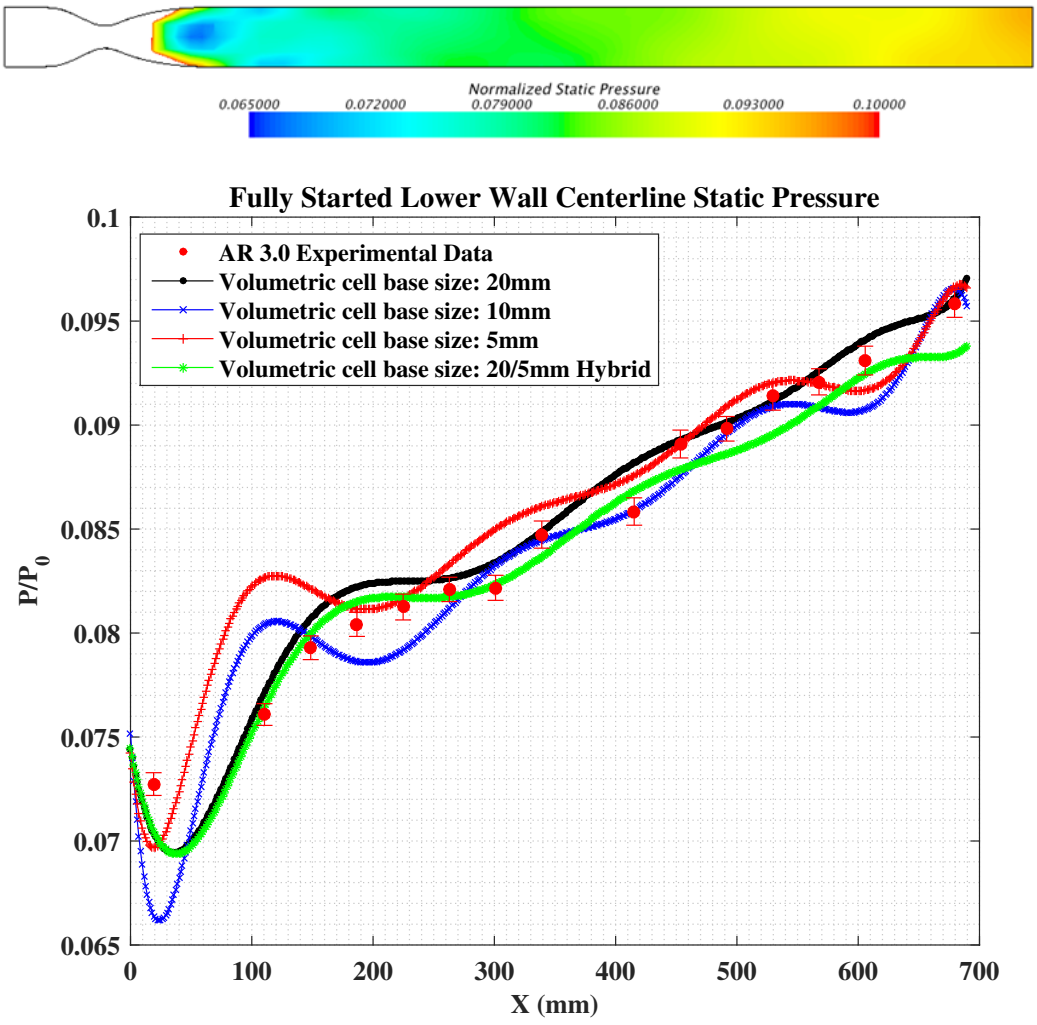

Figure 4.17: Lower wall longitudinal axis normalized pressure distribution: experiment vs simulation for various mesh resolution.

the upstream region of the duct. The coarse measurement capabilities and geometric constraints of the supersonic pitot rake shown in Chapter 3 do not allow the upstream boundary layer to be adequately resolved experimentally. The numerical results will therefore be used in the isolator length relation modification work discussed in Chapter 6.

Comparison of numerical and experimental data for the aspect ratio 3.0 case is shown for both upstream (X=90mm) and downstream (X=600mm) stations in Fig. 4.19 for the derivation of Mach number obtained at the centerline (Y = 0mm). Experimental data and subsequent Mach number derivations for both stations are shown in Fig. 3.16a-b. The coarseness of the experimental

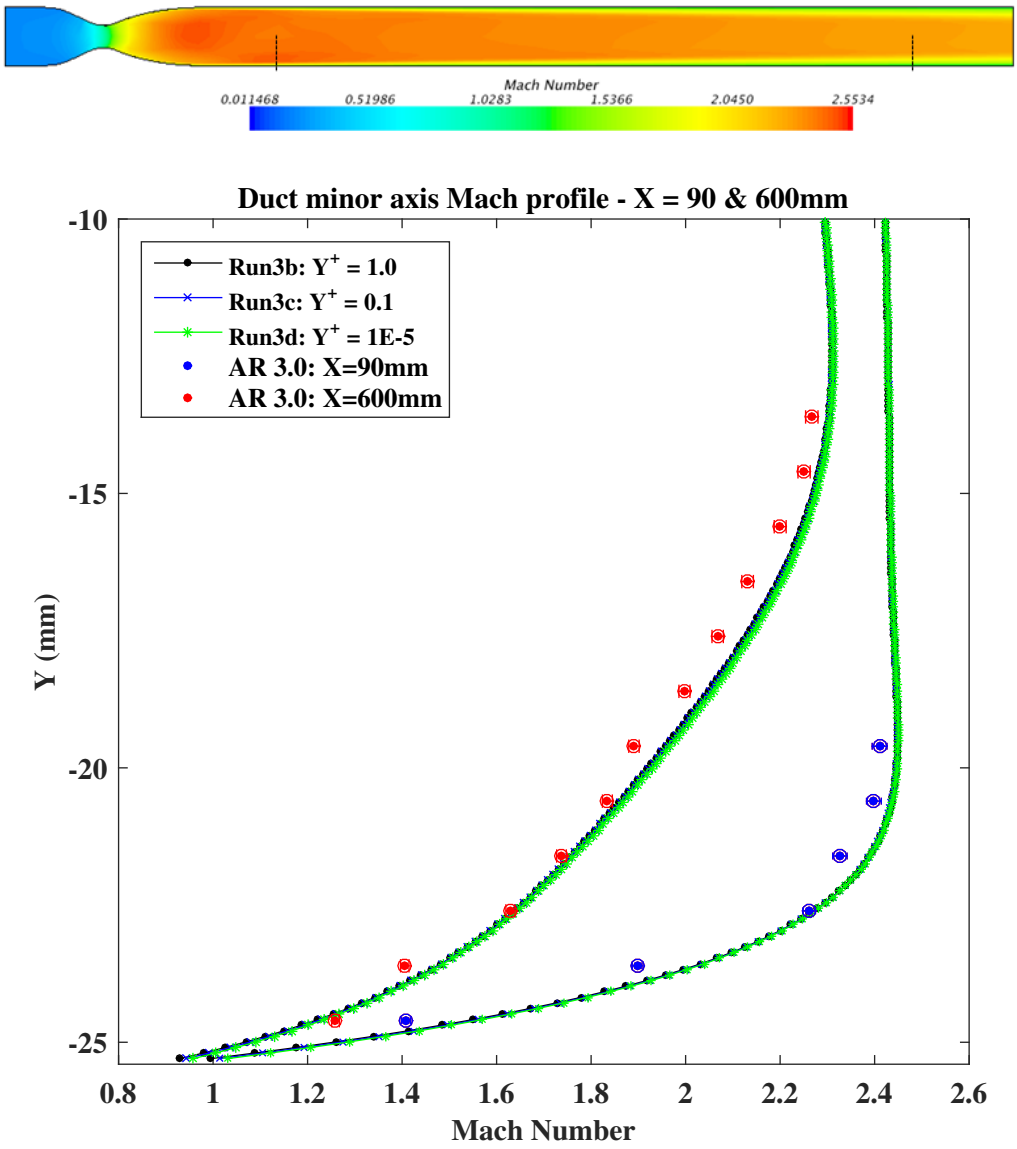

Figure 4.18: Duct minor axis Mach profile at mid-point for both upstream and downstream stations: experiment vs simulation for various Y^+ values. Width of experimental data point represents the error bandwidth.

measurements are clearly shown in Fig. 4.19, with the closest measurement located 3mm from the side wall. Experimental and numerical results show good overall correlation. The resolution of the numerical results is used to calculate more accurate θ_2 values in the modification of the isolator length relation presented in Chapter 6.

Correlation results are quantitatively expressed in Table 4.2 in the form of a Root Mean

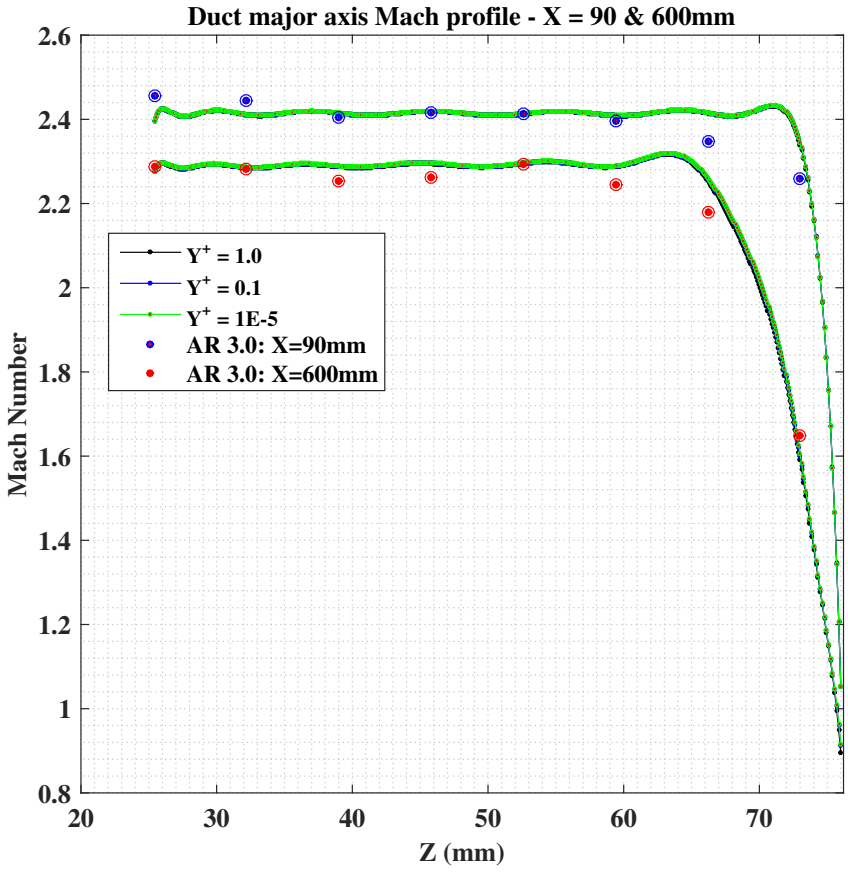

Figure 4.19: Duct major axis Mach profile at mid-point for both upstream and downstream stations: experiment vs simulation for various Y^+ values. Width of experimental data point represents the error bandwidth.

Square Error (RMSE) analysis (Eq. 4.11) and the evaluation of the average and maximum percent difference between the experimental and computational results.

$$RMSE = \sqrt{\frac{\sum_{i=1}^{n} (y_{exp} - y_{sim})^2}{n}} \tag{4.11}$$

The longitudinal static pressure data comparison (Fig. 4.17) shows good agreement for all cell base size considered. The hybrid mesh that is chosen for the simulations predicts the centerline static pressure behavior to within a maximum deviation of 3.15%.

The computational Mach boundary layer profile analysis shows that the performance for $Y^+ = 1.0$, $Y^+ = 0.1$, and $Y^+ = 1E-5$ is nearly identical for both minor- and major-axis

Curve	RMSE	$[\%Diff]_{avg}$	$[\%Diff]_{max}$
20mm cell (Fig. 4.17)	0.0012 (P/P_0)	1.21	3.28
10mm cell (Fig. 4.17)	0.0023 (P/P_0)	1.97	8.72
5mm cell (Fig. 4.17)	0.0020 (P/P_0)	2.05	8.64
Hybrid cell (Fig. 4.17)	0.0011 (P/P_0)	1.14	3.15
$Y^+ = 1.0$ (X=90mm) (Fig. 4.18)	0.2916 (Mach)	10.46	25.73
$Y^+ = 0.1$ (X=90mm) (Fig. 4.18)	0.2934 (Mach)	10.22	25.45
$Y^+ = 1E-5$(X=90mm) (Fig. 4.18)	0.2951 (Mach)	10.23	25.32
$Y^+ = 1.0$ (X=600mm) (Fig. 4.18)	0.1355 (Mach)	7.29	17.42
$Y^+ = 0.1$ (X=600mm) (Fig. 4.18)	0.1382 (Mach)	7.13	17.40
$Y^+ = 1E-5$ (X=600mm) (Fig. 4.18)	0.1423 (Mach)	7.11	17.22
$Y^+ = 1.0$ (X=90mm) (Fig. 4.19)	0.2922 (Mach)	9.51	27.97
$Y^+ = 0.1$ (X=900mm) (Fig. 4.19)	0.2914 (Mach)	9.01	27.91
$Y^+ = 1E-5$ (X=900mm) (Fig. 4.19)	0.2909 (Mach)	9.00	27.89
$Y^+ = 1.0$ (X=600mm) (Fig. 4.19)	0.1569 (Mach)	6.98	10.64
$Y^+ = 0.1$ (X=600mm) (Fig. 4.19)	0.1566 (Mach)	6.92	10.62
$Y^+ = 1E-5$ (X=600mm) (Fig. 4.19)	0.1563 (Mach)	6.91	10.62

Table 4.2: Validation of the numerical simulations against experimental data: correlation quality

boundary layers, prompting the use of the $Y^+ = 1.0$ boundary layer for computational efficiency. It is furthermore observed that the downstream boundary layer is more accurately resolved, given the larger number of experimental measurements in the thicker boundary layer. The average experimental value is predicted to within 5% in the downstream minor- and major-axis boundary layer. Nevertheless, the experimental measurements in the upstream region shows a fair correlation, with average Mach profiles predicted to within 10%.

4.3.3 Major and Minor Axis Boundary Layer Profile

The coarseness of the experimental boundary layer profiles resolved with the pitot probe and particularly the pitot rake is shown in Figs. 4.18-4.19. Confidence in the numerical approach established through the verification and validation work presented above allows for the simulations to be used higher resolution calculations of major and minor axis boundary layer parameters such as δ, $\delta*$, and θ. All calculations presented below are performed with the $Y^+ = 1.0$ simulation results.

Results for the aspect ratio 3.0 configuration are shown Fig. 4.20 and Table 4.3. The courseness of the experimental measurement along the duct major axis is highlighted by the su-

perimposition of the rake measurements highlighted by the white dots. Lateral plane contours of Mach number are shown for X=90mm and X=600mm locations. The location of the 1.6mm (1/16") inner diameter major axis rake probes and the 0.8mm (1/32") inner diameter minor axis pitot probe positions are drawn to scale. Data from the simulations is acquired at 500 distinct points along the half minor and major axis as indicated by the dashed black lines. Boundary layer profile resolution at the upstream plane is particularly important, as major axis θ_2 is used alongside minor axis θ in Chapter 6 to compute a $\theta' = \sqrt{\theta_1^2 + \theta_2^2}$ for use in the modification of existing shock train length relations as a function of rectangular isolator parameters.

Calculations of $\delta*$ and θ shown in Table 4.3 indicate that the momentum thickness (Eq. 3.8) of the major axis boundary layer is lower than the minor axis boundary layer, also referred to the nozzle bounded boundary layer. This difference is particularly noticeable in the downstream plane, where θ_2 is 42% less than θ_1. Conditions at the upstream station are more uniform, with θ_2 only being 8% less than θ_1. Likewise, the boundary layer shape factor (Eq. 3.9) is comparable at the upstream plane, but the major axis shape factor is 16% larger than the minor axis shape factor at the downstream plane. Larger H factors indicate larger adverse pressure gradients and boundary layers more susceptible to separation. It is thus suspected that the major axis boundary layer will separate ahead of the minor axis boundary layer in the downstream region, an observation that is revisited in the analysis of the three-dimensional shock train front in Chapter 5.

Results for the experimental aspect ratio 6.0 configuration are shown Fig. **??** and Table **??**. Similar observations to the aspect ratio 3.0 case are made. The experimental measurement of the inlet region boundary layer (X=90mm), which is on the order of 3mm thick, is not expected to yield an accurate derivation of momentum thickness due to the measurement coarseness. As with the aspect ratio 3.0 case, the major axis boundary layer is more susceptible to separation compared to the nozzle bounded boundary layer, according to the boundary layer shape factor. The inlet and outlet major axis shape factor is 10% and 5% larger than the respective minor axis shape factor. This effect is noticeable in the discussion of shock train formation in Chapter 5, where major-axis boundary layer separation events precede the minor axis boundary layer separation.

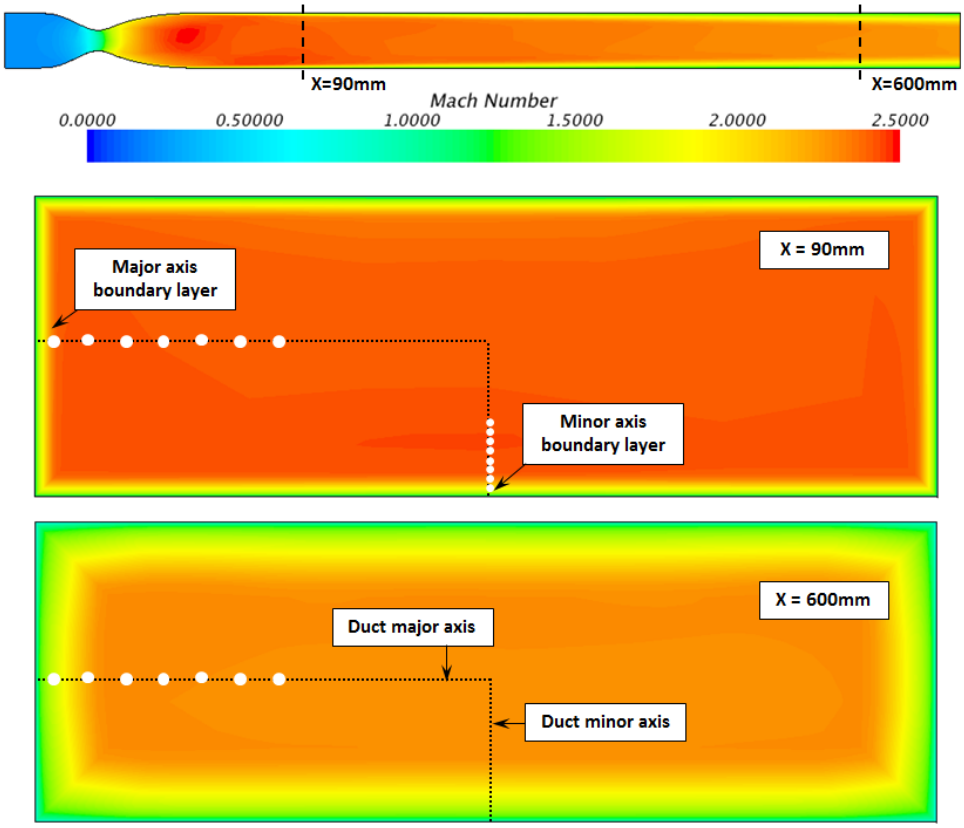

Figure 4.20: Aspect ratio 3.0 lateral plane contours of Mach number.

	$Inlet(X = 90mm)$		$Outlet(X = 600mm)$	
	Minor axis	Major axis	Minor axis	Major axis
$\delta(experiment)$	4.17	3.0	9.90	10.0
$\delta^*(experiment)$	1.01	0.98	3.38	3.16
$\theta(experiment)$	0.28	0.24	1.01	0.96
$\delta(CFD)$	3.45	3.35	10.52	10.50
$\delta^*(CFD)$	0.99	0.97	4.1	2.84
$\theta(CFD)$	0.25	0.23	1.31	0.76
$H(CFD)$	3.96	4.2	3.13	3.73

Table 4.3: Aspect ratio 3.0 inlet and outlet boundary layer parameters: experiment compared to computation (units of mm).

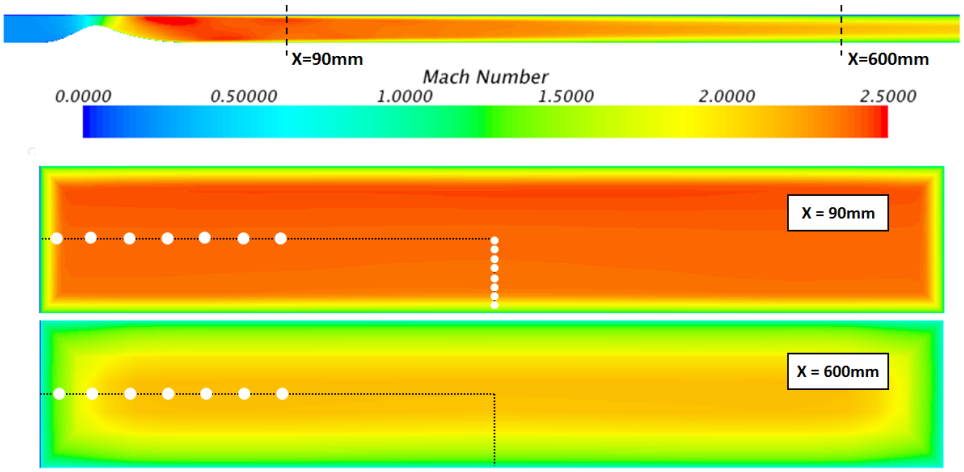

Figure 4.21: Aspect ratio 6.0 lateral plane contours of Mach number.

	$Inlet(X = 90mm)$		$Outlet(X = 600mm)$	
	Minor axis	Major axis	Minor axis	Major axis
$\delta(experiment)$	3.89	3.0	9.71	10.0
$\delta^*(experiment)$	0.55	0.51	2.34	2.47
$\theta(experiment)$	0.27	0.17	1.11	1.15
$\delta(CFD)$	2.97	3.50	9.32	11.12
$\delta^*(CFD)$	0.99	0.98	2.69	3.29
$\theta(CFD)$	0.27	0.17	0.77	0.91
$H(CFD)$	3.66	5.71	3.46	3.61

Table 4.4: Aspect ratio 6.0 inlet and outlet boundary layer parameters: experimental compared to computation (units of mm).

Chapter 5: Analysis of the Shock Train/Boundary-Layer Interaction Front

This chapter focuses on the analysis of the shock train leading edge front interacting with the boundary layer. Chapter 6 documents the study of the flow physics across the entirety of the isolator duct. In particular, the focus in this chapter is on the effects of flow three-dimensionality on the formation of the shock train front and associated boundary layer separation induced pressure rise.

To form an initial qualitative understanding of the shock train formation, the structure is simultaneously visualized from two different perspectives for the first time to reveal the extent of the three-dimensionality in the rectangular flow field. A surface oil-flow visualization study is presented to shed light on the symmetry around the duct centerline. The application of quantitative synthetic schlieren confirms the observations made through the multiplane shadowgraph technique by resolving the density gradient magnitude in various regions of the initial shock train front. Complementary quantitative lower wall fast response dynamic pressure surveys are subsequently carried out to analyze the flow separation time-scales across the duct-major axis. High temporal bandwidth, narrow depth-of-focus point measurements of shock train leading edge oscillatory frequency and velocity component are obtained using the Focusing Schlieren Deflectometry Velocimeter to compare the flow behavior in the center- and side-wall flow regions. Lastly, secondary steady state Computational Fluid Dynamics studies are performed to compare to the experimental observations and offer additional insight into the three-dimensional flow field.

5.1 Visualization of Corner Flow Separation

Multiplane shadowgraph images, obtained through the experimental apparatus described in Fig. 3.20, are analyzed and observations regarding corner flow separation and flow three-dimensionality are made. Two shadowgraphs are presented for each aspect ratio. The apparent strength of the shock structures present (i.e. the contrast and thickness with which the structures 'appear' in the image) depends on both the magnitude of the disturbance and the effective integration length across which the refraction of light occurs. First, observations are made in the traditional sense in that each plane (step 1 & 2) is analyzed with the line-of-sight property (disturbances integrated along the entire optical axis) in mind. Subsequently, observations from both planes are combined to draw conclusions about the three-dimensionality of the flow field (step 3).

5.1.1 Aspect Ratio 3.0 Multiplane Shadowgraph

Observations related to Fig. 5.1a are made in-depth and in a step-wise fashion to accurately describe the hybrid oblique/normal shock front. Similar observations can be made in Fig. 5.1b. Figure 5.1b is used to describe the wave angle behavior after the detailed description of the shock train front in Fig. 5.1a.

5.1.1.1 Shock feature discussion in Fig. 5.1a

Step 1 - XY-Plane Analysis: Two separate multiplane shadowgraph frames are shown for the AR 3.0 case in Fig. 5.1. Analyzing the XY-plane of Fig. 5.1a, initial observations regarding the shock structure can be made. A right running oblique shock wave (1u) originates from the upper wall boundary layer separation, as does a left running oblique shock wave (1l) from the lower wall boundary layer separation. The interaction with the upper boundary layer at X=540mm is clearly visible, with the lower wall interaction likewise extending to approximately X=540mm with the detail obstructed by the lower wall boundary layer.

There are two left running shock waves originating from the lower wall boundary layer sep-

aration, corresponding to the corner flow separation in the starboard and port side lower corners of the isolator respectively. Corner flow separation occurs more symmetrically in the upper wall for this specific instance, but symmetry is a variable depended on the boundary layer and flow parameters at a specific instant. The left and right running waves intersect near the longitudinal centerline (3) at X=580mm, and again this intersection appears relatively wide since we have two pairs of waves (originating from the lower and upper starboard and port side corners) intersecting along the Z-axis. The structures coalesce into refracted shocks that interact with the raised boundary layer at X=596mm for the upper (4u) and X=593mm for the lower (4l) structure. Interaction of the refracted features with the raised boundary layer results in the coalescence of shock structures into what appears a normal structure of variable strength (5). A re-acceleration region separates the primary structure from the secondary normal structure (6), which occurs approximately 1.2 duct heights behind the primary structure. Additionally, window aberrations (8) must be discarded from analysis. The re-acceleration zone is analyzed in more detail in Chapter 6.

Step 2 - XZ-Plane Analysis: Red dotted lines are drawn to visualize the comparison of structures seen in the XY- and XZ-plane image pair. The XZ-planes shown in Fig. 5.1 represent the starboard half of the isolator duct, with Z=0mm symbolizing the duct centerline. Due to the geometric constraints regarding the placement of the front-surface mirrors inside the wind tunnel structure, interactions between the shock front and side wall (Z=76mm) are not completely visualized. Projections can be made and compared to the location of shock/boundary-layer interaction in the XY-plane. The upper starboard corner interaction (1u) occurs at approximately X=540mm. The trailing edge of the lower wall boundary layer interaction is annotated at approximately X=558mm.

Intersection between the corner oblique shocks occurs at X=580mm and Z=37mm away from centerline (3), with the two separate shocks coalescing into a single stronger feature (4). This coalescence represents the refracted features (4u and 4l) shown in the XY-plane of Fig. 5.1a. Interaction of the refracted features with the raised boundary layer can be seen in (5), occurring at X=593mm and Z=18mm. A normal structure (5') proceeds toward the center-axis (Z=18mm

to Z=0mm) while an additional normal structure (5") travels toward the side-wall (Z=18mm to Z=35mm). This is a product of the interaction between the refracted structure and the separated boundary layer and could likewise be a means for the flow parameters behind the weaker oblique shock (from Z=35mm to Z=18mm) to match the thermodynamic magnitudes of the flow behind the more normal structure (Z=18mm to Z=0mm).

A strong normal structure (5) spawns out of this interaction, which is comparable in location to the normal structure (5) shown in the XY-plane image. The second derivative of the re-acceleration zone density gradients are too small to be visualized with the current setup. The secondary normal structure is clearly visible (6) however, representing a strong disturbance, suggesting in part that the re-acceleration zone contributes greatly to increasing the Mach number and strengthening the interaction. The lower portion of the secondary normal shock (6') is redirected due to the thermodynamic flow parameters behind the primary shock front below Z=35mm differing in magnitude form those above Z=35mm, since that is where the coalesced normal structure (5') begins. Additional interaction with the side wall boundary layer (6") will result in bifurcation of the normal shock.

Step 3 - XY-/XZ-Plane Analysis: Corner flow separation represents the initiation of the shock train formation shown in Fig. 5.1a. If the separation was more planar (occurring along the entire side wall Y-axis as seen in the XZ-plane), than by definition of the line-of-sight nature of the shadowgraph technique, disturbances ought to show in the region between the left (2l) and right (2u) running shocks in the XY-plane view. A similar observation can be made for the boundary layer separation seen in the XY-plane. If assumed planar (occurring along the entire Z-axis as seen in the XY-plane), disturbances would show in the region bounded by the primary wave structure (2, 3, 4, 5) and centerline in the XZ-plane image. Light refraction through both of these regions are minimal, thus initial boundary layer separation is expected to occur at the duct corners.

Observing both XY- and XZ-plane structures once more, the strengthening of the shock features as they approach center-axis indicate that either the effective integral lengths and/or

strength of the disturbances increase. Initially confined to a small effective integration length at the corners (1u, 1l), the growth of the shock plane (2u, 2l) as it approaches the intersection (3) and beyond (4, 5) account for the increased visibility of the structures. The significant strengthening of the structures toward the center flow field regions in the XZ-plane (5, 5', 5") indicate larger boundary layer separations near the center region resulting in stronger wave angles and higher pressure gradients. From the observations above, it is clear that the primary structure of the AR 3.0 shock train, which appears as a planar oblique structure in the traditional XY-plane field of view, is in reality a hybrid oblique/normal structure.

5.1.1.2 Wave angle discussion in Fig. 5.1b

The observations made in steps 1-3 for Fig. 5.1a can be similarly made for the flow field in Fig. 5.1b. Additionally, shock wave angles with respect to the lower and upper walls (XY-plane) and isolator starboard wall and centerline (XZ-plane) are annotated to further evaluate the behavior and strength of the shock train leading edge features captured in both perspectives. These observations are complemented by XY-plane shock strength derivations through visualization and static pressure measurements discussed in Section 5.5 and Fig. 5.16.

Step 1: XY-Plane Analysis (Fig. 5.1b): Since the Mach number varies considerably along the duct major axis, the $\theta - \beta - M$ relations are not used explicitly to derive the effective boundary layer separation (deflection) angle. This discussion is reserved for Section 5.5. However, assuming a constant Mach number of 2.35 in the downstream section of the aspect ratio 3.0 isolator (Table 3.1), approximate boundary layer separation angle order of magnitudes can be provided. The right and left running incident shock waves have an approximate wave angle of 37.33^o and 36.10^o respectively, corresponding to an approximate deflection angle of 13^o. A reduction in refracted wave angle is observed downstream of the intersection point. With the incident oblique shock planes generally not identical in magnitude, the creation of a slip surface can be envisioned downstream of the intersection point (3) in the area bounded by the refracted shocks 4u and 4l. Owing to the entropy difference but pressure equivalence between the upper and lower wall shock

process, the creation of a slip line process is not visualized due to the inadequate sensitivity of the multiplane shadowgraph technique.

Step 2: XZ-Plane Analysis (Fig. 5.1b): The shock wave angles visible in the XZ-plane are discussed and compared to the above descriptions. The incident oblique shocks corresponding to the lower and upper wall corner separation zones are characterized by shock wave angles of 46.32^o and 47.66^o respectively. These angles are approximately 22% larger than the observed shock angles in the XY-plane, and correspond to a boundary layer separation deflection angle of 21^o (38% larger than the deflection angle derived from the XY-plane perspective).

The transition to the more normal shock feature is clearly visible in the XZ-plane perspective of Fig. 5.1b. The coalesced refracted shock angle is measured at 55.92^o. Gradually increasing in strength (thickness and contrast), the refracted structure transitions through a wave angle of 73.3^o to a completely normal shock structure in the centerline of the duct starting at a lateral location of approximately Z=10mm from the centerline.

The definition of the shock train front is more uniform and defined in the XZ perspective than it is in the XY perspective. This is a characteristic of visualizing a curved shock feature using a line-of-sight visualization technique. Since the shock train is curved about the vertical (duct minor) Z-axis and the XZ-plane integrates the disturbances along the Z-axis, the resulting visualization is more defined along the XZ-plane.

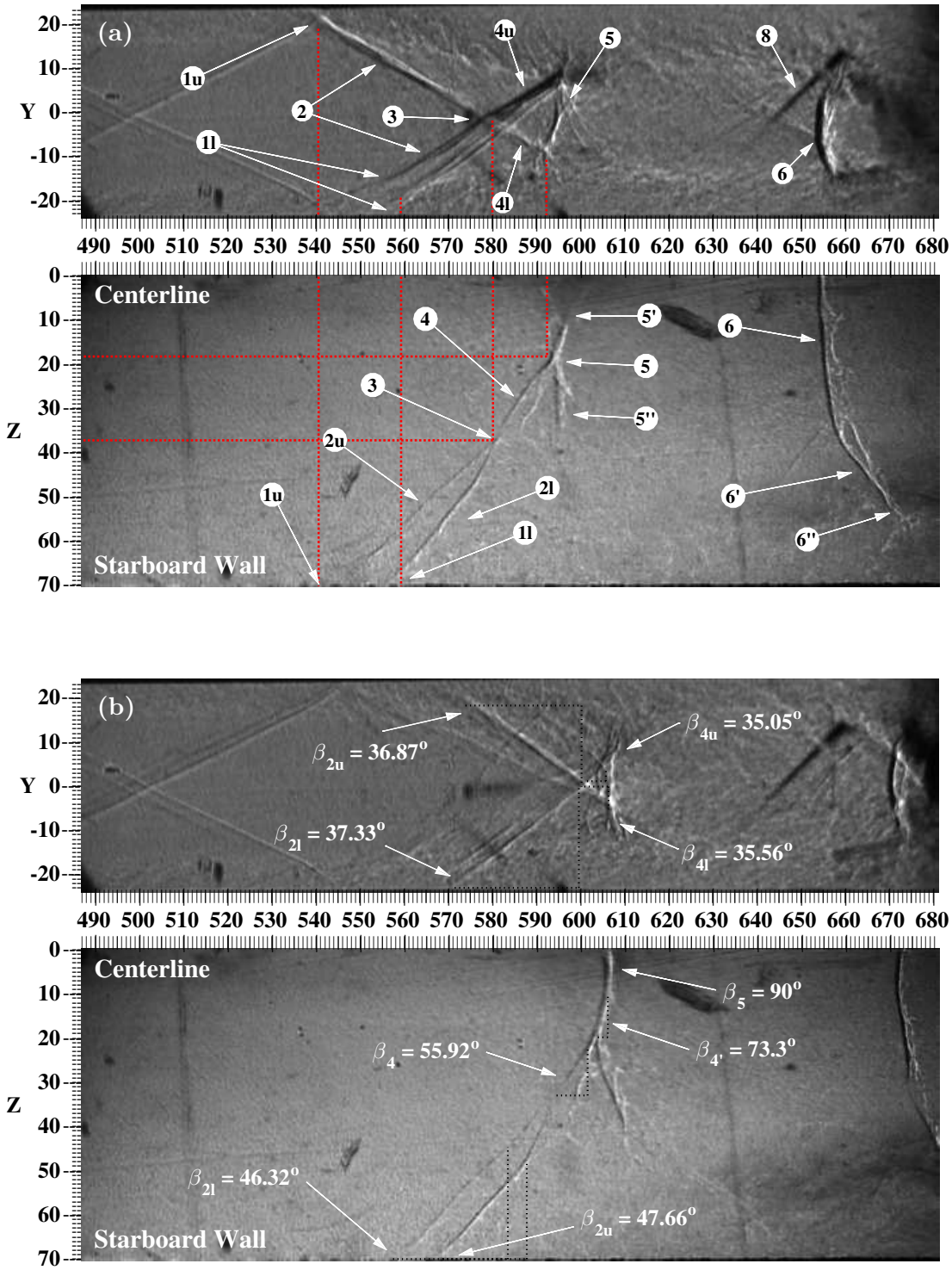

Figure 5.1: Aspect ratio 3.0 downstream section multiplane shadowgraphy. XZ-plane representing the starboard half of the isolator duct: (a) P_3/P_0 : 0.125 ± 0.003, $\tau = 0.158$, (b) P_3/P_0 : 0.119 ± 0.004, $\tau = 0.149$.

5.1.2 Multiplane Shadowgraph Shock Front Reconstruction

The shadowgraph image in Fig. 5.1a is utilized to reconstruct the three-dimensional shock train front. The XY-plane image is used to produce the XY-coordinates of specific features in the flow field such as the boundary layer edges, initial oblique shocks, and normal shock structures. Edges of interest are traced using the different color reference points (Fig. 5.2a). The traditional planar interpretation of shock train structures discussed in Chapters 1 & 2 correspond to the utilization of the [X,Y] coordinate space to reconstruct the image from a two-dimensional perspective, assuming the initial oblique structure occurs from wall to wall. This representation is shown in Fig. 5.2b.

The accompanying XZ-plane representation is used to construct an [X,Y,Z] coordinate composition of the three-dimensional shock train front, shown in Fig. 5.2c. To complete the full test-section width representation of the shock train, the structure is assumed to be symmetric about the lower-wall longitudinal axis.

The shock front reconstruction in Fig. 5.2c helps visualize the hypothesized three-dimensional shock front described in the previous section. It furthermore shows the departure from the traditional two-dimensional analysis and terminology of planar shock train fronts (Fig. 5.2b). The initial corner separation along with the incident oblique shock intersection point is annotated in three-dimensional space. The transition from oblique to normal shock within the shock train front is accompanied by an increase in boundary layer separation magnitude.

The reconstruction presented in Fig. 5.2c represents the vertical shock front only, and does not account for the dynamics typically occurring immediately downstream of the shock structure. To more easily visualize this process, Fig. 5.3a shows the intersection of two oblique shock planes emanating from a pair of orthogonal 10^o ramps representing a corner boundary layer separation from the lower and side wall. This corner boundary layer separation case will spawn oblique shock planes due to the flow being turned into itself, with the shock planes outlined in the green shade in Fig. 5.3b. The locus of points where the two shock waves intersect is highlighted in darker green. This locus, projected vertically toward the lower wall ramp, is displayed in Fig. 5.2c.

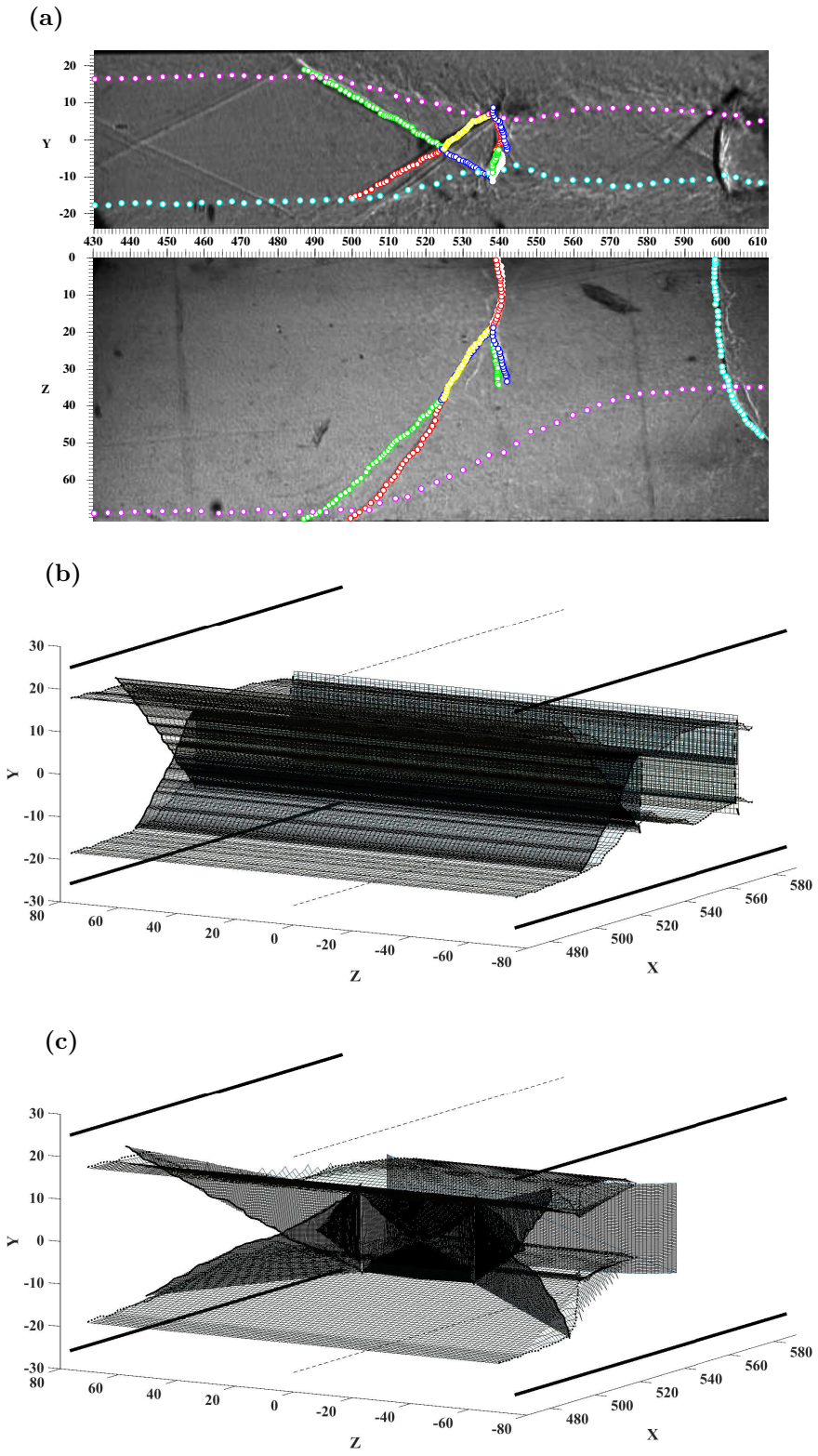

Figure 5.2: Aspect Ratio 3.0 shock train front two- and three-dimensional image reconstruction: (a) sample multiplane shadowgraph image (Fig. 5.1a), (b) [X,Y] coordinate reconstruction obtained from XY image plane, (c) [X,Y,Z] coordinates obtained from the XY/XZ image plane.

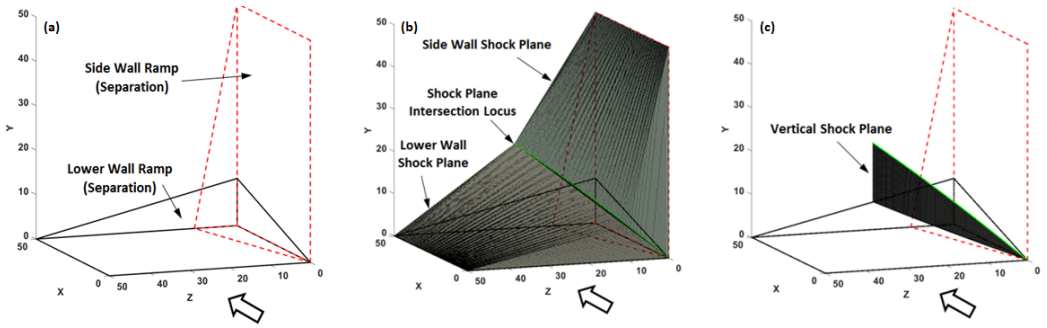

Figure 5.3: The vertical shock train front reconstruction process visualized using the intersection of two orthogonal wedge-induced oblique shock planes.

Extending the boundary layer separation and shock formation discussion down to the isolator walls, the sketch provided in Fig. 5.4 visualizes the expected boundary layer separation behavior along the isolator major and minor axis at a generic planar location in the duct. Comparison to an upstream plane with fully attached boundary layer is also shown, with boundary layer thickness approximately that measured at the downstream station of the aspect ratio 3.0 configuration (Table 3.1). The boundary layer separation profiles are shown for both side- and nozzle bounded wall boundary layers, and are projected on the respective walls of the duct.

The lower momentum thickness observed in the side-wall boundary layer through experimentation and computation (Table 3.1-3.2) results in a boundary layer more susceptible to separation. This indicates that the side-wall (minor axis) boundary layer separates ahead of the nozzle bounded (major axis) boundary layer. The velocity profiles show the no-slip wall imposed zero velocity increasing to the freestream velocity at the edge of the boundary layer. The core area of the flow is reduced due to the shock train leading edge associated boundary layer separation, leaving smaller areas of supersonic flow downstream of each consecutive shock train structure. Mie-scattering visualization is used to experimentally visualize the decreasing core area of the aspect ratio 1.0 isolator in Chapter 6.

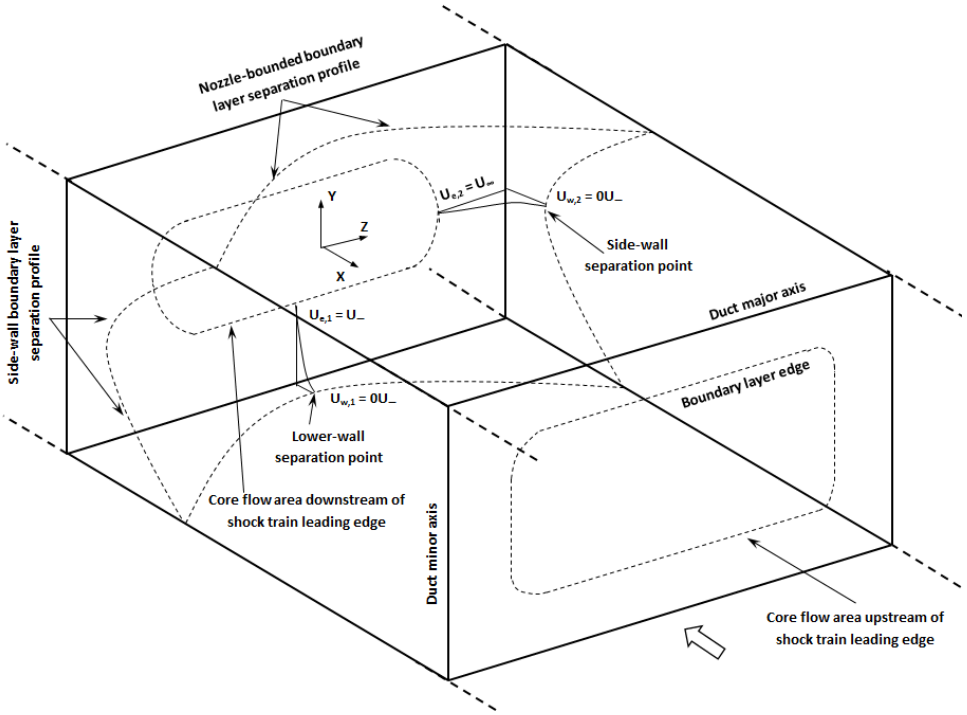

Figure 5.4: Sketch of the three-dimensional boundary layer separation projected onto the isolator walls.

5.1.3 Aspect Ratio 6.0 Multiplane Shadowgraph

To compare the effects of aspect ratio on the resulting corner flow separation, Fig. 5.5 shows two frames of the AR 6.0 shadowgraph analysis. Due to the additional 50.8mm of acrylic the XZ-plane light beam has to traverse along with the compressible background noise of the image, the XZ-plane image intensity values are scaled such that 1% of the data is saturated at low and high intensities to improve contrast and clarity. Observations made in the analysis of the XY-planes in Fig. 5.5a-b are to be compared to the XY-plane analysis of Fig. 5.1a-b to avoid repetition. Figure 5.5a is used to describe the shock structures, whereas Fig. 5.5b annotates the observed shock wave angles.

Primary structure behavior is similar to that observed in the AR 3.0 case, as right and left running waves intersect and subsequent refractions interact with the separated boundary layer. Strong disturbances are shown downstream of the refracted structures. Due to the smaller cross-

sectional dimensions of the AR 6.0 duct and the reduced length scales of the shock train elements, a total of four normal structures can be seen following the primary structure in both Fig. 5.5a-b. Normal shock locations are observed at X = 545mm, 578mm, 610mm, and 635mm in Fig. 5.5a and X = 542mm, 575mm, 603mm, and 630mm in Fig. 5.5b. From these qualitative observations, it is observed that the separation length decreases by 1.31, 1.25, and 0.98 duct heights in Fig. 5.5a and 1.29, 1.11, and 1.06 duct heights in Fig. 5.5b. Bulk flow upstream of each consecutive normal shock is closer to sonic transition, and thermodynamic variables and their gradients reduce in 'relative' magnitude, resulting in the shock structure showing up less clear (reduction in $\delta^2\rho/\delta y^2$ value) in regions of increasingly mixed flow. This gradual diffusion process is described in more detail in Section 6.3.

More interesting differences between both aspect ratios arise in the XZ-plane images. As seen in Fig. 5.5a-b, the normal component (5') of the hybrid oblique-normal primary structure is significantly more extensive than its AR 3.0 counterpart, with transition from oblique to normal occurring at approximately Z=48mm (5), which is a distance of 1.88 duct heights removed from the isolator centerline (compared to 0.7 duct heights in the AR 3.0 case). The transition between incident (2) and refracted (4) shock features is accompanied by a small increase in wave angle (3). As seen in the XZ-planes of the AR 6.0 images, the primary structure is followed by strong normal structures (6, 7, 8). Variation in behavior of the secondary normal structures (6', 7', 8') are influenced by both the change in thermodynamic variables above and below the oblique/normal transition point (5) and the interaction with side-wall boundary layer. The variation in integrity of shape and strength of these structure indicate gradual flow deceleration.

Differences and similarities between the AR 6.0 and 3.0 configurations are furthermore shown in Fig. 5.5b in terms of the observed shock wave angles. The freestream Mach number in the downstream section of the aspect ratio 6.0 isolator is 3% lower than it is for the aspect ratio 3.0 isolator at 2.27 (Table 3.1). The aspect ratio dependent decrease in Mach number is accompanied by an increase in backpressure for a given shock train leading edge position. Since the shock train is held in the downstream end for a longer backpressure rise range, the backpressure for a given

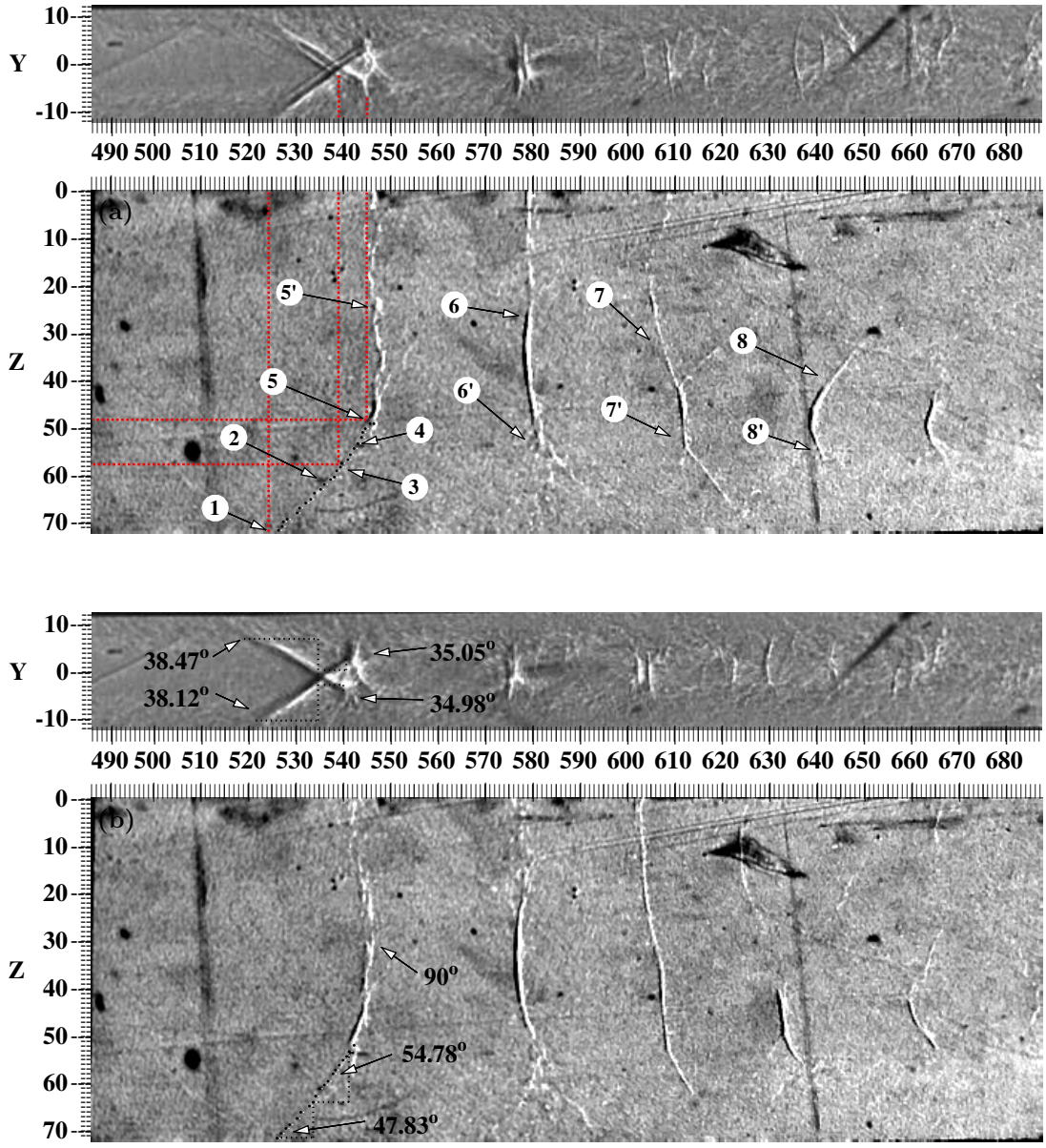

Figure 5.5: AR 6.0 multiplane shadowgraph. XZ-plane representing the starboard half of the isolator duct: (a) $P_3/P_0 : 0.263 \pm 0.003$, $\tau = 0.308$, (b) $P_3/P_0 : 0.265 \pm 0.004$, $\tau = 0.310$.

shock train leading edge position in the downstream station is generally higher in the aspect ratio 6.0 case. This is shown in Fig. 3.7b, where the pressure tap at X = 600mm senses the shock train arrival for a backpressure of $P_3/P_0 = 0.26$, compared to $P_3/P_0 = 0.21$ for the aspect ratio 3.0 configuration (a 20% increase). A higher backpressure results in a more significant adverse pressure

gradient inside the boundary layer, resulting in the higher magnitude boundary layer separation angle.

The combination of lower Mach number and higher boundary layer separation (deflection) angle leads to the similarities in wave angle measurements between the aspect ratio 6.0 (Fig. 5.5b) and the aspect ratio 3.0 configuration (Fig. 5.1b). The upper and lower wall incident oblique shock wave angles of 38.47^o and 38.12^o (an averaged 3% increase over the aspect ratio 3.0 configuration) suggests the lower Mach number may still play a dominant effect in the formation of the initial shock train front. An approximate deflection angle of 14^o is derived from the $\theta-\beta-Mach$ relations representing a 7.1% increase over the aspect ratio 3.0 boundary layer deflection angle, highlighting the effects of the larger back pressures in the larger aspect ratio (smaller cross-sectional area) isolators.

The aspect ratio 6.0 observed XZ-plane perspective corner wave angle is nearly identical to the aspect ratio 3.0 configuration, only representing a slight increase of 2%. This can again be attributed to the combination of lower Mach number and higher backpressure and boundary layer adverse pressure gradient. One additional observation that can be made in the XZ-plane is the upstream corner flow separation length scale compared to the center flow field boundary layer separation/shock train leading edge location. The leading edge of the shock train (lower wall) is located at an approximate longitudinal location of X=525mm, whereas the normal shock is established at X=546mm. This represents a separation length scale of approximately 0.83 duct heights, an 18% decrease compared to the 1.02 duct height separation observed in the downstream aspect ratio 3.0 duct (Fig. 5.1). Shock train length scales are discussed in more detail below.

5.1.4 Comparison of Shock Train Structure Length Scales

Comparing the corner separation length scales in the downstream station of the experimental aspect ratio 3.0 and 6.0 isolators with constant width allows for the analysis of duct height on three-dimensional shock train formation. Based on the experimental multiplane shadowgraph observations presented above, several shock train length scales can be examined.

The total width of the primary shock train structure in the XY-plane perspective, or the length scale between initial corner flow separation and the location of the primary normal shock (X_{15}), is composed of length scales X_{13} and X_{35} (adding up to X_{15}) following the annotations used in Figs. 5.1a and 5.5a. All experimental length scale measurements are averaged over 10 distinct shadowgraph images and normalized by the respective duct height. Average corner flow separation length scales (X_{15}) of 1.02 and 0.81 duct heights with respect to the center flow separation are observed in the aspect ratio 3.0 and 6.0 isolators respectively. These are divided into the incident shock length scales (X_{13}) of 0.70 and 0.61 duct heights, as well as the refracted shock length scales (X_{35}) of 0.32 and 0.19 duct heights.

Similarly, the XZ-perspective can be examined and normalized length scales of Z_{13}, Z_{35}, and Z_{15} can be compared. Since the XZ perspective field of view does not extend all the way to the isolator side-wall, the extra lateral axis length scale not visualized is added to the value of Z_{13}. Over the same 10 distinct shadowgraph images, the aspect ratio 3.0 length scales are averaged to $Z_{13} = 0.75$, $Z_{35} = 0.39$, and $Z_{15} = 1.14$ duct heights. Similar observations for the averaged aspect ratio 6.0 length scales result in $Z_{13} = 0.75$, $Z_{35} = 0.38$, and $Z_{15} = 1.13$. Although the shock front is significantly more two-dimensional in the aspect ratio 6.0 configuration, a reduction in duct height with constant width still results in identical lateral axis length scales regarding the formation of the shock train with respect to the duct center axis.

The length scales are furthermore visualized in the inviscid approximation of the multiplane shock train structure in Fig. 5.6a. The incident shock wave angles of 37^o and 38^o for the aspect ratio 3.0 and 6.0 configurations respectively, averaged across 10 distinct shadowgraph images, are symmetric for upper and lower walls. The longitudinal shock train leading edge location is identical for both aspect ratios at $X = 0.25H_{AR3}mm$. Allowed to progress to the duct center-axis, the subsequent refracted shock angles were averaged to approximately 35^o and 36^o respectively and allowed to progress to the derived aspect ratio 3.0 and 6.0 boundary layer separation thickness of 12mm (0.23 duct heights) and 9mm (0.35 duct heights) respectively.

Annotated in Fig. 5.6a, the inviscid approximation underpredicts the aspect ratio 3.0 X_{13}

length scale by about 5.7%, while it overpredicts the aspect ratio 6.0 X_{13} length scale by approximately 4.7%. The inviscid refracted shock length scales (X_{35}) are overpredicted by 5.8% and 13.6% compared to the experimental values respectively. The increased boundary layer separation magnitude with respect to duct height in the higher aspect ratio duct significantly limits the refracted shock length scale, contributing to the overall lower separation distance between the initial corner flow and center flow field separation found in higher aspect ratio isolators.

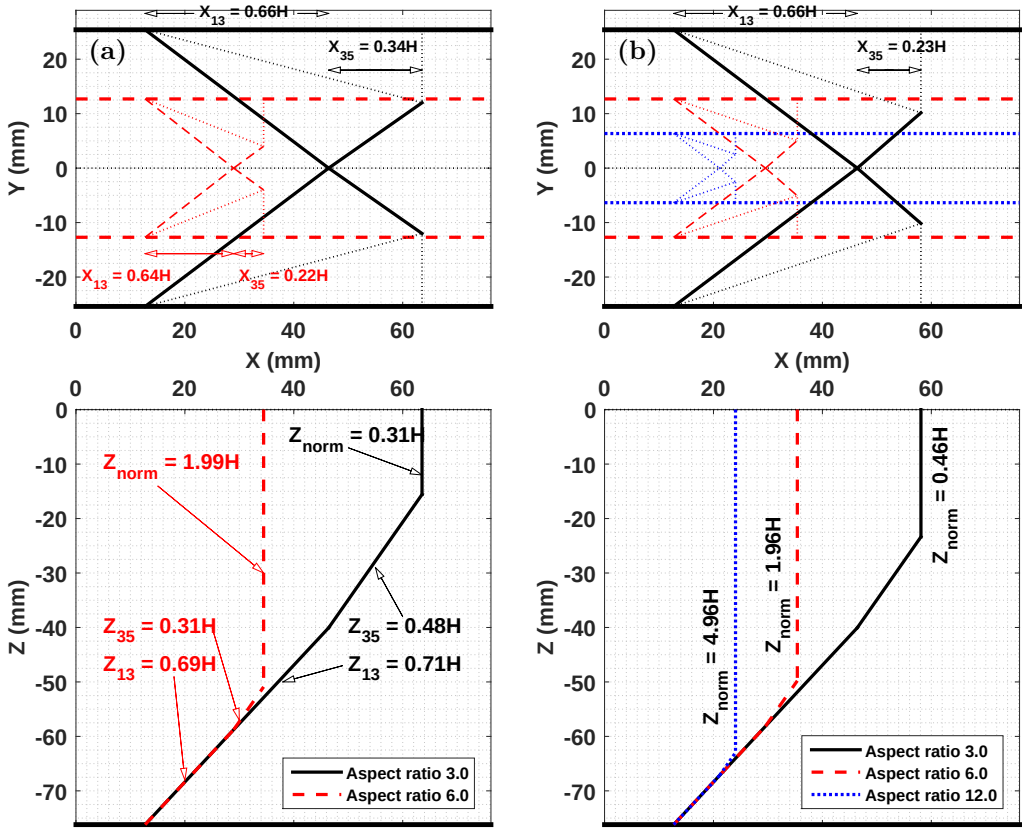

Figure 5.6: Inviscid approximation to the shock train length scales: (a) experimentally derived wave angles for aspect ratio 3.0 and 6.0 comparison, and (b) comparison of the normal shock length scale for aspect ratio 3.0, 6.0, and 12.0 using identical flow parameters.

The inviscid approximation of the XZ-plane structures in the aspect ratio 3.0 and 6.0 configurations is formed by utilizing the experimentally observed XZ-perspective wave angles in combination with the longitudinal length scales (X_{13} and X_{35}) derived above. Lateral axis inviscid length scales of Z_{13} and Z_{35} can be compared to the experimental values discussed above. Additionally,

the lateral width of the normal structure is normalized with respect to the duct height as Z_{norm}. As is shown in the experimental multiplane flow visualizations (Figs. 5.1 and 5.1), the reduction in height whilst keeping the duct width constant reduces the 'absolute' range of the oblique portion of the shock train, forcing the normal structure to be established at an earlier lateral axis location from the side wall.

The increased two-dimensionality of the shock train is observed in Fig. 5.6b, where the aspect ratio range is extended to 12.0. Unlike Fig. 5.6a, XY and XZ incident shock angels are kept constant at 37^o and 47^o respectively across all cases. Furthermore, the maximum boundary layer separation magnitude is kept fixed at $0.2H$. Lateral (half) width of the normal component, Z_{norm}, is increased by 76% between aspect ratio 3.0 and 6.0 configurations, and again by 60% between aspect ratio 6.0 and 12.0 configurations. Figure 5.6b furthermore shows the effect of duct height on the degree of isolator shock train front three-dimensionality.

5.1.5 Aspect Ratio 1.0 Multiplane Shadowgraph

The aspect ratio 1.0 multiplane shadowgraph analysis is obtained with the experimental setup shown in Fig. 3.22. The XZ-plane perspective is captured around the duct centerline, with the lower and upper wall inserts restricting the field of view width to approximately 40mm in the XZ plane. With the XZ plane visualization a priority and the 45^o front surface mirrors placed outside of the test section, the total field of view provided by the 250mm diameter parabolic schlieren mirrors cannot resolve the entire XY plane. Subsequently, the edge of the parabolic mirror is visible in the XY plane visualization, yet care was taken to visualize at least half of the XY-plane perspective.

Two multiplane visualizations taken 10ms apart of the aspect ratio 1.0 shock train are shown in Fig. 5.7a-b, with features of interest marked appropriately. Discussion regarding the shock train structure will solely focus on the differences from the aspect ratio 3.0 & 6.0 cases discussed above. As can be seen in the XY plane visualization of Fig. 5.7a, the incident oblique shock interaction (1) results in the formation of a relatively small normal shock structure (2) around the duct center-axis.

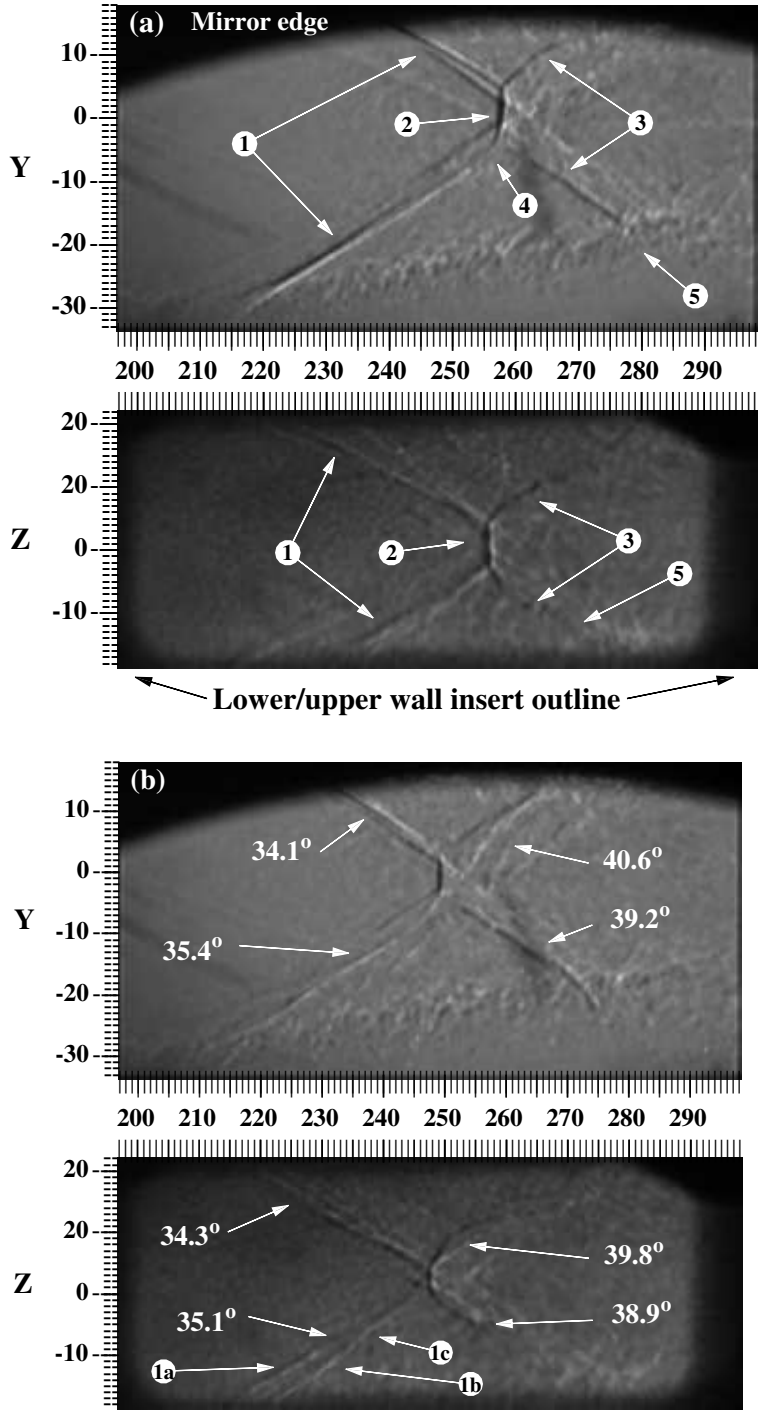

Figure 5.7: Aspect ratio 1.0 multiplane shadowgraph of shock train front. XZ-plane visualized about the center-line: (a) $P_3/P_0 : 0.134 \pm 0.002$, $\tau = 0.597$, (b) $P_3/P_0 : 0.138 \pm 0.003$, $\tau = 0.611$.

Refracted shock structures (3) propagate downstream and interact with the separated boundary layer (5).

It is shown that the refracted shock structures occur downstream of the primary normal shock component in the aspect ratio 1.0 isolator (in contrast to the aspect ratio 3.0 & 6.0 configurations). Since the XZ-plane field of view does not extend all the way to the side wall, the corner separation length scale is analyzed in the XY-plane perspective. Lower wall shock/boundary-layer interaction occurs between X=210mm and 215mm, with formation of the normal shock component occurring at X=257mm. With the width and height both equal to 66.675mm, the corner flow length scale is equivalent to 0.68 duct heights. Owing in part due to a duct width reduction of 56% and a height increase of 23%, this length scale is 33% and 16% smaller than the X_{15} length scales for the aspect ratio 3.0 and 6.0 configurations discussed above.

The XZ-plane perspective shows that the shock train front is predominantly oblique in nature, with the transition from oblique to normal shock structure significantly more abrupt (4). Above all else, the XY-plane and XZ-plane structures look significantly more identical than those in the aspect ratio 3.0 and 6.0 cases.

The capability to visualize the XZ-plane around the lower/upper wall centerline also shows the symmetry between port- and starboard sides of the isolator duct. The approximated XY- and XZ-plane incident and refracted shock wave angles are annotated in Fig. 5.7b. It is shown that for the aspect ratio 1.0 configuration, the shock train front is symmetrical about the duct center-axis along both the minor- and major duct directions, characterized by shock angles that are nearly identical in magnitude. The observed refracted shock angles are approximately 12% larger than the incident shocks angles, with symmetry maintained between the XY- and XZ-perspectives.

The observations above are in contrast to the aspect ratio 3.0 and especially the aspect 6.0 configurations, where the hybrid oblique/normal shock train visualized in the XZ-plane is not symmetric to the planar oblique shock front visualized in the XY-plane. Since the XZ-plane visualization is limited to approximately $\pm 20mm$ from the center-axis, detailed corner flow behavior cannot be visualized. Signs of distinct, upper and lower wall corner flow separation is visible in the XZ-plane visualization of Fig. 5.7b, and annotated as 1a and 1b accordingly. The oblique shock plane intersection point is also visible, annotated as 1c.

5.2 Surface Oil-Flow Visualization

A minor oil-flow visualization side-study was performed in the aspect ratio 3.0 configuration to explore lower-wall centerline behavior and symmetry. A flat black anodized isolator lower-wall plate was used in conjunction with a mineral oil-paraffin mixture for maximum contrast. Images were taken at an exposure of 80 μs and a frame-rate of 250Hz through the port-side window in real time using the IDT NR3-S1 camera with a set of six 1200 lumen LED bulbs providing adequate test-section lighting for the desired exposure time. Visualization oil was applied to the lower-wall and starboard side-wall prior to evacuating the facility in preparation for the wind tunnel run. Due to this process taking on the order of around five minutes, gravitational run-off resulted in the side-wall region not being adequately covered by the start of the run. Nevertheless, great uniformity was maintained on the lower wall as results below describe.

A series of three images is shown in Fig. 5.8a-c showing the progression of the shock train front, highlighted by white arrows, propagating upstream. Large oblique angled separation regions are visible near the starboard corner on the lower isolator wall. Transition and turning of the structure to a more normal orientation near the centerline is shown in Figs. 5.8b-c, with what appears multiple shock structure ripples following the initial shock front. Symmetry around the lower-wall centerline (outlined by a dashed white line) is observed. Given the lateral axis field-of-view limitation however, this does not provide evidence of full span symmetry, as the port-side corner interaction cannot be observed. Given the sensitivity to boundary layer conditions, corner separation initiation location can vary between the starboard and port-side walls. Secondary observations on the starboard side side-wall shows the upstream propagation of an oblique structure with a wave angle that is increasing as it approaches the side-wall centerline. Furthermore, the upstream propagation of a bright spot on the side-wall indicates that a large collection of oil particles entrained in potentially reversed flow is present.

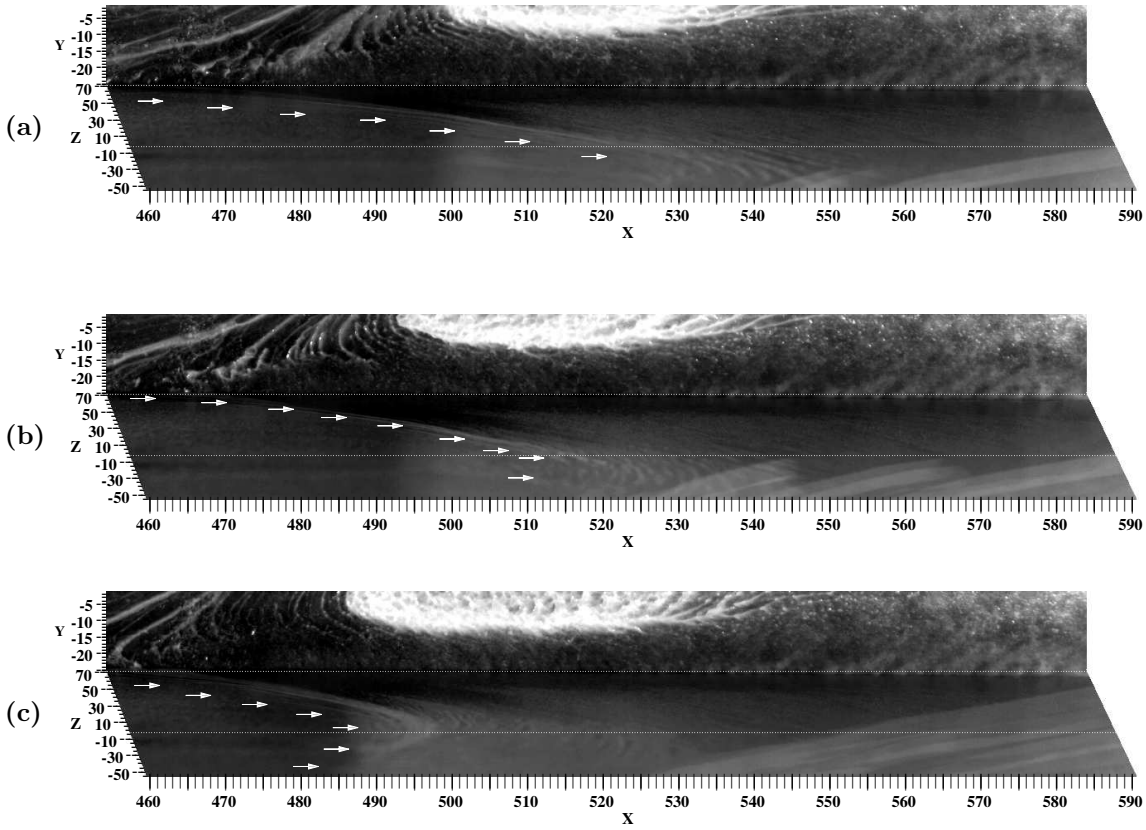

Figure 5.8: Oil flow visualization of Aspect Ratio 3.0 shock train propagation around the lower-wall longitudinal axis.

5.3 Planar Estimation of Shock Train Leading Edge Density Gradient Distribution

The formation of the hybrid oblique/normal shock train is expected to distribute the density gradient magnitude according to the interaction strength inside the shock train front. The BOS method is utilized in this study to map the distribution of global density gradient magnitude in the shock train structure. Although the BOS method is still a single perspective line-of-sight visualization technique, quantification of the interaction strength can provide insight into the validity of the traditional two-dimensional planar assumption.

Shock trains are visualized in both upstream and downstream station of both aspect ratios and compared to the traditional spark schlieren images. For each case, two separate BOS images are shown taken at consecutive timesteps (image acquisition frequency of 250Hz) and are annotated

by the normalized duct backpressure (P_3/P_i) and normalized run time (τ).

Significantly removed from the inlet plane of the isolator, the freestream Mach number at the downstream visualization station (Fig. 5.9) is reduced to approximately 2.35 and the observable boundary-layer thickness (δ) grows to approximately 9mm. The baseline schlieren (Fig. 5.9a) shows significant boundary-layer separation on both lower and upper walls, instigating the formation of a pair of oblique shocks of opposite families. Refracted shock/separated boundary-layer interaction is marked with increased magnitudes of density gradient, signifying a larger magnitude in refraction angle of light rays through the flow field. Referencing the multiplane visualization of Fig. 3.20b, this region hosts the normal segment of the hybrid shock front, causing light refraction and density gradient magnitude to increase. Maximum particle displacement was calculated to be approximately 8 pixel, translating to a maximum density gradient of $7760kg/m^3/$,, mainly located in the secondary normal shock. The normal portion of the primary hybrid shock front is characterized by a density gradient on the order of 4600-5400 $kg/m^3/m$. The weak density gradient representation in the oblique portion of the hybrid shock front (on the order of $3100kg/m^3/m$) is primarily due to the thin shock features originating from the preliminary corner flow separation regions, limiting the integration width along which the light refraction (and thus the pixel displacement) takes place. The sensitivity of BOS furthermore allows the visualization of the reacceleration features between the primary and secondary normal shock structures in the form of expansion fans and reflected compression waves which merge to form the secondary normal shock.

Shock train visualization at the upstream station of the aspect ratio 3.0 isolator is presented in Fig. 5.10. Characterized by a higher backpressure and a thinner incoming boundary-layer (δ = 3.2mm), overall residence time of the structure in the upstream station is significantly shorter compared to the downstream station. Due to its proximity to the inlet plane, freestream Mach number is approximately 2.45. The increase in both Mach number and boundary-layer separation tendency increases the primary oblique shock wave angle, generating a stronger density gradient at the intersection of the opposing shock families. Although maximum pixel displacement was of comparable magnitude to the downstream case, the leading edge shock front is characterized by

significantly stronger features in the upstream station. This echoes observations made with the multiplane shadowgraph technique that shows the normal portion of the hybrid oblique/normal shock front growing as the shock train propagates upstream [69]. The re-acceleration zone between the primary and secondary shock element remains visible. Secondary shock formation is dynamic as it interacts with the re-acceleration zone, with a strong albeit curved normal shock visible downstream of the primary shock element.

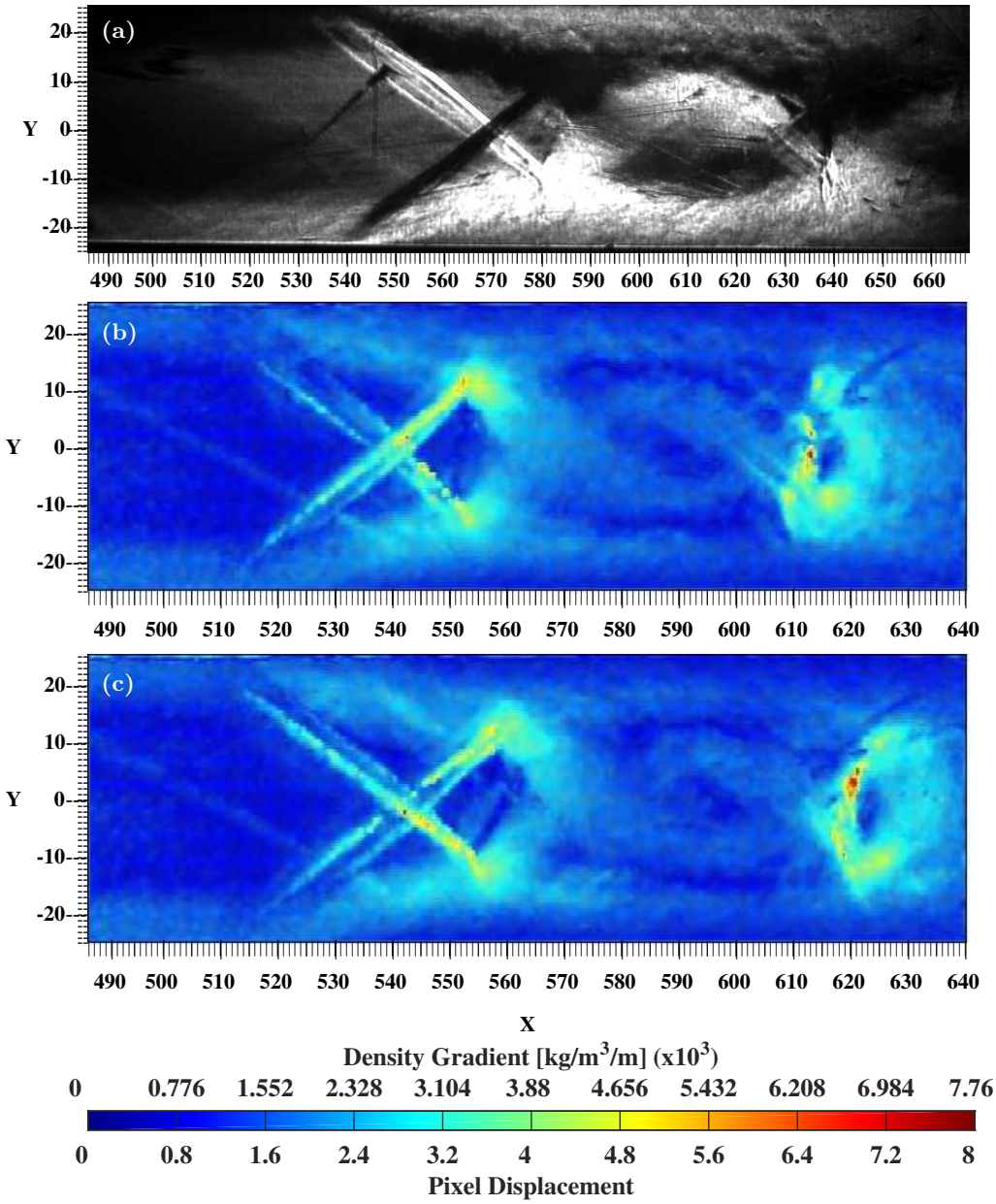

Figure 5.9: Aspect ratio 3.0 downstream visualization: (a) traditional schlieren baseline (P_3/P_i=0.2179, τ=0.4530), (b) (P_3/P_i=0.2180, τ=0.4529), (c) (P_3/P_i=0.2174, τ=0.4530).

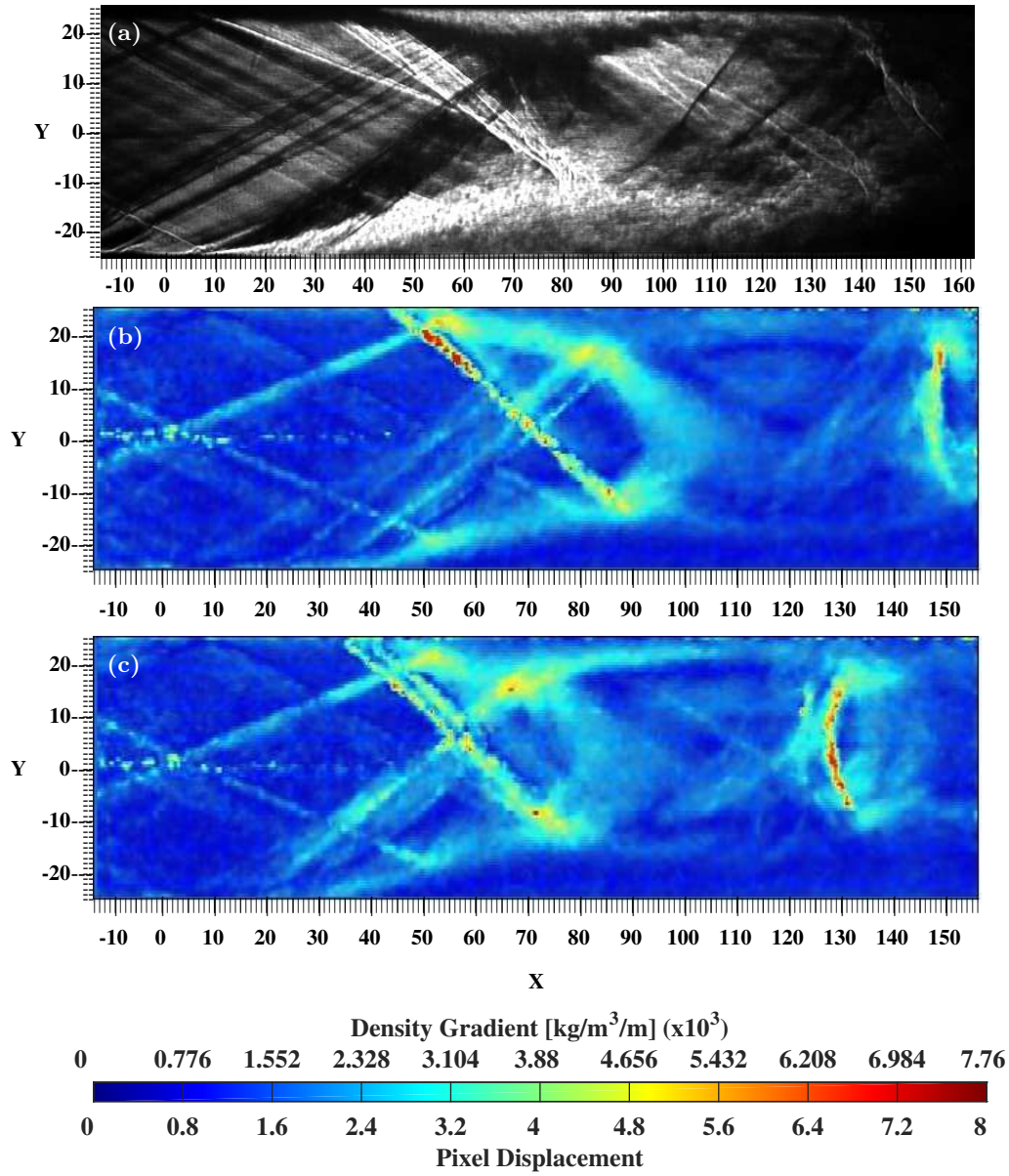

Figure 5.10: Aspect ratio 3.0 upstream visualization: (a) traditional schlieren baseline (P_3/P_i=0.3876, τ=0.9708), (b) (P_3/P_i=0.3868, τ=0.9706), (c) (P_3/P_i=0.3870, τ=0.9708).

Performance of the BOS technique is evaluated in regions of lower contrast and signal-to-noise ratio due to constrained geometry in the aspect ratio 6.0 case (Fig. 5.11 representing the downstream visualization station). A freestream Mach number of 2.15 and a boundary-layer thickness of 11mm occupy the field of view. Shock components are visible by examining the behavior of the boundary-layer and the leading edges of the shock features. For comparison purposes, pixel displacement scale was set to equal the aspect ratio 3.0 evaluation. Most of the expansion region detail is obscured by the thick boundary-layer occupying the visualization station. Observing the BOS images in Fig. 5.11b-c, clear distinction between the shock components and their respective spacing can be made. Distinct boundary layer edges can be made out both upstream the primary shock train structure and in between subsequent shock groups. A clear collection of multiple shock groups is visible in the BOS representation. Leading edge shock train definition however suffers due to low signal-to-noise ratio in the confined geometry, though the characteristic increase in density gradient magnitude just behind the initial oblique portion is still observed. The multiplane shadowgraph application to the aspect ratio 6.0 duct (Fig. 3.20c) indicated a significant presence of the normal portion within the hybrid oblique/normal shock train front. These areas of strong refraction are not visible in the BOS application.

Visualization in the aspect ratio 6.0 upstream station is characterized by a Mach number of 2.31 and an incoming boundary-layer thickness of 2.98mm. The dominance of the normal shock in the hybrid oblique/normal shock train front (Fig. 3.20c) is represented by the high magnitude density gradient distribution in the majority of the primary shock structure. On the lower spectrum of density gradient representation, the re-acceleration zone between primary and secondary shock structure is still clearly visible. Figure 5.12c represents the shock train shortly before wind tunnel unstart, in a state sensitive to small variations in boundary layer state, as illustrated by the asymmetric nature of the shock train leading edge. Multiple shock train components are clearly visible, as well as a reduced core flow area trailing the shock train in Fig. 5.12c.

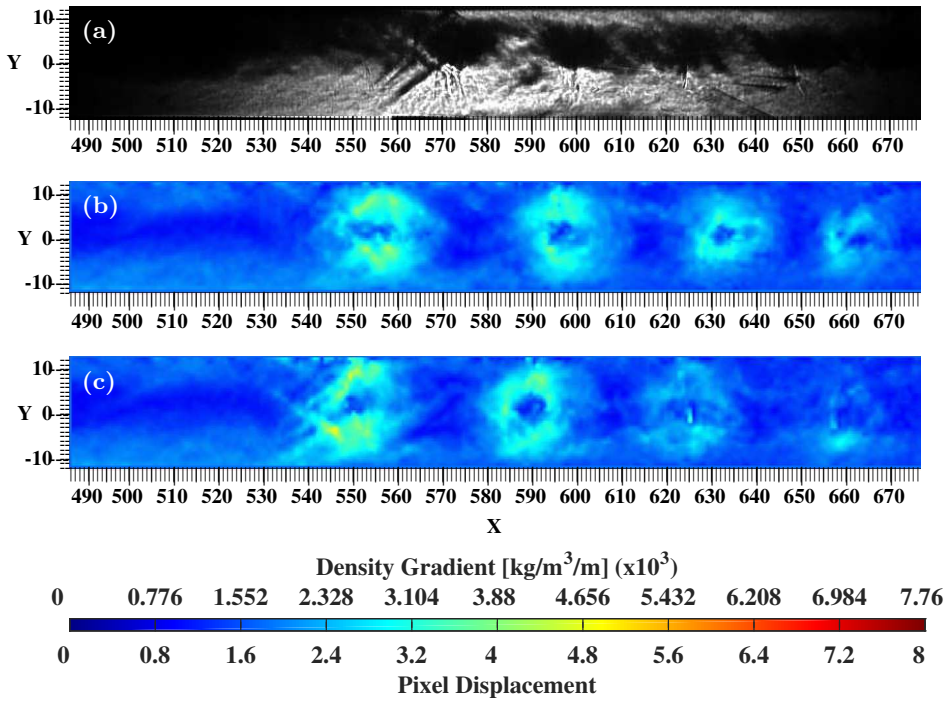

Figure 5.11: Aspect ratio 6.0 downstream visualization: (a) traditional schlieren baseline (P_3/P_i=0.3876, τ=0.4466), (b) (P_3/P_i=0.2011, τ=0.4465), (c) (P_3/P_i=0.1943, τ=0.4466), (d) (P_3/P_i=0.1984, τ=0.4467).

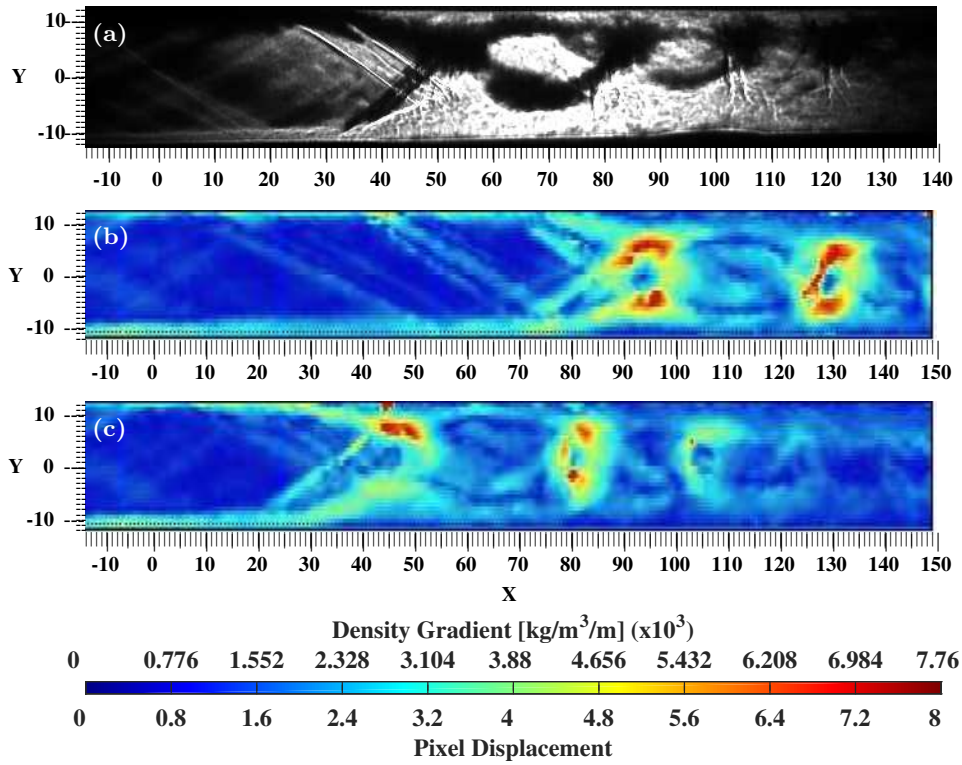

Figure 5.12: Aspect ratio 6.0 upstream visualization: (a) traditional schlieren baseline (P_3/P_i=0.4503, τ=0.9799), (b) (P_3/P_i=0.4501, τ=0.9799), (c) (P_3/P_i=0.4510, τ=0.9800).

5.4 Corner Flow Separation Time-Scale Measurement

Preliminary analysis of dynamic pressure measurement is provided to quantitatively support the qualitative multiplane analysis provided above. The lateral dynamic pressure measurements obtained in the starboard half of station 3 are presented in Fig. 5.13-5.14 for the AR 3.0 and 6.0 cases respectively. The fluctuating component of the dynamic pressure signal (P') is added to the time-averaged steady state static wall pressure (P_s) obtained from the respective longitudinal axis wall static pressure ports. Since the multiplane shadowgraph technique cannot support simultaneous pressure measurement due to the test section plates being made out of Acrylic, the wind tunnel synchronization signal is used to match the 60kHz dynamic pressure signal to the 250Hz shadowgraph signal.

The dynamic pressure sensor analysis described below is summarized in Table 5.1. The first group of data compares the measurements from sensor # 3 (Z=25.4mm) and # 4 (Z=50.8mm) to the recordings made at the duct centerline (sensor # 2), in particular: (a) the time (both absolute and normalized by unstart time) at which the pressure sensors first observe a pressure rise larger than three standard deviations to indicate the arrival of the shock train leading edge, and (b) the average differential pressure rise magnitude. The latter is calculated over a time span equivalent to the flow separation time-scale discussed in the former. The second group of data summarized in Table 5.1 shows two measurements for each of the three individual sensors. The first is the maximum normalized pressure rise, while the second represents the standard deviation of the pressure signal as a measure to determine the 'uniformity ' of the data.

Observing the aspect ratio 3.0 and 6.0 isolator behavior (Fig. 5.13-5.14), the shock train signal is initially occupied with compression events (positive pressure fluctuations) due to the leading edge of the shock train oscillating across the dynamic pressure sensor positions. As the bulk motion propagates upstream, expansion events (negative pressure fluctuations) appear corresponding to the complex structures downstream of the initial compression structure (re-acceleration regime). The re-acceleration regime is described in detail in Chapter 6.

As can be expected, the corner flow separation mechanism initiating the shock train formation discussed above will have a similar effect on the lateral distribution of pressure rise due to boundary layer separation. In the aspect ratio 3.0 case, Fig. 5.13 shows that the pressure rise at the most outboard pressure sensor (P_{K4}) precedes that of the more inboard sensors (P_{K3} and P_{K2}). Initial pressure rise at P_{K4}, exceeding three times the steady state average, was recorded 1.93 seconds before similar recordings were made at P_{K2}.

Given the flow environment, such pressure rise events were associated with boundary layer separation and incipient shock train leading edge arrival. The magnitude of the pressure rise, averaged over the time that P_{K4} measurements lead those of P_{K2}, is lower than the averaged pressure rise at P_{K2} over the same time span (starting when K_2 first senses the shock train leading edge). The stagnation value normalized pressure differentials across the lateral axis locations, averaged across the time span described above, are reported with respect to the magnitude of the centerline pressure sensor (P_{K2}). The centerline interaction is expected to be stronger based on the observations of the hybrid oblique/normal shock train front in Fig. 5.1. The normalized difference in the outboard region amounted to $(P_{K4}-P_{K2})/P_0 = -0.007$. Likewise, P_{K3} recorded shock train arrival 0.22 seconds prior to P_{K2}, with a normalized pressure rise difference of $(P_{K3} - P_{K2})/P_0 = -0.005$.

Similar observations are made in the second group of data, where the maximum pressure rise at K2 is 8% and 5% larger than at K4 and K3 respectively. The calculation of the standard deviation (σ) of the data sample shows that the centerline data is characterized by a lower degree of dispersion, suggesting that the more normal structure in the center-flow field provides a more consistent interaction between the shock train and boundary layer. The calculated standard deviation at the centerline is 55% and 35% lower than the K4 and K3 signals.

Similar observations can be made for the aspect ratio 6.0 case. From analysis in Fig. 5.5, it is observed that the normal component of the primary hybrid oblique/normal shock structure dominates, extending further outboard than the aspect ratio 3.0 case. Likewise, the superimposition of the pressure sensor locations on the shadowgraph image in Fig. 5.14 shows that the most

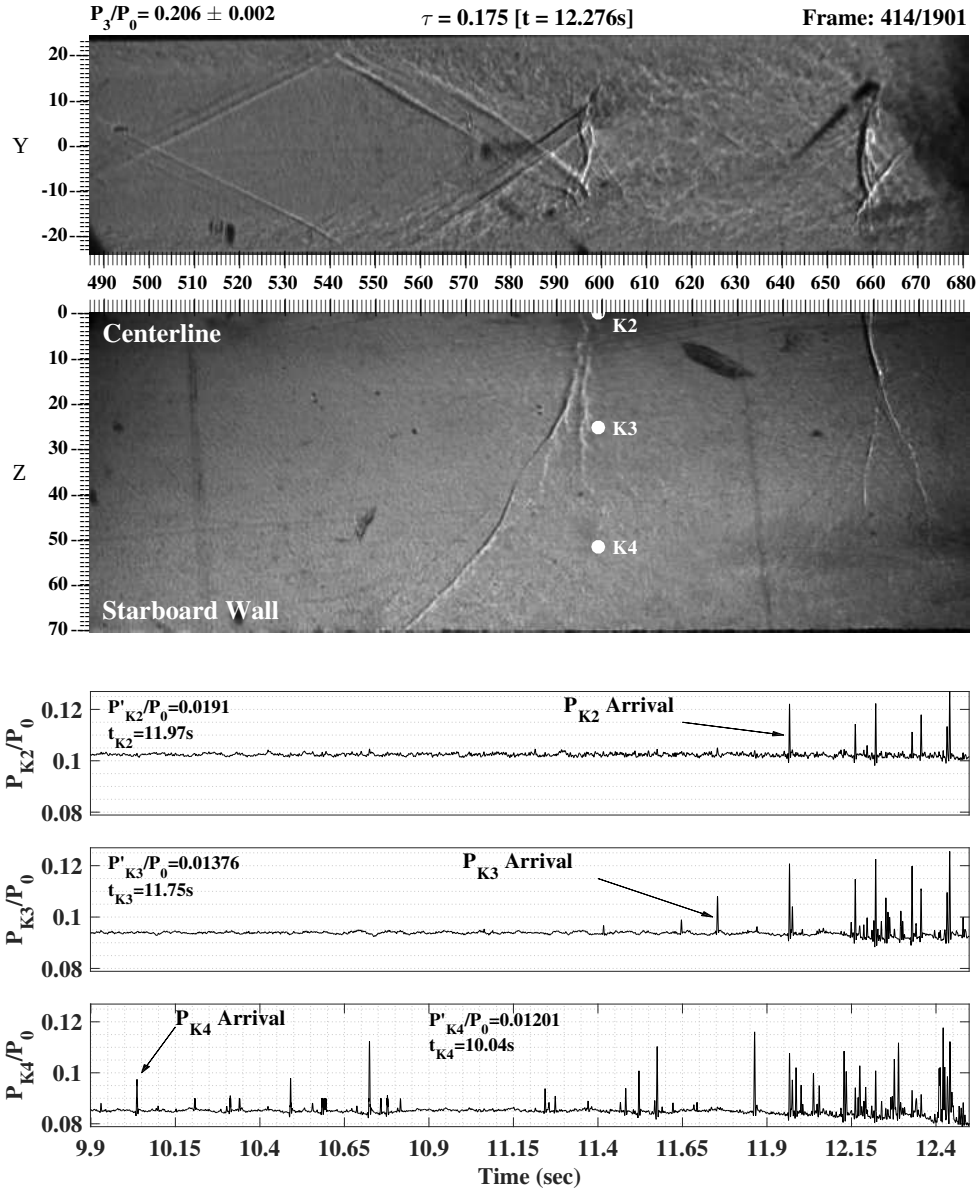

Figure 5.13: Synchronized multiplane shadowgraph and dynamic pressure measurement for aspect ratio 3.0.

outboard sensors lies closely to the 'transition' point from oblique to normal structure. Quantitative dynamic pressure measurement observations supplementing the qualitative visualization analysis of the aspect ratio 6.0 shock train formation in Fig. 5.5 are performed below.

An initial pressure rise at P_{K4} due to boundary layer separation is recorded 1.92 seconds ahead of the measurements at P_{K2}, similar to the measurements obtained in the aspect ratio 3.0 case. Although the corner flow separation length scale of the aspect ratio 6.0 configuration (0.88

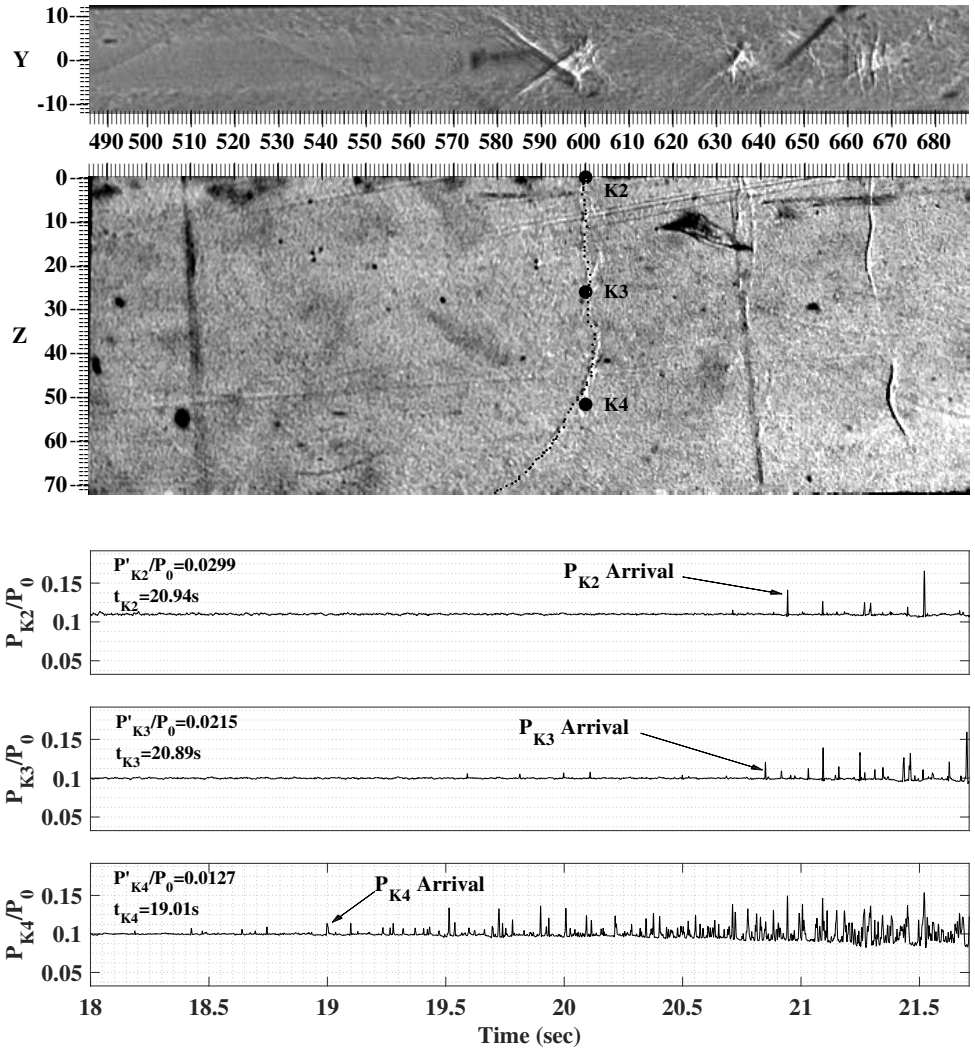

Figure 5.14: Synchronized multiplane shadowgraph and dynamic pressure measurement for aspect ratio 6.0.

duct heights) is lower than the aspect ratio 3.0 configuration (1.0 duct heights), it appears that upstream communication through the subsonic portion of the corner boundary layer could play a more prominent role than in the aspect ratio 3.0 case. Due to the longer unstart time, the normalized difference reduces to $\tau = 0.045$, compared to $\tau = 0.087$ in the aspect ratio 3.0 case (a decrease of 48.3%).

As expected, the more two-dimensional shock train approximation is evident in the comparison between P_{K2} and P_{K3}. Spaced only 0.06 seconds ($\Delta\tau = 0.001$) apart, this represents

	Aspect ratio 3.0		Aspect ratio 6.0	
	$\Delta\tau$ [Δt]	$(P_{Ki} - P_2)/P_0$	$\Delta\tau$ [Δt]	$(P_{Ki} - P_2)/P_0$
K_4 (Z=50.8mm)	0.087 [1.93s]	-0.007 ± 0.001	0.045 [1.92s]	-0.012 ± 0.002
K_3 (Z=25.4mm)	0.010 [0.22s]	-0.005 ± 0.001	0.001 [0.06s]	-0.002 ± 0.001
	$[P/P_0]_{max}$	$\sigma[P/P_0]$	$[P/P_0]_{max}$	$\sigma[P/P_0]$
K_2 (Z=0mm)	0.1270 ± 0.001	0.0013	0.1804 ± 0.002	0.0107
K_3 (Z=25.4mm)	0.1206 ± 0.001	0.0020	0.1750 ± 0.002	0.0121
K_4 (Z=50.8mm)	0.1177 ± 0.001	0.0029	0.1536 ± 0.001	0.0124

Table 5.1: Summary of dynamic pressure analysis comparing initial measurement of incipient unstart at P_{K4} (Z=50.8mm) and P_{K3} (Z=50.8mm) to P_{K2} (Z=0mm)

a 72% decrease from the aspect ratio 3.0 corresponding measurement. Along with the temporal scale, the difference in boundary layer separation induced pressure magnitude rise between P_{K2} and P_{K3} ($(P_{K3}-P_{K2})/P_0$ = -0.002) is more than 50% lower than the aspect ratio 3.0 configuration ($(P_{K3}-P_{K2})/P_0$ = -0.005), since both P_{K2} and P_{K3} are expected to lie inside the elongated normal shock structure. Furthermore, the expected difference between pressure measurements pertaining to the oblique and normal shock structure is materialized through a $(P_{K4} - P_{K2})/P_0$ value of -0.012, a 41% increase over the aspect ratio 3.0 measurement.

The measurements of the maximum normalized pressure rise and standard deviation furthermore highlight the differences between the aspect ratio 3.0 and 6.0 configurations. As expected, the difference between the pressure rise magnitude of $K2$ and $K3$ is reduced to 3%, compared to a 5% difference in the aspect ratio 3.0 isolator, whereas the difference between the most outboard and centerline sensor increases to 15% compared to 7% in the aspect ratio 3.0 case. This is due to the overall strength of the normal component of the shock train.

It must be noted that the steady state (fully started isolator) static pressure distribution in the downstream region of the isolator is approximately 25% higher in the aspect ratio 6.0 configuration (Fig. 3.7). The dynamic pressure magnitudes recorded at the K2, K3, and K4 positions in the aspect ratio 6.0 configuration are likewise 29%, 31%, and 23% higher than their aspect ratio 3.0 counterparts. The biggest deviation at K3 can be attributed to the more normal structure at that location in the aspect ratio 6.0 configuration. The similar wave angles between

isolator aspect ratios at K2 and K4 (see Fig. 5.1b and 5.5b) contribute to the predicted 25% pressure increase.

5.4.1 Simultaneous Schlieren & Dynamic Pressure Measurement

To compliment the synchronized multiplane schlieren and dynamic pressure surveys presented above, simultaneous spark schlieren was performed during the dynamic pressure measurements. This was primarily performed to ensure that the pressure measurement signals discussed in Figs. 5.13-5.14 presented physical shock train front induced boundary layer separation, and not pressure information propagating through the subsonic sublayer, by comparing the physical shock train leading edge with the dynamic pressure measurements. A secondary observation regarding flow three-dimensionality can be made through this technique by comparing the two-dimensionally projected location of the shock train leading edge front with the three-dimensionally resolved dynamic pressure measurements, further supplementing the observations presented above.

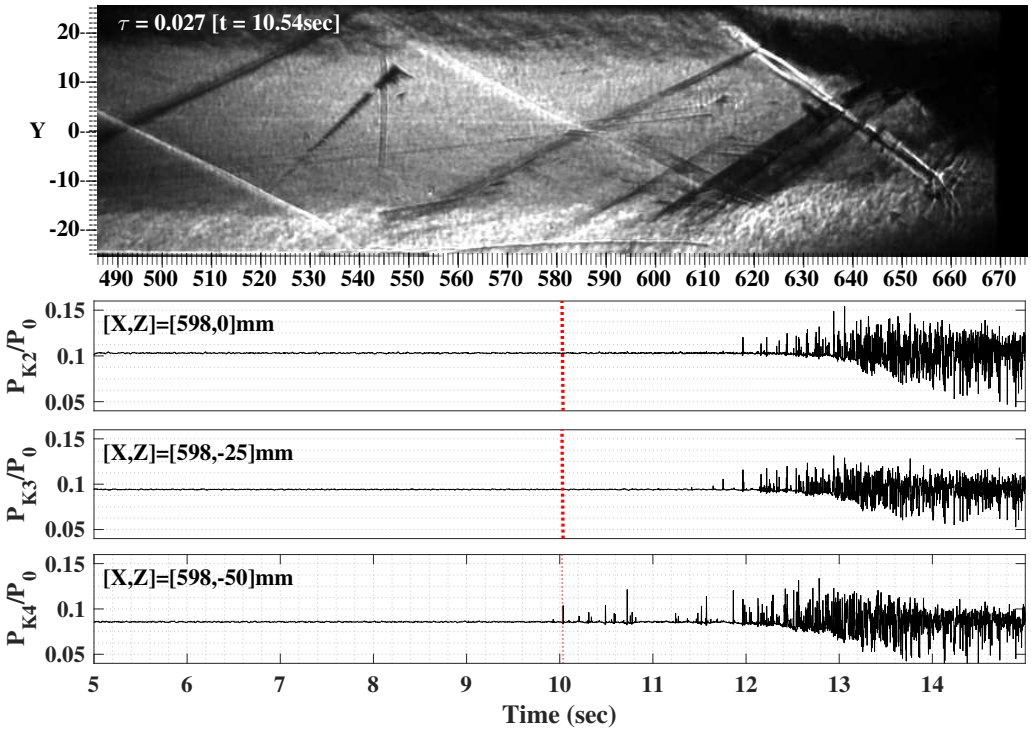

Figure 5.15: Simultaneous spark schlieren & dynamic pressure survey ($3\mu s$ exposure).

Figure 5.15 shows the lower-wall shock train leading edge positioned between X=595 and 605mm during the time at which the first boundary layer separation signal was measured by the outboard sensor (K_4). Although the shock structure is located at approximately the same longitudinal location as the dynamic sensor station (X=598mm), only the outboard sensor captures the boundary layer separation induced pressure rise. As can be seen in Fig. 5.13, the outboard sensor is located in the oblique shock region driven by upstream corner flow boundary layer separation. The centerline (K_2) and Z=25mm sensor (K_3) are located in the normal shock dominated region driven by center flow field boundary layer separation.

The line-of-sight perspective of the single plane schlieren flow visualization technique only allows limited observations to be made regarding flow three-dimensionality. Although the lower wall shock train leading edge appears relatively wide, with the shock/boundary-layer interaction spanning approximately 10mm, it is difficult to draw appropriate conclusions regarding the shape of the actual shock train front. The multiplane flow visualization technique, accompanied by a major-axis pressure survey, allows previously unattained insight into the complex flow physics of shock trains confined in rectangular isolators.

5.5 Resolving Leading Edge Shock Train Strength through Wall Pressure Measurements

Acquisition of the isolator wall pressure distribution presents the most reliable and convenient method of tracking the shock train leading edge position. Wall-bound pressure measurements of boundary layer separation can furthermore approximate the strength of the shock wave associated with the flow separation. The pressure ratio across an oblique shock derived from shock theory is shown in Eq. 5.1. Along with the freestream Mach number in the upstream and downstream stations (Table 3.1), the pressure ratio measured by the longitudinal centerline static wall pressure survey can be used to estimate the wave angle (β) of the shock train leading edge. Once the wave angle is known, $\theta - \beta - Mach$ relations can be used to derive the deflection angle θ which corresponds to approximate boundary layer separation angle. The approximations for shock

wave and deflection angles presented below for the aspect ratio 3.0 and 6.0 configurations can be compared to the multiplane observations made in Fig. 5.1b and 5.5b.

$$\frac{P_2}{P_1} = 1 + \frac{2\gamma}{\gamma+1}\left[(M_1 sin(\beta))^2 - 1\right] \tag{5.1}$$

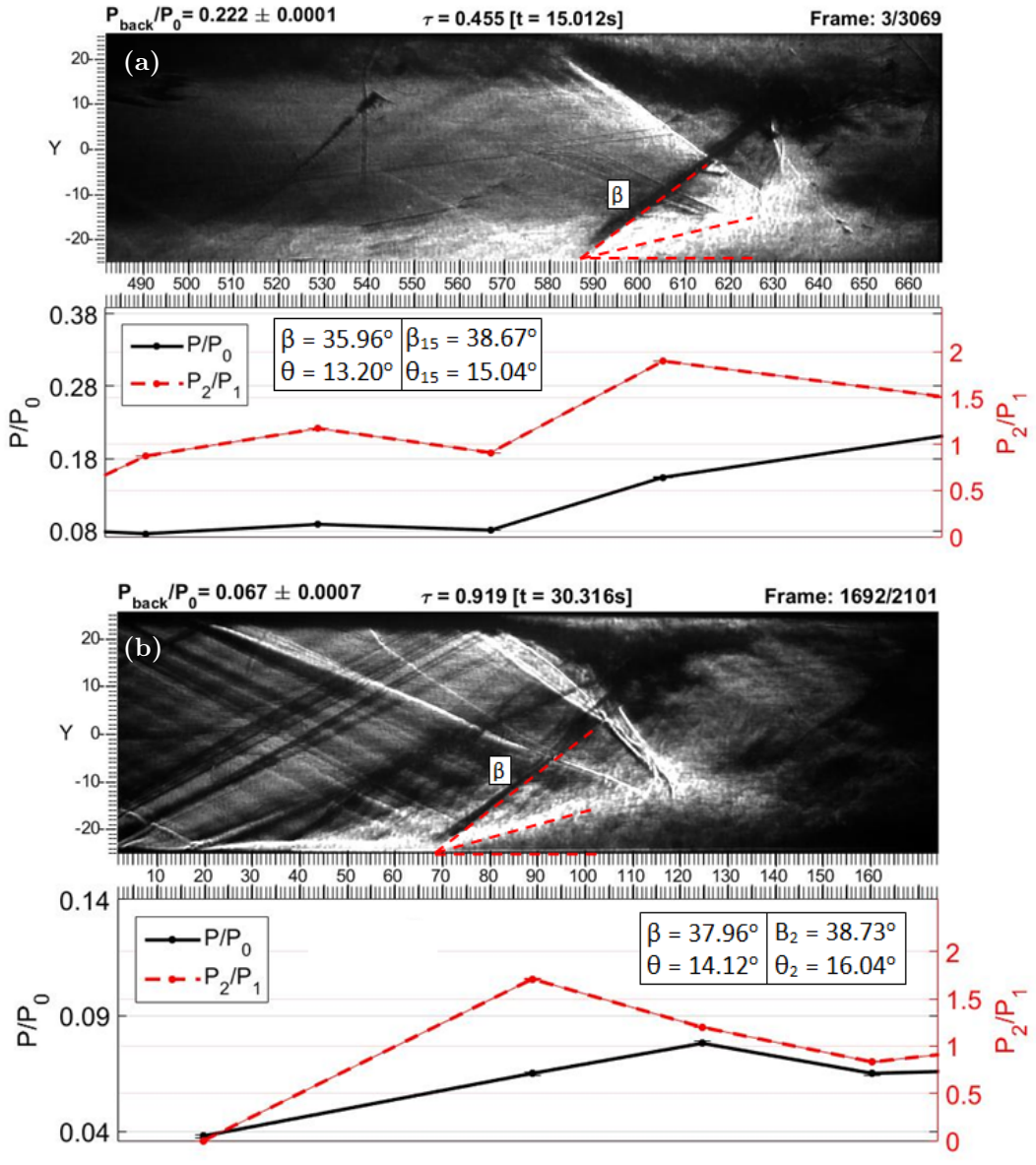

Figure 5.16: Evaluating shock train leading edge strength through synchronized schlieren and wall static pressure measurement: (a) downstream station [P_3/P_i=0.222, τ=0.455], and (b) upstream station [P_3/P_i=0.354, τ=0.919].

Synchronized traditional XY-plane spark schlieren and centerline static pressure measure-

ment is acquired to compare the static pressure derived shock wave angle to the visualization, with results for the aspect ratio 3.0 configuration shown in Fig. 5.16a-b. The lower-wall static pressure measurements are acquired at the same instance as the spark schlieren image, with data marker position corresponding to the physical location of the static wall pressure tap on the lower wall. Data marker size diameter indicates the bounds of the error in the measurements. The dark line represents the raw static pressure data at the schlieren image instance, while the red data represents the static pressure difference P_2/P_1, where P_2 represents the pressure acquired downstream of the shock train leading edge, and P_1 acquired upstream of the shock train leading edge. Estimates for wave and deflection angle are listed in the top right of the static pressure plot with derivations from the schlieren image noted in the left box, and approximations derived from the shock relations shown in the right box.

As is shown in Fig. 5.1a-b, the centerline region of the flow is dominated by the normal shock structure. This is also the region where the static pressure measurements are obtained to derive the deflection and shock angle through Eq. 5.1 and the $\theta - \beta - Mach$ relation. The visually derived deflection and shock wave angle of the downstream shock shown in Fig. 5.16a is smaller than the values derived from the centerline pressure measurement. This is expected since the visually derived deflection and shock angle represents that of the primary oblique shock wave near the outer regions of the duct. Similar observations can be derived from the upstream station shown in Fig. 5.16b. Angle calculations derived from centerline data are not much larger than the visually derived angles. Shock formation along the center-axis of the duct do not occur directly at the wall itself, so static pressure measurements obtained flush to the wall are not expected to capture the large pressure rise across the more normal shock structures near the center-axis. Influence from the oblique shock dominated outboard regions, where shock interactions extend to the wall itself, are measured at the centerline through the separated boundary layer.

Similar observations can be made for the synchronized static pressure and spark schlieren visualization of the aspect ratio 6.0 configuration, shown in Fig. 5.17. Angle derivations from centerline data are slightly larger than those derived from the shock train visuals. Comparison

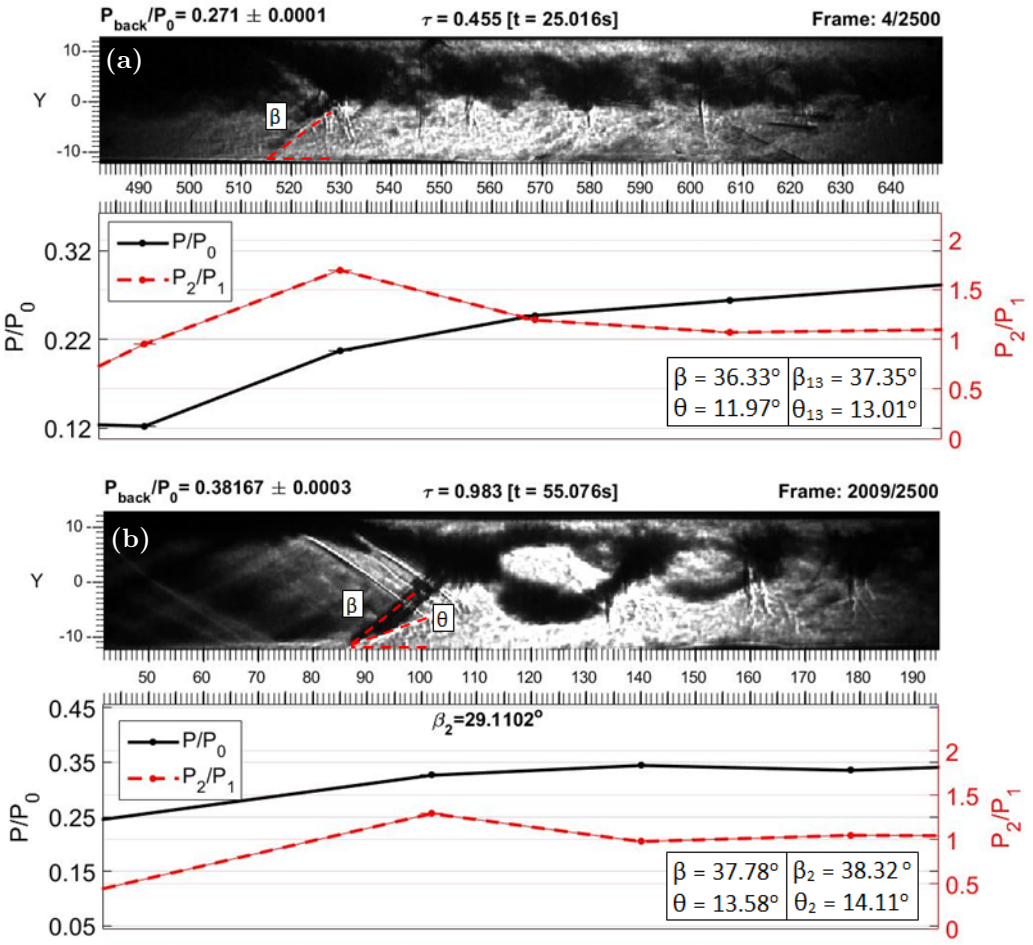

Figure 5.17: Evaluating shock train leading edge strength through synchronized schlieren and wall static pressure measurement: (a) downstream station [P_3/P_i=0.271, τ=0.346], and (b) upstream station [P_3/P_i=0.381, τ=0.983].

between the aspect ratio 3.0 and 6.0 wave angles derived from the spark schlieren visualizations echo those made in Figs. 5.1b and 5.5b. Overall, the measurements show that the strength of the outer region leading edge oblique portion of the shock train front can be reasonably estimated through pressure measurements along the centerline of the duct. These measurements furthermore show that the normal shock interactions located along the centerline occur along the center-axis and do not extend significantly to the isolator walls.

5.6 Shock Train Leading Edge Oscillation Frequency and Velocity Component Measurement

The Focusing Schlieren Deflectometry Velocimeter configuration described in Chapter 3 and calibrated in Chapter 4 is used to measure high-temporal bandwidth oscillatory frequency and velocity component signals of the shock train leading edge. Measurements are obtained at a sample frequency of 200kHz. Comparisons between the two aspect ratios, center-axis and side-wall flow regions, and primary and secondary shock train structures are made. Given that the deflectometry data obtained within the highly dynamic and compressible region of the shock train lacks the periodic structure introduced in the acoustically forced speaker test (Chapter 4), a conditional sampling approach is applied to increase the signal-to-noise of the velocimetry velocity calculations. The four-step technique is briefly outlined below followed by the discussion of the resulting observations.

5.6.1 Conditional Sampling of the Deflectometry Data

Step 1: Select the region of interest: Figure 5.19 shows the deflectometry data obtained by two sensors placed 2mm apart and focused along the center-axis of the duct. The top image shows the fiber probes (diameter enlarged 500% for clarity) superimposed on a typical spark schlieren image. The bottom two images show the raw photodiode data of both sensors as they acquire variations in light intensity caused by the passing of the primary (oblique) and secondary (secondary normal) shock structures. The magnitude of the photodiode signal is a function of the strength of the density gradient deflecting the light ray through the test section.

Selecting a region that includes shock activity is the first step toward analyzing the shock train motion. Figure 5.19 provides a close-up (5ms in duration) look at the behavior of the shock train. The events labeled 'shock pair' signal the presence of the passing shock train, with an upstream propagating shock pinging the downstream (APD2) photodiode prior to pinging the upstream (APD1) photodiode. This type of propagation is called 'Upstream Translation'

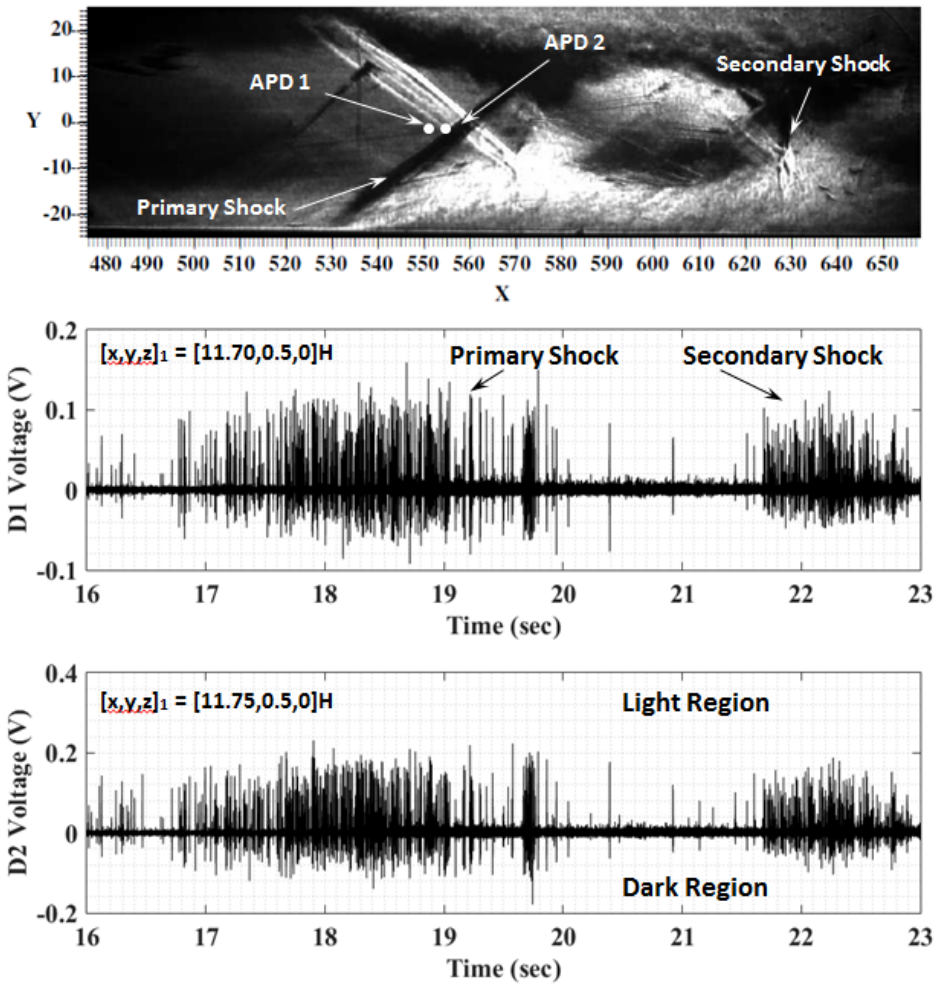

Figure 5.18: Location of deflectometry velocimeter probes and associated photodiode data for the aspect ratio 3.0 shock train.

(UT). The opposite happens for a downstream propagating shock train, as shown in the second pairing in Fig. 5.19, with this being called 'Downstream Translation' (DT). The characterization of the transient shock train dynamics requires two consecutive velocity measurements in order to distinguish the intend of the shock train. Four different modes are described in Section 5.6.2. Cases where the refractive entities (the shock train, pressure waves, etc.) only excite one photodiode are not to be evaluated in the calculation of shock train oscillation frequency and velocity component.

Step 2: Select the proper voltage cutoff: To improve the signal-to-noise ratio, a selective voltage cutoff is desired to separate the shock train results from the baseline readings. This baseline will vary to some extent from run to run so selective cutoff is required. Figure 5.20a

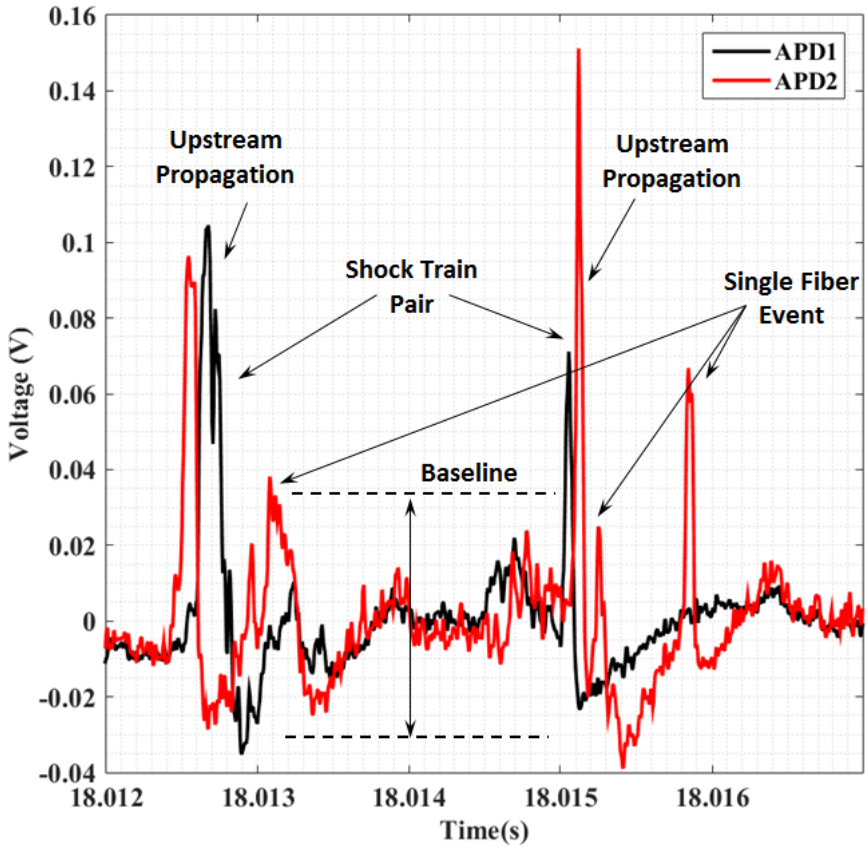

Figure 5.19: Classification of the velocimeter data shown in a 5ms sample of the raw data.

shows the selective visualization of prevalent deflectometry readings, showing two peak pairs and two instances of isolated events. The high cutoff voltage in this example, 0.35V, is chosen to more clearly illustrate the procedure. This voltage cutoff is lowered closer to the baseline when obtaining shock train propagation data. At this point, we assign the 'driving' and 'driven' signals according to the number of relevant peaks that are present in the sampling region. The signal with the lesser number of peaks will be referred to as the driving signal (APD1 in this example), while the signal with the most peaks is the driven signal (APD2 in this example). The idea behind the driving and driven signal concept is that the number of peak pairs will be limited by the number of driving peaks, given that it is the minimum of the two. This will allow the conditional sampling algorithm to intelligently select peak pairs over a wide range of data samples.

Step 3: Select shock train peak pairs: The algorithm has to be capable of automatically

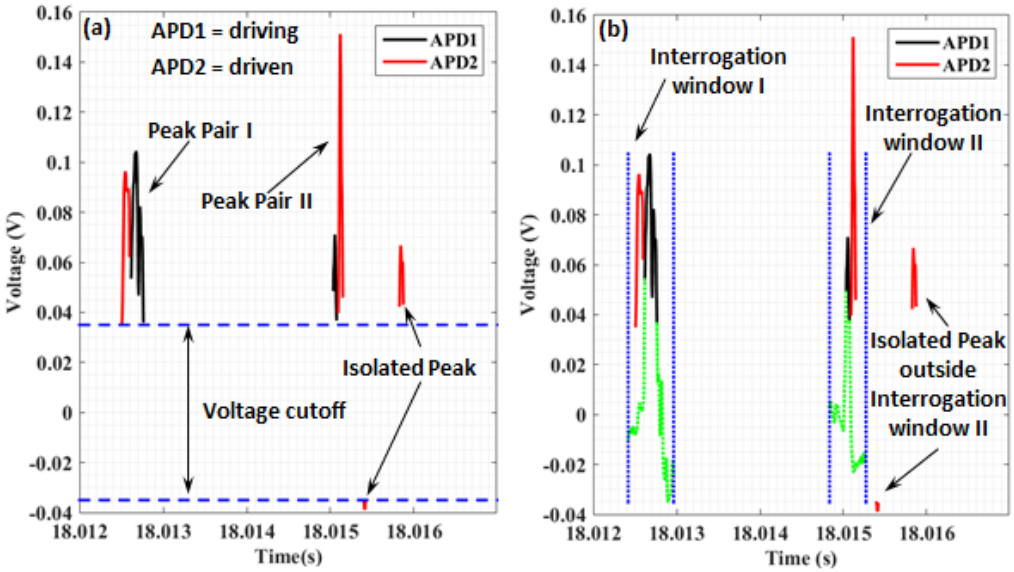

Figure 5.20: Selection of the velocimetry cross-correlation interrogation windows through a voltage threshold: (a) application of the threshold to isolate peak pairs, and (b) selection of cross-correlation interrogation window width.

selecting peak pairs and discarding isolated events. To accomplish this, a user defined interrogation window size was established to the left and right of the individual driving peaks. Interrogation window size was related to the minimum expected velocity of the shock train oscillation. If the oscillatory velocity was expected to be on the order of 5m/s, then for the given displacement of the two sensors (2mm), the interrogation window spanned approximately 200s from the base of each peak. Figure 5.20b shows these interrogation windows and the voltage readings of the bounded driving peaks for completeness. For each driving peak, the driven signal was analyzed and checked to see if it would fall within the respective interrogation window. If two or more driving peaks were present in a single driven interrogation window, magnitude and position of the driven signal were analyzed and the best fit chosen to pair with the driving signal in question. Figure 5.20b summarizes the procedure for the two driving peaks shown.

Step 4: Velocity calculation: After intelligently obtaining shock train peaks, the cross-correlation procedure described in Eqn. 4.10 can be applied to calculate velocity. Figure 5.21 shows the final peak-pair signals of both photo-diodes contained within the interrogation window in question. A simple 'peak-matching' procedure is introduced to check the velocity calculations

performed by the cross-correlation procedure. This calculation simply compares the timestamps of the maximum peak of both signals, followed by the velocity calculation. Though this works well for sharply defined peaks, the cross-correlation procedure is preferred to cover a wider range of signal quality. The cross correlation procedure outlined in Eqn. 4.10 is applied for each peak pair. An additional conditional procedure is applied to the cross-correlation to increase the quality of the velocity calculation by actively selecting sharp density-gradient peaks representative of the passing shock train structure.

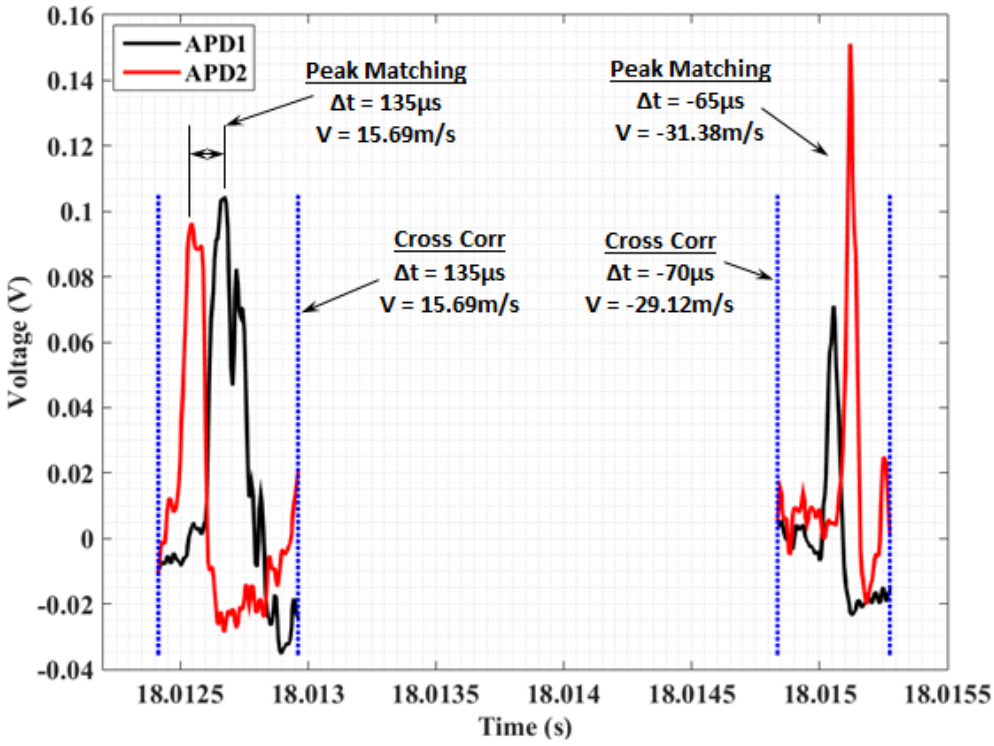

Figure 5.21: Comparison between the peak-matching and cross-correlation methods for calculating shock train average velocities.

Figure 5.22a-b represents the cross-correlation procedure for both peak-pairs shown in Fig. 5.21. The additional conditional procedure to improve signal-to-noise ratio is outlined below with the first step annotated in Fig. 5.22b and the second step annotated in italics in Fig. 5.22a.

In the first step, the maximum cross-correlation coefficient is located and a user defined time-bound equal is implemented to the left and right of the maximum. The first conditional

criteria that the cross-correlation peak (and thus that particular velocity calculation) needs to meet is the sharpness of the peak. If the left and right maximum at the time-bounds (left and right red dots) are less than 50% of the maximum cross-coefficient (horizontal red line), the cross-correlation results passes the first criteria. In case the peak is broad enough so that the maxima do no fall below the 50% line, the time-bound are doubled and the criteria evaluated again. If it does not meet the second pass, the peak is discarded (and the second conditional criteria) is not evaluated. The aforementioned time-bound is initialized as $\pm 100\mu s$ and the second pass is evaluated at $\pm 200\mu s$ if necessary.

The second criteria (annotated in Fig. 5.22a) involves evaluating the maximum outside of the left and right time-bounds, as marked by the blue dot). If the outside maximum is located below a certain cutoff (75% of the maximum cross-coefficient in this example), the second criteria is met. Given the quality of both peak-pairs, both criteria are met.

The maximum cross-correlation coefficient in the first interrogation window (Fig. 5.22a) occurs at a time-lag of $+135\mu s$ (upstream translation). Given the known Δx between the sensors of 2mm, a velocity of 15.7m/s is calculated. The second interrogation window (Fig. 5.22b) produces a maximum coefficient at a time-lag of $-70\mu s$, resulting in a velocity of -29.1m/s.

5.6.2 Average Oscillatory Shock Train Velocity Measurement

The conditional sampling algorithm described above was used to evaluate the oscillatory nature of the shock train propagation seen in the aspect ratio 3.0 and 6.0 rectangular isolator ducts. A total of 6 comparison studies are performed, as summarized below.

1. center-axis vs. side-wall primary shock train structure behavior (aspect ratio 3.0).
2. primary vs. secondary shock train structure in the center-axis region (aspect ratio 3.0).
3. aspect ratio 3.0 vs. aspect ratio 6.0 flow behavior of primary structure around the center axis.
4. aspect ratio 3.0 vs. aspect ratio 6.0 flow behavior of primary structure near the side-wall.

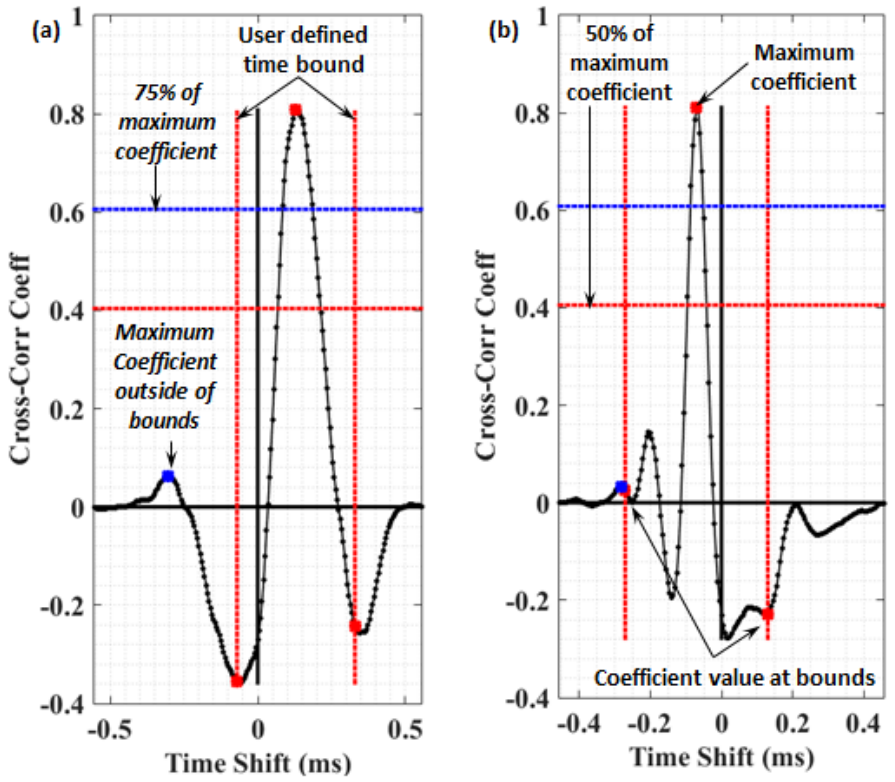

Figure 5.22: Conditional procedure to generate high signal-to-noise cross-correlation velocity derivations. From Fig. 5.21: (a) peak pair I, and (b) peak pair II.

5. center-axis vs. side-wall primary shock train structure behavior (aspect ratio 6.0).

6. primary vs. secondary shock train structure in the center-axis region (aspect ratio 6.0).

All studies are performed in the downstream third of the test section, with the three-dimensional coordinate of the photodiode fibers listed in the summary tables. The [X,Y] coordinate set corresponds to the two-dimensional position on the image plane, whereas the Z coordinate corresponds to the plane of sharp focus chosen for the particular data set. A detailed discussion of the data reduction for case study I is provided below, with summarized results and discussion presented for all subsequent case studies to follow.

5.6.2.1 Data reduction

The conditional sampling method described above is used to analyze peak pairs over a span of 1000ms. A convenient means to visualize the four possible modes of translation is presented in Fig. 5.23, utilizing the center-axis data from case study I. It is important to remember that an individual measurement from both fibers is used to calculate a single velocity. For this configuration, the four possibilities that are shown in the quadrant plot are:

1. present velocity is negative but next velocity is positive (upstream vibrating mode).
2. present velocity is positive and next velocity is positive as well (upstream translating mode).
3. present velocity is positive but next velocity is negative (downstream vibrating mode).
4. present velocity is negative and next velocity is negative as well (downstream translating mode).

Figure 5.23 shows the distribution of the calculated velocity components for the center-axis observation using the U_n and U_{n+1} axis where U_n represents the current velocity component and U_{n+1} represents the subsequent velocity component. Quadrant numbers correspond to the numerated list presented below. The calculated velocity components obtained across a data window of 1000ms acquired at 200kHz is shown. Each quadrant contains the number of velocity components (peaks) successfully resolved through the conditional sampling method, as well as the average, median, and standard deviation (σ) of the velocity data. The maximum, mean, and minimum values of all the upstream and downstream (both translation and vibration) components are shown in the title.

The chaotic nature of the shock train oscillation is observed in the quad plot distribution shown in Fig. 5.23. The distribution between upstream and downstream propagating behavior is relatively symmetrical however, with translating and vibrating occurrences nearly identical. The normal distributions for each of the velocity modes are shown in Fig. 5.24, with the vertical lines indicating one positive and negative standard deviation removed from the mean. The most coherent

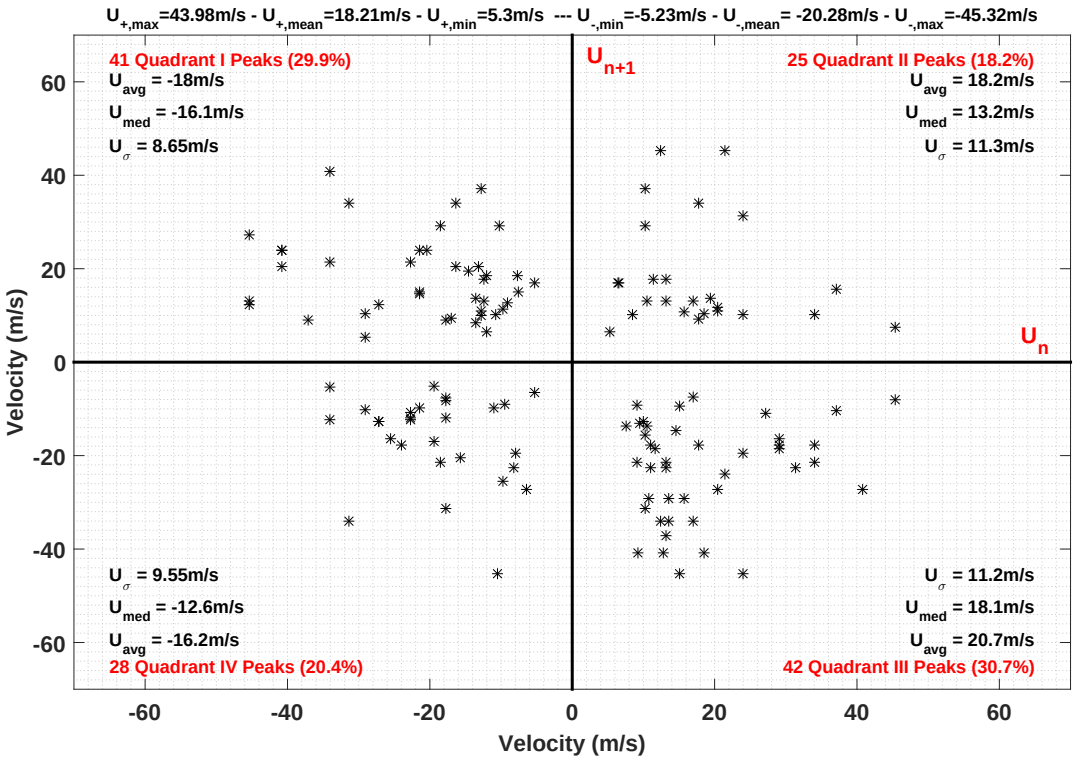

Figure 5.23: Average oscillation velocity quadrant plot for aspect ratio 3.0: center-axis portion of case study I.

data set is that of the upstream vibrating mode (quadrant I), where the standard deviation is 48% of the mean (compared to 62%, 54%, and 58% for quadrants II,III, and IV respectively).

The freestream velocity in the downstream station of the isolator is approximately 549m/s (Tab. 3.1). This means that the average velocity component for each quadrant is 3.2%, 3.3%, 3.7%, and 2.9% freestream velocity respectively. The majority of the flow behavior captured covers the vibrating mode (83 occurrences vs. the 53 occurrences of the translating mode). Finally, although it is propagating against the freestream flow direction, the upstream translation occurs at a slightly higher average velocity than the downstream translation (11% faster). Though not statistically significant due to the relatively low number of data points present, analysis such as that performed in Fig. 5.23 can help shed light on the behavior of the higher-level dynamic nature of shock train propagation by analyzing the velocity scales by which the shock train interacts with the isolator

flow.

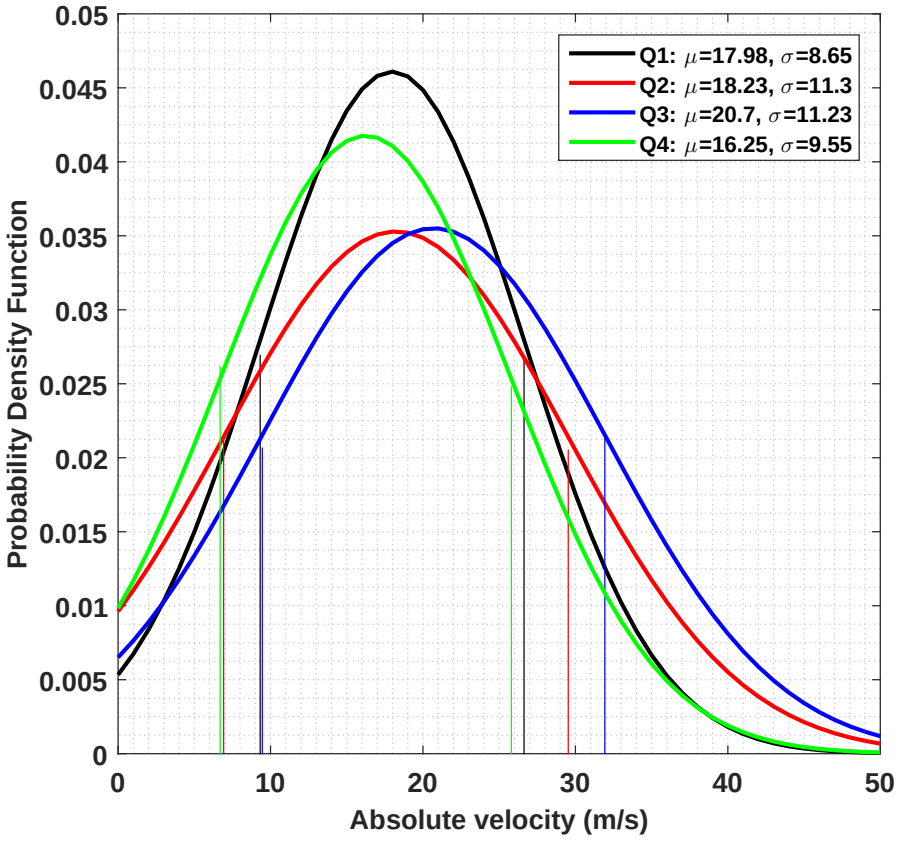

Figure 5.24: Normal distribution of absolute average velocity components for FSDV case study I.

5.6.2.2 Case Study I-VI Analysis

The results for all case studies are summarized in Table 5.2. All four velocity components are labeled in total velocity (m/s) units, as well as normalized with respect to the freestream velocity (U_e) at the point of measurement for the specific aspect ratio configuration in question. The recorded freestream velocity for the downstream regions of the aspect ratio 3.0 and 6.0 configurations are 553m/s and 530m/s respectively (Table 3.1). Finally, the percentage of each quadrant is also listed to look at the distribution of the shock train dynamic behavior.

The right most column lists the number of times the shock train crosses the photodiode

sensor pair in the vibration mode, to provide an estimate of shock train front oscillation frequency. Shock train oscillation frequencies obtained in the center-axis flow region can be compared to the diffuser driven Helmholtz resonance estimations for aspect ratio 3.0 and 6.0 configurations provided in Fig. 3.5, with a fair degree of comparison achieved.

Case Study I: The first case study compares the aspect ratio 3.0 flow behavior at the center-axis to the behavior at the side wall. As discussed in Fig. 5.1 and conceptualized in Fig. 5.2, the corner regions spawn the oblique shock planes that interact and transform into a normal structure near the duct's center-axis. Boundary layer separation at the mid-point of both the minor and major axis planes of the duct is expected to happen downstream of the corner flow separation. Stronger interactions at the center-axis (location of normal shock) provide larger pressure changes downstream of the shock structure, which in turn can be responsible for larger magnitudes of fluctuation as it interacts with the incoming free stream flow. The following observations are summarized in Table 5.2:

- The oscillatory velocity components are larger across all four quadrants in the center-axis (18.32) compared to the side wall region (12.15m/s), predominantly due to the stronger interactions forcing the structures in the upstream and downstream directions. The average velocity component (across all four modes) is 33% larger in the center-axis.

- Along with the larger velocity component, the observed total oscillation frequency is 67% larger in the center flow region compared to the side wall flow. Two characteristics of the flow field can drive this behavior. First, due to the strong disturbances in the center-axis flowfield, the shock induced photodiode signal is much stronger, leading to a 'potential' increase in either the quality of the signal capture and cross correlation process or the total number of frequency pairs captured.

- The overall oscillation frequency measured along the center-axis compares well to the frequency predicted by the Helmholtz driven behavior in Fig. 3.5.

Case Study II: The second case study evaluates the difference between the primary and

secondary shock structures, with both measurements obtained at the center-axis.

- Since both structures are normal in nature around the duct's center-axis, interaction strength and light fluctuation magnitude (hence signal and cross-correlation quality) between the two structures are comparable.

- The secondary shock structure oscillates at a frequency comparable to the primary structure, only 13% lower. Both structures would be exposed to close to similar driving Helmholtz frequencies in the center region of the flow field. A comparison between side-wall flow in different shock regions is proposed for future study to more clearly observe the role of the side-wall region in influencing the center flow dynamics.

- The overall velocity component of the secondary normal structure (25.6m/s) is larger than the primary structure (18.32m/s) by approximately 28%. The pressure magnitudes upstream and downstream of the secondary shock structure are expected to be larger than the corresponding pressures for the primary structure. These larger pressure magnitudes attribute to stronger interactions and higher oscillation velocities of the secondary shock structure.

Case Study III: Aspect ratio 3.0 and 6.0 center-axis primary shock structures are compared in case study III. The multiplane visualization technique showed that the three-dimensionality of the primary shock structure is constrained with an increase in aspect ratio, with the normal shock structure dominating the aspect ratio 6.0 shock train front (Fig. 5.1-5.5).

The shadowgraph visualization can offer some information regarding the apparent strength of the flow features through the analysis of the thickness and contrast. However, since it is a line-of-sight technique, end-effects can play a large role in smearing the apparent strength of the features in the core flow area, particularly in a geometrically constraint flow like the aspect ratio 6.0 configuration.

Instead, the apparent strength of the normal shock feature across aspect ratios can be observed in Table 5.1, where the observed shock boundary layer interaction magnitude of the aspect ratio 6.0 centerline dynamic pressure sensor is 41% higher than the aspect ratio 3.0 case.

Stronger shock features in turn will result in larger pressures potentially applying a larger force per unit area on the shock structure. Observations regarding the difference between the center-axis primary shock train element in the aspect ratio 3.0 and 6.0 configurations are made below:

- The average velocity component is increased by 12.0% between the aspect ratio 3.0 (18.32m/s) and 6.0 (20.81m/s) configurations. This increase in shock velocity component can be attributed to the 'stronger' normal shock interactions in the center flow field.
- Due to the lower freestream velocity in the aspect ratio 6.0 configuration, the normalized velocity component increases by 16.5% as the aspect ratio is increased from 6.0 to 3.0. The observed increases in velocity component are less than half of the observed pressure magnitude increase, suggesting a more complex relationship between the shock/boundary layer induced pressure magnitude and shock velocity component.
- Although the velocity component increases, the overall oscillation frequency of the primary structure decreases by approximately 20% as aspect ratio is increased. This is expected from the reduction in cross-sectional area decreasing the Helmholtz frequency, as discussed in Fig. 3.5.

Case Study IV: Aspect ratio 3.0 and 6.0 side-wall interactions are compared in case study IV. Side-wall boundary layer analysis (Table 3.2) suggests that the aspect ratio 6.0 side-wall boundary layer is characterized by a lower momentum content than the aspect ratio 3.0 side wall boundary layer. Provided that this results in more readily separable boundary layer, the pressure magnitudes of the interactions subsequently increase, provided a slight increase in the velocity computation from the photodiode signal.

- The average side-wall velocity component for the aspect ratio 6.0 configuration (18.025m/s) is approximately 32% higher than the aspect ratio 3.0 side wall region (12.15m/s), with the normalized velocity average increasing by 34%.
- The increase in side-wall velocity component is inline with the more gradual increase in center flow velocity as the isolator aspect ratio is increased (Case III). The aspect ratio 6.0

configuration is characterized by the two-dimensional shock front, and thus the differences between the center flow and side wall dynamics can be expected to be lower. It appears that the increased interaction strength in the center flow field results in a more dynamic side wall region. This is observed in Case V below.

- The lower momentum content observed in the aspect ratio 6.0 side wall region results in more separable boundary layer, and an 11% increase in shock train oscillation frequency is observed in the side wall region. This is in contrast to the 20% decrease in oscillation frequency observed in the center-axis as discussed above.

Case Study V: Observations made from the comparison between the center-axis and side-wall structure in the aspect ratio 6.0 case reflect some of the observations made in the multiplane shadowgraph analysis presented in Fig. 5.1-5.5:

- The average velocity component in the center flow region (20.81m/s) is approximately 12.6% higher compared to the side wall region (18.17m/s), primarily due to the stronger interactions found in the center flow region. This is in contrast to the difference of 33% in the aspect ratio 3.0 configuration (Case I). The more two-dimensional nature of the shock train in the aspect ratio 6.0 likewise can result in potentially more two-dimensional shock train dynamics.

- The oscillation frequency remains 53% higher in the center region of the flow field however, suggesting that the structure is still more susceptible to disturbances in the freestream than the anchored side-wall region.

Case Study: VI Finally, observations between the primary and secondary shock structures are made in the aspect ratio 6.0 configuration (similar to Case II for the aspect ratio 3.0 case).

- The increase in interaction magnitude between the upstream and downstream regions of the secondary structure again provides larger overall oscillatory velocity components compared to the primary structure. An average velocity component increase of 10.8% is observed, compared to a 28% increase in the aspect ratio 3.0 configuration.

- There is more uniformity between the primary and secondary normal shock structures in the aspect ratio 6.0 case compared to the aspect ratio 3.0 isolator due to the fact that the two structure are much more similar in composition, both being dominated by the normal shock structure to similar extends (Fig. 5.5).

- The observed oscillation frequency of the primary structure is only 4.6% higher than the secondary structure. This is a reduction from the approximately 13% difference in the aspect ratio 3.0 configuration, further illustrating the potential effects of a more two-dimensional flow field.

.

Table 5.2: FSDV velocity component results for case studies I-VI. Right most column refers to the number of vibration mode velocity components calculated. Freestream velocity for aspect ratio 3.0 & 6.0 are 549m/s and 528m/s (Table 3.1)

Region of Interest	Coordinate	Q1 [UV] (m/s)	Q2 [UT] (m/s)	Q3 [DV] (m/s)	Q4 [DT] (m/s)	Events/sec
Case Study I: Aspect ratio 3.0 primary shock train structure [center axis vs. side-wall]						
Center-axis	[11.75,0.5,0]H	18.18 [0.033U_e,29.9%]	18.2 [0.033U_e,18.2%]	20.7 [0.037U_e,30.7%]	16.2 [0.029U_e, 20.4%]	83
Side-wall	[11.75,0.5,1.5]H	12.21 [0.022U_e,28.8%]	13.15 [0.024U_e,28.8%]	11.25 [0.020U_e,28.8%]	12.02 [0.021U_e,12.1%]	27
Case Study II: Aspect ratio 3.0 center-axis shock train structure [primary vs. secondary shock structure]						
Primary Shock	[11.75,0.5,0]H	18.18 [0.033U_e,29.9%]	18.2 [0.033U_e,18.2%]	20.7 [0.037U_e,30.7%]	16.2 [0.029U_e, 20.4%]	83
Secondary Shock	[11.75,0.5,0]H	25.6 [0.047U_e,27.8%]	21.7 [0.039U_e,34.4%]	25.4 [0.046U_e,26.2%]	29.7 [0.054U_e,9.84%]	71
Case Study III: Center-axis primary shock train structure [aspect ratio 3.0 vs. 6.0]						
Aspect ratio 3.0	[11.75,0.5,0]H	18.18 [0.032U_e,29.9%]	18.2 [0.033U_e,18.2%]	20.7 [0.037U_e,30.7%]	16.2 [0.030U_e, 20.4%]	83
Aspect ratio 6.0	[11.75,0.5,0]H	20.45 [0.039U_e,29.6%]	20.78 [0.040U_e,27.3%]	22.02 [0.041U_e,28.8%]	19.98 [0.038U_e,12.1%]	65
Case Study IV: Side-wall primary shock train structure [aspect ratio 3.0 vs. 6.0]						
Aspect ratio 3.0	[11.75,0.5,1.5]H	12.21 [0.022U_e,28.8%]	13.15 [0.024U_e,28.8%]	11.25 [0.020U_e,28.8%]	12.02 [0.021U_e,12.1%]	27
Aspect ratio 6.0	[11.75,0.5,3]H	18.36 [0.035U_e,28.8%]	17.15 [0.032U_e,27.3%]	18.75 [0.035U_e,28.8%]	17.84 [0.033U_e,12.1%]	30
Case Study V: Aspect ratio 6.0 primary shock train structure [center axis vs. side-wall]						
Center axis	[11.75,0.5,0]H	20.45 [0.039U_e,29.6%]	20.78 [0.040U_e,27.3%]	22.02 [0.041U_e,28.8%]	19.98 [0.038U_e,12.1%]	65
Side wall	[11.75,0.5,3]H	18.36 [0.027U_e,28.8%]	17.15 [0.029U_e,27.3%]	18.75 [0.030U_e,28.8%]	17.84 [0.028U_e,12.1%]	30
Case Study VI: Aspect ratio 6.0 center-axis shock train structure [primary vs. secondary shock structure]						
Primary Shock	[11.75,0.5,0]H	20.45 [0.039U_e,29.6%]	20.78 [0.040U_e,27.3%]	22.02 [0.041U_e,28.8%]	19.98 [0.038U_e,12.1%]	65
Secondary Shock	[11.75,0.5,0]H	23.58 [0.044U_e,28.8%]	22.18 [0.041U_e,27.3%]	22.89 [0.043U_e,29.6%]	24.67 [0.046U_e,12.1%]	62

5.7 RANS Simulations of Isolator Shock Train Formation

Both the fully started and partially unstarted modes of operation are simulated through the RANS calculations. The fully started cases are discussed in Chapter 3, with the partially unstarted simulations discussed below. Results from the aspect ratio 3.0 configuration are compared in detail to the experimental results discussed thus far in this chapter. Simulations are furthermore performed for the axisymmetric aspect ratios of 1.0 and 6.0, and the half nozzle aspect ratio 6.0 configuration. Observations are made regarding the effects of aspect ratio on shock train formation and compared to the experimental results obtained in this Chapter.

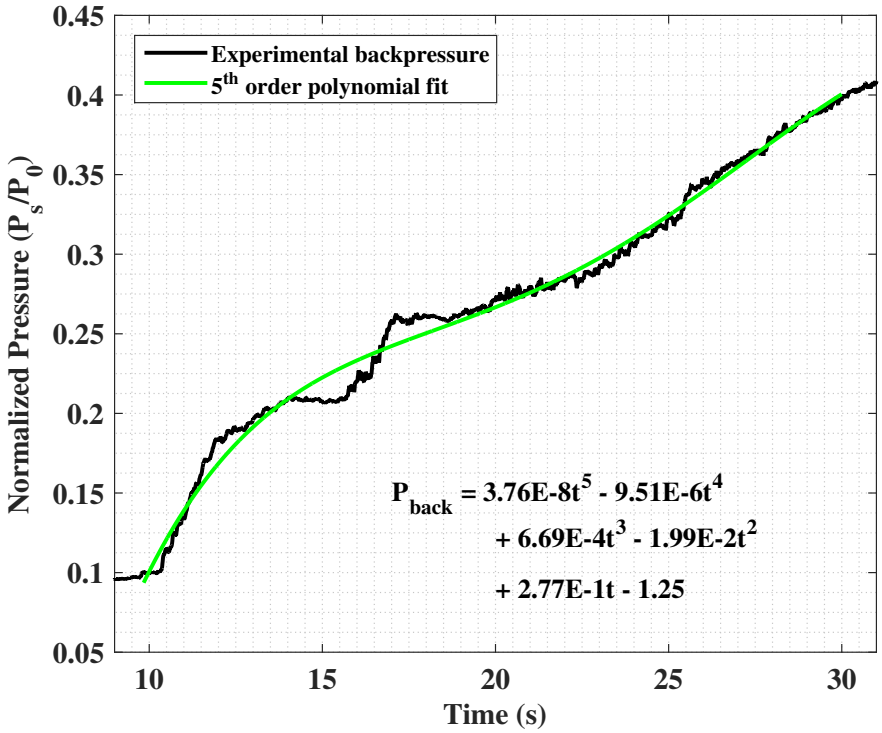

Figure 5.25: Derivation of the time-dependent polynomial backpressure equation for partially unstarted isolator RANS simulations based on aspect ratio 3.0 experimental backpressure measurement.

To simulate the partially unstarted mode of operation, the static back pressure boundary condition is increased in accordance with the time-dependent experimental back pressure measurement shown in Fig. 3.7a for the aspect ratio 3.0 case. All simulations performed in this work

are steady-state calculations, yet the time-dependent experimental backpressure measurement provides a pressure magnitude to assign to the outlet condition of the simulation to approximate a given time step of the experiment. The aspect ratio 3.0 experimental backpressure is provided again in Fig. 5.25, with only the partially unstarted portion of the run-time shown. A 5th order, least squares polynomial fit is applied to the experimental data and is shown in green, with the polynomial coefficients shown in the plot. Rather than obtaining a single value directly from the experimental data for a given time, this polynomial approximation is used to evaluate the accuracy of the approach for potential future time-dependent simulations that would require a time-dependent backpressure function.

5.7.1 Aspect Ratio 3.0 Simulations and Comparison to Experiment

The shock train formed inside the aspect ratio 3.0 isolator is shown in Fig. 5.26 representing the XY-plane and XZ-plane center-axis perspectives, along with geometric scaling in mm to compare the features. Shape factor analysis of the major and minor boundary layer profiles in Chapter 4 revealed that the major axis boundary layer is more susceptible to separation compared to its nozzle bounded (minor axis) boundary layer counterpart. This results in the XZ perspective shock foot boundary layer interaction location preceding that of the XY perspective, occurring at a longitudinal location of approximately X=340mm for the XZ plane interaction compared to X=370mm for the XY plane interaction.

The shock front is visualized isometrically in Fig. 5.27. A density threshold is utilized to clip density values less than $0.23 kg/m^3$ expected to occur upstream of the shock front. The corner boundary layer separation (1) is shown to occur approximately one duct height upstream of the centerline separation (2). Furthermore as discussed in Chapter 4, the higher shape factor of the major axis boundary layer results in more susceptible boundary layer separation as compared to the minor axis (3). The shock train front is therefore expected to located further upstream along the side-wall than the nozzle bounded lower/upper walls. Since it was not captured by the multiplane shadowgraph, the hypothesized three-dimensional shock train front structure visualized

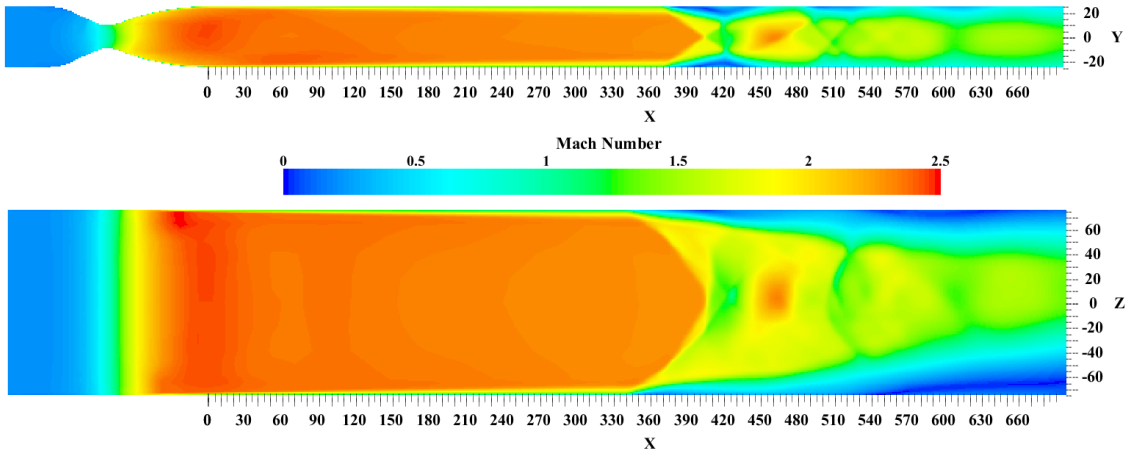

Figure 5.26: XY- and XZ-plane perspective of aspect ratio 3.0 RANS shock train formation $[P_3/P_0 = 0.3]$.

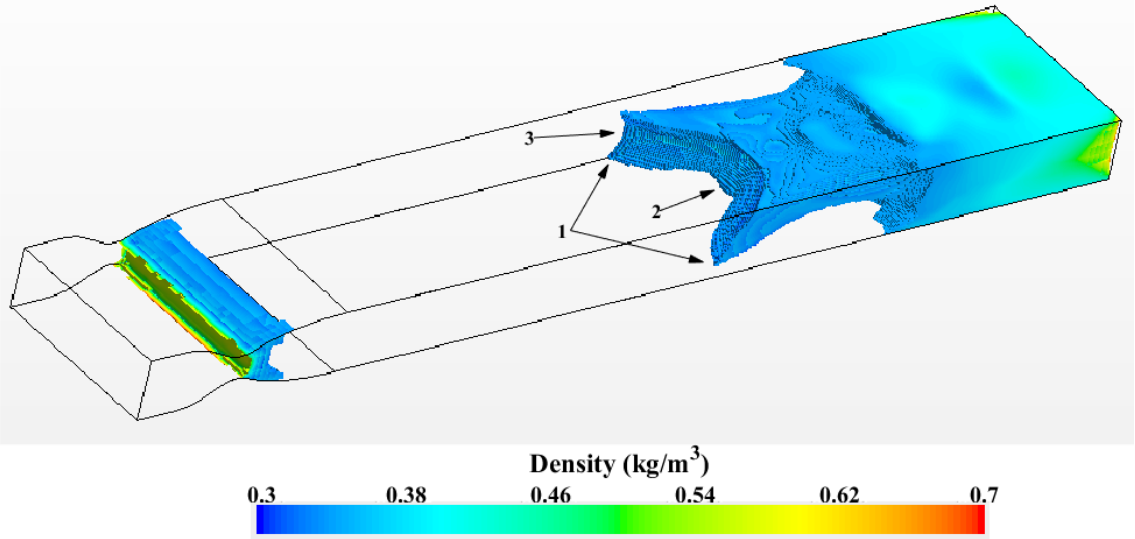

Figure 5.27: Isometric perspective of density threshold showing three-dimensional shock front (aspect ratio 3.0 RANS) $[P_3/P_0 = 0.3]$.

in the image reconstruction of Fig. 5.2 does not clearly show the flow separation point along the side-wall. The side-wall separation can be visualized to occur slightly upstream of the initial corner oblique shock planes intersection that is presented in Fig. 5.2.

A qualitative comparison between the experimentally obtained XY-plane shock visual and the steady-state computational calculation is performed in Fig. 5.28, with the color-map represent-

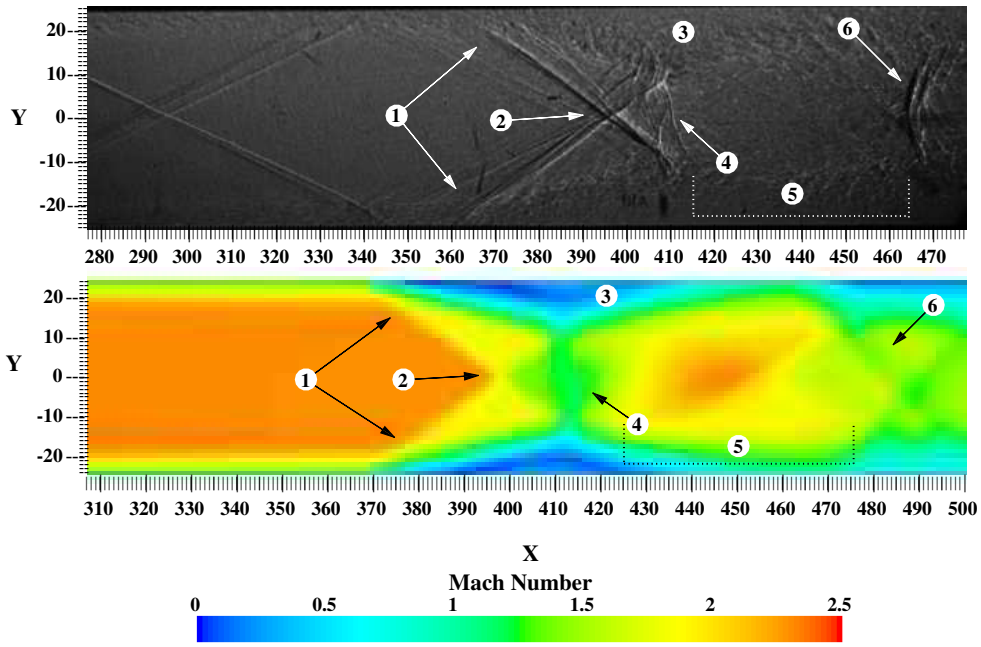

Figure 5.28: Experimental and computational comparison of aspect ratio XY-plane shock perspective. $[P_3/P_0 = 0.3]$.

ing contours of Mach number. The experimental schlieren image was acquired at a backpressure ratio (P_3/P_0) of 0.3, which is likewise the outlet pressure conditions used in the steady-state calculation shown. At this pressure setting (and subsequent longitudinal shock location in the duct), the incoming boundary layer thickness is on the order of 6mm (0.23") in both the experiment and simulation. The initial XY-plane shock train front is oblique in nature (1), with shock angles on the order of 37^o in both cases. The shock train leading edge is located at X=360mm in the experimental case, whereas its location is slightly downstream at X=370mm in the simulation. It is important to remember that the experimental (top) image represents a lateral axis line-of-sight integration of the derivative of the density gradient, whereas the simulation represents a single slice along the lateral axis. Thus, the location of the shock train leading edge in the experimental image corresponds to the corner flow separation visible in the XZ-perspective (Fig. 5.29).

The oblique shock intersection point occurs approximately at the centerline of the duct (2), and is accompanied by boundary layer separation (3) that reaches a maximum magnitude of approximately 15mm (0.6") from lower and upper walls in both cases. The oblique front is

followed by a shock structure of normal nature (4) that provides deceleration to subsonic conditions. Higher pressure gradients downstream of the normal structure compared to those inside the separated boundary layer push the boundary layer back towards the wall allowing the formation of an acceleration zone (5). This acceleration process is described in greater detail in Chapter 6. Finally, a secondary structure is formed downstream of the primary oblique structure (6), which is clearly normal in nature as shown in the spark schlieren image. The simulation does not acquire the normal structure but instead resolves a set of oblique shocks spawning from the secondary boundary layer separation. Potential grid refinement in this region can improve resolution of the shock features, which are expected to be relatively thin, for future investigation.

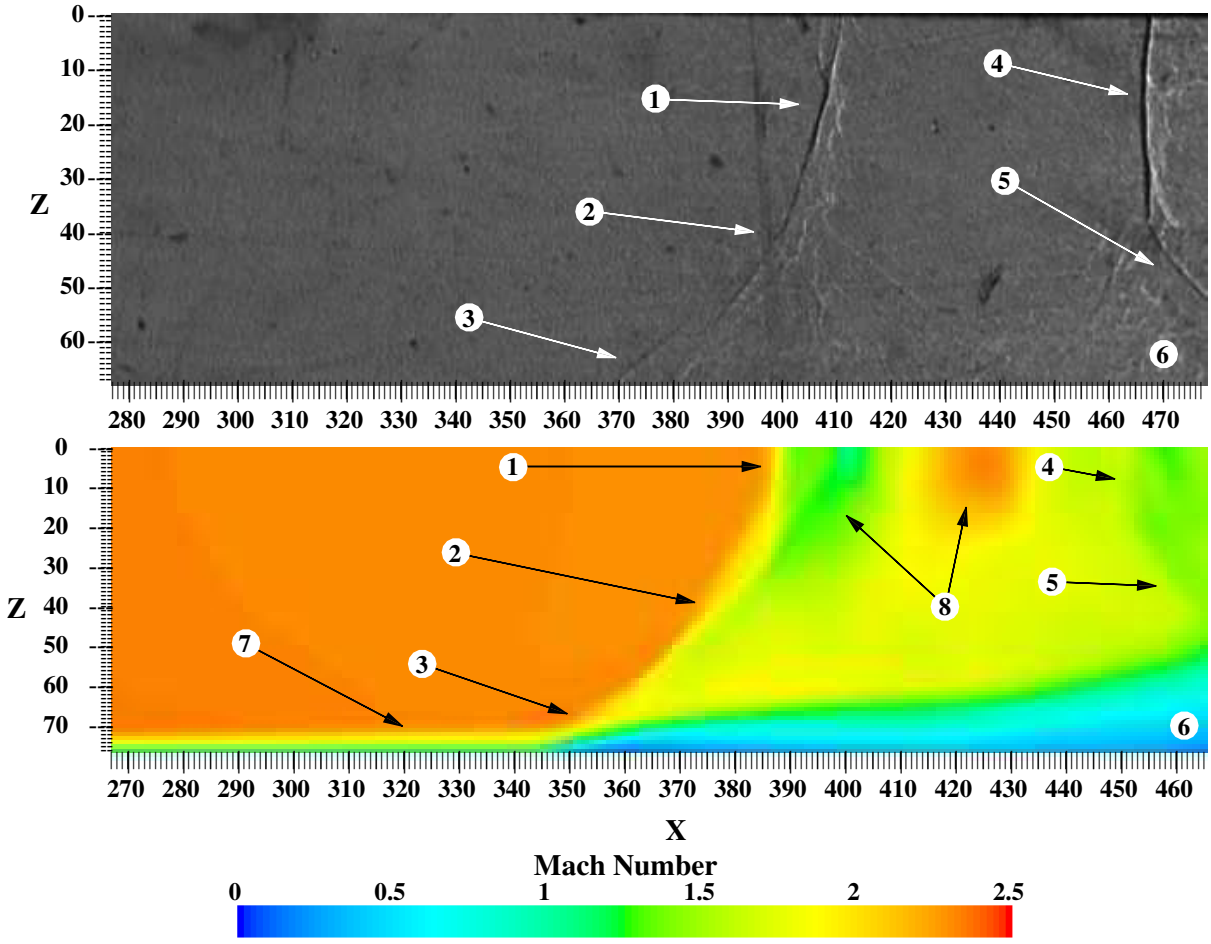

Figure 5.29: Experimental and computational comparison of aspect ratio XZ-plane shock perspective. $[P_3/P_0 = 0.3]$.

A similar comparison between experiment and computation is made for the XZ-plane perspective of the shock train shown in Fig. 5.29, showing the half width of the aspect ratio 3.0 test section. The transition between normal and oblique structure from the center to the outboard regions (1-3) is clearly visible in both images, along with the magnitude of flow deceleration increasing behind the normal shock front closest to the center-axis region (8). The secondary normal shock structure is shown interacting differently to the flow downstream of the center normal portion of the primary shock(4) and the outboard oblique portion of the primary shock (5) due to the different flow states behind each. The shock angle decreases further away from centerline (particularly visible in Fig. 5.1a). Slightly visible through a disturbed density gradient region in the experimental visualization, the sidewall boundary layer separation and interaction region (6) is of comparable magnitude in the computational study. Unlike the experimental measurement, the computational visualization extends all the way to the side-wall, with an approximately 5mm (0.19") thick side-wall boundary layer present.

One additional perspective of the XY and XZ mid plane representation of the aspect ratio 3.0 shock train is shown in Fig. 5.30. The transition of the shock train leading edge between the XY and XZ planes is similarly followed by the deceleration and re-acceleration zones prior to the secondary shock feature. A tertiary shock train feature is also visible. Finally, the continuous boundary layer separation induced core-area reduction does not suggest complete boundary layer re-attachment. The state of the exit plane core flow with respect to shock train position is further discussed in Chapter 6.

5.7.2 Effect of Aspect Ratio on Shock Train Formation

Simulations performed for other aspect ratios are discussed briefly below, with the main focus of discussion centered on the effect of aspect ratio on the formation of the three-dimensional shock front. Results are compared to the experimental observations made in Figs. 5.1, 5.5, and 5.7. All steady-state calculations discussed were performed with a static backpressure boundary condition of $P_3/P_0 = 0.3$.

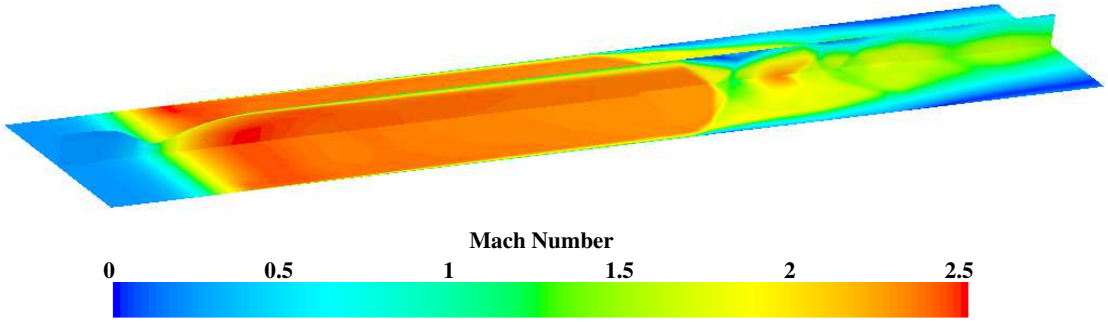

Figure 5.30: XY and XZ mid plane isometric perspective of aspect ratio 3.0 RANS shock train formation [$P_3/P_0 = 0.3$].

The XY- and XZ-plane perspectives of the aspect ratio 1.0 shock train is shown in Fig. 5.31. Although this computational aspect ratio 1.0 isolator utilizes the same Mach 2.5 nozzle as the aspect ratio 3.0 and 6.0 configurations, which is lower than the Mach 2.7 nozzle used in the experimental aspect ratio 1.0 configuration described in Fig. 3.6, qualitative comparisons between experiment and computation can still be made. The position of the shock train is shown to be more symmetric along both XY and XZ perspectives, with shock/boundary layer interaction occurring at approximately X=390mm in both planes, which is approximately 20mm downstream of the aspect ratio 3.0 leading edge. As is expected from Fig. 5.7, the shock train is oblique in nature from both perspectives. The isometric perspective of the three-dimensional shock front shown in Fig. 5.32 shows a very symmetrical structure around the isolator center-axis, with side- and lower/upper wall separation occurring symmetrically. This is expected from the observations made in Fig. 5.7.

The half-nozzle experimental aspect ratio 6.0 (also discussed in Fig. **??**) is shown in Fig. 5.33. As can be seen from the XZ-plane perspective, the shock front is dominated by the normal portion of the hybrid structure, making it more two-dimensional in nature. Larger deceleration zones are subsequently located behind the shock train front. Side-wall shock/boundary layer interaction (X = 425mm) occurs upstream of the lower/upper wall shock/boundary layer interaction

(X = 450mm). The shock train leading edge/boundary layer interaction occurs 55mm downstream of the aspect ratio 3.0 configuration, making the shock train 15% shorter. A similar observation is discussed in the experimental measure of shock train length in Chapter 6. The side wall and corner separation regions occur approximately one height upstream of the center flow separation region, compared to an estimated 0.88 duct heights in the experimental case (Fig. 5.5). The isometric perspective of the shock train front through the application of the density threshold is shown in Fig. 5.34. As discussed in Section 5.1, the shock train front is dominated by the normal shock structure and the whole feature is considerably more two-dimensional than the aspect ratio 3.0 and 1.0 configurations.

Even with the computations run to convergence, a slight degree of flow field asymmetry is noticeable around the center axis, particularly at the exit plane of the isolator. The higher aspect ratio isolator operation approaches the shock separation mode regime discussed in Fig. 2.5. This mode is characterized by large three-dimensional asymmetric separation regions where the pressure behavior along any given lateral cross-section is non-uniform, resulting in asymmetric flow features particularly in regions of large values of adverse pressure gradient near the outlet of the isolator duct.

This is likewise observed in the axi-symmetric aspect ratio 6.0 configuration shown in Fig. 5.35. With an axi-symmetric nozzle isolator duct height of 50.8mm (2.0”), the total isolator width is increased to 304.8mm (12.0”). The XY-plane perspective shows a very clear rendition of the multiple component shock train and associated re-acceleration zones before the flow diffuses to near sonic conditions at the isolator outlet. Diffusion to near sonic conditions, along with a reduced supersonic core flow area at the exit plane occurs for all aspect ratios considered. As can be seen in the XZ-plane perspective, the shock train front is still dominated by the normal shock portion of the hybrid structure.

Side-wall separation (X = 280mm) still leads the center flow field separation (X = 330mm) by approximately one duct height. The early onset of boundary layer separation compared to even the aspect ratio 3.0 case can be attributed to the increase in isolator cross-sectional area. The

computational aspect ratio 6.0 configuration with a duct height of 50.8mm (2.0") features a cross-sectional area of $15,484mm^2$, which is of course double the aspect ratio 3.0 cross sectional area of $7,742mm^2$ and quadruple the experimental aspect ratio 6.0 cross sectional area of $3,871mm^2$. As discussed in Fig. 3.7 for the experimental aspect ratios of 3.0 and 6.0, the lower mass flow area for lower cross-sectional ducts results in a slower rate of backpressure rise. This results in the lower cross-sectional area isolator shock train leading edge being located further downstream for the same backpressure ratio. A similar case can be made for an increase in the isolator cross-sectional area as observed in Fig. 5.35. Lastly, the re-acceleration zones seen in the XY-plane perspectives are also clearly marked in the XZ-plane, with shock angles decreasing as distance from center axis is increased due to the different flow states behind the normal and oblique portions of the shock train. The re-acceleration zone is discussed in greater detail in Chapter 6.

The computational efforts considered in this work were limited to steady state RANS simulations to resolve the formation of the three-dimensional shock front. Future time-dependent studies can reveal additional details regarding the shock train dynamics and unsteadiness. Additional detail, particularly in the boundary layer interactions, can be resolved through the use of direct numerical methods rather than the approximations utilized in the RANS approach. Finally, additional studies can reveal the extent of the flow quality at the isolator exit plane prior to entering the combustor region. Significantly diffused flow at the isolator exit, characterized by large scale boundary layer separation, is observed in all aspect ratios shown. This will play a critical role in the parameterization of combustor performance in the subsonic mode of operation that requires the shock train inside the isolator.

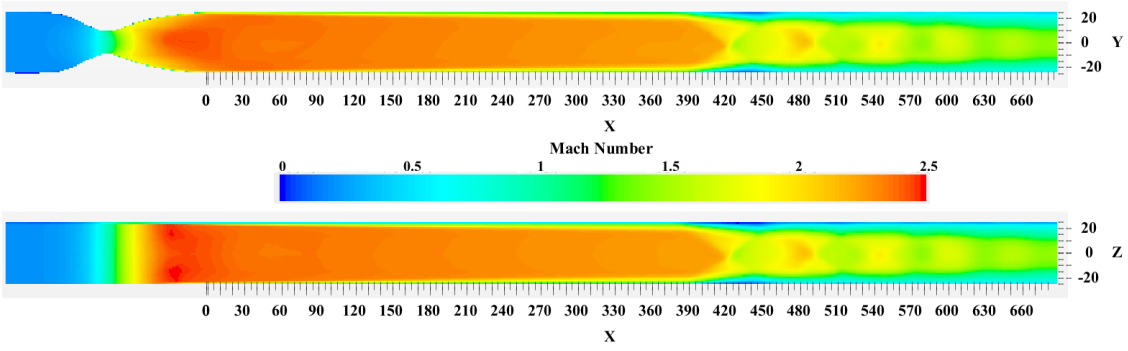

Figure 5.31: XY- and XZ-plane perspective of computational aspect ratio 1.0 configuration RANS shock train formation $[P_3/P_0 = 0.3]$.

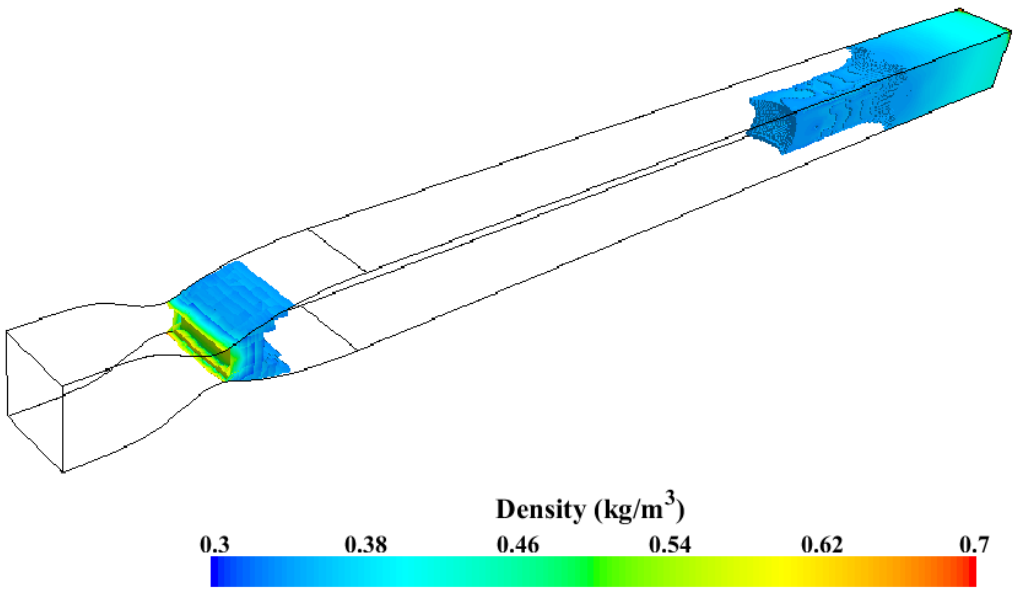

Figure 5.32: Isometric perspective of density threshold showing three-dimensional shock front (computational aspect ratio 1.0 configuration RANS) $[P_3/P_0 = 0.3]$.

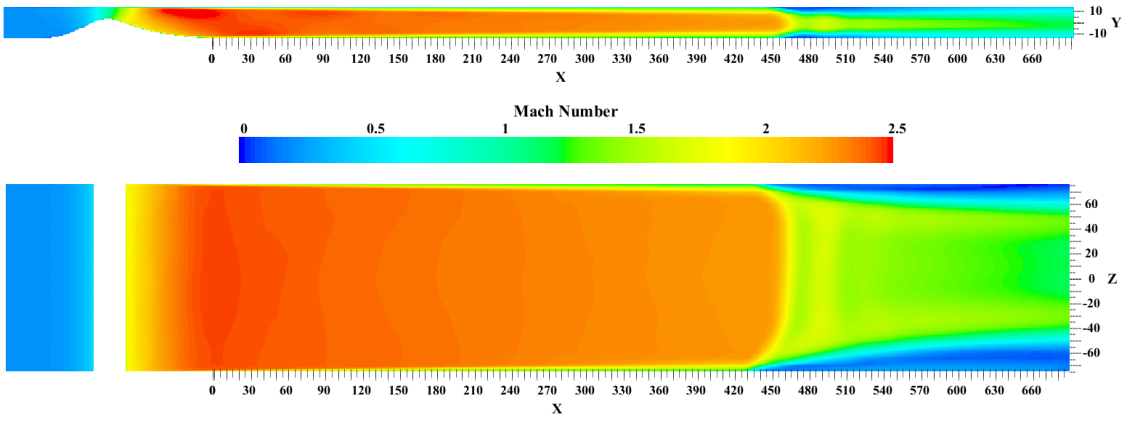

Figure 5.33: XY- and XZ-plane perspective of the experimental aspect ratio 6.0 configuration RANS shock train formation $[P_3/P_0 = 0.3]$.

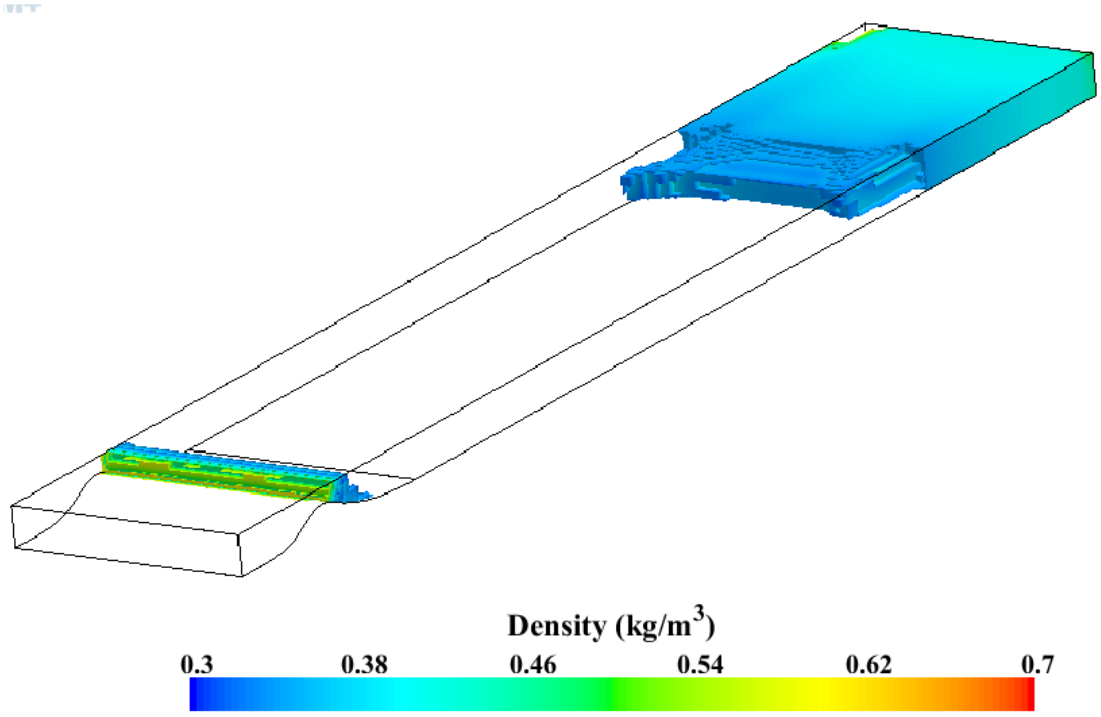

Figure 5.34: Isometric perspective of density threshold showing three-dimensional shock front (experimental aspect ratio 6.0 configuration RANS) $[P_3/P_0 = 0.3]$.

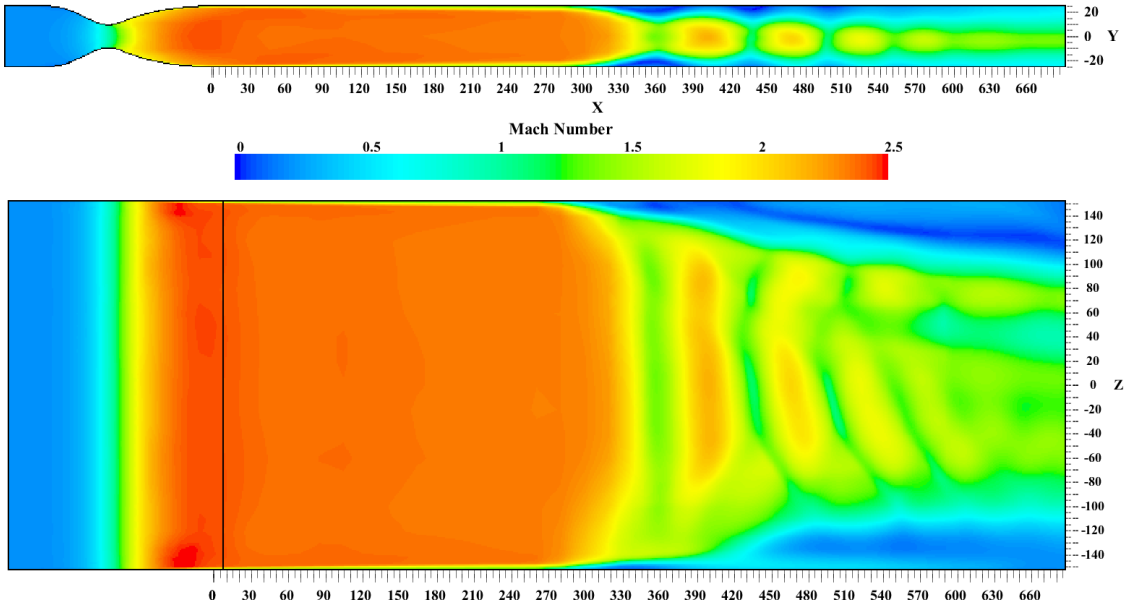

Figure 5.35: XY- and XZ-plane perspective of the computational aspect ratio 6.0 configuration RANS shock train formation [$P_3/P_0 = 0.3$].

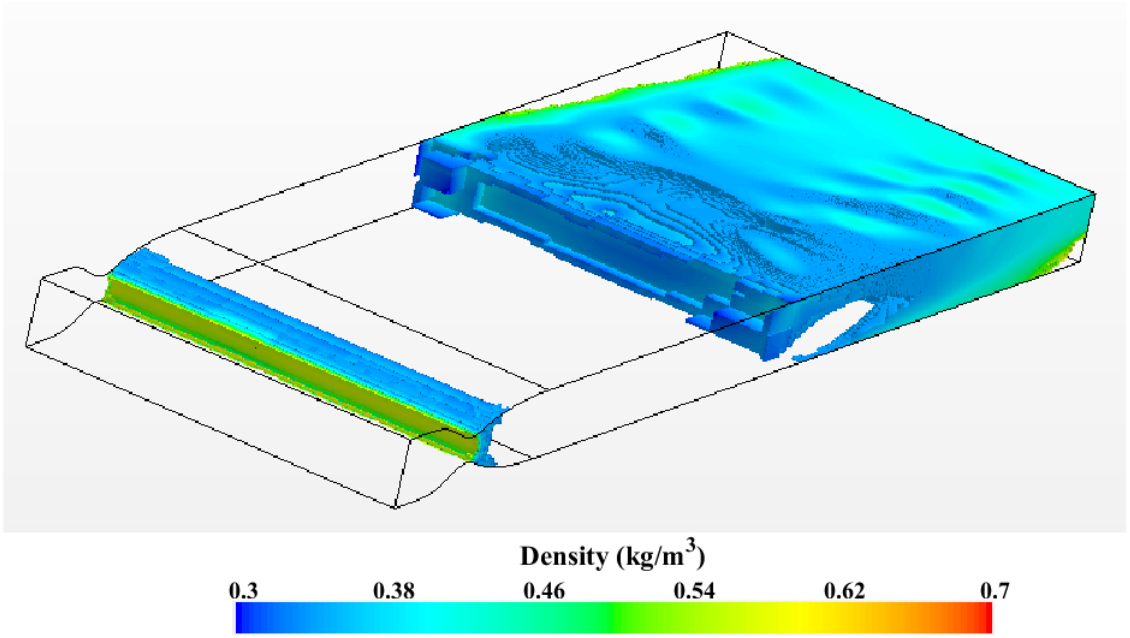

Figure 5.36: Isometric perspective of density threshold showing three-dimensional shock front (computational aspect ratio 6.0 configuration RANS) [$P_3/P_0 = 0.3$].

Chapter 6: Global Isolator Flow Physics

This chapter focuses on the analysis of the flow physics across the entirety of the isolator duct. In particular, the focus in this chapter is on the introduction of a modified isolator shock train length relation based on experimental measurements and observations of the three-dimensional flow physics described in Chapter 5. Several side-studies are also presented in this chapter including synchronized full isolator length schlieren and wall pressure measurement, the description of the shock train re-acceleration process accompanied by quantitative static pressure analysis derived from the CFD studies, isolator exit state Fanno flow calculations, and exit plane YZ-plane Mie-scattering flow visualization comparing the core flow area before and after shock train passage.

6.1 Rectangular Isolator Shock Train Length Relations

6.1.1 Experimental Derivation of Shock Train Length

Experimental measurements of pseudo shock train length (Fig. 1.6) are obtained using the 16 isolator lower wall centerline static pressure taps (Fig. 3.4). An example of pseudo shock train length derivation utilizing the static pressure measurement is shown in Fig. 6.1, which represents the pressure data at a single instance in time. The pseudo shock train is defined as both the shock train (composed of the visible shock structures) and the downstream mixing region (continuous static pressure rise), according to Fig. 1.6. The leading edge of the shock train is marked with the vertical green line, defined as the location of either: (a) a 5% increase from the fully started pressure levels ($(P_i/P_0)_{steady}$), or (b) an increase of ΔP ($P_i - P_{i-1}$) of five standard deviation values from the fully started pressure level. The average static pressure distribution of the fully started flow (steady flow) is shown in Fig. 6.1 as the magenta line for reference. For more accurate

measurements near the outlet plane of the isolator, an additional pressure tap at X=631.19mm was used to offset the otherwise large separation between pressure measurements.

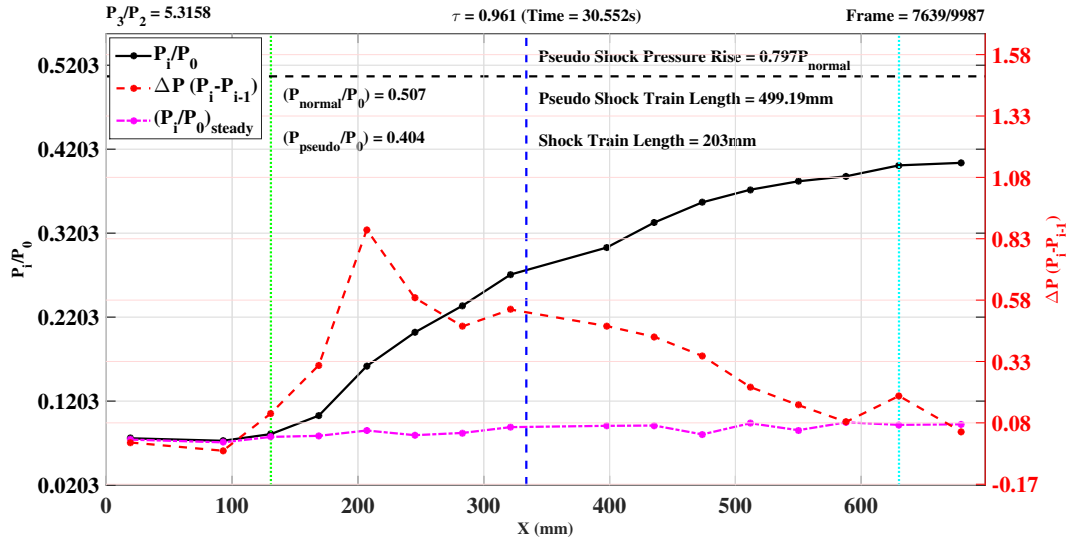

Figure 6.1: Experimental measurement of the pseudo shock train length relation.

The length of the observed shock train structure (visible density gradient in the form of shocks) is marked by the vertical blue line as derived from visualization studies. The trailing edge of the entire pseudo shock region, marked by the vertical cyan line, is marked by the vertical cyan line, defined as the location of either: (a) a $\leq 1\%$ increase of the next available downstream P_i/P_0 measurement, or (b) an increase of ≤ 1 fully started flow pressure level standard deviation. Final pressure rise at the end of the pseudo shock can be compared to the pressure expected behind a single normal shock at the same inlet flow parameters, denoted by the horizontal black line. The average static pressure rise behind the shock train in both aspect ratios 3.0 and 6.0 configurations is approximately 80% that of the normal shock pressure rise.

6.1.2 Original and Modified Shock Train Length Relation

Duct longitudinal centerline axis static pressure are used in combination with the upstream corner flow separation length scale to derive an estimate of the total pseudo shock train length. As described in the multiplane shadowgraph analysis in Chapter 5, corner flows separate ahead

of the center flow field by approximately one duct height in both the aspect ratio 3.0 and 6.0 configurations. This length scale is added to the centerline measurements to resemble the true leading edge location of the pseudo shock train and its total length. Resulting length values for various levels of isolator pressure ratio (backpressure rise) are shown in the Fig. 6.2 for both aspect ratios, among the shock train relations discussed below. The error-bars resemble the spacing between the static pressure taps of 38mm, accounting for the leading edge location uncertainty.

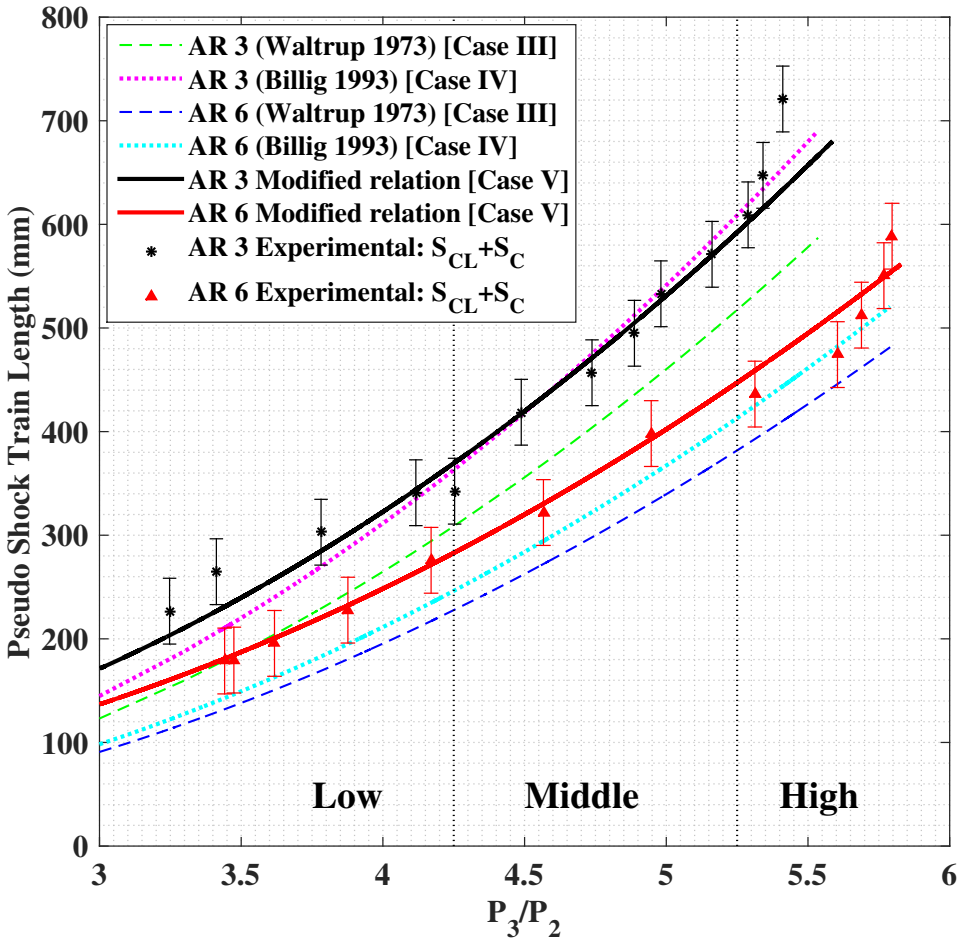

Figure 6.2: Correlations between experimental shock train length and original empirical relations of Waltrup & Billig (Eq. 6.1), Billig's original rectangular modification (Eq. 1.2), and the proposed θ' modification (Eq. 6.3).

The original shock length relation by Waltrup & Billig, rewritten in Eq. 6.1, is compared to the experimental data in Fig. 6.2 for both aspect ratios. Both the Waltrup & Billig original (Eq.

6.1) and later Billig modification (Eq. 6.2) utilize the S_{CL} term for shock train length to indicate that the relationship is based on centerline pressure measurements alone.. The duct diameter is replaced by the duct height, and θ and $\Re_{theta}$ are evaluated along the duct minor axis only. The value for Mach number, θ, and $\Re_{theta}$ are all evaluated at the inlet of the isolator duct. The shock length relation based on circular ducts is shown underestimating the experimentally derived pseudo shock train length across the entire pressure ratio regime. This is somewhat expected, given that the quadratic equation of Eq. 6.1 was derived from a large experimental parametric data set based on circular ducts where the three-dimensional flow features discussed in this thesis are not expected to play a large role.

$$S_{CL} = 50\frac{D^{1/2}\theta^{1/2}}{(M_2^2-1)Re_{\Theta}^{1/4}}(\frac{P_3}{P_2}-1)+170(\frac{P_3}{P_2}-1)^2 \tag{6.1}$$

Quantitative analysis of the correlation strength is shown in the form of a Root Mean Square Error (RMSE) analysis in Table 6.1. RMSE is calculated according to Eq. 4.11, where y_{exp} represents the experimentally derived shock train length and y_{sim} can be substituted by y_{cor} to resemble the correlation derived shock train length value for a given pressure ratio respectively. Case I represents the correlation between Eq. 6.1 and the shock train length derived from the centerline measurement only. Case III represents the correlation between Eq. 6.1 and the total length of the pseudo shock train (centerline pressure length in addition to the corner length scale), which is shown in Fig. 6.2. As expected, accounting for the true length of the pseudo shock train by including the corner separation length scales worsens the correlation between the experimental shock train length values and those predicted by Eq. 6.1. Case III RMSE averages 78.2 and 57.8 across the entire pressure ratio range for aspect ratio 3.0 and 6.0 configurations respectively, with the highest RMSE occurring at the larger pressure ratios for both aspect ratios, where three-dimensional effects can be expected to be more severe.

Improvement is shown through the application of the rectangular modification introduced by Billig in 1993, and restated in Eq. 6.2. As discussed in Chapter 1, the theoretical derivation includes a $Re_{\theta}^{1/5}$ term, which results in longer shock train lengths for identical isolator inlet parameters as

compared to Eq. 6.1. Case II of the RMSE analysis shown in Table 6.1 represents the correlation between the pure centerline derived data and the length values predicted by Eq. 6.2. Case IV, presented in Fig. 6.2, represents the correlation between total psuedo shock experimental length and the relationship derived shock train length. RMSE analysis suggests that with the inclusion of the total psuedo shock train length (Case IV), the aspect ratio 3.0 average correlation improves across the entire pressure regime by 22%. Correlation for the aspect ratio 6.0 configuration worsens however, with average RMSE error increasing by 56% from Case II to Case IV. Performance of a reliable shock train length relation for rectangular ducts must take into account the effect of aspect ratio, as current methods do not translate favorably across aspect ratios.

$$S_{CL} = 50\frac{H^{1/2}\theta^{1/2}}{(M_2^2-1)Re_{\Theta}^{1/5}}(\frac{P_3}{P_2}-1) + 170(\frac{P_3}{P_2}-1)^2 \tag{6.2}$$

The proposed rectangular isolator modification to Waltrup & Billig's 1973 original relation for circular ducts is expressed in Eq. 6.3, and shown as Case V in Fig. 6.2 and Table 6.1. The updated shock train length relation, termed the θ' modification, accounts for three distinct characteristics common to rectangular isolators. Where Billig's original 1993 rectangular modification utilized a power decrease from $Re_{\theta}^{1/4}$ to $Re_{\theta}^{1/5}$ to yield overall longer shock train lengths, the currently proposed modification looks to include the specific characteristics of the rectangular isolator to account for the impact on increased isolator shock train lengths:

$$S = 50\frac{D_H^{1/2}\theta'^{1/2}}{(M_2^2-1)Re_{\Theta'}^{1/4}}(\frac{P_3}{P_2}-1) + 170(\frac{P_3}{P_2}-1)^2 + S_C \tag{6.3}$$

- First, the potential for a planar nozzle geometry fed rectangular duct to generate major- and minor-axis boundary layer asymmetry is accounted for in terms of the θ' parameter, which represents a square root of sums of the minor axis θ_1 and major axis θ_2 values. This concept is visualized in Fig. 6.3 to account for the importance of θ' in the boundary layer separation driven shock train dynamics. Including the value of θ_2 increases the overall magnitude of $\frac{\theta^{1/2}}{Re_{\theta}^{1/4}}$ thus increasing the overall shock train length.

- Second, the effect of aspect ratio is included in terms of the hydraulic diameter, which is calculated according to the following equation: $D_H = \frac{2H_1H_2}{H1+H_2}$. H_1 and H_2 represent the minor and major axis duct lengths scales (height and width) respectively. Higher aspect ratios result in a lower hydraulic diameter values, 1.7 compared to 3.0 for the aspect ratio 6.0 and 3.0 configurations respectively. This contributes to the lower shock train lengths expected for higher aspect ratio ducts, as can be seen in the experimental shock train length representation in Fig. 6.2 and the discussion in Fig. 3.7.

- Lastly, the experimentally derived corner shock boundary layer separation length scale is added in the form of the S_C term. For the aspect ranges considered in the experimental and computational approach, the corner flow separation is shown to precede the center flow field separation by approximately one duct height.

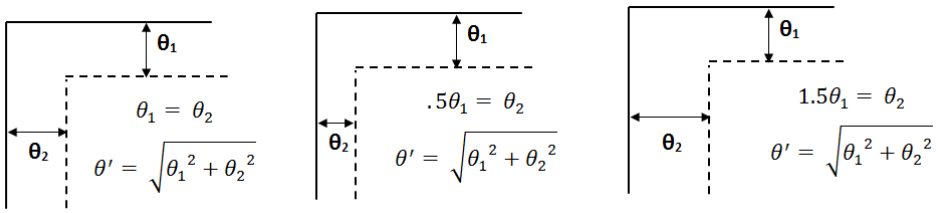

Figure 6.3: Conceptualization of the θ' parameter used in the shock train length relation modification.

The θ' modification is only compared to the total pseudo shock train length values provided in Fig. 6.2 and is listed as Case V in Table 6.1. Compared to the aspect ratio 3.0 Cases III and IV, the θ' modification provides a 64% and 10% average correlation improvement respectively (across the entire pressure ratio spectrum). Correlation is furthermore improved for the aspect ratio 6.0 case, where 79% and 63% improvements in average RMSE are shown for Cases III and IV respectively.

Providing a reliable shock train length relationship model that holds for a wide range of aspect ratios is critical in yielding a reliable isolator design tool. The original relation by Waltrup & Billig was shown to provide favorable correlation for a wide range of diameters in the original

	$AR3.0$			$AR6.0$		
Case	Low	Middle	High	Low	Middle	High
I	31.6	18.7	76.8	9.8	20.4	33.7
II	18.7	61.2	42.3	5.9	8.8	30.2
III	70.1	50.4	114.0	48.6	59.0	66.0
IV	37.2	22.4	34.1	35.2	34.4	34.5
V	21.2	18.7	46.0	4.3	6.9	27.4

Table 6.1: Root Mean Square Error analysis results for aspect ratio 3.0 and 6.0 shock train length relations. 'Low' pressure ratio represents $P_3/P_2 < 4.25$, 'Middle' pressure ratio represents $4.25 < P_3/P_2 < 5.25$, and ' High' represents $P_3/P_2 > 5.25$

.

1973 study [58]. The later rectangular modification by Billig has not been exposed to as many verification studies, with Sullins' work on low aspect ratio rectangular ducts being the principle reference [60]. The trend of improved correlation for higher aspect ratio can prove to be an important attribute of the θ' modified relation.

6.1.3 Isolator Length Critical Pressure Ratio

The critical pressure ratio as a function of isolator length is plotted in Fig. 6.4. As the shock train leading edge is first detected at a certain static pressure measurement station, the P_3/P_2 (P_{out}/P_{in}) pressure ratio is noted and the 'isolator length' is calculated by subtracting the position of the pressure tap from the total isolator length. This is akin to that specific pressure measurement location being the inlet plane of our shortened isolator. This particular P_3/P_2 is called the critical pressure ratio ($(P_{out}/P_{in})_{crit}$) as it would mean that leading edge shock train/inlet interaction is imminent. Like the analysis of Fig. 6.2, the error bar width accounts for the separation in pressure taps used to evaluate the location of the shock train leading edge, while the marker size accounts for the uncertainty in the critical pressure ratio calculation. The experimental data is fitted with two different correlations based on the observed behavior of the system, a quadratic fit for isolator pressure ratios below 5.0 and a linear fit for pressure ratios greater than 5.0.

The aspect ratio 3.0 configuration is capable of supporting a larger critical pressure ratio prior to unstart for isolators less than 300mm in length, corresponding to a $(P_{out}/P_{in})_{crit}$ ¡ 5.0.

A quadratic polynomial fit is applied to this segment, which provides a favorable correlation for the aspect ratio 3.0 experimental data, and a reasonable correlation within the error bounds for the aspect ratio 6.0 configuration. Correlation coefficients are shown for the quadratic correlation provided. For isolator lengths larger than 300mm, the higher aspect ratio is capable of supporting higher $(P_{out}/P_{in})_{crit}$ ratios. This region in the isolator operational regime also appears significantly more linear, with the linear approximation providing favorable correlation within the bounds of the experimental error.

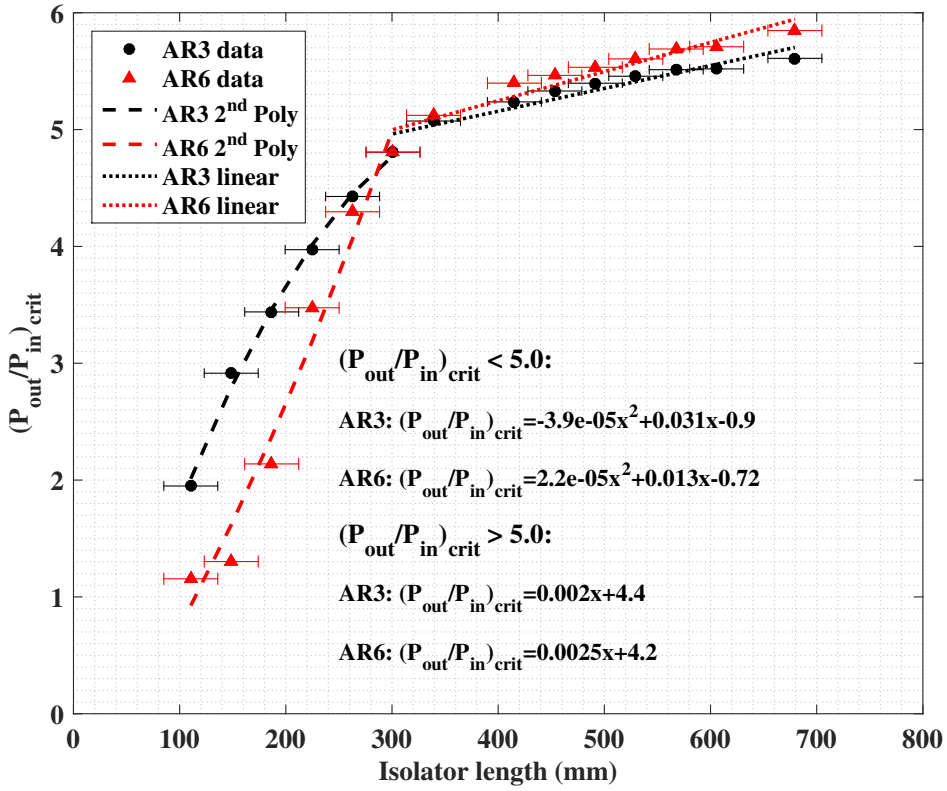

Figure 6.4: Critical pressure ratio as a function of isolator length for aspect ratio 3.0 and 6.0.

6.2 Global Isolator Shock Train Dynamics

To study the global isolator shock train propagation behavior, a synchronized horizontal knife-edge schlieren visualization of the entire test section length with accompanying lower wall

centerline static pressure measurements is performed. Results are presented in Fig. 6.5 for six individual time steps. The pressure data points in the bottom plot are aligned with their respective locations in the top schlieren visualization, with marker size representing the error bounds of the experimental measurement. Since the parabolic schlieren mirror are only 250mm in diameter, four different runs are performed utilizing the reference backpressure tunnel trigger system to stitch the different images into one large test section image.

The normalized static pressure behavior is shown on the left axis of the pressure plot, while the pressure difference ($\frac{P_{i+1}-P_i}{P_0}$) is shown on the right axis. The latter is included to highlight the static pressure change between consecutive pressure taps as the magnitudes of the normalized pressures are rather low. As shown in Fig. 3.1, the wind tunnel window frame and test section structure obstructs the most downstream portion of the isolator from being viewed. While the isolator is 698.5mm long, the field of view only extends 647mm from the isolator origin. The most downstream pressure tap (X=679.45mm) is thus out of view from the schlieren visualization area. The $\frac{P_{i+1}-P_i}{P_0}$ measurement is included in part to show the behavior of the most downstream pressure tap. Finally, the pressure taps in the diffuser section used to evaluate the experimental boundary conditions for the CFD simulations (Fig. 3.38) were not yet available at the time of this pressure survey, hence the most downstream pressure tap is the aforementioned isolator pressure tap at X=679.45mm.

The first time step (Fig. 6.5a) represents the fully started mode of the isolator duct, where the backpressure is low enough to keep the boundary layer attached inside the isolator section and thus no shocks form. The $\frac{P_{i+1}-P_i}{P_0}$ line shows a steadily increasing wall static pressure value due to frictional effects inside the duct. The second time step (Fig. 6.5b) represents the first instance of backpressure rise as measured by the most downstream isolator static pressure tap. A sharp increase in the $\frac{P_{i+1}-P_i}{P_0}$ ratio is seen to occur at the downstream end of the isolator (1). Boundary layer separation and incipient shock train formation, still out of view of the schlieren window, is observed to occur for critical $\frac{P_{back}}{P_0}_{crit}$ ratios exceeding 0.11 for the aspect ratio 3.0 study. Critical backpressure ratios for the aspect ratio 6.0 configuration were found to be comparable although

the initial backpressure rate of increase is slower (Fig. 3.7b)

The third timestep (Fig. 6.5c) shows the primary shock train structure located inside the duct, with the preliminary corner separation occurring at X=555mm from the origin (2). The pressure tap at X=567.69mm measures the boundary layer separation induced magnitude (3). The closest pressure tap in the upstream direction (X=529.59mm) does not sense the pressure change (4). As was seen in the experimental and computational analysis of the lower wall boundary layer, the subsonic boundary layer is relatively small. Limited upstream subsonic boundary layer communication is observed in the isolator configurations studied.

The fourth timestep (Fig. 6.5d) shows the secondary normal shock established in the test section at X=590mm (5), approximately 90mm upstream of the initial corner separation (6). Pressure rise, first measured by the X=491mm pressure tap (7), is gradual across the visible shock train structure. The secondary normal shock structure, embedded in the center axis region of the flow field, does not noticeably change the pressure behavior measured by the wall bound static pressure taps.

The fifth timestep (Fig. 6.5e) shows the pseudo shock feature, where the pressure rise occurs across the visible shock train structure (8) and the subsequent interaction region (9). The majority of the pressure rise occurs across the visible structure (8), as can be seen by the values of the $\frac{P_{back}}{P_0}$ curve. The reduction in pressure change slope, which marks the end of the pseudo shock region as evaluated by the criteria stated along with Fig. 6.1 is noticeable toward the downstream end of the isolator (10). The final timestep shows (Fig. 6.5e) the shock structure located inside the second visualization quadrant, with the lower wall corner separation/leading edge located at an approximate longitudinal location of X=165mm (11) and detected by the X=148mm pressure tap (12). Once more, the reduction in $\frac{P_{back}}{P_0}$ toward the downstream end of the diffuser signals the end of the pseudo shock region (13). Overall pressure rise occurs gradually.

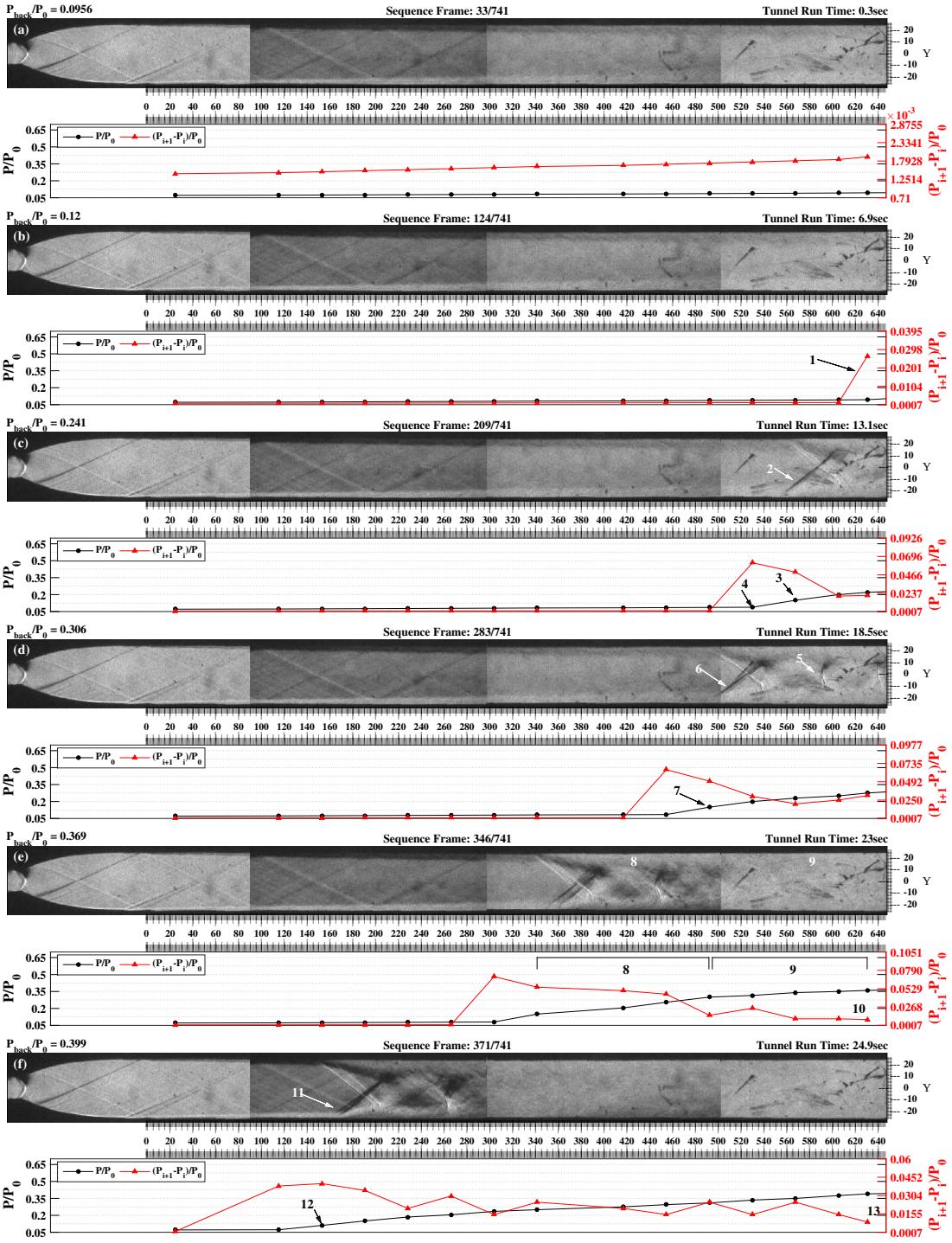

Figure 6.5: Synchronized time history representation of isolator shock train propagation and lower wall centerline static pressure measurement.

6.3 Shock Train/Boundary Layer Interaction and the Re-Acceleration Process

An important component of the visible shock train length is the re-acceleration process, briefly described and shown in Chapter 5. The number of components in the shock train depend in part on the nature of the acceleration process and when it yields a diffused and bulk subsonic flow. To more thoroughly understand the re-acceleration process, the fundamental structure of the shock/boundary layer interaction is revisited in Fig. 6.6, with the size of the subsonic boundary layer greatly enlarged for illustration purposes. Along with the re-acceleration process sketch in Fig. 6.7, it is important to remember that Fig. 6.6 represents a simplified two dimensional representation of the flow physics in the isolator, which as shown in Chapter 5, is highly three-dimensional in nature. Nevertheless, breaking the complex three-dimensional shock front down into simplified two-dimensional analysis allows for the formation of valid observations that hold at least in a certain span along the duct lateral axis.

The two dimensional perspective schematic of the shock/boundary layer interaction presented in Fig. 6.6 is based on illustrations provided by Shapiro [26]. In the traditional description of the shock/boundary layer sketch the incident shock, labeled as the 'upper wall shock train leading edge' in Fig. 6.6, is assumed to cause the initial boundary layer growth and separation. Subsequently, pressure gradients propagating upstream through the subsonic portion of the boundary layer result in the formation of compression wavelets that merge into an upstream compression shock, labeled as the 'lower wall shock train leading edge'.

In the description of the shock train/boundary layer interaction however, the boundary layer growth and separation is assumed to be initially caused by pressure gradients stemming from combustor disturbances downstream of the isolator, and the formation of the upper and lower wall shock train leading edges (as depicted in Fig. 6.6) are a consequence of said boundary layer separation. The following description offers a generalized outline of the lower wall shock train/boundary layer interaction in the two-dimensional perspective, yet similar observations can be expected along the upper wall region.

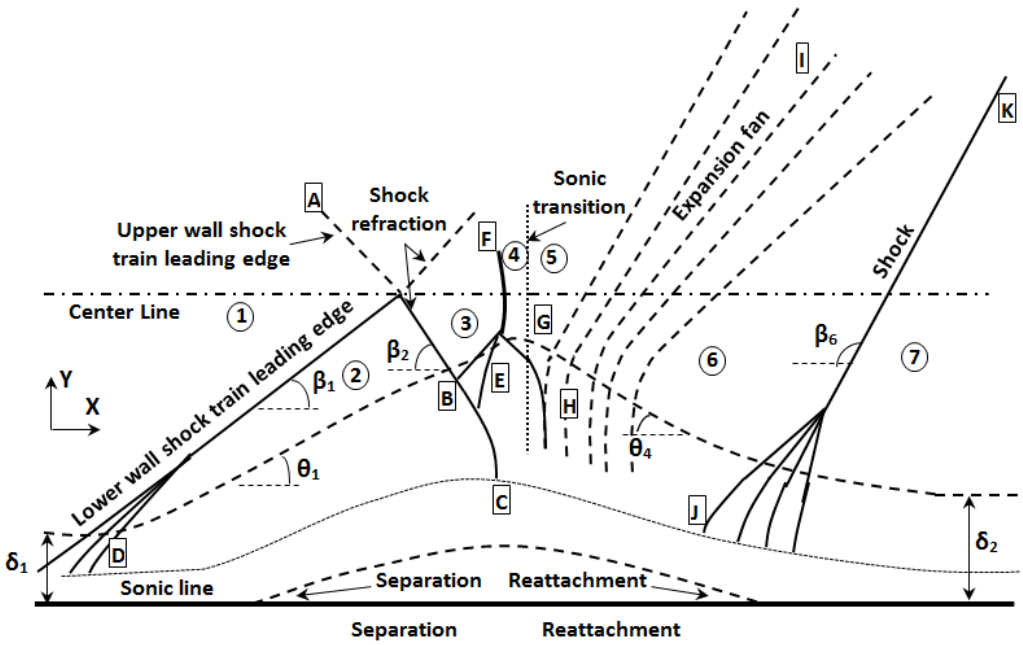

Figure 6.6: Two-dimensional sketch of the shock train/boundary layer interaction [adapted from Ref. [26]].

- The boundary layer separation causes the formation of boundary layer embedded compression wavelets (D), which ultimately merge into the 'lower wall shock train leading edge' on the lower wall. This initial boundary layer separation magnitude is characterized with a deflection angle θ_1, which guides the formation of the β_1 initial oblique shock front as discussed in Fig. 5.16. A corresponding event occurs along the upper wall and forms the 'upper wall shock train leading edge' .

- The 'upper wall shock train leading edge' (A-B) interacts with the separated boundary layer and continues down to the sonic line as the shock (B-C). Due to the changing velocity profile inside the boundary layer, the shock (B-C) bends as it propagates toward the sonic line. Shock wavelets (E) refract off of this shock bend and coalesce into the normal structure (E-F).

- The region immediately downstream of the normal structure (E-F), region 4, is expected to be subsonic. Because the interaction between the normal shock (E-F) and the separated

boundary layer provides pressure gradients that further increase the boundary layer thickness in region (E), the subsonic portion of the flow re-accelerates to sonic conditions due to a reduction in core flow area. This phenomena is governed by the 'Area-Velocity Relation ' , $\frac{dA}{A} = \frac{dU}{U}(M^2 - 1)$, which states that a subsonic flow passing through a control volume of decreasing cross-sectional area will accelerate.

- The pressure levels near region (G) are expected to be higher than the boundary layer embedded region (F) because the stream in region (G) progresses through shocks of larger strength. This causes the streamlines to turn back to the wall and forces the boundary layer to reattach, turning toward the wall at a turning angle of approximately θ_4. The flow is thus supersonic and accelerating in region 5, since the Area-Velocity Relation states that a supersonic flow passing through a control volume of increasing cross-sectional area will accelerate.

- The turning of the boundary layer toward the wall will turn the flow streamlines away from each other, and thus generate expansion features along the path (H-I). These features furthermore accelerate the flow field. Due to the presences of the lower wall boundary, continuity dictates that the flow will turn back into itself. This turning action causes compression wavelets (J) to form along the concave part of the turning boundary layer. These wavelets ultimately coalesce into the compression shock (J-K).

- Flow is shown to re-attach in this schematic, stemming from experimental observations made in the downstream region of the aspect ratio 3.0 configuration (Fig. 5.16a). Flow re-attachment is also observed in the upstream region of the aspect ratio 3.0 configuration (Fig. 5.16b). Re-attachment is not as clearly shown in the aspect ratio 6.0 configuration, which aligns with computational observations made by Nedungadi & Van Wie [39] which showed that boundary layer separation is less likely to re-attach with an increase in either Mach number or aspect ratio.

6.3.1 The Shock Train Re-Acceleration Process

The sketch provided in Fig. 6.6 represents a generic shock train leading edge/boundary layer interaction condition and serves as an introduction to the description of the re-acceleration process below. Sketched in Fig. 6.7, the process description covers the primary oblique and secondary normal structures, but is expected to continue to occur downstream of this pair and generate additional normal structures until the flow diffuses to subsonic in the bulk. The sketch does not include the depiction of the sonic line but shock structures propagating into the boundary layer are shown changing in direction to account for the velocity profile inside the boundary layer. Figure 6.6 can be referenced for greater detail pertaining some of the generalized descriptions presented below.

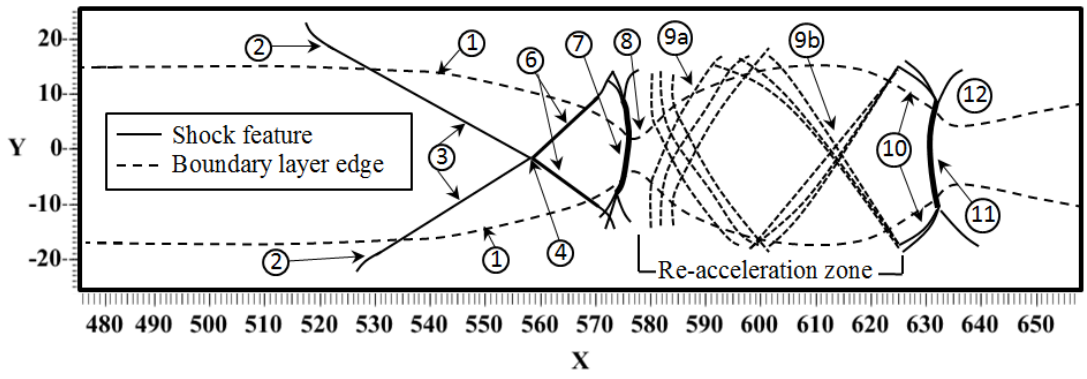

Figure 6.7: Two-dimensional sketch of the shock train re-acceleration process.

As discussed, the boundary layer separation (1) causes the streamlines to turn into each other and initiate the formation of compression wavelets inside the upstream boundary layer (2) that ultimately coalesce into the oblique shock structure (3). The initial oblique shock planes intersect (4) and form a pair of refracted shock structures (6). Due to the interaction with the separated boundary layer, the refracted shock structure is bend as it propagates along the boundary layer, causing compression wavelets to refract from the bend shock structure and form the first normal shock structure (7). Interaction between the normal shock (7) and the separated boundary layer further increases the separation magnitude, allowing the subsonic flow directly downstream

of the normal shock to re-accelerate to sonic conditions via the Area-Velocity Relation. Due to the passage across stronger shock structure, the larger pressure gradients in the center-axis region compared to those in the boundary layer push the boundary layer back toward the wall, resulting in the formation of an expansion fan (9a). This expansion fan interacts with and reflects from the opposing wall boundary layer sonic line. Together with the boundary layer turning parallel to the wall due to the continuity requirement, this results in the formation of compression wavelets that ultimately coalesce into a compression feature (9b). Finally, this compression feature interacts with the boundary layer and sonic line to result in refracted structures (10) to coalesce into the secondary normal structure (11). Subsequently, interaction with the boundary layer causes boundary layer thickening and the re-acceleration process is repeated downstream of the secondary normal shock structure (12).

6.3.2 The Re-Acceleration Process Across Aspect Ratios

A quantitative static pressure analysis of the re-acceleration process is performed below, with a centerline probe survey evaluating longitudinal pressure values along the lower wall, starboard side wall, and center-axis. Lower wall and side-wall values are acquired 1mm from the test section wall. Through evaluating the static pressure behavior, shock location and magnitude can be compared between the different areas of interest. Interaction magnitude for the different re-acceleration zones observed are summarized in Table 6.2 in terms of $\Delta P/P_0$ measurement.

Figure 6.8 shows the centerline static pressure behavior in the aspect ratio 3.0 configuration. The isometric representation of the three-dimensional shock front shown in Fig. 5.27 can be referenced in the below discussion. As expected, the side-wall boundary layer shows the first signs of separation induced static pressure rise at X=380mm, with a magnitude of $\Delta P/P_0 = 0.12$. The lower wall separation, more gradual in nature, occurs downstream at X=405mm and reaches an initial $\Delta P/P_0$ magnitude of 0.16. The center-axis shock location is located at a longitudinal position of X=437.5mm. Due to the strong normal shock system and the high Mach number located in the center-axis flow region, a $\Delta P/P_0$ magnitude of 0.48 is recorded.

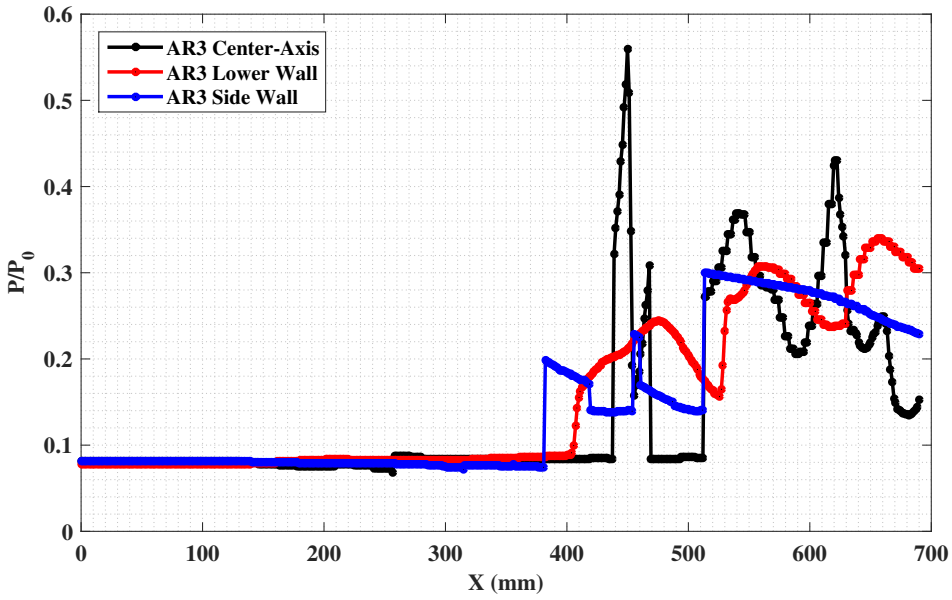

Figure 6.8: Aspect ratio 3.0 longitudinal static pressure survey of the re-acceleration region for the center-axis, centerline side-wall, and centerline lower wall data probes.

The effect of the compression and expansion features in the re-acceleration zones are noticeable downstream of the initial static pressure rise. With the backpressure ratio (P_3/P_0) at 0.3 in this steady state computation, the centerline probes show three distinct re-acceleration events. The strength of the features (and the values of $\Delta P/P_0$) increase as the re-acceleration zones progress downstream, owing to the extent of the supplementary normal structures that occur downstream of the primary shock structure. While the side-wall probe shows the re-acceleration process ending at X=513mm and diffusing toward the isolator exit plane, the lower-wall and center-axis probes show a more sustained re-acceleration regime with more gradual compression and expansion processes.

Similar observations can be made for the aspect ratio 6.0 and 1.0 configurations shown in Fig. 6.9-6.10. The shock front in the aspect ratio 6.0 case is shown to be much more two-dimensional in nature (Fig. 5.34), and is likewise observed in the centerline data shown in Fig. 6.9. The side-wall and lower-wall centerline boundary layer separation pressure rise are observed to occur at X=249.1mm and 270.8mm respectively, approximately 0.85 duct heights apart. The center-axis probe measures the initial static pressure rise at X=280mm, only 0.4 duct heights downstream of

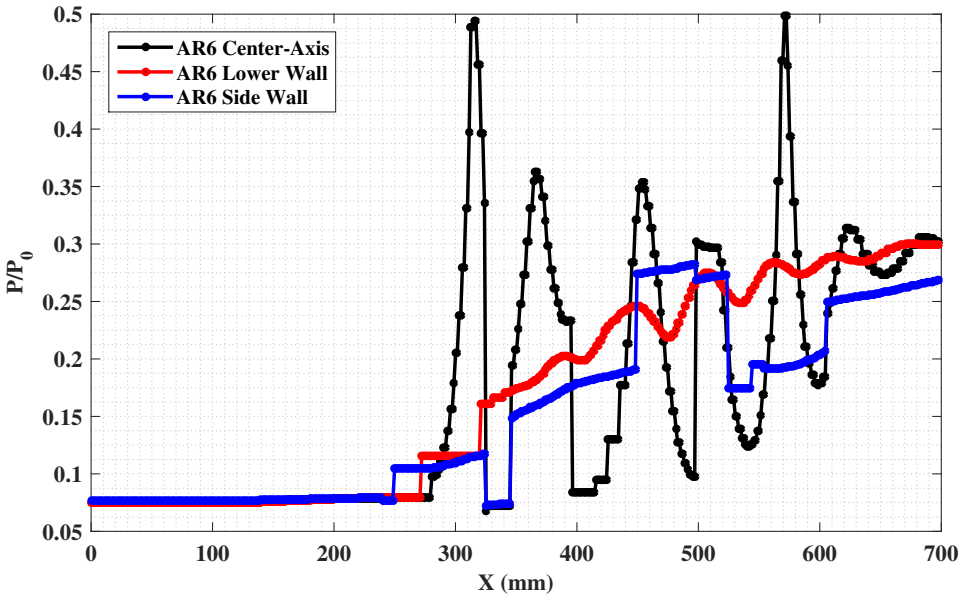

Figure 6.9: Aspect ratio 6.0 longitudinal static pressure survey of the re-acceleration region for the center-axis, centerline side-wall, and centerline lower wall data probes.

the lower-wall bounded measurement.

The strength of the center axis feature decreases as the aspect ratio is increased to 6.0, as the initial $\Delta P/P_0$ rises to 0.41, a 15% decrease over the aspect ratio 3.0 pressure rise. While the initial lower wall $\Delta P/P_0$ behavior demonstrates a piece-wise interaction, the overall re-acceleration processes evaluated by the lower-wall and center-axis probes are again more gradual in nature, whereas the side-wall re-acceleration process is more abrupt over the re-acceleration regime. $\Delta P/P_0$ behavior as evaluated over the initial piece-wise interaction is lower for the side-wall interaction as compared to the lower-wall interaction, $\Delta P/P_0 = 0.03$ and 0.09 respectively. Furthermore, the compression (pressure rise) events are observed to take place over a longer longitudinal distance than the expansion (pressure decrease) events, due to the gradual formation of the shock structures composing the compression process.

The isometric view of the aspect ratio 1.0 shock front is shown to be more three-dimensional and symmetric about the center-axis than the higher aspect ratios evaluated (Fig. 5.32). This is likewise observed in the behavior of the static pressure centerline probes in Fig. 6.10. The

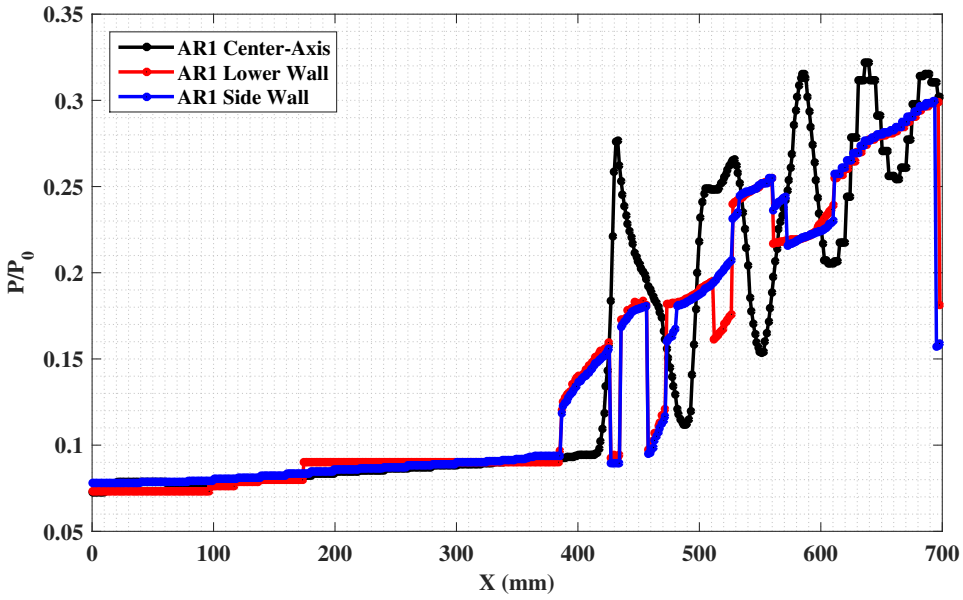

Figure 6.10: Aspect ratio 1.0 longitudinal static pressure survey of the re-acceleration region for the center-axis, centerline side-wall, and centerline lower wall data probes.

boundary layer separation pressure rise occurs simultaneously along the side and lower walls at an approximate longitudinal location of X=385mm. This separation is on the order of 1.2 duct heights upstream of the initial center-axis static pressure rise.

The strength of the initial center-axis structure is far lower than that of the aspect ratio 3.0 and 6.0 configuration, with the observed $\Delta P/P_0 = 0.18$ being 62.5% and 56% lower respectively. The symmetry of the lower and side wall boundary layer separation behavior continues throughout the entire re-acceleration region. The $\Delta P/P_0$ rise of 0.06 of the side and lower wall structures are nearly identical. This is less than the $\Delta P/P_0 = 0.12$ of aspect ratio 3.0 case and the more piece-wise side-wall interaction of the aspect ratio 6.0 configuration ($\Delta P/P_0 = 0.20$).

Re-acceleration zone strengths are summarized in Table 6.2 below for all aspect ratios. In general, the initial shock interaction is the strongest in terms of relative pressure jump across the shock. The strongest feature in each aspect ratio is found near the center-axis, owing to the higher Mach number and more normal shock structure present. Lower and side-wall interaction strength generally occurs with the same order of magnitude, and overall interaction strength decreases as

	$AR1.0$			$AR3.0$			$AR6.0$		
$Zone\#$	Center	Lower	Side	Center	Lower	Side	Center	Lower	Side
1	0.18	0.06	0.06	0.48	0.16	0.12	0.42	0.08	0.03
2	0.15	0.10	0.10	0.28	0.15	0.09	0.29	0.04	0.07
3	0.15	0.09	0.09	0.13	0.10	0.16	0.27	0.04	0.08
4	0.12	0.06	0.07	-	-	-	0.20	0.05	0.07
5	0.06	0.04	0.04	-	-	-	0.27	0.04	-
6	-	-	-	-	-	-	0.14	0.02	-

Table 6.2: Re-acceleration zone strengths ($\Delta P/P_0$) for aspect ratio 1.0, 3.0, and 6.0 (center-axis, lower-wall, and side-wall).

a function of increased longitudinal location.

6.4 Isolator Duct Fanno Flow Approximation

A Fanno flow side study is performed to validate the one dimensional, steady, adiabatic, and shockless model's ability to predict flow states in the fully started isolator (i.e. no shock train present). A detailed description and derivation of the well-known Fanno flow approximation can be found in various instructional texts [26, 156, 157] and is only briefly described here. The Fanno flow model represents the frictional viscous forces as shear stress acting on the fluid at the wall with uniform properties over any cross section, as illustrated in Fig. 6.11

Modeling of the viscous forces as a wall shear force allows for the use of the mass, momentum, and energy conservation equations with the wall shear force contributing one additional surface force into the conservation of momentum balance. The inclusion of the wall shear stress surface force is critical, as the driving force behind the change in Fanno-flow properties along the duct is friction at the wall of the duct. This is illustrated in Eqn. 6.4, where the change in Mach number between the entrance (station 2) and exit (station 3) of the isolator duct is a function of total duct length, rectangular duct hydraulic diameter (D_H), and local friction coefficient f defined as $f = \frac{2\tau_w}{\rho u^2}$ [156]. Using the experimentally measured values of M_3 and M_2, aspect ratio 3.0 & 6.0 friction coefficients of approximately 0.0042 and 0.0047 are derived, which are on the order of magnitude of the recommended value of $f = 0.005$ for a $Re > 10^5$ and a surface roughness of

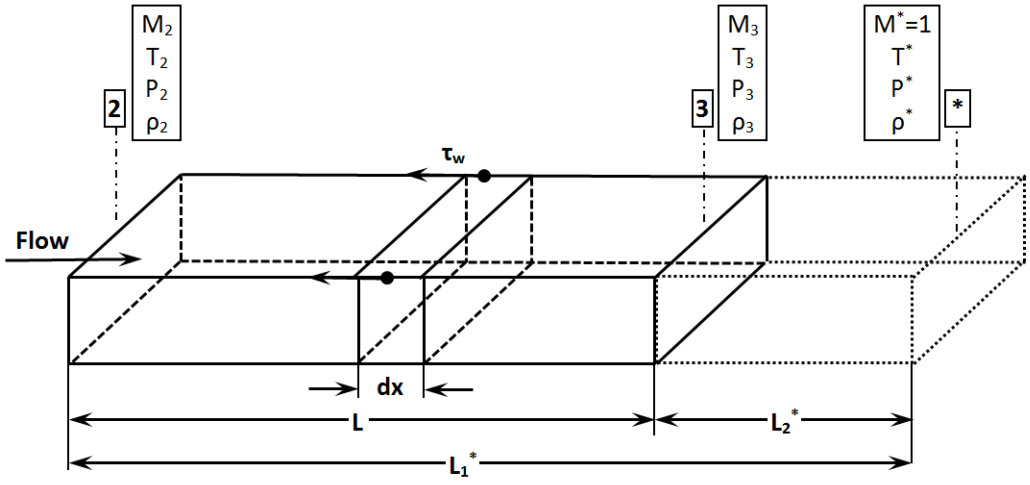

Figure 6.11: Fanno flow: One dimensional flow with friction and the sonic reference condition.

$0.001D_H$ [156, 158].

$$\int_{x_2}^{x_3} \frac{4f dx}{D_H} = \left[\left(\frac{-1}{\gamma M^2} \right) - \left(\frac{\gamma+1}{2\gamma} \right) ln \left(\frac{M}{1+\frac{\gamma-1}{2}M^2} \right) \right]_{M_2}^{M_3} \tag{6.4}$$

Given the isolator inlet flow conditions, isolator length, hydraulic diameter, and friction coefficient approximation, the Fanno flow model allows for the calculation of the flow parameters at the exit plane of the isolator. Results from the Fanno flow calculation described below are compared to experimentally derived exit plane condition in Table 6.3. Since the outlet conditions (including Mach number) are unknown, Eq. 6.4 is solved by using the sonic flow reference (*) according to Eq. 6.5. Rather than directly solving for the end conditions, the flow is solved for a certain isolator length (L^*) that results in the initially supersonic flow diffusing to sonic conditions ($M_3 = 1.0$ in Eq. 6.4). Given that the flow at the isolator outlet is supersonic, a longer isolator length L_1^* is needed to diffuse the flow to sonic conditions, as shown in Fig. 6.11.

$$\int_{x_2}^{L*} \frac{4f dx}{D_H} = \left[\left(\frac{-1}{\gamma M^2} \right) - \left(\frac{\gamma+1}{2\gamma} \right) ln \left(\frac{M}{1+\frac{\gamma-1}{2}M^2} \right) \right]_{M_2}^{1} \tag{6.5}$$

With the isolator coordinate $x_2 = 0$, Eq. 6.5 can be rewritten as Eq. 6.6, where M_2 is the Mach number at the isolator inlet plane and $\bar{f}$ is the average friction coefficient across the isolator

duct's longitudinal axis and is defined as $\bar{f} = \frac{1}{L_1^*}\int_0^{L_1^*} f dx$.

$$\frac{4\bar{f}L_1^*}{D_H} = \frac{1-M_2^2}{\gamma M_2^2} + \frac{\gamma+1}{2\gamma} ln\left[\frac{(\gamma+1)M_2^2}{2+(\gamma-1)M_2^2}\right] \tag{6.6}$$

For a given isolator inlet Mach number (M_2), a value for $\frac{4\bar{f}L_1^*}{D_H}$ can be calculated through the right hand side of Eq. 6.6. The fraction $\frac{4\bar{f}L}{D_H}$ can be directly calculated through the known isolator length L. As illustrated in Fig. 6.11, an additional reference length scale can be defined as $L_2^* = L_1^* - L$. It follows then that a value of $\frac{4\bar{f}L_2^*}{D_H}$ can be calculated according to $\frac{4\bar{f}L_2^*}{D_H} = \frac{4\bar{f}L_1^*}{D_H} - \frac{4\bar{f}L}{D_H}$. Finally, since L_2^* starts at the physical isolator exit plane, the value of M_2^* calculated through Eq. 6.6 using the value of $\frac{4\bar{f}L_2^*}{D_H}$ represents the Mach number at the actual isolator exit plane (M_3).

Since the flow is assumed to be adiabatic throughout the isolator, isentropic relations can be employed to relate the flow parameters of temperature, pressure, and density at the exit to those at the entrance through the fact that the total conditions are constant, as shown in the left column of Eq. 6.7. Using the sonic reference conditions, the left column can be transformed into the middle column of Eq. 6.7 by assuming the exit plane Mach number is 1.0. Through the use of the known inlet Mach number (M_2), values for $\frac{T^*}{T_2}$, $\frac{P^*}{P_2}$, and $\frac{\rho^*}{\rho_2}$ can be calculated. Furthermore, the calculation of M_3 discussed in the previous paragraph allows for the calculation of the $\frac{T^*}{T_2}$, $\frac{P^*}{P_2}$, and $\frac{\rho^*}{\rho_2}$ values. The right column of Eq. 6.7 can then be used to calculate the flow parameters at the outlet plane of the physical isolator duct.

$$\begin{array}{lll}
\frac{T_3}{T_2} = \frac{\frac{T_0}{T_2}}{\frac{T_0}{T_3}} = \frac{2+(\gamma-1)M_2^2}{2+(\gamma-1)M_3^2} & \frac{T}{T^*} = \frac{\gamma+1}{2+(\gamma+1)M^2} & T_3 = \frac{T_3}{T^*}\frac{T^*}{T_2}T_2 \\
\frac{P_3}{P_2} = \frac{M_1}{M_2}\left[\frac{2+(\gamma-1)M_2^2}{2+(\gamma-1)M_3^2}\right]^{1/2} \iff \frac{P}{P^*} = \frac{1}{M}\left[\frac{(\gamma+1)}{2+(\gamma-1)M^2}\right]^{1/2} \iff & P_3 = \frac{P_3}{P^*}\frac{P^*}{P_2}P_2 \\
\frac{\rho_3}{\rho_2} = \frac{M_2}{M_3}\left[\frac{2+(\gamma-1)M_2^2}{2+(\gamma-1)M_3^2}\right]^{-1/2} & \frac{\rho}{\rho^*} = \frac{1}{M}\left[\frac{2+(\gamma-1)M^2}{\gamma+1}\right]^{-1/2} & \rho_3 = \frac{\rho_3}{P^*}\frac{\rho^*}{\rho_2}\rho_2
\end{array} \tag{6.7}$$

Results summarized in Table 6.3 compare the experimentally derived flow conditions against the Fanno flow calculations at the exit plane of the isolator. Velocity is calculated through the relationship between Mach number and speed of sound. It is shown that the Fanno flow approxi-

	Experimental	Fanno	% Difference
Aspect ratio 3.0			
M_3	2.34 ± 0.026	2.38	-1.75
$T3(K)$	137.43 ± 1.79	135.01	1.76
P_3/P_0	0.083 ± 0.002	0.079	4.03
$\rho_3(kg/m^3)$	0.212 ± 0.004	0.211	1.08
$V_3(m/s)$	549.44 ± 7.12	554.51	-0.85
Aspect ratio 6.0			
M_3	2.27 ± 0.026	2.21	2.62
$T3(K)$	149.16 ± 1.95	145.42	2.51
P_3/P_0	0.078 ± 0.002	0.081	-3.90
$\rho_3(kg/m^3)$	0.184 ± 0.003	0.198	-7.91
$V_3(m/s)$	528.15 ± 6.84	535.18	-1.33

Table 6.3: Fully started Fanno flow approximation and comparison to experiment (aspect ratio 3.0 & 6.0).

mation is very capable of predicting the isolator exit plane conditions in the fully started mode of operation.

6.5 Isolator Exit Plane Flow Condition

The secondary planar Mie-scattering side-study, described in Chapter 3, is used to visualize the YZ-plane perspective in the aspect ratio 1.0 isolator configuration (Fig. 3.33). The laser sheet is focused at the outlet of the isolator (X=490mm, 7.4 duct heights from the origin) and is used to evaluate the flow conditions before and after the shock train passage. Although the IDT NR3-S camera is used in this experiment, the single pulse rate of the Nd:YAG laser is limited to approximately 12Hz. Therefore, shock train dynamics are not captured. The focus of this Mie-scattering application is to evaluate the boundary layer behavior of the steady-state pre- and post-shock train passage. Observations regarding core flow reduction and overall flow uniformity are presented.

The Mie-scattering field of view is presented in Fig. 6.12. The baseline image (Fig. 6.12a) shows the local reflection of the laser sheet off of the isolator port-side window in the lower left corner of the image. While the outside of the tunnel geometry was covered in black cloth to minimize reflections, the interior of the wind tunnel (mat gray steel color) was not altered and

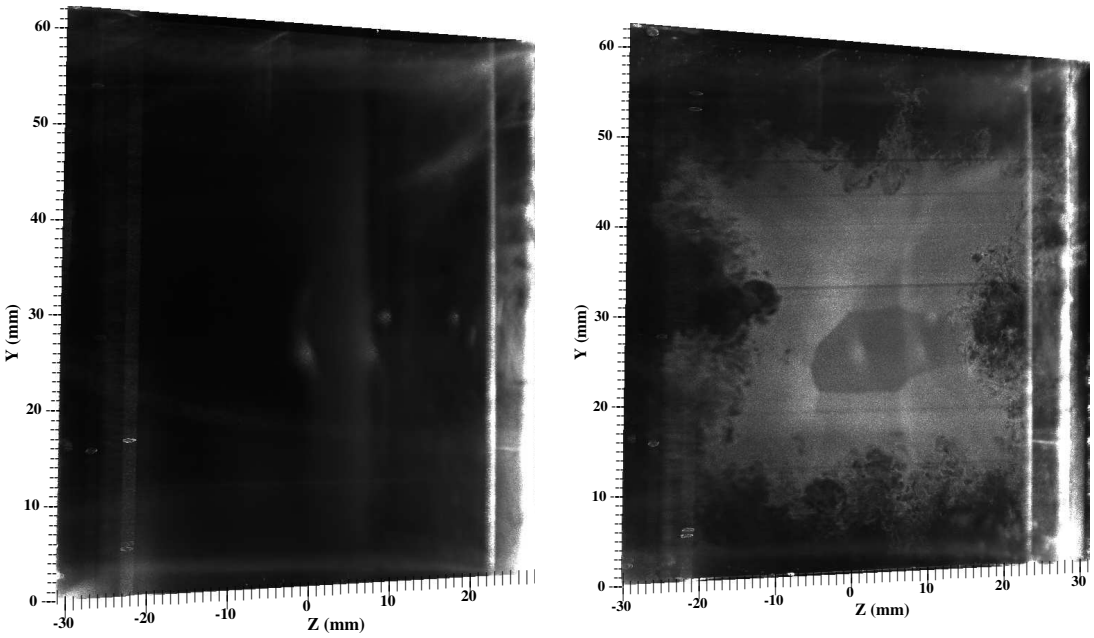

Figure 6.12: T9 Calibration wind tunnel Mie-scattering: (a) baseline image, and (b) flow image.

thus a certain degree of reflectivity was unavoidable. Nevertheless, boundary layer features in all four duct corners are recognizable, as is shown in the flow image of Fig. 6.12b. At this downstream location the minor-axis boundary layer is approximately 11mm thick, whereas the base of the major-axis boundary layer is approximately 15mm thick. The minor axis boundary layer thickness corresponds that calculated by pitot probe measurements obtained near the outlet of the isolator.

To calculate the change in core flow area between pre and post shock train flow states, the edge of the boundary layer is traced and the area contained by the boundary is calculated, as shown in Fig. 6.13. Results for three consecutive images for both states are summarized in Table 6.4. Although not a statistical source of information due to low sample rates, the observations presented below shed some perspective on the mass flow and the uniformity of the flow 'entering the combustor'. A more uniform flow field and larger core flow area would increase the mass flow and reduce the variation in total temperature at the exit plane of the isolator, potentially increasing combustor performance [3].

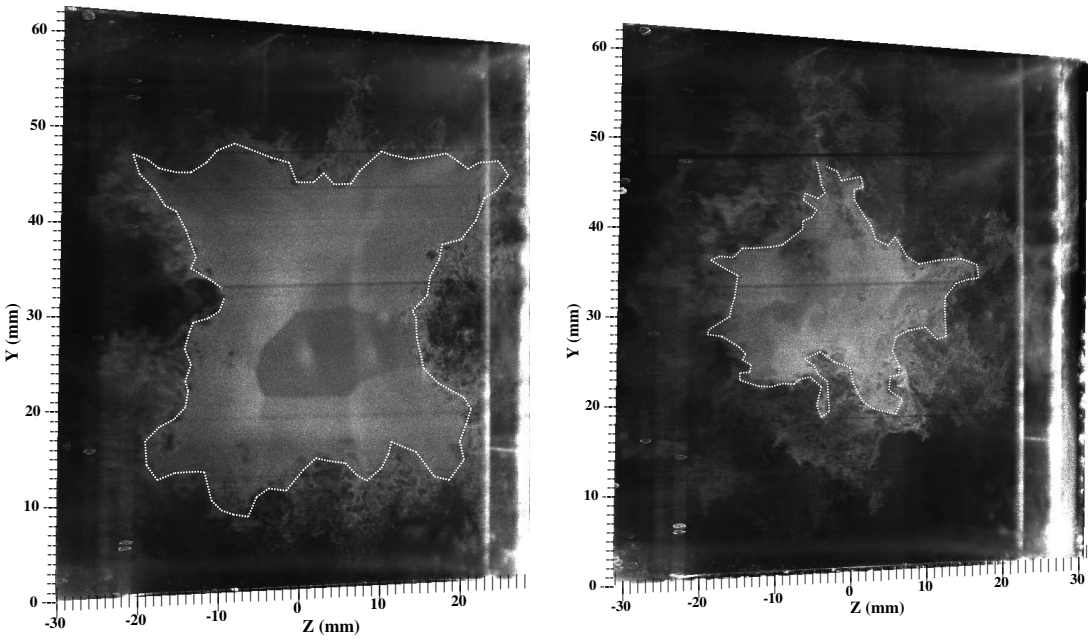

Figure 6.13: Calculation of the core-flow area: (a) pre-shock train arrival, and (b) post-shock train arrival.

Boundary layer edge detection is performed manually, and is defined as the qualitative boundary between the higher temperature region in the boundary layer and the colder temperature region in the freestream that results in the brighter and dimmer regions respectively. Results in Table 6.4 suggest that the average pre-shock train core area at the isolator exit plane is approximately 35% of the isolator cross-sectional area. Image to image variation of the pre-shock train core area calculation does not exceed more than 3%. The average post-shock train core area calculation is approximately 14% of the isolator cross-sectional area. This is a reduction in core-area of 60% compared to the pre-shock train arrival.

The analysis of the core flow cross sectional area in an isolator supporting a shock train structure as a function of longitudinal location is explored in Fig. 6.14. Mach contours are plotted at specific cross-sectional planes with the reference plane located at the initial location of the shock train leading edge/boundary layer interaction (X=395mm), and subsequent planes plotted one duct height (50.8mm) downstream of the reference plane. Two additional planes, one at the origin and another one duct height upstream of the reference plane, are provided. A Mach number

Case	Total Area (mm^2)	Core Area (mm^2)	% Reduction
Pre-shock train arrival			
Image #157	4530.6	1590.8	64.9
Image #158	4530.6	1604.8	64.6
Image #159	4530.6	1560.8	65.5
Post-shock train arrival			
Image #189	4530.6	576.8	87.3
Image #190	4530.6	642.4	86.8
Image #191	4530.6	597.7	86.5

Table 6.4: Comparison of flow core-area between pre- and post-shock train passage of three consecutive planar Mie-scattering images (12Hz).

threshold of ten percent of the freestream Mach number, evaluated at [Y,Z]=(0,0)mm, is used to define the boundary of the core flow. Mach number magnitudes are evaluated for each cross-sectional coordinate and a core flow boundary is formed, with subsequent calculation of the core flow area.

The uniformity of the RANS flow field results in the symmetrical flow fields shown in Fig. 6.14. The isolator inlet plane is characterized by a thin boundary layer, with the core flow taking up 89% of the test section. Natural boundary layer growth results in the core flow area reducing to 64% at X=345mm. The Initial boundary layer separation is visible in the upper right corner for X = 395mm. Progressing through the shock train and re-acceleration zones, a continuously decreasing core flow area is expected. At the exit plane, the core flow is reduced to 11% of the cross-sectional area. This only 15% less than the experimental core flow area averaged across the three post shock train images in Table 6.4, where the core flow area was estimated to be 13% of the total test section cross sectional area.

Analysis on the implications of the shock train induced reduction in isolator core-flow area to the isolator and combustor performance are limited in this study, as are the available works in literature that evaluate this effect. As Fig. 6.13-6.14 and Table 6.4 show, the effect of shock train interaction with the isolator boundary layer must also be thoroughly understood in the exit plane of the isolator, to more accurately predict combustor performance in the ramjet-mode of operation of the dual-mode scramjet where isolator shock train formation is an inherent part of the operational state.

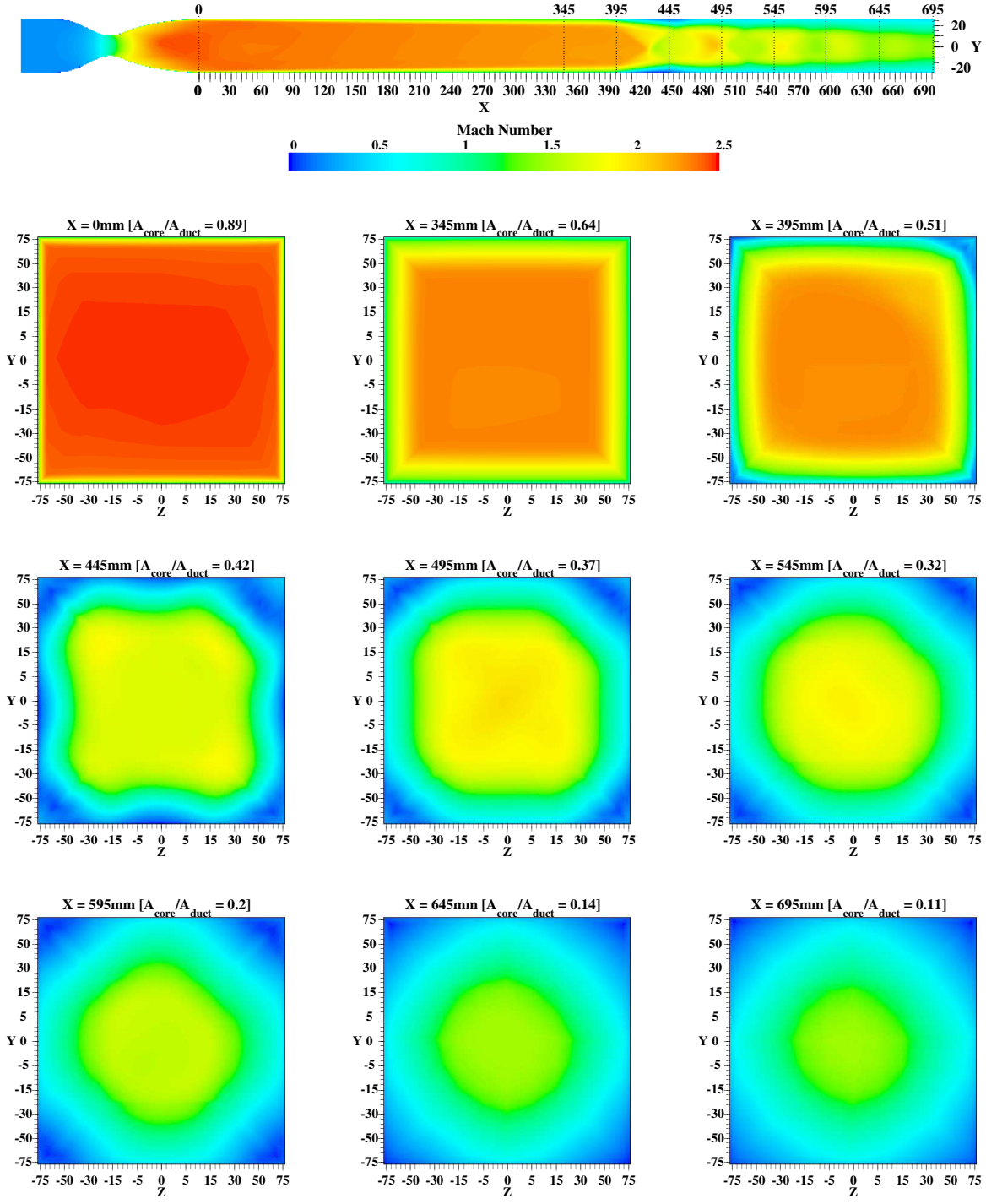

Figure 6.14: Core-flow area reduction calculation from aspect ratio 1.0 RANS simulation at different longitudinal YZ-planes.

Chapter 7: Concluding Remarks

7.1 Summary and Major Results

A detailed experimental study of aspect ratio 1.0, 3.0 and 6.0 isolator shock trains with design inflow Mach number of 2.7 (aspect ratio 1.0) and Mach number of 2.5 (aspect ratio 3.0 and 6.0) is performed. Shock train front three-dimensionality is qualitatively and quantitatively observed and static and dynamic wall pressure measurements are evaluated. Additional high temporal bandwidth analysis of shock train dynamics is performed to compare the shock train oscillation frequency and velocity component as a function of location along the duct lateral (major) axis. Duct minor- and major-axis boundary layers are experimentally resolved using single pitot probe and pitot rake measurements, and subsequent observations regarding boundary layer asymmetry are made. Complementary three-dimensional RANS simulations utilizing the two-equation $k-\omega$ turbulence model are performed to compare to the experimental observations, evaluate the capabilities of the RANS approach to resolve three-dimensional flow physics, and provide higher resolution near-wall data acquisition.

7.1.1 Visualization of the Three-Dimensional Shock Train Front

Efforts to differentiate the visualization of the shock train from the traditional single perspective two-dimensional projection line-of-sight techniques of schlieren and shadowgraph was one of the main objectives in this study. Two non-traditional visualization techniques were employed. First, a multiplane shadowgraph method was conceptualized to resolve the density gradient derivative from two simultaneous orthogonal perspectives. Second, the synthetic schlieren (BOS) technique was utilized to resolve the global density gradient magnitude within the shock train structure.

7.1.1.1 Shock Train Visualization from Two Simultaneous Perspectives

The highly three-dimensional shock train front is visualized from two perspectives simultaneously for the first time. The novel multiplane shadowgraph visualization method developed shows that the previously termed planar (oblique) shock train structure is in actuality a hybrid oblique/normal shock structure (Fig. 5.1). The formation of this shock front is driven by the initial low momentum boundary layer separation. The effect of aspect ratio on shock train formation was studied and observations are summarized below:

- As illustrated in the three-dimensional vertical shock plane reconstruction of the aspect ratio 3.0 isolator shock train leading edge (Fig. 5.2c), the low momentum boundary layer separation spawns the formation of four oblique shock planes that merge in the center flow field as a normal structure. Corner flow separation is located upstream from the center flow separation by approximately one duct height for all three aspect ratios evaluated.

- The distribution between the oblique and normal portions of the shock train front varies with respect to aspect ratio. The aspect ratio 1.0 shock train is characterized by a very three-dimensional, axisymmetric shock front (Figs. 5.7 and 5.32). A small normal shock structure is observed near the center-axis but the oblique shock is by far the more dominant feature, with a single transition occurring approximately 0.1 duct height from center-axis.

- The degree of shock front three-dimensionality decreases as aspect ratio increases, with the aspect ratio 3.0 shock train front (Figs. 5.1 and 5.27) showing a more balanced oblique/normal hybrid shock front. Transition between the oblique and normal structure occurs in two distinct regions, approximately 1.4 and 0.8 duct heights from the isolator centerline respectively.

- Continuing the trend of decreased three-dimensionality, the aspect ratio 6.0 shock train front (Figs. 5.5 and 5.34) is dominated by the normal structure. A single transition between the initial oblique shock and center flow normal shock occurs 1.9 duct heights away from the isolator centerline.

- Although the degree of three-dimensionality varies with aspect ratio, the low momentum corner flow separation is observed to occur approximately one duct height upstream of the center flow field separation for all cases considered. It appears that the minor-axis length scale plays a role in determining the magnitude with which the initial oblique shock affects the center flow field and initiates separation in that region.

- A complementary lower wall, instantaneous oil-flow study in the aspect ratio 3.0 configuration allowed for the visualization of the shock train dynamics around the lower-wall centerline. Shock train front symmetry around the centerline was observed as the system progressed upstream.

7.1.1.2 Synthetic Schlieren Optimization and Shock Train Analysis

The synthetic schlieren (BOS) method was utilized to analyze the global distribution of density gradient magnitude within the aspect ratio 3.0 and 6.0 shock train structure. A relationship calculating the density gradient as a function of cross-correlation pixel displacement, magnification factor, experimental geometric parameters, and the Gladstone Dale coefficient was derived (Eq. 4.7). Observations are summarized below:

- Global density gradient magnitude analysis of the primary shock train structure in the aspect ratio 3.0 configuration shows that the downstream interaction strength in the refracted normal shock portion of the primary structure is approximately 35% stronger than the strength of the initial oblique shock portion (Fig. 5.9).

- Analysis in the upstream region of the aspect ratio 3.0 duct shows the increased strength in the initial oblique portion of the shock train, owing to the thinner and higher magnitude boundary layer separation and higher freestream Mach numbers (Fig. 5.10).

- The downstream section of the aspect ratio 6.0 isolator is characterized by a thick boundary layer that obscures a significant portion of the shock train detail. The application of the knife-edge in the traditional schlieren approach highlights this problem by emphasizing

the light/dark contrast (top figure in Fig. 5.11). The lower resolution BOS method, relying on interrogation window resolved measurements of pixel displacements, suffers in the downstream region as well (Fig. 5.11).

- The BOS performance improves in the upstream region of the isolator, with more distinct shock train/boundary layer interactions providing a clearer distinction between the oblique and normal component of the shock train front. The aspect ratio 6.0 structures are stronger than those found in the aspect ratio 3.0 configuration, owing to the increased two-dimensionality and the increased prevalence of the normal structure. The density gradient magnitude increases by approximately 65% between oblique and normal shock train components of the primary structure.

Although they are both single perspective line of sight techniques, the BOS method highlights the relative strength of the features much more clearly than the traditional knife-edge schlieren technique. In a case where multiplane shadowgraphy is not feasible, the application of the single perspective BOS can still reveal a preliminary level of detail regarding the flow three-dimensionality by projecting the shock structure's overall strength. The significant increase in density gradient magnitude between the incident (oblique) and refracted (normal) shocks within the primary shock train structure alludes to the presence of vastly different shock structures.

Prior to utilizing the technique for shock train analysis, an extensive background pattern optimization study was performed to: (a) improve the resolution of the shock features, and (b) improve the accuracy of density gradient estimation through the use of a known density gradient magnitude, stationary oblique compression shock. Results of the optimization work are summarized below:

- Background particle density and diameter were varied and it was found that the background pattern characterized by an image density of N=75 and a particle diameter range of 0.3-0.75mm (0.01-0.03"), equivalent to a range of 2-5 camera pixels multiplied by the magnification factor, provided the highest resolution image and the most accurate representation of the known density gradient (Fig. 4.3).

- The optimized grid was quantitatively compared to a known density gradient magnitude through the derivation of Eq. 4.7. The synthetic schlieren technique under resolved the density gradient magnitude by approximately 10% (Fig. 4.4).

7.1.2 Computational Fluid Dynamics Analysis of Three-Dimensional Shock Train

The experimental visualizations discussed above are complemented by the application of three-dimensional RANS based on the two equation $k-\omega$ turbulence model. The aspect ratio 1.0, 3.0, and 6.0 configurations were modeled. The aspect ratio 6.0 computational control volume included both the experimental half-nozzle configuration and a double planar axi-symmetric nozzle configuration. Both fully started (no shock train present) and partially unstarted (shock train present) steady state computations were performed.

The goal of the computational work was to: (a) compare the results to the experimental data set being established, (b) quantitatively evaluate the capability of the RANS approach to resolve the complicated flow physics inside the rectangular isolator, and (c) offer additional insight into the flow field. Observations are summarized below.

- Mesh sensitivity and boundary layer y^+ dependency studies were performed for validation and verification purposes. The experimentally derived lower-wall centerline static pressure (Fig. 4.17) and vertical boundary layer surveys (Figs. 4.18-4.19) were compared to computational results in the fully started case (no shock train present), with correlation results summarized in Table 4.2. The computations were able to resolve the longitudinal lower wall centerline static pressure behavior and the minor- and major-axis boundary layer Mach profiles within 3%, 10%, and 5% averaged difference from the experimentally derived data.

- Qualitative comparison of the experimental aspect ratio 3.0 multiplane shadowgraph and lower wall centerline oil flow visualization with the computational result (Figs. 5.28-5.29) shows that the RANS based modeling approach captures all of the major features within the shock train structure. Experimental observations regarding upstream corner flow separation length scales discussed above likewise hold for the numerical simulation results across all

aspect ratios considered.

- The isometric, three-dimensional shock train front visualization using density threshold (Figs. 5.27, 5.34, and 5.32) offers additional insight into the behavior of the side wall boundary layer separation mechanics. Utilizing the high resolution computational boundary layer analysis capabilities, the side-wall (major-axis) boundary layer characteristics are compared to the nozzle bounded (minor-axis) boundary layer parameters. Summarized in Tables 4.3-**??** for the aspect ratio 3.0 and 6.0 (half nozzle) configurations, it is found that the side-wall boundary layer shape factor (separation tendency) is up to 18% larger for the aspect ratio 3.0 case, and 10% larger for the half nozzle aspect ratio 6.0 case.

The shock train re-acceleration process described in Fig. 6.7 is evaluated through the analysis of lower wall and side-wall centerline, as well as isolator center-axis static pressure behavior in Figs. 6.8-6.10. The strength of the re-acceleration zones are summarized in Table 6.2.

- The aspect ratio 1.0 boundary layer separation (Figs. 5.32, 6.10) is found to be the most symmetric around the center-axis, with the side-wall and lower-wall boundary layers separating at roughly the same longitudinal location upstream of the center-axis shock location. The symmetry holds in the observed strength of the side-wall and lower-wall shock train/boundary layer interaction (Table 6.2).

- The boundary layer separation in aspect ratio 3.0 and 6.0 configurations are less symmetrical around the center-axis, with the side-wall boundary layer separating upstream of lower wall boundary layer. The aspect ratio 3.0 case, with a larger shape factor discrepancy between minor- and major-axis boundary layer than the aspect ratio 6.0 case, sees the side-wall boundary layer separation occur 1/2 duct height ahead of the lower-wall separation. The aspect ratio 6.0 shock train front, being more two-dimensional, has a side-wall separation 0.4 duct heights upstream of the lower-wall flow separation.

- The strength of the center-axis shock train structures are found to be strongest in the aspect ratio 3.0 case, where the $\Delta P/P_0$ jump across the primary structure is 0.48. The aspect ratio

6.0 and 1.0 configurations experience a 12% and 60% lower shock strength respectively. The former can be attributed to the interaction strength being spread out of a laterally longer normal structure, while the latter is due to the fact that the oblique/normal shock transition occurs less than .1 duct height from the center-axis.

- In the aspect ratio 3.0 and 6.0 configurations, the side-wall shock/boundary layer interactions are weaker than their lower-wall counterparts. An approximate 20% and 10% decrease respectively is found in the aspect ratio 3.0 and 6.0 side-wall shock induced static pressure increase with respect to the shock induced static pressure increase at the lower wall.

7.1.3 Evaluation of the Shock Train Dynamics

A series of fast response, high temporal bandwidth measurements were obtained at different coordinates within the experimental aspect ratio 3.0 and 6.0 configurations to study the dynamics of the isolator shock train. Wall bounded dynamic pressure measurements were obtained along the duct lateral axis, comparing center-flow to outboard flow boundary layer induced pressure rise. High temporal bandwidth measurements of light fluctuations were made non-intrusively at three-dimensional coordinates within the isolator duct utilizing the Focusing Schlieren Deflectometry Velocimeter technique, allowing for the comparison of shock train oscillation frequency and oscillation velocity between the center flow and side wall regions.

7.1.3.1 Duct Major Axis Dynamic Pressure Survey

The lower wall dynamic pressure content between the center flow and outboard flow regions were analyzed, and compared to the visualization efforts summarized above. The main focus of this study was to evaluate the upstream corner flow temporal time-scale.

- Outboard flow separation, observed in Figs. 5.1 and 5.5 is measured to occur on the order of 2 seconds ahead of the center flow field separation across both aspect ratios.

- As expected, the magnitude of the boundary layer separation/shock interaction decreases as the distance from the centerline is increased. Compared to the normal shock interaction in

the center region of the duct, the strength of the oblique shock interaction in the outboard region is reduced by 7% in the aspect ratio 3.0 configuration. With the flow field significantly more two-dimensional in the aspect ratio 6.0 configuration, and normal portion of the shock dominating much of the center-flow field region, the difference in interaction magnitude is found to be approximately 17%.

- Since the most outboard pressure sensor is still located 25mm away from the corner region of the isolator, the observations of separation time-scale and magnitude are expected to continue their respective trends as measurements closer to the corner regions are obtained.

- Spectral content analysis was limited, showing the low-frequency content across the lateral axis was contained below 100Hz. Due to the randomness of the signal in the boundary layer, characteristic frequency peaks as a function of lateral position from centerline were indistinguishable. The application of the focusing schlieren deflectometry technique allowed for a more coherent measurement of shock train oscillation frequency, as summarized below.

7.1.3.2 Evaluation of Oscillation Frequency and Velocity Component

The shock train oscillation frequency and velocity component were evaluated at distinct coordinates along the duct lateral axis for the aspect ratio 3.0 and 6.0 configurations utilizing the Focusing Schlieren Deflectometry Velocimeter setup (Fig. 3.26-3.30). The performance parameters of this diagnostic tool are summarized in Table 3.3. Case studies within a single aspect ratio included the comparison between the primary and secondary shock train structure, as well as the comparison between center-axis (Z=0mm) and side-wall (Z=76mm) measurements. All measurements were made along the duct half height (Y=0mm). Observations made are summarized below and in Table 5.2.

- For both configurations tested, reductions in the oscillation frequency (67% and 54%) and the average velocity component (33% and 14%) of the primary shock structure are observed as distance from the centerline (center-axis) is increased toward the side wall. As viewed from

the duct half-height, the shock structure is attached to the initial side wall separation in the low Mach number and total pressure region of the side-wall boundary layer. Both Mach and total pressure increase as distance to the center-axis is reduced and could increase the magnitude of the shock structure response to potential flow disturbances. LES simulations performed by Garnier [40] noted that in the overall low frequency ($f < 100$) shock train behavior, the frequencies found in the corners and boundary layers were lower than those found in the freestream by approximately 80%.

- The behavior of the primary shock structure at the center-axis as compared to the side wall region is observed to be more two-dimensional (smaller change in oscillation frequency and velocity component) in the aspect ratio 6.0 configuration compared to the aspect ratio 3.0 isolator. This observation aligns with the fact that the aspect ratio 6.0 shock front is resolved as a more two dimensional structure in both experiment and computation.

- Comparison between center-axis primary hybrid structure and secondary normal structure measurements for both aspect ratios indicate that the primary structure oscillates at a slightly higher frequency (increase of 14.5% and 4.6%) but at a lower average velocity than the secondary normal structure (decrease of 28% and 11%). The increase in velocity component between the primary and secondary structure can in part be attributed to the higher pressures upstream and downstream of the secondary normal shock compared to the primary structure.

- As the two studies, primary shock side-wall vs. center axis and center-axis primary shock vs. secondary normal shock, are compared between the aspect ratio 3.0 and 6.0 isolator configurations, it is shown that the more two-dimensional aspect ratio 6.0 shock front approximation drives a more uniform flow field relative to the aspect ratio 3.0 configuration. Changes in both shock train frequency and average velocity component between the structures (center-axis vs. side wall and primary vs. secondary structure) for the aspect ratio 6.0 configurations are lower and transitions more gradual.

7.1.4 Shock Train Length Estimation

Traditional correlations for isolator shock train length derived by Walturp & Billig (Eq. 6.1 and 6.2) are compared to the modified relation (Eq. 6.3) provided in Fig. 6.2. The experimental and computational observations summarized above were used to update the original relation based on circular ducts (6.1), to include the effects of minor- and major-axis boundary layer asymmetry ($\theta' = \sqrt{\theta_1^2 + \theta_2^2}$), isolator aspect ratio magnitude (D_H), and upstream corner flow separation length scale (S_C). The effects of each rectangular isolator characteristic are briefly summarized below, followed by a summary of the correlations performance comparison.

- Based on experimentally and computationally derived flow parameters at the inlet of the isolator, the major-axis boundary layer's shape factor was found to be 6% and 10% higher than the minor-axis boundary layer for the aspect ratio 3.0 and 6.0 configurations respectively. Including the θ_2 measurement resulting in an overall larger θ' as compared to the traditionally used θ_1 in the original relations. The lower momentum side-wall separation ($theta_2$) is expecting to produce a longer shock train length compared to observations solely based on minor-axis centerline measurements using θ_1.

- Experimental derivation of shock train length (Fig. 6.1) illustrated that the mixing length of the shock train is longer for smaller aspect ratios. Likewise, the hydraulic diameter ($D_H = \frac{2H_1H_2}{H_1H_2}$) is larger for the smaller aspect ratio duct, thus increasing the overall shock train length for smaller aspect ratios as evaluated in the numerator of Eq. 6.3.

- Finally, the corner boundary layer separation length scale plays a significant role in accurately predicting the total shock train length, as properly resolving the corner separation yields the most accurate location of the shock train leading edge. For the aspect ratios evaluated in this study, the corner flow is observed to separate one duct height upstream of the center flow field. This is quantified in the addition of the S_C parameter in Eq. 6.3.

The performance of all shock train length correlations (Eqs. 6.1, 6.2), and 6.3) is graphically compared to experimental measurements of shock train length in Fig. 6.2. An associated Root

Mean Square Error (RMSE) analysis is performed for all cases in Table 6.1. When compared against experimental measurements accounting for the upstream corner separation (Cases III-V), the introduced rectangular modification decreases the RMSE (averaged across the entire pressure ratio regime) by 10% in the aspect ratio 3.0 case, and by 60% in the aspect ratio 6.0 configuration compared to the original rectangular modification introduced by Billig (Eq. 6.2).

Past comparison of the original rectangular modification (Eq. 6.2) to experimental data has been largely confined to smaller aspect ratios. The vast improvement in correlation quality for the higher aspect ratio configuration brought about by the introduction of the new rectangular modification (Eq. 6.3) illustrates the importance of accounting for a wide range of aspect ratios when evaluating the performance of the correlation.

7.2 Contributions & Impart of Research

Although isolator shock trains have been studied since the dual-mode scramjet cycle was introduced in the 1960s, the flow field is not yet thoroughly understood. What has previously been termed a 'planar oblique' shock train is in fact quiet three-dimensional. The three-dimensional flow effects on shock train formation initiated by the rectangular aspect ratio isolator are studied in detail for the first in literature. Potential contributions of the new observations and measurements pertaining to the isolator flow physics in this work are discussed below. This is followed by a brief discussion on the contribution in diagnostics development.

- An experimental data set is provided that proves the importance of taking into account the three-dimensional features inside the rectangular isolator duct. The experimental approaches and reasoning applied in this thesis can be applied to a wider range of isolators. In particular, the diagnostic techniques applied can be used to study three-dimensional effects of the relatively uncharted 'shock separation mode' as proposed by Penzin (Fig. 2.5, Ref. [12]).

- Experimental measurements and observations regarding three-dimensional flow structures in the isolator flow field have been lacking in literature, preventing adequate comparison to Computational Fluid Dynamics work performed targeting this specific area of interest.

The secondary numerical study presented in this research is a first step toward comparing experimentally derived measurements and observations regarding three-dimensional isolator shock train fronts to numerical simulations. Additionally, the ability for RANS modeling to resolve the complicated isolator flow physics is presented and discussed.

- As discussed in Chapter 2, the ability to accurately predict the leading edge of shock train structure is critical in preventing inlet unstart. All of the previous works correlating boundary layer separation induced pressure rise to shock train leading edge location have depended on centerline lower wall pressure measurements. This provides the location of the center-flow field separation, but does not account for the low momentum upstream corner flow length scale. Since this length scale is observed to be approximately one duct height for all the aspect ratios studied, utilizing the centerline pressure measurements alone would grossly misinterpret the shock train leading edge location.

- Shock train leading edge detection algorithms as part of a Propulsion System Controller of a flight-worthy scramjet would benefit from the measurements of pressure in the outboard regions of the duct, in addition to the traditional longitudinal axis measurements. If complexity of flow parameter measurement in flight is to be kept at a minimum, the upstream separation length scale of the low momentum corner flow can be studied more extensively amongst a wider range of aspect ratios. If the separation length scale of approximately one duct height holds among a wider range of aspect ratios, that value could be included in the traditional centerline pressure measurement based isolator leading edge detection system.

- Although the observations made in this study deal with Mach 2.5 rectangular isolator shock train flow fields, the concepts and importance of the three-dimensional flow features as well as the development of the appropriate diagnostic tools to be able to resolve this three-dimensionality, can extend beyond the isolator flow regime. To more thoroughly understand flow structures in shock tubes, supersonic ejectors, inlet diffusers and combustor regions of a ram or scramjet cycle, or any other common flow field that is characterized by confined

internal supersonic flows characterized by shock/boundary layer interaction, the observations made in this study can serve as a foundation upon which similar measurements suitable to the respective flow field can be made.

Along with the conceptualization of the multiplane shadowgraph technique, the refinement and optimization of the Background Oriented Schlieren and Focusing Schlieren Deflectometry presented a large portion of the diagnostic development efforts. Each of these relatively non-traditional techniques allowed for the evaluation of the three-dimensional flow field, and can be applied across a wide range of flow regimes. Specific contributions are summarized below.

- The novel multiplane shadowgraph concept can be introduced to facilities that have the optical axis to support the desired field of views. This would allow simultaneous visualization of a variety of flow fields from multiple perspectives to substitute the single planar perspectives traditionally resolved through a laboratory schlieren/shadowgraph setup. This can be an alternative to the application of tomographic schlieren that traditionally requires a rotating test section.

- The background pattern optimization approach outlined in Chapter 4 can be applied to a wide range of flow regimes with a similarly wide range of $\delta\rho/\delta y$ values. Furthermore, the digital and mechanical background pattern projection concepts (Fig. 3.25) can be used to realize fully customizable patterns in large field of view applications, where directly applying the pattern on the wind tunnel wall is prohibitive due to the flow field present or the desire to keep the background pattern flexible.

- The back-lit cutoff grid design procedure outlined in Chapter 3 (Table 3.3 and Fig. 3.27) and further discussed in Chapter 4 allows for the design of a more flexible and higher performing focusing schlieren device by directly controlling the cutoff grid opaque line separation. In addition to a more easily manufactured cutoff grid allowing a more parametric approach to the systems performance, the construction of the focusing schlieren system can become more standardized by largely taking the guess-work and art out of the traditional source grid

exposed cutoff grid construction.

7.3 Recommendations for Future Work

The dual-mode scramjet flow field represents a collection of highly complex and coupled flow regimes. The initial study of fundamental flow features such as the isolator shock train bodes well to the simplification of the flow replication. Initial observations regarding the effects of rectangular isolators on shock train three-dimensionality presented in this study can be used to motivate future work in facilities that more accurately portrays the scramjet flow field. Recommendations for future work are thus categorized in two distinct groups that would further improve the understanding of shock train dynamics: (a) additional work that can be performed in similar cold-flow atmospheric indraft wind tunnels, and (b) future work performed in facilities that incorporate a more realistic scramjet flow path.

- The experimental studies performed in this research focused on the effects of rectangular isolator aspect ratio, keeping the isolator inlet flow Mach number constant. Other parametric studies can be performed to grow the experimental data set regarding the three-dimensional shock front. Exploring the isolator operation modes set forth in Fig. 2.5 would continue to contribute to an unrepresented area in isolator shock train literature.

- Supplementary parametric studies, such as including variations in the incoming boundary layer thickness and turbulence levels, energizing the outboard boundary layer region through the introduction of rakes and wedges, or reducing the susceptibility of separation through boundary layer suction or bleed will likewise address some of the remaining questions in literature.

- Additional diagnostic techniques can be introduced to expand the experimental data base. Given the appropriate light source, the focusing schlieren technique can be utilized in the visualization configuration (Fig. 3.31). A high intensity coherent light source such as Copper vapor laser has been used successfully in the past (Ref [127]). Likewise, real time Pressure

Sensitive Paint (PSP) measurements can be utilized to render a global view of the near-wall boundary layer separation region behavior.

In the actual dual-mode scramjet cycle, the isolator is located between the low pressure isolator and higher pressure combustor regions. Different ground-test facility approaches can be taken to more realistically simulate the isolator flow field.

- Entropy matched conditions provided by higher isolator inlet plane temperatures will inevitably play a role in the thermal profile of the isolator boundary layer. It has been shown that higher temperature boundary layer profiles are less susceptible to separation (Ref. [159–161]), and thus can play an important role in the boundary layer separation driven physics of the transient isolator shock train. Likewise, increase viscosity effects must be studied in heated inflows.

- In flight conditions, the backpressure disturbances governing the isolator shock train dynamics are largely generated by combustion-induced flow blockage. Replacing the mechanical backpressure rise with a combustion driven one can explore the more complex isolator-combustor interactions. Fuel injection induced flow blockage is expected to be significantly more three-dimensional than the more uniform two-dimensional mechanical backpressure rise approach. Together with the preheated flow field, the effects of combustion driven backpressure rise need to be understood as part of improving confidence in the ground-test systems.

The steady state computational work carried out in this research was of secondary nature, prompting the use of the RANS modeling approach due to its flexible and easily implementable nature. Although favorable comparisons were made with experimental observations, the application of more direct approaches such as Large Eddy Simulations (LES) could vastly improve the understanding of the flow three-dimensionality in the duct, particularly in the region of the boundary layer/shock train interaction. Furthermore, more extensive time-dependent simulations can reveal additional information regarding the shock train dynamics within the duct.

Overall, it is shown that geometrically confined compressible flow interactions in rectangular ducts need to be studied from multiple perspectives if a thorough understanding of the flow features is to be derived. In particular, the performance of the isolator can no longer be evaluated on observations and measurements obtained along one axis alone. The experimental approaches developed in the pursuit of a better understanding of shock train/boundary layer interaction in a three-dimensional flow field can also be extended to a wide range of other flow regimes and geometries.

Chapter A: Derivations for Schlieren Based Diagnostic Techniques

The majority of the diagnostic techniques used to acquire the results discussed in Chapter 5 and 6 (multiplane shadowgraph, traditional schlieren/shadowgraph, Background Oriented Schlieren, and Focusing Schlieren Deflectometry) depend on the schlieren principle. The concept is introduced in Chapter 1 and Fig. 1.7, and is discussed in detail in this Appendix. The mathematical construct behind the schlieren effect contributed greatly to the optimization and refinement of the Background Oriented Schlieren and Focusing Schlieren Deflectometry techniques.

Figure A.2a-c shows the concept behind the schlieren effect, which is driven by two main principles: the frequency invariance and Huygen's principle [115]. The former states that the frequency of light rays remains independent of the medium through which it travels. As shown in Eq. A.1a-e, the speed of light through a medium c' is inversely proportional to the medium's index of refraction (Eq. A.1a). Likewise, the frequency of the light field strength variation ω is inversely proportional to the wavelength of the incident light λ (Eq. A.1c). Combining Eqn. A.1a and c provides the calculation of c' as a function of ω, λ, and n (Eq. A.1e). Applying the frequency invariance principle, we notice that since the frequency remains constant, the wavelength λ must decrease the same amount as the velocity ratio. Furthermore, since the wavelet wavelength λ_m increases for lower n, the wavelet radius will grow at a faster rate for lower n. This process is illustrated in Fig.A.2a-c, showing the state of three individual wavelets at an initial time $t = t_0$ and some later time $t = t_n$.

$$c' = \frac{c}{n} \tag{A.1a}$$

$$\lambda_m = \frac{\lambda}{n} \tag{A.1b}$$

$$\omega = \frac{c}{\lambda} \tag{A.1c}$$

$$\omega = \frac{c'n}{\lambda} \tag{A.1d}$$

$$c' = \frac{\omega\lambda}{n} \tag{A.1e}$$

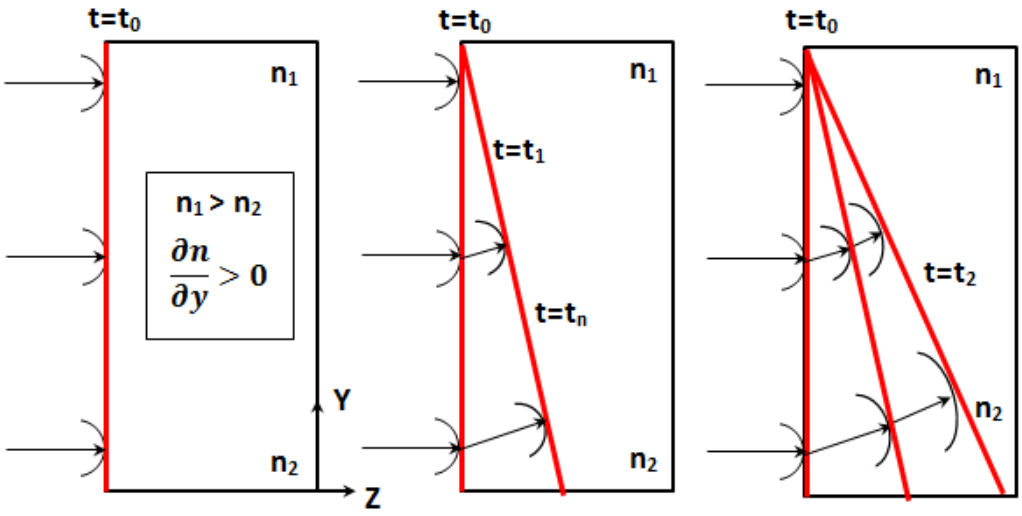

Figure A.1: Illustration of schlieren phenomena: frequency invariance and Huygen's principle.

The second driver behind the schlieren effect is Huygen's principle, which states that the light wave front is tangent to the wavelets shown in Fig. A.2a-c. Since the local speed of light is higher for lower n, wavelets propagate at a higher velocity and thus experience a faster growth. This causes the light wavefront to bend or refract toward regions with larger n, as is shown in Fig. A.2b-c. Quantifying this refraction magnitude as a function of the density gradient present in the flowfield is the principle upon which the BOS refinement process is based, as described in Chapter 4.

The frequency invariance and Huygen's principle can be used to derive the relationship between refraction angle and density gradient magnitude, repeated from Chapter 4 (Eq. 4.4) as Eq. A.2. The schlieren effect is illustrated in detail in Fig. A.2, with the derivation to follow based on the geometric interpretation of the wave front in Fig. A.2c.

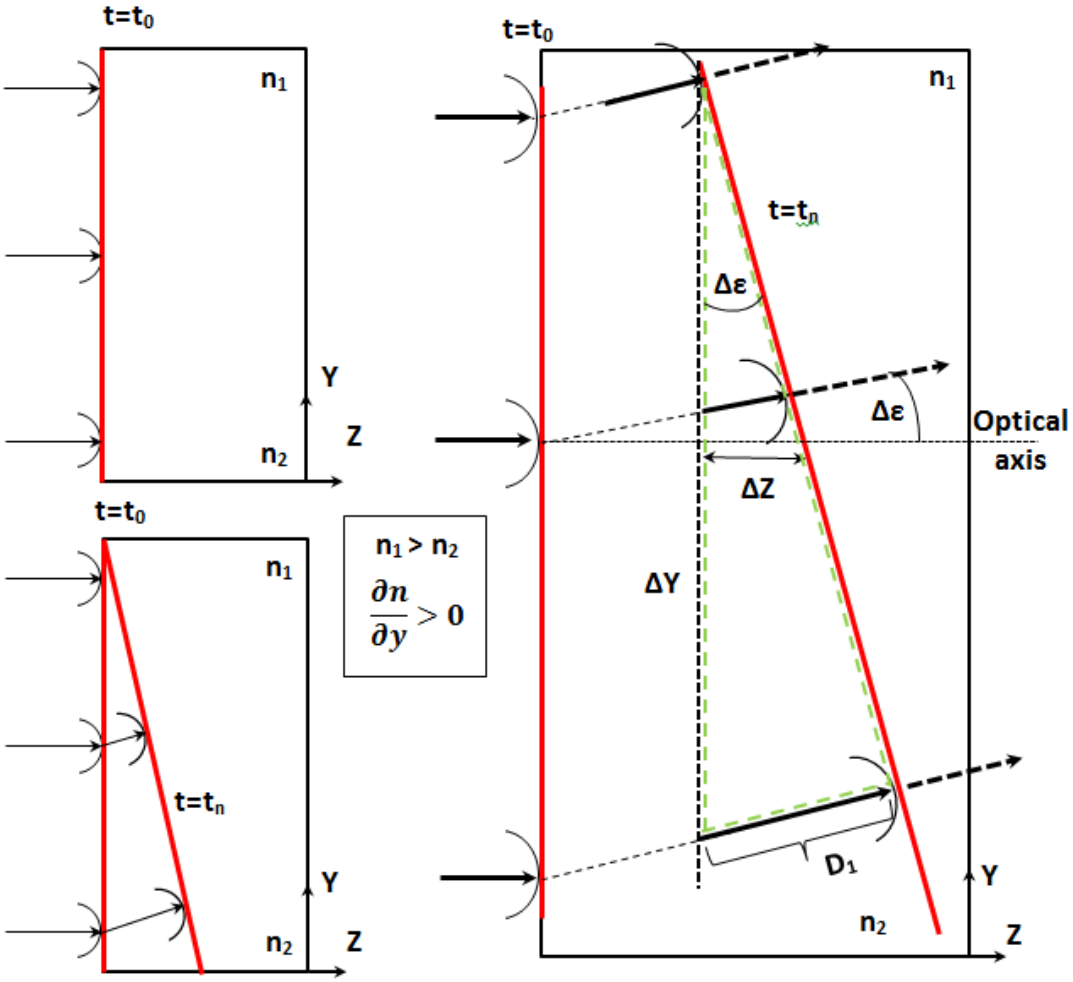

Figure A.2: Geometric interpretation of the schlieren phenomena.

$$\varepsilon = \frac{G(\lambda)}{n}\int_0^{Z_T}\frac{\delta\rho}{\delta x}dz = \frac{G(\lambda)}{n}\frac{\delta\rho}{\delta x}Z_T \tag{A.2}$$

The magnitude of the refraction of the light ray ($\Delta\epsilon$) is a function of: (1) the refraction index gradient, and (2) the distance over which the light ray propagates. Calculating the distance a light ray travels inside the medium involves the product between the velocity and the time spent traveling. This distance is also called the Optical Path Length (OPL). For the local speed of sound in the lower n_2 region of the test section, the distance (OPL_2) traveled becomes:

$$OPL_2 = \frac{c}{n_2}t \tag{A.3}$$

Calculating the difference in OPL between a region with low and high index of refraction yields the distance D_1:

$$D_1 = \frac{c}{n_2}\Delta t - \frac{c}{n_1}\Delta t = c_2'\Delta t - c_1'\Delta t \tag{A.4}$$

The light refraction angle is then calculated through a simple trigonometry relation and the small angle approximation is applied:

$$\sin(\Delta\epsilon) = \Delta\epsilon = \frac{\frac{c}{n_2}\Delta t - \frac{c}{n_1}\Delta t}{\Delta y} \tag{A.5a}$$

$$\Delta\epsilon = \frac{\frac{c}{n_2} - \frac{c}{n_1}}{\Delta y}\Delta t \tag{A.5b}$$

Since time of travel is the distance divided by velocity, the Δt term in Eqn. A.5 is replaced by Eqn. A.6a, allowing the calculation of $\Delta\epsilon$ according to Eqn. A.6b.

$$\Delta t = \frac{\Delta z}{\frac{c}{n}} = \frac{n}{c}\Delta z \tag{A.6a}$$

$$\Delta\epsilon = \frac{n}{c}\frac{\frac{c}{n_2} - \frac{c}{n_1}}{\Delta y}\Delta z \tag{A.6b}$$

Eqn. A.6b can be simplified by multiplying both sides of the equation by the product of $n_2 n_1$, according to Eqn. A.7a. Further cancellations result in Eqn. A.7b.

$$(n_2 n_1)\Delta\epsilon = \frac{n}{c}\frac{\frac{cn_2n_1}{n_1} - \frac{cn_2n_1}{n_1}}{\Delta y}\Delta z \tag{A.7a}$$

$$\Delta\epsilon = \frac{n}{n_2 n_1}\frac{n_1 - n_2}{\Delta y}\Delta z \tag{A.7b}$$

Equation A.7b is evaluated by taking the limit as Δy approaches zero. This results in a change of Δ reducing to an incremental change of d, the difference $(n_1 - n_2)$ reducing to dn, and the quotient $\frac{n}{n_1 n_2}$ reducing to $\frac{1}{n}$. Taking the limit as Δy goes to zero results in:

$$\frac{d\epsilon}{dz} = \frac{1}{n}\frac{dn}{dy} \tag{A.8}$$

Due to the small magnitude of the refraction angle, the incremental change in ϵ can be approximated as the slope of the refracted ray, according to

$$d\epsilon = \frac{dy}{dz} \tag{A.9a}$$

$$\frac{d(\frac{dy}{dz})}{dz} = \frac{1}{n}\frac{dn}{dy} = \frac{d^2y}{dz^2} \tag{A.9b}$$

The Z-axis integrated refractive index occurs in both the X- and Y-directions, providing the relations for $\frac{d^2x}{dz^2}$ and $\frac{d^2y}{dz^2}$ in Eqn. A.10.

$$\frac{d^2x}{dz^2} = \frac{1}{n}\frac{dn}{dx} \tag{A.10a}$$

$$\frac{d^2y}{dz^2} = \frac{1}{n}\frac{dn}{dy} \tag{A.10b}$$

Finally, Eqn. A.10 is integrated according to Eqn. A.11a (for $\frac{dn}{dy}$) to provide the components of ray deflection in the X- and Y-axis, provided by Eqns. A.11b-c:

$$\int \frac{d^2y}{dz^2} = \epsilon_y = \int_0^{Z_T} \frac{1}{n}\frac{dn}{dy}dz \tag{A.11a}$$

$$\epsilon_x = \frac{1}{n}\int_0^{Z_T} \frac{dn}{dx} dz \tag{A.11b}$$

$$\epsilon_y = \frac{1}{n}\int_0^{Z_T} \frac{dn}{dy} dz \tag{A.11c}$$

Eq. A.11 is the basis for the derivation of the relationship between the refraction angle and the density gradient through the Gladstone-Dale relation, as described in Chapter 4 (Eqns. 4.1-4.4)

Bibliography

[1] Curran, E., Heiser, W., and Pratt, D., "Fluid phenomena in scramjet combustion systems," *Annual Review of Fluid Mechanics*, Vol. 28, No. 1, 1996, pp. 323–360.

[2] Waltrup, P., "Liquid-Fueled Supersonic Combustion Ramjets: A Research Perspective," *Journal of Propulsion*, Vol. 3, No. 6, November-December 1987.

[3] Heiser, W., Pratt, D., Daley, D., and Mehta, U., "Technical Background," *Hypersonic Airbreathing Propulsion*, edited by P. J.S., American Institute of Aeronautics and Astronautics, 1994.

[4] Smayda, M., Vogel, P., Schultz, I., Hanson, R., Foelsche, R., Tsai, C., Cresci, D., and Goyne, C., "Hypervelocity Testing of a Dual-Mode Scramjet," *50th AIAA Aerospace Sciences Meeting inclduing the New Horizons Forum and Aerospace Exposition*, Nashville, TN, January 2012.

[5] Billig, F. S., "Combustion processes in supersonic flow," *Journal of Propulsion and Power*, Vol. 4, No. 3, 1988, pp. 209–216.

[6] Cockrell, C., Auslender, A., Guy, R. W., McClinton, C. R., and Welch, S. S.

[7] Sanders, B. W. and Weir, L. J., "Aerodynamic design of a dual-flow mach 7 hypersonic inlet system for a Turbine-Based Combined-Cycle hypersonic propulsion system," *AIAA 2008-030015, NASA/CR2008*, Vol. 215214, 2008.

[8] Olds, J. R., "Results of a Rocket-Based Combined-Cycle SSTO Design Using Parametric; MDO Methods," 1994.

[9] Curran, E. T. and Sull, F. D., "The Utilization of Supersonic Combustion Ramjet Systems at Low Mach Numbers," Tech. rep., DTIC Document, 1964.

[10] Billig, F., Waltrup, P., and Stockbridge, R., "Integral-rocket dual-combustion ramjets: a new propulsion concept," *Journal of Spacecraft and Rockets*, Vol. 17, No. 5, 1980, pp. 416–424.

[11] Curran, E. T., "Scramjet engines: the first forty years," *Journal of Propulsion and Power*, Vol. 17, No. 6, 2001, pp. 1138–1148.

[12] Penzin, V., "Experimental Investigation of Supersonic Flows with Separated Regions in Ducts." Tech. rep., DTIC Document, 1995.

[13] Chase, R. and Tang, M., "A history of the nasp program from the formation of the joint program office to the termination of the hystp scramjet performance demonstration program," *International Aerospace Planes and Hypersonics Technologies*, 1995, p. 6031.

[14] Kumar, A., Drummond, J., McClinton, C., and Hunt, J.

[15] Voland, R. T., Huebner, L. D., and McClinton, C. R., "X-43A hypersonic vehicle technology development," *Acta Astronautica*, Vol. 59, No. 1, 2006, pp. 181–191.

[16] McClinton, C. R., "X-43 Scramjet Power Breaks the Hypersonic Barrier: Dryden Lectureship in Research for 2006," *AIAA paper*, Vol. 1, 2006, pp. 2006.

[17] Springer, A., "50 Years of NASA Aeronautics Achievements," *46th AIAA Aerospace Sciences Meeting and Exhibit*, p. 859.

[18] Hank, J. M., Murphy, J. S., and Mutzman, R. C., "The X-51A scramjet engine flight demonstration program," *AIAA Paper*, Vol. 2540, 2008, pp. 2008.

[19] Rondeau, C. M. and Jorris, T. R., "X-51A Scramjet Demonstrator Program: Waverider Ground and Flight Test," Tech. rep., DTIC Document, 2013.

[20] Smart, M. K., Hass, N. E., and Paull, A., "Flight data analysis of the HyShot 2 scramjet flight experiment," *AIAA journal*, Vol. 44, No. 10, 2006, pp. 2366–2375.

[21] Dolvin, D., "Hypersonic International Flight Research and Experimentation (HiFiRE)," *AIAA paper*, Vol. 2581, 2008, pp. 2008.

[22] Bille, M. and Lorenz, R., "Requirements for a Conventional Prompt Global Strike Capability," Tech. rep., DTIC Document, 2001.

[23] Woolf, A. F., "Conventional prompt global strike and long-range ballistic missiles: background and issues," DTIC Document, 2014.

[24] WALTRUP, P. and BILLIG, F., "Precombustion shock structure in scramjet engines," *8th Joint Propulsion Specialist Conference*, 1972, p. 1181.

[25] Carroll, B. F. and Dutton, J. C., "Characteristics of multiple shock wave/turbulent boundary-layer interactions in rectangular ducts," *Journal of Propulsion and Power*, Vol. 6, No. 2, 1990, pp. 186–193.

[26] Shapiro, A. H., "The dynamics and thermodynamics of compressible fluid flow," *New York: Ronald Press, 1953-54*, Vol. 1, 1953.

[27] Nussdorfer, T. J., "Some observations of shock-induced turbulent separation on supersonic diffusers," Tech. rep., DTIC Document, 1954.

[28] Ikui, T., Matsuo, K., and NAGAI, M., "The mechanism of pseudo-shock waves," *Bulletin of JSME*, Vol. 17, No. 108, 1974, pp. 731–739.

[29] IKUI, T., MATSUO, K., and SASAGUCHI, K., "Modified diffusion model of pseudo-shock waves considering upstream boundary layers," *Bulletin of JSME*, Vol. 24, No. 197, 1981, pp. 1920–1927.

[30] Kim, H., *An experimental study of weak normal shock-wave/turbulent boundary-layer interaction in internal ows*, Ph.D. thesis, Ph. D. Thesis, Kyushu University, Japan, 1991.

[31] Matsuo, K., Miyazato, Y., and Kim, H.-D., "Shock train and pseudo-shock phenomena in internal gas flows," *Progress in Aerospace Sciences*, Vol. 35, No. 1, 1999, pp. 33–100.

[32] West, J. E. and Korkegi, R. H., "Supersonic interaction in the corner of intersecting wedges at high Reynolds numbers," *AIAA Journal*, Vol. 10, No. 5, 1972, pp. 652–656.

[33] Korkegi, R. H., "On the structure of three-dimensional shock-induced separated flow regions," *AIAA Journal*, Vol. 14, No. 5, 1976, pp. 597–600.

[34] Bruce, P., Burton, D., Titchener, N., and Babinsky, H., "Corner effect and separation in transonic channel flows," *Journal of Fluid Mechanics*, Vol. 679, 2011, pp. 247–262.

[35] Burton, D. and Babinsky, H., "Corner separation effects for normal shock wave/turbulent boundary layer interactions in rectangular channels," *Journal of Fluid Mechanics*, Vol. 707, 2012, pp. 287–306.

[36] Babinsky, H., Oorebeek, J., and Cottingham, T., "Corner effects in reflecting oblique shock-wave/boundary-layer interactions," *51st AIAA Aerospace Sciences Meeting p*, Vol. 859, 2013.

[37] Reda, D. C. and Murphy, J. D., "Shock wave/turbulent boundary-layer interactions in rectangular channels," *AIAA Journal*, Vol. 11, No. 2, 1973, pp. 139–140.

[38] Shang, J., Hankey, W., and Petty, J., "Three-dimensional supersonic interacting turbulent flow along a corner," *AIAA Journal*, Vol. 17, No. 7, 1979, pp. 706–713.

[39] Nedungadi, A. and Van Wie, D., "Understanding isolator performance operating in the separation-shock mode," *AIAA paper*, Vol. 3832, 2004, pp. 2004.

[40] Garnier, E., "Stimulated Detached Eddy Simulation of three-dimensional shock/boundary layer interaction," *Shock waves*, Vol. 19, No. 6, 2009, pp. 479–486.

[41] Baruzzini, D., Domel, N., and Miller, D. N., "Addressing corner interactions generated by oblique shock-waves in unswept right-angle corners and implications for high-speed inlets," *50th AIAA Aerospace Sciences Meeting: AIAA p*, Vol. 275, 2012.

[42] Bisek, N. J., "Sidewall Interaction of a Supersonic Flow over a Compression Ramp," .

[43] D'Ambrosio, D. and Marsilio, R., *Shock-induced separated structures in symmetric corner flows*, NASA Langley Research Center. Institute for Computer Applications in Science and Engineering [ICASE], 1995.

[44] Nikuradse, J., *Untersuchung über die Geschwindigkeitsverteilung in turbulenten Strömungen*, Vdi-verlag, 1926.

[45] Prandtl, L., *über den Reibungswiderstand stromenderluft*, Ergeb. Aerodyn. Versuch., 1927.

[46] Prandtl, L., *Essentials of fluid dynamics: With applications to hydraulics aeronautics, meteorology, and other subjects*, Hafner Pub. Co., 1952.

[47] Brundrett, E. and Baines, W., "The production and diffusion of vorticity in duct flow," *Journal of Fluid Mechanics*, Vol. 19, No. 03, 1964, pp. 375–394.

[48] Melling, A. and Whitelaw, J., "Turbulent flow in a rectangular duct," *Journal of Fluid Mechanics*, Vol. 78, No. 02, 1976, pp. 289–315.

[49] Hoagland, L. C., "FULLY DEVELOPED TURBULENT FLOW IN STRAIGHT RECTANGULAR DUCTS–SECONDARY FLOW, ITS CAUSE AND EFFECT ON THE PRIMARY FLOW (thesis). Technical Report No. 2," Tech. rep., Massachusetts Inst. of Tech., Cambridge, 1960.

[50] Gessner, F. and Jones, J., "On some aspects of fully-developed turbulent flow in rectangular channels," *Journal of fluid mechanics*, Vol. 23, No. 04, 1965, pp. 689–713.

[51] Launder, B. and Ying, W., "Prediction of flow and heat transfer in ducts of square cross-section," *Heat and Fluid Flow*, Vol. 3, No. 2, 1973.

[52] TAMAKI, T., TOMITA, Y., and YAMANE, R., "A study of pseudo-shock: 1st report, λ-type pseudo-shock," *Bulletin of JSME*, Vol. 13, No. 55, 1970, pp. 51–58.

[53] TAMAKI, T., TOMITA, Y., and YAMANE, R., "A study of pseudo-shock: 2nd report, X-type pseudo-shock," *Bulletin of JSME*, Vol. 14, No. 74, 1971, pp. 807–817.

[54] Om, D. and Childs, M. E., "Multiple transonic shock-wave/turbulent boundary-layer interaction in a circular duct," *AIAA journal*, Vol. 23, No. 10, 1985, pp. 1506–1511.

[55] Carroll, B. F. and Dutton, J. C., "Multiple normal shock wave/turbulent boundary-layer interactions," *Journal of Propulsion and Power*, Vol. 8, No. 2, 1992, pp. 441–448.

[56] Matsuo, K., Mochizuki, H., Miyazato, Y., and Gohya, M., "Oscillatory Characteristics of a Pseudo-Shock Wave in a Rectangular Straight Duct." *JSME International Journal Series B Fluids and Thermal Engineering*, Vol. 36, No. 2, 1993, pp. 222–229.

[57] Crocco, L., "One-dimensional treatment of steady gas dynamics," *Fundamentals of Gas Dynamics*, Vol. 3, 1958, pp. 183–186.

[58] Waltrup, P. and Billig, F., "Structure of shock waves in cylindrical ducts," *AIAA journal*, Vol. 11, No. 10, 1973, pp. 1404–1408.

[59] Billig, F. S., "Research on supersonic combustion," *Journal of Propulsion and Power*, Vol. 9, No. 4, 1993, pp. 499–514.

[60] Sullins, G. and McLafferty, G., "Experimental results of shock trains in rectangular ducts," *AIAA paper*, Vol. 5103, 1992.

[61] Liepmann, H. W. and Roshko, A., *Elements of gasdynamics*, Courier Corporation, 1957.

[62] Spalart, P. R. and Allmaras, S. R., "A one-equation turbulence model for aerodynamic flows," 1992.

[63] Menter, F. R., "Two-equation eddy-viscosity turbulence models for engineering applications," *AIAA journal*, Vol. 32, No. 8, 1994, pp. 1598–1605.

[64] Ferri, A., "Mixing-controlled supersonic combustion," *Annual Review of Fluid Mechanics*, Vol. 5, No. 1, 1973, pp. 301–338.

[65] Elghobashi, S., "Equilibrium chemical reaction of supersonic hydrogen-air jets (the ALMA computer program)," *NASA STI/Recon Technical Report N*, Vol. 77, 1977, pp. 16289.

[66] Knight, D., "Improved numerical simulation of high speed inlets using the Navier-Stokes equations," *18th Aerospace Sciences Meeting*, 1980, p. 383.

[67] White, M., Drummond, J., and Kumar, A., "Evolution and application of CFD techniques for scramjet engine analysis," *Journal of Propulsion and Power*, Vol. 3, No. 5, 1987, pp. 423–439.

[68] Zheltovodov, A., "Advances and problems in modeling of shock wave turbulent boundary layer interactions," *Proceedings of the International Conference on the Methods of Aerophysical Research, Novosibirsk, Russia, Part I*, 2004, pp. 149–157.

[69] Geerts, J. and Yu, K., "Corner Flow Separation from Shock Train/Turbulent Boundary-Layer Interactions in Rectangular Isolators," *20th AIAA/3AF International Space Planes and Hypersonic Systems and Technologies Conference*, 2015.

[70] Geerts, J. and Yu, K., "Shock Train Length Measurements and Improved Correlations for Rectangular Ducts," *The 22nd International Symposium on Air Breathing Engines*, 2015.

[71] Gessner, F., "The origin of secondary flow in turbulent flow along a corner," *Journal of Fluid Mechanics*, Vol. 58, No. 01, 1973, pp. 1–25.

[72] Gessner, F. B., "TURBULENCE AND MEAN-FLOW CHARACTERISTICS OF FULLY-DEVELOPED FLOW IN RECTANGULAR CHANNELS." 1964.

[73] Goebel, T. P., *A Theoretical Study of Inviscid, Supersonic Flow Along a Corner Formed by the Intersection of Two Wedges*, Ph.D. thesis, 1969.

[74] Korkegi, R. H., "Effect of transition on three-dimensional shock-wave/boundary-layer interaction," *AIAA Journal*, Vol. 10, No. 3, 1972, pp. 361–363.

[75] Charwat, A. F. and Redekeopp, L., "Supersonic interference flow along the corner of intersecting wedges." *AIAA Journal*, Vol. 5, No. 3, 1967, pp. 480–488.

[76] Morgan, B., Duraisamy, K., and Lele, S. K., "Large-eddy simulations of a normal shock train in a constant-area isolator," *AIAA journal*, Vol. 52, No. 3, 2014, pp. 539–558.

[77] Shang, J. and Hankey, W., "Numerical solution for supersonic turbulent flow over a compression ramp," *AIAA Journal*, Vol. 13, No. 10, 1975, pp. 1368–1374.

[78] Gessner, F. and Emery, A., "A Reynolds stress model for turbulent corner flowsPart I: Development of the model," *Journal of Fluids Engineering*, Vol. 98, No. 2, 1976, pp. 261–268.

[79] Hung, C. and MacCormack, R., "Numerical solution of three-dimensional shock wave and turbulent boundary-layer interaction," *AIAA Journal*, Vol. 16, No. 10, 1978, pp. 1090–1096.

[80] Shang, J. and Hankey, W., "Numerical solution of the Navier-Stokes equations for a three-dimensional corner," *AIAA Journal*, Vol. 15, No. 11, 1977, pp. 1575–1582.

[81] Jones, T. P. and Baumann, E., "Evaluation of the X-43A scramjet engine controller performance by Monte Carlo technique," *EVALUATION*, Vol. 20, 2003, pp. 23.

[82] Hurrell, H. G., *Analysis of shock motion in ducts during disturbances in downstream pressure*, National Advisory Committee for Aeronautics, 1957.

[83] Cole, G. L., Crosby, M. J., and Neiner, G. H., "Design and performance of a digital electronic normal shock position sensor for mixed-compression inlets," 1969.

[84] Dustin, M. O., Cole, G. L., and Wallhagen, R. E., "Determination of normal-shock position in a mixed compression supersonic inlet," 1971.

[85] Dustin, M. O. and Cole, G. L., "Performance comparison of three normal-shock position sensors for mixed-compression inlets," 1973.

[86] Dustin, M. O., Cole, G. L., and Neiner, G. H., "Continuous-output terminal-shock-position sensor for mixed-compression inlets evaluated in wind tunnel tests of YF-12 aircraft inlet," 1974.

[87] Lawrence D, H., Kenneth E, R., Edward G, R., David W, W., and Earl H, A., "Hyper-X Flight Engine Ground Testing for X-43 Flight Risk Reduction," 2001.

[88] Sajben, M., Donovan, J. F., and Morris, M. J., "Experimental investigation of terminal shock sensors for mixed-compression inlets," *Journal of Propulsion and Power*, Vol. 8, No. 1, 1992, pp. 168–174.

[89] Le, D. B., Goyne, C. P., Krauss, R. H., and McDaniel, J. C., "Experimental study of a dual-mode scramjet isolator," *Journal of Propulsion and Power*, Vol. 24, No. 5, 2008, pp. 1050–1057.

[90] Donbar, J. M., Linn, G. J., Srikant, S., and Akella, M. R., "High-frequency pressure measurements for unstart detection in scramjet isolators," *AIAA Paper*, Vol. 6557, 2010, pp. 2010.

[91] Srikant, S., Wagner, J., Valdivia, A., Akella, M., and Clemens, N., "Unstart detection in a simplified-geometry hypersonic inlet-isolator flow," *Journal of propulsion and power*, Vol. 26, No. 5, 2010, pp. 1059–1071.

[92] Hutzel, J. R., Decker, D. D., Cobb, R. G., King, P. I., Veth, M. J., and Donbar, J. M., "Scramjet isolator shock train location techniques," *49th AIAA Aerospace Sciences Meeting*, 2011, pp. 2011–402.

[93] Hu, J., Chang, J., Qin, B., Wang, L., Bao, W., and Qin, J., "Scramjet Isolator Shock-Train Leading-Edge Position Modeling Based on Equilibrium Manifold," *Journal of Aerospace Engineering*, 2013.

[94] Le, D. B., Goyne, C. P., and Krauss, R. H., "Shock train leading-edge detection in a dual-mode scramjet," *Journal of Propulsion and Power*, Vol. 24, No. 5, 2008, pp. 1035–1041.

[95] Le, D. B., "Scramjet Isolator Flow Studies," *fuel*, Vol. 1000, 2002, pp. 5.

[96] Wagner, J., Yuceil, K., Valdivia, A., Clemens, N., and Dolling, D., "Experimental investigation of unstart in an inlet/isolator model in Mach 5 flow," *AIAA journal*, Vol. 47, No. 6, 2009, pp. 1528–1542.

[97] Ikui, T. and Matsuo, K., "Researches of supersonic flow iwth teh shock wave as main subject," *Bulletin of JSME*, Vol. 72, No. 609, 1969, pp. 1306–12.

[98] Oka, T., Ono, D., and Miyazato, Y., "Study of Shock Trains and Pseudo-Shock Waves in Constant Area Ducts," .

[99] Fischer, C. and Olivier, H., "Experimental investigation of the shock train in an isolator of a scramjet inlet," *AIAA paper*, , No. 2011-2220, 2011.

[100] Tan, H.-J., Sun, S., and Yin, Z.-L., "Oscillatory flows of rectangular hypersonic inlet unstart caused by downstream mass-flow choking," *Journal of Propulsion and Power*, Vol. 25, No. 1, 2009, pp. 138–147.

[101] Fejer, A. A., Heath, G. L., and Driftmyer, R. T., "An Investigation of Constant Area Supersonic Flow Diffusion," Tech. rep., DTIC Document, 1964.

[102] Lustwerk, F., *The Influence of Boundary Layer on the" normal" Shock Configuration*, Massachusetts Institute of Technology, Guided Missiles Program, 1950.

[103] Rose, W. C., *A method for analyzing the interaction of an oblique shock wave with a boundary layer*, National Aeronautics and Space Administration, 1970.

[104] Billig, F., Dugger, G., and Waltrup, P., "Inlet-combustor interface problems in scramjet engines," *Institut de Mecanique des Fluides, International Symposium on Air Breathing Engines, 1 st, Marseille, France*, 1972, p. 1972.

[105] Billig, F., "Design of supersonic combustors based on pressure-area fields," *Symposium (International) on Combustion*, Vol. 11, Elsevier, 1967, pp. 755–769.

[106] Bement, D., Stevens, J., and Thompson, M., "Measured operating characteristics of a rectangular combustor/inlet isolator," *AIAA paper*, , No. 90-2221, 1990.

[107] Sullins, G., "Demonstration of mode transition in a scramjet combustor," *Journal of Propulsion and Power*, Vol. 9, No. 4, 1993, pp. 515–520.

[108] Rice, T., "High aspect ratio isolator performance for access-to-space vehicles," *AIAA*, Vol. 7041, 2003, pp. 2003.

[109] Selamet, A., Dicky, N., and Novak, J., "Theoretical, computational and experimental investigation of Helmholtz resonators with fixed volume: lumped versus distributed analysis," *Journal of sound and vibration*, Vol. 187, No. 2, 1995, pp. 358–367.

[110] Larcombe, M. and Peto, J., *The response times of typical transducer-tube configurations for the measurement of pressures in high-speed wind tunnels*, HM Stationery Office, 1966.

[111] Devenport, W. J. and Schetz, J. A., "Boundary layer codes for students in java," *ASME Fuids Engineering*, 1998.

[112] Schetz, J. A. and Bowersox, R. D., *Boundary layer analysis*, American Institute of Aeronautics and Aeronautics, 2010.

[113] Xu, S. and Martin, M. P., "Assessment of inflow boundary conditions for compressible turbulent boundary layers," *Physics of Fluids (1994-present)*, Vol. 16, No. 7, 2004, pp. 2623–2639.

[114] Smits, A. J. and Dussauge, J.-P., *Turbulent shear layers in supersonic flow*, Springer Science & Business Media, 2006.

[115] Settles, G. S., *Schlieren and shadowgraph techniques: visualizing phenomena in transparent media*, Springer Science & Business Media, 2012.

[116] Goldhahn, E. and Seume, J., "The background oriented schlieren technique: sensitivity, accuracy, resolution and application to a three-dimensional density field," *Experiments in Fluids*, Vol. 43, No. 2-3, 2007, pp. 241–249.

[117] Thielicke, W. and Stamhuis, E. J., "Pivlab-time-resolved digital particle image velocimetry tool for matlab," *Published under the BSD license, programmed with MATLAB*, Vol. 7, No. 0.246, 2010, pp. R14.

[118] Richard, H., Raffel, M., Rein, M., Kompenhans, J., and Meier, G., "Demonstration of the applicability of a background oriented schlieren (BOS) method," *Laser Techniques for Fluid Mechanics*, Springer, 2002, pp. 145–156.

[119] Atcheson, B., Heidrich, W., and Ihrke, I., "An evaluation of optical flow algorithms for background oriented schlieren imaging," *Experiments in fluids*, Vol. 46, No. 3, 2009, pp. 467–476.

[120] Schardin, H., "Schlieren methods and their applications," *Ergebnisse der Exakten Naturwissenschaften*, Vol. 20, 1942, pp. 303–439.

[121] Burton, R. A., "A modified schlieren apparatus for large areas of field," *JOSA*, Vol. 39, No. 11, 1949, pp. 907–907.

[122] Kantrowitz, A., "A sharp-focusing schlieren system," *Journal of the Aeronautical Sciences (Institute of the Aeronautical Sciences)*, Vol. 17, No. 5, 2012.

[123] Boedeker, L. R., *Analysis and construction of a sharp focussing Schlieren system*, Ph.D. thesis, Massachusetts Institute of Technology, 1959.

[124] Weinstein, L. M., "An improved large-field focusing schlieren system," *AIAA paper*, Vol. 567, 1991.

[125] McIntyre, S. and Settles, G., "Optical experiments on axisymmetric compressible turbulent mixing layers," *29th AIAA Aerospace Sciences Meeting*, Vol. 1, 1991.

[126] Jenkins, F. A., White, H. E., et al., "Fundamentals of physical optics," 1937.

[127] VanDercreek, C. P., Smith, M. S., and Yu, K. H., "Focused schlieren and deflectometry at AEDC hypervelocity wind tunnel No. 9," *AIAA Paper*, Vol. 4209, 2010.

[128] Floryan, D., Hofferth, J., and Saric, W., "Design, Assembly, and Calibration of a Focusing Schlieren System," .

[129] Hofferth, J., Humble, R., Floryan, D., and Saric, W., "High-bandwidth optical measurements of the second-mode instability in a Mach 6 quiet tunnel," *AIAA Paper*, Vol. 378, 2013, pp. 2013.

[130] Kovasznay, L. S., "Technique for the optical measurement of turbulence in high speed flow," *Heat Transfer Fluid Mechanics Institute, American Society of Mechanical Engineers, Berkeley, CA*, 1949.

[131] Clay, W., Herrmann, J., and Slattery, R., "Statistical properties of the turbulent wake behind hypervelocity spheres," *Physics of Fluids (1958-1988)*, Vol. 8, No. 10, 1965, pp. 1792–1801.

[132] Taylor, L. and Thompson, L., "Analysis of turbulence by schlieren photography," *AIAA Journal*, Vol. 7, No. 10, 1969, pp. 2030–2031.

[133] Garg, S. and Settles, G., "Measurements of a supersonic turbulent boundary layer by focusing schlieren deflectometry," *Experiments in Fluids*, Vol. 25, No. 3, 1998, pp. 254–264.

[134] Tsotsas, E. and Mujumdar, A. S., *Modern Drying Technology, Volume 3: Product Quality and Formulation*, Vol. 1, John Wiley & Sons, 2011.

[135] Hoffmann, K. A. and Chiang, S. T., "{Computational fluid dynamics, Vol. 1}," *Wichita, KS: Engineering Education System*, 2000.

[136] Tu, J., Yeoh, G. H., and Liu, C., *Computational fluid dynamics: a practical approach*, Butterworth-Heinemann, 2012.

[137] Blazek, J., *Computational Fluid Dynamics: Principles and Applications:(Book with accompanying CD)*, Elsevier, 2005.

[138] Kim, S. D. and Song, D. J., "Modified shear-stress transport turbulence model for supersonic flows," *Journal of aircraft*, Vol. 42, No. 5, 2005, pp. 1118–1125.

[139] Wilcox, D. C. et al., *Turbulence modeling for CFD*, Vol. 2, DCW industries La Canada, CA, 1998.

[140] Spalart, P., Jou, W., Strelets, M., and Allmaras, S., "Comments on the feasibility of LES for wings, and on a hybrid RANS/LES approach," *Advances in DNS/LES*, Vol. 1, 1997, pp. 4–8.

[141] Raffel, M., Tung, C., Richard, H., Yu, Y., and Meier, G., "Background oriented stereoscopic schlieren (boss) for full scale helicopter vortex characterization," *In 9th international symposium on flow visualization*, 2000, pp. 23–24.

[142] Kirmse, T., Agocs, J., Schröder, A., Schramm, J. M., Karl, S., and Hannemann, K., "Application of particle image velocimetry and the background-oriented schlieren technique in the high-enthalpy shock tunnel Göttingen," *Shock waves*, Vol. 21, No. 3, 2011, pp. 233–241.

[143] Hargather, M. J. and Settles, G. S., "Background-oriented schlieren visualization of heating and ventilation flows: HVAC-BOS," *HVAC&R Research*, Vol. 17, No. 5, 2011, pp. 771–780.

[144] Leopold, F., "The application of the colored background oriented schlieren technique (CBOS) to free-flight and in-flight measurements," *Instrumentation in Aerospace Simulation Facilities, 2007. ICIASF 2007. 22nd International Congress on*, IEEE, 2007, pp. 1–10.

[145] Vinnichenko, N.A., Z. I. G. F. U. A., "Study of Background Oriented Schlieren Method Accuracy by Means of Synthetic Images Analysis," *22nd International Symposium on 22nd International Symposium*, IEEE, 2011.

[146] Raffel, M., Willert, C. E., Wereley, S. T., and Kompenhans, J., *Particle Image Velocimetry*, Springer, 2007.

[147] Henderson, L., "The vector refraction law for shock waves," *Shock Waves*, Vol. 2, No. 2, 1992, pp. 103–112.

[148] Taub, A., "Refraction of plane shock waves," *Physical Review*, Vol. 72, No. 1, 1947, pp. 51.

[149] Markhotok, A. and Popovic, S., "Refractive phenomena in the shock wave dispersion with variable gradients," *Journal of Applied Physics*, Vol. 107, No. 12, 2010, pp. 123302.

[150] Adrian, R. J. and Westerweel, J., *Particle image velocimetry*, No. 30, Cambridge University Press, 2011.

[151] Nobach, H. and Honkanen, M., "Two-dimensional Gaussian regression for sub-pixel displacement estimation in particle image velocimetry or particle position estimation in particle tracking velocimetry," *Experiments in fluids*, Vol. 38, No. 4, 2005, pp. 511–515.

[152] Disimile, P. J., Toy, N., and Savory, E., "Effect of planform aspect ratio on flow oscillations in rectangular cavities," *Journal of fluids engineering*, Vol. 122, No. 1, 2000, pp. 32–38.

[153] Tam, C. K., "The acoustic modes of a two-dimensional rectangular cavity," *Journal of Sound and Vibration*, Vol. 49, No. 3, 1976, pp. 353–364.

[154] Rossiter, J., "Wind tunnel experiments on the flow over rectangular cavities at subsonic and transonic speeds," Tech. rep., Ministry of Aviation; Royal Aircraft Establishment; RAE Farnborough, 1964.

[155] Heller, H. H., Holmes, D., and Covert, E. E., "Flow-induced pressure oscillations in shallow cavities," *Journal of sound and Vibration*, Vol. 18, No. 4, 1971, pp. 545–553.

[156] Anderson, J. D., *Modern compressible flow: with historical perspective*, McGraw Hill Higher Education, 1990.

[157] White, F. M. and Corfield, I., *Viscous fluid flow*, Vol. 3, McGraw-Hill New York, 2006.

[158] Schlichting, H., "Boundary-layer theory," 1968.

[159] Liepmann, H. W. and Fila, G. H., "Investigation of effects of surface temperature and single roughness elements on boundary-layer transition," 1947.

[160] Chapman, D. R., "Temperature and velocity profiles in the compressible laminar boundary layer with arbitrary distribution of surface temperature," *Journal of the Aeronautical Sciences (Institute of the Aeronautical Sciences)*, Vol. 16, No. 9, 2012.

[161] Nosenchuck, D. M., "Passive and active control of boundary layer transition," 1982.